Testing Fundamental Lorentz Symmetries of Light

A thesis presented

by

Michael Andrew Hohensee

to

The Department of Physics

in partial fulfillment of the requirements

for the degree of

Doctor of Philosophy

in the subject of

Physics

Harvard University

Cambridge, Massachusetts

May 2009

Thesis advisor

Ronald L. Walsworth

Author

Michael Andrew Hohensee

Testing Fundamental Lorentz Symmetries of Light

Abstract

We explore the phenomenology of potential violations of Lorentz symmetry for electromagnetic fields. In particular, we focus on ways to constrain effects that would lead to isotropic variations of the vacuum speed of light from its canonical value c, which defines the Lorentz coordinate transformation. Using the framework provided by the Standard Model Extension (SME), we consider the consequences of such isotropic Lorentz symmetry violations on the saturation spectra of relativistic ions, the resonances of passive optical cavities, and the engineering of and observations made at high energy particle colliders. We show that fractional deviations of the speed of light in vacuum from c are constrained about zero by $-5.8 \times 10^{-12} \leq \tilde{\kappa}_{tr} \leq 1.2 \times 10^{-11}$. This improves upon previous limits by a factor of 1.2 million, implying that $-4 \text{ mm/s} \leq \Delta c \leq 2 \text{ mm/s}$.

This thesis is written from the standpoint of AMO physics, which has historically dedicated significant attention to the relativistic properties of light. We make the phenomenological predictions of the SME more accessible to the AMO and burgeoning Quantum Information communities by deriving the quantized Hamiltonian representation of the free Lorentz-violating electromagnetic potentials.

We also present theoretical studies of electromagnetically induced transparency (EIT) and the classical transport of quantum coherence in warm atomic ensembles enclosed in anti-relaxation coated vapor cells. We demonstrate that random classical transport of quantum coherence can be harnessed to coherently couple two or more optical modes. These coherent couplings are optically controllable, and can in the idealized limit be used to simulate the action of arbitrary optical elements.

Finally, we report on experiments regarding the stability of atomic frequency standards based on coherent population trapping (CPT) resonances. We demonstrate that the error signal produced by a CPT reference, used to stabilize a clock's electronic

oscillator, is the sum of many signals produced by the several optical sidebands used to produce and interrogate the CPT resonance. These sideband signals are generally more sensitive to fluctuations in the properties of the interrogating laser than the total clock signal. Our results suggest that these sidebands can be used to stabilize the laser without sacrificing the clock's short-term stability.

Contents

II   Coherent Phenomena in Anti-Relaxation Coated Cells and New Ways to Stabilize Atomic Frequency Standards   **97**

List of Figures

List of Tables

Papers and Publications

1. *Particle-Accelerator Constraints on Isotropic Modifications of the Speed of Light*
   M. A. Hohensee, R. Lehnert, D. F. Phillips, and R. L. Walsworth, Phys. Rev. Lett. 102, 170402 (2009).

2. *Slow-light dynamics from electromagnetically-induced-transparency spectra*
   M. Klein, M. A. Hohensee, Y. Xiao, R. Kalra, D. F. Phillips, and R. L. Walsworth, accepted to Phys. Rev. A (2009).

3. *The N+CPT Clock Resonance*
   M. Crescimanno and M. A. Hohensee, J. Opt. Soc. Am. B 25, 2130-2139 (2008).

4. *Slow Light Beamsplitter*
   Y. Xiao, M. Klein, M. A. Hohensee, L. Jiang, D. F. Phillips, M. D. Lukin, and R. L. Walsworth, Phys. Rev. Lett. 101, 043601 (2008).

5. *Lineshape Asymmetry for joint CPT and three photon N resonances*
   C. Hancox, M. A. Hohensee, M. Crescimanno, D. F. Phillips, and R. L. Walsworth, Opt. Lett. 33, 1536-1538 (2008).

6. *Optimizing slow and stored light for multidisciplinary applications*
   M. Klein, Y. Xiao, A. V. Gorshkov, M. A. Hohensee, C. Leung, M. R. Browning, D. F. Phillips, I. Novikova, and R. L. Walsworth, Proc. SPIE Int. Soc. Opt. Eng. 6904, 69040C (2008).

7. *Ives-Stilwell for the New Millenium*
   M. A. Hohensee, D. F. Phillips, and R. L. Walsworth, in V. A. Kostelecký, ed., Proceedings of the Fourth Meeting on CPT and Lorentz Symmetry, World Scientific, Singapore, (2008).

8. *Optimizing the storage and retrieval efficiency of a solid-state quantum memory through tailored state preparation* M. D. Eisaman, S. Polyakov, M. A. Hohensee, J. Fan, P. Hemmer, and A. Migdall, Proc. SPIE Int. Soc. Opt. Eng. 6780, 67800K (2007).

9. *Erratum: New methods of testing Lorentz violation in electrodynamics* M. A. Hohensee, A. Glenday, C.-H. Li, M. E. Tobar, and P. Wolf, Phys. Rev. D 75, 049902 (2007).

10. *Toward Manipulating Quantum Information Using Atomic Ensembles* M. D. Lukin, A. Andre, M. D. Eisaman, M. A. Hohensee, D. F. Phillips, C. H. van der Wal, R. L. Walsworth, and A. S. Zibrov, Proc. of the 18th Int. Conf. on At. Phys. (ICAP), (2002).

Acknowledgments

My thanks first go to my thesis advisor, Ron Walsworth, for providing support and excellent advice over the course of my doctoral studies. As his student, I have often been impressed by the way Ron can find simple, broadly relevant insights from seemingly arcanely specialized results. Thanks Ron, not only for being willing to take on a theory student like me, but also for giving me so much freedom and support in my choice of projects, and for sharing with me your unique perspective.

I would also like to thank David Phillips, who helped supervise much of my graduate research, for providing me with advice and moral support throughout my time here at Harvard, and generally acting as a second thesis advisor. I especially thank him for being willing to listen to my sometimes half-baked or otherwise crazy ideas, and for invariably providing thoughtful criticisms and suggestions. Thanks David, for all your help.

Thanks go to my former advisor, Mikhail Lukin, for the support and advice he provided during my first few years at Harvard, and especially for giving me the freedom to engage in theoretical pursuits even though it meant that I would spend less time in his laboratory. I'm also grateful for the friendship and the many helpful discussions I've had with the members of the Lukin group, especially Alexander Zibrov and Axel Andre, from whom I learned so much; and with Matthew Eisaman, Darrick Chang, Jacob Taylor, Liang Jiang, Michal Bajcsy, and Mohammad Hafezi.

Thanks also go to Itay Yavin, not least for his friendship, but also for inadvertently starting me down a path which led to the writing of a substantial portion of this thesis, and for our many stimulating conversations about physics and philosophy. I also want to thank my good friends and collaborators in the Walsworth group, especially Mason Klein, Alex Glenday, Rita Kalra, Matthew Rosen, Yanhong Xiao, Chih-Hao Li, Irina Novikova, and Cindy Hancox, as well as my further-flung collaborators, including Alan Migdall, Michael Crescimanno, Michael Tobar, and Ralf Lehnert. I am also grateful to V. Alan Kostelecký and Matthew Mewes for many helpful discussions.

Thanks are also due to those who have helped me learn how to think about the world around me. First and foremost are my parents, who both made great sacrifices to personally provide me with a wonderful education. I am also grateful to my grandmother Gerda Sanchez, for providing me with a complete high-school chemistry

lab; all my professors at New York University, including John Lowenstein, Andrew Kent, and Tycho Sleator. Special thanks go to Prof. Robert Richardson, for beating the tar out of us in his E&M and quantum mechanics courses.

Thanks again to my parents, Paul and Doris Hohensee, and to Aerin, Kira, Douglas, Gregory, and Dianna. I am also grateful to my mother-in-law Lisa Ellsworth, for driving so far, so often, to help Jen and I manage the sometimes conflicting demands of child-rearing and dissertation writing. Finally, my deepest thanks go to my wife Jennifer, and our son Friedrich. Your steadfast love, support, and encouragement have sustained me through what has at times been an arduous and frustrating process, and your companionship has made my successes the more joyous. Thank you, Jen, for being with me these past nine years. I look forward to many more.

The word is not the thing itself.
The map is not the territory.

–Gilbert Gosseyn

Part I

Testing Fundamental Lorentz Symmetries of Light

Chapter 1

Introduction

The atomic, molecular, and optical (AMO) physics community relies heavily upon the principle of Lorentz invariance in the pursuit of its research goals, as does the broader scientific community. Nature appears to hold Lorentz symmetry in high regard, and so we typically do not concern ourselves with the absolute orientation or motion of our experimental apparatus with respect to an unknown preferred coordinate system. Nor must we worry about the physical properties of our equipment subtly changing on a day to day basis as the Earth moves around the Sun. We can thus focus our attention on the more mundane variations that may be caused by changes in the local environment and component degradation.

The properties of light are of particular importance because, aside from gravity, electromagnetism dominates every aspect of our personal interactions with Nature. It is of particular importance to AMO physics, in that light is often the most precise standard of measure available to experimenters. This is in part the reason that the speed of light, $c \equiv 2.99792458 \times 10^8$ m/s has been elevated to the status of a fundamental constant, providing the basis for the definition of length in the International System of Units [1]. Experimental measures of the frame-independent isotropy of the speed of light have been carried out in one form or another since the early 1880's, and provided the inspiration for Special and General Relativity, which together have formed the cornerstone of our present extremely successful (if nevertheless incomplete) understanding of the laws of Nature.

Tests sensitive to Lorentz symmetry violations giving rise to shifts and anisotropies in the speed of light are of general interest to the study of high energy physics, since such symmetry breaking is a general feature of non-commutative field theories [2] and can also appear in theories which break the gravitational equivalence principle [3]. These effects can be phenomenologically understood using the effective field theory framework provided by the Standard Model Extension (SME) [4, 5]. The properties of the SME most relevant to this thesis are reviewed in Chapter 2. Modern versions of the famed Michelson-Morley experiment have ruled out anisotropies in the speed of light to the level of one part per 10^{18} [6, 7]. Given such results, it is then somewhat surprising that as late as 2005 [8–10], comparatively little could be said about the degree to which the speed of light might evidence *isotropic* deviations from its canonical value. As late as 2005, the best constraints on such isotropic violations of Lorentz symmetry were at the part per 10^5 level [8]. In Chapter 3 of this thesis, we demonstrate an improvement of this limit by more than five orders of magnitude, such that we can rule out the presence of an isotropic shift in the vacuum speed of light at the level of a few mm/s [10]. At the time of submission of this thesis, our result constitutes the world's best direct experimental constraint on isotropic variations in the speed of light [11].

As evidenced in the following chapters, the wide range of classical and quantum effects that even minute violations of Lorentz symmetry can generate is a testament to the deep impact that Einstein's Relativity postulates have had on the development of modern physics. In an effort to expand our understanding of how deeply these effects might be felt, we present in Chapter 4 a derivation of the quantized Hamiltonian for the free Lorentz-violating electromagnetic potential. Although the quantized Lagrangian representation of this theory has been known for some time [4,5], comparatively little has been known about the Hamiltonian representation of the quantized theory. This is of some concern, since most modern investigations of physics at low energy scales rely heavily on the Hamiltonian formalism. Such is the case for the AMO and quantum optics communities, and is doubly true of the relatively young field of quantum information. It is our hope that the work presented in Chapter 4 may be an aid in relating advances in the field of quantum information to a new

understanding of fundamental physics.

1.1 Historical Overview

Since Einstein's seminal work on the electrodynamics of moving bodies [12], where the theory of special relativity was first put forth, the properties of light, and in particular its speed of propagation through space, have played a central role in the development of modern physics. In his 1905 publication, Einstein offered the principle of relativity in the form of two postulates. *i)* the speed of light c is the same in all inertial frames, and *ii)* the laws of physics take the same form in all inertial frames. The first postulate was first used to define a system of time and space coordinates in one inertial frame S, and then to derive a relation between the coordinates of S and a similarly defined set of coordinates in the moving frame S'. This represented a comparatively simple derivation of the Lorentz-Fitzgerald [13] coordinate transformation, which replaces the Galilean transformation

$$
\begin{aligned}
t' &= t, & y' &= y, \\
x' &= x - vt, \quad \text{and} \quad z' &= z,
\end{aligned}
\tag{1.1}
$$

where the origin of S' moves with constant velocity $\vec{v} = v\hat{x}$ in the coordinates of S, with

$$
\begin{aligned}
t' &= \frac{1}{\sqrt{1 - (v/c)^2}} \left(t - \frac{vx}{c^2} \right), & y' &= y, \\
x' &= \frac{1}{\sqrt{1 - (v/c)^2}} \left(x - vt \right), \quad \text{and} \quad z' &= z.
\end{aligned}
\tag{1.2}
$$

This step, in conjunction with the requirement that the laws of physics be defined identically in all frames, allowed Einstein to straightforwardly demonstrate the theoretical unification of the electric and magnetic forces, by showing that the force exerted on a moving charge q by interaction with the magnetic field generated by an electric current could be understood as a purely electrostatic force after making the transformation (1.2) into the charge q's rest frame.

Since 1905, special relativity, also known as the principle of Lorentz invariance, has been demonstrated to apply extremely well to the physics of every known particle or field. Its broad application to virtually every field of scientific endeavor has significantly informed our present understanding of the Universe and made possible one of the greatest and most rapid expansions of mankind's theoretical and technological capabilities in human history. At this point, experience strongly suggests that Lorentz invariance is at least an approximate symmetry of Nature. The question as to whether it may be an exact symmetry, however, has yet to be answered. Although this problem must ultimately be resolved experimentally, our theoretical understanding of the properties of Lorentz symmetry have changed significantly since 1905. In particular, our view of the potential underlying causes of Lorentz violation has changed dramatically over the past century. Thus we begin this portion of the thesis with a brief historical review.

1.1.1   Early Demonstrations of Lorentz Invariance

The earliest experimental test of Lorentz invariance was carried out by Albert A. Michelson in 1881 [14], nearly a quarter century prior to Einstein's publication of the theory inspired by its results. Working under the assumption that electromagnetic waves represented propagating excitations of an underlying physical medium known as the ether, Michelson reasoned that the distance traveled by light moving back and forth between two fixed points on the Earth, as measured in the rest frame of the ether, must depend upon the orientation of the optical path relative to the Earth's motion through the ether. Specifically, if the Earth moves with velocity $\vec{v}$ through the ether, and V is the speed at which light propagates through the ether, then the time required for light to travel a distance D between two points on Earth is simply $2D/V$ if the light travels perpendicularly to $\vec{v}$, and $2DV/(V^2 - v^2)$ if it travels parallel to $\vec{v}$. By constructing an apparatus to interfere two beams of light which have traveled back and forth along perpendicular paths, and subsequently rotating this apparatus relative to the Earth, Michelson was able to demonstrate that the speed with which the Earth moves through the ether could be no larger than half of

the Earth's orbital velocity, provided that (1.1) holds. Subsequent experiments by Michelson and Morley [15] placed stronger constraints upon $\vec{v}$, while more recent tests have limited our speed relative to the ether to be no more than $|\vec{v}| \leq 0.3$ nm/s [6, 7].

The null result of the Michelson-Morley experiments was explained in 1904 by Hendrik A. Lorentz under the hypothesis that the linear dimension of an object moving with velocity $\vec{v}$ with respect to the ether must contract in the direction parallel to the motion [13]. This Lorentz-Fitzgerald contraction had the same functional form as the relativistic length contraction put forth by Einstein, and was thus formally consistent with special relativity, although the Lorentz-Fitzgerald model lacked the broader applicability of the postulates of relativity. These theoretical developments ultimately motivated the Kennedy-Thorndike experiments, in which one arm of a Michelson interferometer was shortened so as to make the resulting interference pattern sensitive to deviations of the time-dilation factor from that predicted by the Lorentz-Fitzgerald/relativistic coordinate transformations (1.2) [16].

As noted by Kennedy and Thorndike in [16] and derived in detail by Herbert E. Ives [17, 18], in the absence of additional constraints motivated by the theory, the null results of the Michelson-Morley and Kennedy-Thorndike experiments only constrained the properties of the Lorentz transformation such that the ratio of any relativistic length contraction along the boost velocity $\vec{v}$ to that which may occur at right angles to the motion must be

$$\left(\sqrt{1 - (v/c)^2}\right)^{n+1} : \left(\sqrt{1 - (v/c)^2}\right)^n, \tag{1.3}$$

and that the frequency shift due to time dilation experienced by a moving clock relative to a stationary one must be

$$\left(\sqrt{1 - (v/c)^2}\right)^{1-n} : 1. \tag{1.4}$$

The uncertainty regarding the proper value of n motivated Ives and G. R. Stilwell to make a direct measurement of the relativistic time dilation factor by isolating the transverse Doppler shift from light emitted by rapidly moving atoms, yielding results consistent with $n = 0$, and thus consistent with the Lorentz-Fitzgerald transformation [19].

1.1.2   Kinematic Models: The RMS Framework

Taken together, the results of the Michelson-Morley, Kennedy-Thorndike, and Ives-Stilwell tests provided experimental evidence that Nature's laws are consistent with the principle of Lorentz invariance. Indeed, as H. P. Robertson showed in 1949, it is possible to infer the principle of Lorentz invariance solely from their results [20]. Building upon Robertson's work, Reza Mansouri and Roman U. Sexl constructed a kinematic framework, commonly referred to as the Robertson-Mansouri-Sexl (RMS) framework, to test the postulates of relativity. In this model, the existence of a preferred frame Σ in which light travels isotropically at speed c is postulated, while the properties of light in all other frames is left undefined. The RMS Lorentz transformation from a frame S moving with velocity $-v\hat{x}$ relative to Σ becomes

$$
\begin{aligned}
T &= \frac{1}{a}(t + vx/c^2), \\
X &= x/b + \frac{v}{a}(t + vx/c^2), \\
Y &= y/d, \\
Z &= z/d,
\end{aligned}
\tag{1.5}
$$

or in terms of a boost from the preferred Σ frame into S,

$$
\begin{aligned}
t &= aT - bv(X - vT)/c^2, \\
x &= b(X - vT), \\
y &= dY, \\
z &= dZ,
\end{aligned}
\tag{1.6}
$$

where a, b, and d are arbitrary even functions of v/c which tend to 1 as $v \to 0$. The form of the infinitesimal RMS-framework Lorentz transformation can then be determined at any order in v/c by taking their expansion

$$
a = 1 + (\hat{\alpha} - 1/2)\left(\frac{v}{c}\right)^2 + \mathcal{O}\left[\left(\frac{v}{c}\right)^4\right],
\tag{1.7}
$$

$$
b = 1 + (\hat{\beta}^* + 1/2)\left(\frac{v}{c}\right)^2 + \mathcal{O}\left[\left(\frac{v}{c}\right)^4\right],
\tag{1.8}
$$

$$
d = 1 + \hat{\delta}\left(\frac{v}{c}\right)^2 + \mathcal{O}\left[\left(\frac{v}{c}\right)^4\right].
\tag{1.9}
$$

where we intend the symbol $\hat{\beta}^*$ to be distinct from the usual relativistic meaning of $\beta = v/c$. Comparison of (1.6) with (1.2) reveals that to second order in v/c, special relativity predicts $\hat{\alpha} = \hat{\beta}^* = \hat{\delta} = 0$. If this condition is not met, then the speed of light must generally be anisotropic in any but the preferred frame Σ. By 2003, modern versions of the Michelson-Morley, Kennedy-Thorndike, and Ives-Stilwell tests had constrained $|\hat{\beta}^* - \hat{\delta}| \leq 1.5 \times 10^{-9}$ [21], $|\hat{\alpha} - \hat{\beta}^*| \leq 6.9 \times 10^{-7}$ [22], and $|\hat{\alpha}| \leq 2.2 \times 10^{-7}$ [23].

The kinematic RMS framework provides a means to make predictions about the manner in which the two postulates of relativity may be violated, but is of limited use in determining the physics that such violations should be attributed to. Were a modern-day Michelson-Morley experiment to provide evidence that any of the RMS parameters were non-zero, it would immediately prompt us to ask whether massive particles obeyed the same velocity and time transformation laws. Questions of this kind cannot be adequately addressed by purely kinematic model with three parameters.

1.1.3 Dynamical Models: The Standard Model Extension

The principle of Lorentz invariance has been a cornerstone of both General Relativity (GR) and the Standard Model (SM) of particle physics. These theories have been used with great success to describe the laws of Nature, but have not as yet been fully reconciled with one another. Both GR and the SM are commonly believed to represent the low-energy limit of a single theory, unified at energies approaching the Planck scale (10^{19} GeV). The development of string theory has presented us with a variety of ways in which this unification might occur, but there is presently no way to directly probe physics at the Planck scale. This fact, coupled with the realization in the late 1980's that string theories could potentially give rise to spontaneous Lorentz symmetry violation at low energy scales [24, 25], has driven a resurgence of interest in tests of Lorentz invariance.

Such spontaneous Lorentz violation could occur if the vacuum states of the complete theory required some tensor-valued fields to acquire nonzero vacuum expectation

values (vevs) [24, 25]. Under these circumstances, the behavior of any fields which couple to such vevs would vary according to the orientation and boost of the chosen coordinates. Any low energy effective field theory that fails to account for the detailed (high energy) dynamics of the fields with nonzero vevs could then appear to violate the second postulate of Relativity.

The idea that physics at high energy scales can lead to broken symmetries at low energies is not new. In the context of the Standard Model, for example, the existence of a Higgs boson can be inferred from spontaneous violation of electroweak symmetry. Another example is presented by the phenomenon of ferromagnetism, where rotational symmetry in a system of fermions is spontaneously broken as it is cooled past the Curie temperature. Thus experimental searches for evidence of broken Lorentz symmetries are motivated by what light they may shed upon the properties of physics at high energy scales, much as we now use the breaking of the electroweak symmetry to infer the properties of the Higgs. In this context, experimental probes of Lorentz invariance can be motivated by the prospect of completing, rather than falsifying a Lorentz invariant theory.

As an aid to the development of a new generation of Lorentz symmetry tests, V. Alan Kostelecký and his collaborators have developed an effective field theory framework capable of describing arbitrary violations of Einstein's second postulate of Relativity, termed the Standard Model Extension (SME) [4, 5, 26]. The framework of the SME preserves both General Relativity and the Standard Model as limiting cases, while also providing all Lorentz-scalar operators that can be constructed from the SM fields which nevertheless violate Lorentz invariance. By systematic characterization of the physical consequences of Lorentz symmetry violation, the SME permits particular unification theories to be indirectly excluded on the basis of the effective field theory they produce at low energies. The SME has been the basis for the analysis of many experimental probes of Lorentz symmetry [11], including tests involving photons [6, 8, 9, 21, 27–45], electrons [46–62], protons and neutrons [63–77], as well as mesons, muons, neutrinos, the Higgs, and gravity [11].Note that since the SME makes no particular distinction as to the root cause of any Lorentz symmetry violations, it may also be used to describe Lorentz violation that does not arise spontaneously. It may

also be used to interpret the results of experimental measurements of the $\hat{\alpha}$, $\hat{\beta}^*$ and $\hat{\delta}$ coefficients of the kinematic RMS framework (see (1.9)), provided that a sufficiently detailed understanding of the experiment's physical components exists. The SME, however, offers us far greater specificity in understanding and constraining various underlying causes and consequences of Lorentz violation than is afforded by purely kinematic models.

1.2   Observer vs. Particle Lorentz Invariance

When evaluating a theory which is said to satisfy the twin postulates of relativity, *i.e.* that is Lorentz invariant, it is important to note that these postulates may be considered independently. The first postulate, when stripped of its specific relationship with the speed of light, simply indicates that the time and spatial coordinates of one inertial frame may be related to those of another inertial frame via a Lorentz transformation (equation (1.2)). The second postulate adds the further requirement that the laws of physics take the same form in all inertial frames related by the Lorentz transformation.

Theories which satisfy the first postulate may be said to be Lorentz invariant under changes in the observer's rest frame: things which move at the speed of light c will be observed to have the same speed in all inertial observer frames. This is often described as "observer Lorentz invariance". That this should be the case has more to do with our freedom to use an arbitrary set of coordinates to describe the behavior of a physical system without fear of affecting the experimental outcome by mere virtue of having made that choice. A more formal example of this fact may be found in [78], where the action for two massless scalar fields Ψ and Φ is written as:

$$S = \frac{1}{2} \int \sqrt{-g}\, d^4x \left(g^{\alpha\beta} \partial_\alpha \phi \partial_\beta \phi + (g^{\alpha\beta} + \tau^{\alpha\beta}) \partial_\alpha \psi \partial_\beta \psi \right), \qquad (1.10)$$

where $g^{\alpha\beta}$ and $\tau^{\alpha\beta}$ are arbitrary symmetric tensors which represent fixed (and potentially Lorentz-symmetry violating) background fields which are not necessarily equal to one another. If the action S is to be a physically meaningful quantity in a theory

describing the behavior of systems which do not particularly care about the coordinate system in which we describe them, it must be a Lorentz scalar. That is, S is invariant under all transformations applied equally to the coordinates x^μ, the Ψ and Φ fields, and the background fields $g^{\alpha\beta}$ and $\tau^{\alpha\beta}$. At the outset, we are free to choose coordinates such that either $g^{\alpha\beta}$ or $g^{\alpha\beta} + \tau^{\alpha\beta}$ equal $\eta^{\alpha\beta} = \mathrm{diag}(1, -1, -1, -1)$. After making this selection, we find that transformations of the defined coordinates of the form (1.2), leave both $\eta^{\alpha\beta}$ and the quantity S invariant. This implies that the evolution of any particular system, *e.g.* , particle velocities, sequences of events, as expressed in one inertial frame can be related to how that evolution would appear in any other inertial observer frame by a Lorentz transformation. Thus postulating that a physical theory must be invariant under Lorentz transformations of an observer's coordinates is actually an extremely powerful statement, as it implies that the evolution of a physical system is independent of the representation we choose for it. Although this idea is now commonly taken for granted by of the scientific community to the extent that it is rarely articulated, it should be noted that this was not the case for much of human history, and even today is not universally appreciated.

While Einstein's first postulate can be understood as being related to the fundamental problem of separating reality from our theoretical representations, his second postulate places a far stronger constraint upon those representations. It requires that the detailed form of each term in the integrand of (1.10) must be invariant under a Lorentz transformation. That is, the outcome of an experiment must not depend upon the inertial rest frame in which it is performed. In general, the second postulate can be enforced upon either the Ψ or the Φ fields by suitable choice of our initial coordinates. If $\tau^{\alpha\beta}$ is not the same (up to an overall constant) as $g^{\alpha\beta}$, however, the second postulate cannot hold for both Ψ and Φ in any one set of coordinates. This situation can occur if the dynamics of one or both of the two underlying $\tau^{\alpha\beta}$ or $g^{\alpha\beta}$ fields explicitly violate the second postulate, and also if $\tau^{\alpha\beta}$ and $g^{\alpha\beta}$ represent different vacuum expectation values of fields whose dynamics *are* fully Lorentz covariant. As noted in part 1.1.3, examples of such symmetry violations in fully consistent physical theories are easily found in both high energy and condensed matter physics.

Chapter 2

The Standard Model Extension

In this chapter, we provide an overview of the subset of the Standard Model Extension (SME) most relevant to this thesis, and outline some of the physical effects which are caused by violations of particle Lorentz covariance. Specifically, we focus upon the terms in the photon sector of the SME which do not give rise to birefringence, as described in part 2.2. Prior to the work described in Chapter 3, the isotropic contribution of these terms, parameterized by $\tilde{\kappa}_{tr}$, was one of the most poorly constrained parameters in the SME. Several of the results described in Chapter 3 rely upon the fact that Lorentz violation manifests itself as a frame-dependent variation in the laws of physics, and that the inertial frame which best approximates the coordinate system of an Earthbound laboratory changes slowly over the course of the sidereal day and year. This time-dependence is given in [28] to first order in the Earth's boost velocity $\vec{\beta}$, but the precision of the most recent experiments (see part 3.2) is such that useful bounds on Lorentz-violation can be obtained from doubly suppressed terms at second order in $\vec{\beta}$. Thus part 2.3 outlines the derivation of the $\tilde{\kappa}$ boost transformation to all orders in $\vec{\beta}$, leaving the derivation of the exact expression for Appendix A. In part 2.4, we review a subset of the matter-sector SME coefficients which have been shown [27, 28, 39, 79] to be equivalent up to a coordinate redefinition with the non-birefringent photon-sector SME coefficients, and describe the properties of the coordinate transformation that relates them in part 2.5. We begin by specifying the standard reference frame in which experimental constraints on the SME may

be conveniently related to one another.

2.1   The Sun-Centered Celestial Equatorial Frame

Observer Lorentz covariance requires the action to be a Lorentz scalar. As a result, Lorentz symmetry violation for particle transformations implies that the coefficients describing that violation be frame-dependent. This implies that all experimental constraints on Lorentz-violating couplings are invariably tied to the specific inertial frame in which the apparatus was constructed. Since the inertial frame approximating that of a laboratory fixed to the Earth's surface changes with time and geographic location as the Earth orbits the Sun (see part 2.3), comparisons between the constraints derived by different experiments cannot be accomplished without taking account of how the contributing SME parameters transform when written in different inertial frames. By convention, experimental bounds on terms in the SME are typically reported in terms of their values in the Sun-Centered Celestial Equatorial Frame (SCCEF).

The choice of the SCCEF, depicted in Figure 2.1, as the standard reference frame has a number of advantages. First and most obviously, the velocity of the Earth with respect to the Sun is well known, and can be straightforwardly tied to the date and time that experimental observations are made. Because the North-South polar axis of the SCCEF is aligned with the apparent rotation of the celestial sphere as seen from Earth, observations of astrophysical sources as seen from Earth can be easily related to how they would appear in the SCCEF by a simple boost and rotation about this axis.

For experiments performed in laboratories affixed to the Earth's surface, the transformation from the SCCEF to a laboratory frame in which the z-axis points vertically upwards, the y-axis points east, and the x-axis points south is given in [28] by the rotation matrix

$$R^{jJ} = \begin{pmatrix} \cos\chi\cos\omega_\oplus T_\oplus & \cos\chi\sin\omega_\oplus T_\oplus & -\sin\chi \\ -\sin\omega_\oplus T_\oplus & \cos\omega_\oplus T_\oplus & 0 \\ \sin\chi\cos\omega_\oplus T_\oplus & \sin\chi\sin\omega_\oplus T_\oplus & \cos\chi \end{pmatrix}, \tag{2.1}$$
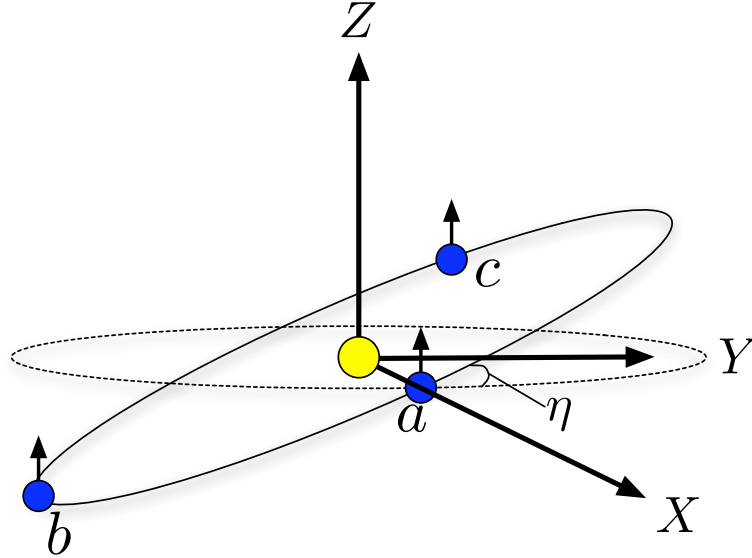
Figure 2.1: Schematic diagram of the Sun-Centered Celestial Equatorial Frame. Z is aligned along the Earth's orbital axis, while X points in the direction of the vernal equinox depicted with the Earth at point a. The dashed ellipse is aligned along the celestial equator, and is thus contained in the XY-plane. The solid ellipse represents the Earth's orbit, which is inclined relative to the celestial equator by $\eta \simeq 23.4°$. Shown at point b is the summer solstice for the northern hemisphere, while c lies between the autumnal equinox and the northern hemisphere's winter solstice.

where the upper case J denotes an index in the SCCEF, while the lower-case roman index j applies to an index in a frame which does not rotate relative to the laboratory. Here, χ is the colatitude of the laboratory, $\omega_\oplus \simeq 2\pi/(23 \text{ h } 56 \text{ min.})$ is the angular sidereal frequency of the Earth's rotation about its axis, and the time $T_\oplus$ is that measured in the SCCEF since the laboratory y-axis coincided with the Y-axis in the SCCEF. This rotation is followed by a boost $\vec{\beta}$. Taking $\Omega_\oplus$ as the Earth's orbital angular frequency, the speed of a fixed laboratory due to the Earth's daily rotation as $\beta_L = \omega_\oplus r_\oplus \sin\chi \lesssim 1.5 \times 10^{-6}$, and the time defined in the laboratory as T, we find that

$$\vec{\beta} = \beta_\oplus \begin{pmatrix} \sin\Omega_\oplus T \\ -\cos\eta\cos\Omega_\oplus T \\ -\sin\eta\cos\Omega_\oplus T \end{pmatrix} + \beta_L \begin{pmatrix} -\sin\omega_\oplus T_\oplus \\ \cos\omega_\oplus T_\oplus \\ 0 \end{pmatrix}, \tag{2.2}$$

where $\beta_\oplus \simeq 10^{-4}$ is the orbital speed of the Earth around the Sun, and $\eta \simeq 23.4°$ is the angle between the plane of the ecliptic and the equatorial XY plane of the SCCEF [28]. This transformation approximates the Earth as a perfect sphere in a circular orbit around the Sun.

By repeating a given experimental test of Lorentz symmetry at different times while the orientation and velocity of the laboratory varies in the SCCEF, different combinations of terms parameterizing Lorentz violation (as defined in the SCCEF) may be constrained. This not only broadens the reach of a given experiment, but can also serve to isolate the observed signals (or their absence) from common sources of systematic error. Since the laboratory frame returns to the same absolute orientation and velocity as measured in the SCCEF once every sidereal day and once a sidereal year, we may conclude that the physical effects of Lorentz symmetry violation must appear at harmonics of $\omega_\oplus$ and $\Omega_\oplus$ [5, 28]. This permits experimental analyses to straightforwardly ignore potentially spurious signals that may appear at other frequencies. For example, perturbations due to solar heating of the area surrounding the laboratory as well as most man-made sources of noise tend to repeat once every 24 hour solar day, which is not quite the sidereal day ($\sim$ 23.93 hrs). Shifts in the laboratory horizontal due to tidal effects or loading of the local water table will repeat after a period of the lunar cycle or solar year [80, 81], which are not exactly the same in sidereal time. Further isolation of the signal from particularly strong source of external noise can sometimes be achieved by active rotation of the experimental apparatus [31, 82].

2.2   Photon Sector

In the photon sector of the minimal SME, the conventional $-\frac{1}{4}F^2$ electromagnetic Lagrangian is augmented to become

$$\mathcal{L} = -\frac{1}{4}F_{\mu\nu}F^{\mu\nu} - \frac{1}{4}(k_F)_{\kappa\lambda\mu\nu}F^{\kappa\lambda}F^{\mu\nu} + \frac{1}{2}(k_{AF})^\kappa \epsilon_{\kappa\lambda\mu\nu}A^\lambda F^{\mu\nu}, \qquad (2.3)$$

where both (k_F) and (k_{AF}) break particle Lorentz symmetry. The (k_{AF}) term also breaks CPT symmetry, and has units of mass. The best constraints upon (k_{AF})

are derived from polarization studies of the cosmic microwave background, and are presently such that the magnitude of each of the four components is estimated to be no larger than $\sim 10^{-43}$ GeV [11, 83]. This is far below the scale at which the elements of (k_F) have been constrained, and is indeed far below the reach of any proposed experimental investigations, which are sensitive to (k_{AF}) at the level of $\sim 10^{-21}$ GeV [83, 84]. Accordingly, we will consider only models in which $(k_{AF}) = 0$ in our subsequent analyses. The (k_F) tensor has the symmetries of the Riemann tensor and a vanishing double trace, and thus actually represents only 19 independent parameters. The dimensionless (k_F) does not generate a photon mass, but instead imparts fractional variations in the phase velocity of electromagnetic waves propagating in a Lorentz-symmetry violating vacuum. These variations can depend upon the both the direction and polarization of the propagating wave. In [28], the (k_F) tensor is re-expressed in the more phenomenologically transparent form as

$$
\begin{aligned}
\mathcal{L} = \frac{1}{2} & \left[(1 + \tilde{\kappa}_{tr}) |\vec{E}|^2 - (1 - \tilde{\kappa}_{tr}) |\vec{B}|^2 \right] \\
& + \frac{1}{2} \left[\vec{E} \cdot (\tilde{\kappa}_{e+} + \tilde{\kappa}_{e-}) \cdot \vec{E} - \vec{B} \cdot (\tilde{\kappa}_{e+} - \tilde{\kappa}_{e-}) \cdot \vec{B} \right] + \vec{E} \cdot (\tilde{\kappa}_{o+} + \tilde{\kappa}_{o-}) \cdot \vec{B},
\end{aligned} \tag{2.4}
$$

where $\tilde{\kappa}_{tr}$ is a scalar; and the 3×3 $\tilde{\kappa}_{e+}$, $\tilde{\kappa}_{e-}$, $\tilde{\kappa}_{o-}$ matrices are traceless and symmetric, while $\tilde{\kappa}_{o+}$ is antisymmetric. In terms of (k_F), the $\tilde{\kappa}$'s are given by

$$
\begin{aligned}
(\tilde{\kappa}_{e+})^{jk} &= -(k_F)^{0j0k} + \frac{1}{4} \epsilon^{jpq} \epsilon^{krs} (k_F)^{pqrs} \\
(\tilde{\kappa}_{e-})^{jk} &= -(k_F)^{0j0k} - \frac{1}{4} \epsilon^{jpq} \epsilon^{krs} (k_F)^{pqrs} + \frac{2}{3} \delta^{jk} (k_F)^{0l0l} \\
(\tilde{\kappa}_{o+})^{jk} &= \frac{1}{2} \left((k_F)^{0jpq} \epsilon^{kpq} - (k_F)^{0kpq} \epsilon^{jpq} \right) \\
(\tilde{\kappa}_{o-})^{jk} &= \frac{1}{2} \left((k_F)^{0jpq} \epsilon^{kpq} + (k_F)^{0kpq} \epsilon^{jpq} \right) \quad \text{and} \quad \tilde{\kappa}_{tr} = -\frac{2}{3} (k_F)^{0l0l}.
\end{aligned} \tag{2.5}
$$

Sums on the repeated roman indices $j, k, m, p, q, r, s = 1, 2, 3$ are implied. We then define the electromagnetic fields, as originally outlined in [3–5] and [27, 28], as

$$
\begin{pmatrix} \vec{D} \\ \vec{H} \end{pmatrix} = \begin{pmatrix} 1 + \tilde{\kappa}_{e+} + \tilde{\kappa}_{e-} + I\tilde{\kappa}_{tr} & \tilde{\kappa}_{o+} + \tilde{\kappa}_{o-} \\ \tilde{\kappa}_{o+} + \tilde{\kappa}_{o-} & 1 + \tilde{\kappa}_{e+} - \tilde{\kappa}_{e-} - I\tilde{\kappa}_{tr} \end{pmatrix} \begin{pmatrix} \vec{E} \\ \vec{B} \end{pmatrix}, \tag{2.6}
$$

then the Lagrangian equations of motion derivable from (2.4) reduce to the form of the Maxwell equations in an anisotropic medium

$$\vec{\nabla} \times \vec{H} - c\,\partial_t \vec{D} = 0, \quad \vec{\nabla} \cdot \vec{D} = 0$$
$$\vec{\nabla} \times \vec{E} - c\,\partial_t \vec{B} = 0, \quad \vec{\nabla} \cdot \vec{B} = 0. \tag{2.7}$$

This implies that the general form of the solution to the wave equation in the Lorentz-violating vacuum is similar to that of a plane wave propagating in an anisotropic medium. We can immediately see that $\tilde{\kappa}_{tr}$ gives rise to an isotropic shift in the effective permeability and permittivity of the vacuum, and thus an isotropic and helicity-independent shift in the speed of light [28]. To determine the effects of the other $\tilde{\kappa}$'s, we need to solve the full dispersion relation. The analogy with electromagnetism in anisotropic media leads us to write the ansatz

$$\vec{E} = \vec{E}_0 e^{-i\omega t + i\vec{k}\cdot\vec{r}} \qquad \text{and} \qquad \vec{B} = \vec{B}_0 e^{-i\omega t + i\vec{k}\cdot\vec{r}}, \tag{2.8}$$

and require that ω, $\vec{k}$, and the fields satisfy the modified Ampère law [4, 5, 27, 28, 52]

$$\left(-\delta^{pq} k^2 - k^p k^q - 2(k_F)^{p\beta\gamma q} k_\beta k_\gamma \right) E^q = 0. \tag{2.9}$$

To leading order in (k_F), this modifies the dispersion relation between ω and $\vec{k}$, yielding

$$\omega_\pm = (1 + \rho \pm \sigma)|\vec{k}|c. \tag{2.10}$$

The $\pm$ subscript on ω and between ρ and σ denotes whether the wave has positive or negative helicity, so that ρ represents a polarization-independent shift of the phase velocity, while σ is a birefringent shift. In terms of (k_F), these parameters are

$$\rho = -\frac{1}{2}\tilde{k}_\alpha{}^\alpha, \qquad\qquad \sigma^2 = \frac{1}{2}\tilde{k}_{\alpha\beta}\tilde{k}^{\alpha\beta} - \rho^2, \tag{2.11}$$

where

$$\tilde{k}^{\alpha\beta} = (k_F)^{\alpha\mu\beta\nu}\hat{k}_\mu \hat{k}_\nu, \qquad\qquad \hat{k}_\mu = k_\mu/|\vec{k}| \tag{2.12}$$

and k_μ is the four-vector $(\omega/c, \vec{k})$, and the relativistic inner product is implied by pairs of repeated subscripted and superscripted greek indices: $A_\mu B^\mu = A_0 B_0 -$

$A_1 B_1 - A_2 B_2 - A_3 B_3$. The ρ and σ governing the dispersion relation for a plane wave propagating in the $+\hat{z}$ direction may be written in terms of the $\tilde{\kappa}$'s as [8]

$$\rho = -\tilde{\kappa}_{tr} + \frac{1}{2}\tilde{\kappa}_{e-}^{33} + \tilde{\kappa}_{o+}^{12} \tag{2.13}$$

and

$$\sigma^2 = \frac{1}{4}\left(\tilde{\kappa}_{o-}^{11} - \tilde{\kappa}_{o-}^{22} - 2\tilde{\kappa}_{e+}^{12}\right)^2 + \frac{1}{4}\left(\tilde{\kappa}_{e+}^{22} - \tilde{\kappa}_{e+}^{11} - 2\tilde{\kappa}_{o-}^{12}\right)^2. \tag{2.14}$$

Note that $\tilde{\kappa}_{tr}$, $\tilde{\kappa}_{o+}$, and $\tilde{\kappa}_{e-}$ govern the polarization-independent shifts, while $\tilde{\kappa}_{e+}$ and $\tilde{\kappa}_{o-}$ describe birefringence. Because the theory is invariant under observer rotations, this division holds for waves propagating in any direction. The division persists under boosts of the observer frame, since observer Lorentz covariance requires that observing birefringent phenomena in one inertial frame implies birefringence in all frames, while its absence in one frame implies its absence in all other frames[1].

The ten birefringent parameters $\tilde{\kappa}_{o-}$ and $\tilde{\kappa}_{e+}$ components of the (k_F) tensor have been constrained at the level of 10^{-37} by spectropolarimetric studies of light emitted from distant stars [27, 28, 37]. A comparatively weak constraint of 10^{-16} on the birefringent $\tilde{\kappa}$'s was obtained in [28] by searching for evidence of birefringence-induced time-splitting of short pulses of light emitted from distant millisecond pulsars and gamma-ray bursts. The far stronger constraint of 10^{-32} [28] and even 10^{-37} for some combinations of $\tilde{\kappa}_{o-}$ and $\tilde{\kappa}_{e+}$ [37] is derived from searches for characteristic correlations between the polarization and wavelength of light observed from distance sources. These constraints are far stronger than the best limits on the nine non-birefringent $\tilde{\kappa}_{tr}$, $\tilde{\kappa}_{o+}$, and $\tilde{\kappa}_{e-}$ parameters, and thus the contribution of the $\tilde{\kappa}_{o-}$ and $\tilde{\kappa}_{e+}$ matrices will be neglected in our subsequent analyses. Taking this approximation, we may write down the fractional shift $\rho(\vec{k})$ in the vacuum phase velocity of light moving in arbitrary directions in terms of its transverse polarization vectors

$$\rho(\vec{k}) = \left[\vec{\epsilon}_1(\vec{k}) \cdot \tilde{\kappa}_{o+} \cdot \vec{\epsilon}_2(\vec{k})\right] - \frac{1}{2}\sum_{r=1}^{2}\left[\vec{\epsilon}_r(\vec{k}) \cdot (\tilde{\kappa}_{e-} + I\tilde{\kappa}_{tr}) \cdot \vec{\epsilon}_r(\vec{k})\right], \tag{2.15}$$

---

[1]This division does *not* persist when the dispersion relation is solved to second order in (k_F). In particular, taking (2.9) to second order in $\tilde{\kappa}_{e-}^{33}$ reveals a fractional difference of $\frac{1}{2}\left(\tilde{\kappa}_{e-}^{33}\right)^2$ between the phase velocities of the two transverse modes propagating in the $+\hat{z}$ direction.

where for each $\vec{k}$, the transverse unit polarization vectors $\vec{\epsilon}_1(\vec{k})$ and $\vec{\epsilon}_2(\vec{k})$ satisfy

$$\vec{\epsilon}_1(\vec{k}) = \vec{\epsilon}_1(-\vec{k}) \quad \vec{\epsilon}_2(\vec{k}) = -\vec{\epsilon}_2(-\vec{k}),$$
$$\text{and} \quad \vec{\epsilon}_1(\vec{k}) \times \vec{\epsilon}_2(\vec{k}) = \hat{k}. \tag{2.16}$$

As an illustrative example of the roles played by the different non-birefringent $\tilde{\kappa}$ parameters, we see that for light traveling along the z-axis in the $+z$ direction, with $\vec{\epsilon}_1(k\hat{z}) = \hat{x}$ and $\vec{\epsilon}_2(k\hat{z}) = \hat{y}$,

$$\rho(k\hat{z}) = \tilde{\kappa}_{o+}^{xy} - \tilde{\kappa}_{tr} - \frac{1}{2}\left(\tilde{\kappa}_{e-}^{xx} + \tilde{\kappa}_{e-}^{yy}\right) = \tilde{\kappa}_{o+}^{xy} - \tilde{\kappa}_{tr} + \frac{1}{2}\tilde{\kappa}_{e-}^{zz}, \tag{2.17}$$

where we have taken advantage of the vanishing trace of $\tilde{\kappa}_{e-}$. For light traveling in the $-z$ direction, however, we find that

$$\rho(-k\hat{z}) = -\tilde{\kappa}_{o+}^{xy} - \tilde{\kappa}_{tr} + \frac{1}{2}\tilde{\kappa}_{e-}^{zz}, \tag{2.18}$$

since (2.16) specifies the sign of $\vec{\epsilon}_{1,2}(\vec{k})$ relative to $\vec{\epsilon}_{1,2}(-\vec{k})$. Thus we see that $\tilde{\kappa}_{tr}$ represents an isotropic fractional reduction in the vacuum phase velocity of light, $\tilde{\kappa}_{e-}$ describes the average shift in the speed of light propagating back and forth along a given axis, and $\tilde{\kappa}_{o+}$ governs the difference in the one-way speed of light along an axis.

The lack of extremely precise knowledge of the distance between the Earth and distant stars, combined with the absence of a cooperative race of aliens providing us with timing information, makes it difficult to directly discern the effects of the non-birefringent $\tilde{\kappa}$s on the vacuum speed of light. Most existing constraints upon these terms must therefore be derived from terrestrial experiments, although as we note in part 3.3.1, new constraints on the photon sector of the SME are likely to come from extended studies of the energy distribution and composition of ultra-high energy cosmic rays.

2.3   Frame-Dependence of $\tilde{\kappa}$

Although the Standard Model Extension is used to describe potential deviations in the behavior of physical systems from complete Lorentz symmetry, symmetry under observer boosts and rotations is preserved. As discussed in part 1.2, this means that

the action, *i.e.* , the value of the Lagrangian integrated over the course of a particular system's evolution in time from one configuration to another must be minimized in all inertial observer frames. This means that the action, and the Lagrangian itself must be a Lorentz scalar, and invariant under observer boosts. Because the Standard Model is itself term by term Lorentz covariant, and the electromagnetic vector potential A_μ in (2.3) transforms like any other covariant four-vector, we find that the transformation of the $\tilde{\kappa}$'s is nontrivial, as it must be if particle Lorentz invariance is to be broken.

To gain a more intuitive understanding of the mixing between $\tilde{\kappa}$'s under boosts, we may consider a simplified model for which, in a particular inertial frame F, only $\tilde{\kappa}_{tr}$ is nonzero. As discussed above, this causes an isotropic shift in the speed of light in the vacuum from its canonical value c. Since the theory is to remain Lorentz invariant under boosts of the observer frame, we may infer that the shifted velocity c_{ph} of any electromagnetic wave in F transforms like any other velocity when observed in a boosted frame F'. If $c_{ph} \neq c$ of a wave is isotropic in F, then its measured velocity in the boosted frame will be different, and in general anisotropic. To leading order in β, the phase velocity component of a wave parallel to the boost will decrease, while the anti-parallel component will be increased. The phase velocities of waves moving perpendicular to the boost in F' are the same as in F at leading order, but acquire identical shifts at second order in β. Thus we may conclude that $\tilde{\kappa}_{tr}$ and $\tilde{\kappa}_{o+}$ mix under boosts at leading order in β, while $\tilde{\kappa}_{tr}$ mixes with $\tilde{\kappa}_{e-}$ at second order. A similar argument may be used to show that $\tilde{\kappa}_{o+}$ and $\tilde{\kappa}_{e-}$ are also mixed at leading order in β. In principle, the complete transformation law can be inferred in a cumbersome fashion from the relativistic velocity addition formula applied to (2.15).

We will now use the Lorentz invariance of the Lagrangian (2.3) to derive the general form of the transformation of the $\tilde{\kappa}$ coefficients under an arbitrary boost $\vec{\beta}$ from one inertial frame to another. We are particularly interested in terms which appear at second order in $\vec{\beta}$. This work extends the perturbative treatment of such boosts previously reported in [28]. There, the transformation is given in terms of a

slightly different representation of the $\tilde{\kappa}$ matrices:

$$\kappa_{DE} = \tilde{\kappa}_{e+} + \tilde{\kappa}_{e-} + I\tilde{\kappa}_{tr}$$

$$\kappa_{HB} = \tilde{\kappa}_{e+} - \tilde{\kappa}_{e-} - I\tilde{\kappa}_{tr} \tag{2.19}$$

$$\kappa_{DB} = \tilde{\kappa}_{o+} + \tilde{\kappa}_{o-} = -\kappa_{HE}^T.$$

For a rotation in space described by the rotation matrix R^{jJ} and a boost β^Q, the leading order transformation is then

$$(\kappa_{DE})^{jk} = T_0^{jkJK}(\kappa_{DE})^{JK} - T_1^{jkJK}(\kappa_{DB})^{JK} - T_1^{kjJK}(\kappa_{DB})^{JK},$$

$$(\kappa_{HB})^{jk} = T_0^{jkJK}(\kappa_{HB})^{JK} - T_1^{jkKJ}(\kappa_{DB})^{JK} - T_1^{kjKJ}(\kappa_{DB})^{JK}, \tag{2.20}$$

$$(\kappa_{DB})^{jk} = T_0^{jkJK}(\kappa_{DB})^{JK} + T_1^{kjJK}(\kappa_{DE})^{JK} + T_1^{jkJK}(\kappa_{HB})^{JK},$$

with

$$T_0^{jkJK} = R^{jJ}R^{kK} \qquad \text{and} \qquad T_1^{jkJK} = R^{jP}R^{kJ}\epsilon^{KPQ}\beta^Q. \tag{2.21}$$

Since the publication of [28], a number of extremely sensitive Michelson-Morley tests have been carried out [6, 7, 21, 22, 29–31, 33, 82, 85]. Such experiments look for differences between the resonant frequencies of a pair of orthogonally mounted optical cavities which depend upon the cavities' orientation in space. Since the resonant frequency is determined by the total phase accumulated by a wave making a round trip within each cavity, and only the differences between the cavities' resonance frequencies contribute to the experimental observable, these tests are primarily sensitive to anisotropic shifts in the average speed of light in space, and thus to $\tilde{\kappa}_{e-}$ [28]. By repeating these experiments over extended periods as the laboratory frame is changed by the rotational and orbital motion of the Earth, the resulting constraints on the value of $\tilde{\kappa}_{e-}$ in a range of different (quasi) inertial frames may be used in conjunction with (2.20) to place weaker constraints upon the $\tilde{\kappa}_{o+}$ parameters. The sensitivity of modern Michelson-Morley experiments to $\tilde{\kappa}_{e-}$ has improved to the extent that they may be used (see part 3.2) to set useful constraints on the isotropic $\tilde{\kappa}_{tr}$ coefficient, despite its second order suppression [86].

We begin with the Lagrangian (2.4) written in terms of $\tilde{\kappa}$. The birefringent $\tilde{\kappa}_{e+}$ and $\tilde{\kappa}_{o-}$ do not mix with $\tilde{\kappa}_{e-}$, $\tilde{\kappa}_{o+}$ or $\tilde{\kappa}_{tr}$ under boosts, and in any case their contribution

to the physics has been constrained by [37] to be at least sixteen and in some cases twenty-one orders of magnitude smaller than any of the most tightly constrained non-birefringent parameters [11]. Dropping the birefringent terms, the Lagrangian in an arbitrary initial frame F is given by

$$\mathcal{L}_F = \frac{1}{2}\left[(1 + (\tilde{\kappa}_{tr})_F)|\vec{E}|^2 - (1 - (\tilde{\kappa}_{tr})_F)|\vec{B}|^2\right]$$
$$+ \frac{1}{2}\left[\vec{E}\cdot(\tilde{\kappa}_{e-})_F\cdot\vec{E} + \vec{B}\cdot(\tilde{\kappa}_{e-})_F\cdot\vec{B}\right] + \vec{E}\cdot(\tilde{\kappa}_{o+})_F\cdot\vec{B}, \tag{2.22}$$

where we have assigned the subscript F to the Lagrangian and to the $\tilde{\kappa}$'s to distinguish them from their values in other inertial frames. Given the dual requirements that the Lagrangian be conserved and that the $\vec{E}$ and $\vec{B}$ fields transform normally, deriving the transformation law is simply a matter of collecting terms. We may write the Lagrangian in terms of the SME coefficients and field variables as seen in the frame F' obtained by a boost of $\vec{\beta}$ from F as

$$\mathcal{L}_F = \mathcal{L}_{F'} = \frac{1}{2}\left[(1 + (\tilde{\kappa}_{tr})_{F'})|\vec{E}'|^2 - (1 - (\tilde{\kappa}_{tr})_{F'})|\vec{B}'|^2\right]$$
$$+ \frac{1}{2}\left[\vec{E}'\cdot(\tilde{\kappa}_{e-})_{F'}\cdot\vec{E}' + \vec{B}'\cdot(\tilde{\kappa}_{e-})_{F'}\cdot\vec{B}'\right] + \vec{E}'\cdot(\tilde{\kappa}_{o+})_{F'}\cdot\vec{B}'. \tag{2.23}$$

Then, since the transformed fields $\vec{E}'$ and $\vec{B}'$ can be written in terms of

$$\vec{E}' = \gamma\left(\vec{E} + \vec{\beta}\times\vec{B}\right) - \frac{\gamma^2}{\gamma+1}\left(\vec{\beta}\cdot\vec{E}\right)\vec{\beta}$$
$$\vec{B}' = \gamma\left(\vec{B} - \vec{\beta}\times\vec{E}\right) - \frac{\gamma^2}{\gamma+1}\left(\vec{\beta}\cdot\vec{B}\right)\vec{\beta}, \tag{2.24}$$

both $\mathcal{L}_F$ and $\mathcal{L}_{F'}$ can be written in terms of the unprimed fields. Since the particular configuration of $\vec{E}$ and $\vec{B}$ is arbitrary, $\mathcal{L}_F = \mathcal{L}_{F'}$ must be satisfied term by term for all terms proportional to $E_j E_k$, $B_j B_k$ and $E_j B_k$ (with $j, k \in \{1, 2, 3\}$) which may appear. The system of equations which results from imposing this term by term equality then yields the relation between $(\tilde{\kappa})_{F'}$ and $(\tilde{\kappa})_F$. From the form of (2.23), we see that many of the resulting expressions are trivial: The expression relating $(\tilde{\kappa}_{e-}^{jk})_F$ to $(\tilde{\kappa}_{e-}^{jk})_{F'}$ for $j \neq k$ is obtained from the equality between the coefficients multiplying $E_j E_k$, while that between $(\tilde{\kappa}_{o+}^{jk})_F$ and $(\tilde{\kappa}_{o+}^{jk})_{F'}$ may be read off by equating coefficients of $E_j B_k$.

From the form of the Lagrangian $\mathcal{L}_F$, we find that $(\tilde{\kappa}_{tr})_F$ is equal to a linear function of the coefficients of E_1^2, E_2^2, and E_3^2. Defining the function $\text{coef}(x, y)$ to be

the coefficient of x in an expression y, we may write these coefficients as

$$C_1 = \text{coef}(E_1^2, \mathcal{L}_F) \qquad C_2 = \text{coef}(E_2^2, \mathcal{L}_F) \qquad C_3 = \text{coef}(E_3^2, \mathcal{L}_F), \qquad (2.25)$$

and subsequently find that

$$
\begin{aligned}
(\tilde{\kappa}_{tr})_F &= \frac{2}{3}\left(C_1 + C_2 + C_3\right) - 1, \\
(\tilde{\kappa}_{e-}^{22})_F &= -\frac{2}{3}\left(C_1 - 2C_2 + C_3\right), \\
(\tilde{\kappa}_{e-}^{33})_F &= -\frac{2}{3}\left(C_1 + C_2 - 2C_3\right),
\end{aligned}
\qquad (2.26)
$$

where we have left out the redundant expression for $\tilde{\kappa}_{e-}^{11} = -\tilde{\kappa}_{e-}^{22} - \tilde{\kappa}_{e-}^{33}$, since $\tilde{\kappa}_{e-}$ is traceless in any frame. To second order in β, the resulting transformation law for the non-birefringent $\tilde{\kappa}$ is

$$
\begin{aligned}
\tilde{\kappa}_{tr}(\vec{\beta}) = {}& \left(1 + \frac{4}{3}|\vec{\beta}|^2\right)\tilde{\kappa}_{tr} + \frac{2}{3}(\beta_1^2 - \beta_2^2)\tilde{\kappa}_{e-}^{22} + \frac{2}{3}(\beta_1^2 - \beta_3^2)\tilde{\kappa}_{e-}^{33} \\
&- \frac{4}{3}\left(\beta_1\beta_2\tilde{\kappa}_{e-}^{12} + \beta_1\beta_3\tilde{\kappa}_{e-}^{13} + \beta_2\beta_3\tilde{\kappa}_{e-}^{23}\right) + \frac{4}{3}\left(\beta_3\tilde{\kappa}_{o+}^{12} - \beta_2\tilde{\kappa}_{o+}^{13} + \beta_1\tilde{\kappa}_{o+}^{23}\right),
\end{aligned}
\qquad (2.27)
$$

$$
\begin{aligned}
\tilde{\kappa}_{e-}^{22}(\vec{\beta}) = {}& \frac{2}{3}\left(|\vec{\beta}|^2 - 3\beta_2^2\right)\tilde{\kappa}_{tr} + \frac{1}{3}\left(\beta_1\beta_2\tilde{\kappa}_{e-}^{12} - 2\beta_1\beta_3\tilde{\kappa}_{e-}^{13} + \beta_2\beta_3\tilde{\kappa}_{e-}^{23}\right) \\
&+ \left[1 + \frac{1}{3}\left(|\vec{\beta}|^2 + \beta_2^2 - \beta_3^2\right)\right]\tilde{\kappa}_{e-}^{22} + \frac{1}{3}\left(\beta_1^2 - \beta_3^2\right)\tilde{\kappa}_{e-}^{33} \\
&+ \frac{2}{3}\left(\beta_3\tilde{\kappa}_{o+}^{12} + 2\beta_2\tilde{\kappa}_{o+}^{13} + \beta_1\tilde{\kappa}_{o+}^{23}\right),
\end{aligned}
\qquad (2.28)
$$

$$
\begin{aligned}
\tilde{\kappa}_{e-}^{33}(\vec{\beta}) = {}& \frac{2}{3}\left(|\vec{\beta}|^2 - 3\beta_3^2\right)\tilde{\kappa}_{tr} + \frac{1}{3}\left(-2\beta_1\beta_2\tilde{\kappa}_{e-}^{12} + \beta_1\beta_3\tilde{\kappa}_{e-}^{13} + \beta_2\beta_3\tilde{\kappa}_{e-}^{23}\right) \\
&+ \frac{1}{3}\left(\beta_1^2 - \beta_2^2\right)\tilde{\kappa}_{e-}^{22} + \left[1 + \frac{1}{3}\left(|\vec{\beta}|^2 + \beta_3^2 - \beta_2^2\right)\right]\tilde{\kappa}_{e-}^{33} \\
&- \frac{2}{3}\left(2\beta_3\tilde{\kappa}_{o+}^{12} + \beta_2\tilde{\kappa}_{o+}^{13} - \beta_1\tilde{\kappa}_{o+}^{23}\right),
\end{aligned}
\qquad (2.29)
$$

$$
\begin{aligned}
\tilde{\kappa}_{e-}^{12}(\vec{\beta}) = {}& \left(1 + \frac{1}{2}(\beta_1^2 + \beta_2^2)\right)\tilde{\kappa}_{e-}^{12} - 2\beta_1\beta_2\tilde{\kappa}_{tr} - \frac{1}{2}\beta_1\beta_2\tilde{\kappa}_{e-}^{33} \\
&+ \frac{1}{2}\left(\beta_2\beta_3\tilde{\kappa}_{e-}^{13} + \beta_1\beta_3\tilde{\kappa}_{e-}^{23}\right) + \beta_1\tilde{\kappa}_{o+}^{13} - \beta_2\tilde{\kappa}_{o+}^{23},
\end{aligned}
\qquad (2.30)
$$

$$\tilde{\kappa}_{e-}^{13}(\vec{\beta}) = \left(1 + \frac{1}{2}(\beta_1^2 + \beta_3^2)\right)\tilde{\kappa}_{e-}^{13} - 2\beta_1\beta_3\tilde{\kappa}_{tr} - \frac{1}{2}\beta_1\beta_3\tilde{\kappa}_{e-}^{22}$$
$$+ \frac{1}{2}\left(\beta_2\beta_3\tilde{\kappa}_{e-}^{12} + \beta_1\beta_2\tilde{\kappa}_{e-}^{23}\right) - \beta_1\tilde{\kappa}_{o+}^{12} - \beta_3\tilde{\kappa}_{o+}^{23}, \tag{2.31}$$

$$\tilde{\kappa}_{e-}^{23}(\vec{\beta}) = \left(1 + \frac{1}{2}(\beta_2^2 + \beta_3^2)\right)\tilde{\kappa}_{e-}^{23} - 2\beta_2\beta_3\tilde{\kappa}_{tr} + \frac{1}{2}\beta_2\beta_3\left(\tilde{\kappa}_{e-}^{22} + \tilde{\kappa}_{e-}^{33}\right)$$
$$+ \frac{1}{2}\left(\beta_1\beta_3\tilde{\kappa}_{e-}^{12} + \beta_1\beta_2\tilde{\kappa}_{e-}^{13}\right) - \beta_2\tilde{\kappa}_{o+}^{12} + \beta_3\tilde{\kappa}_{o+}^{13}, \tag{2.32}$$

$$\tilde{\kappa}_{o+}^{12}(\vec{\beta}) = \left(1 + \frac{1}{2}\left(|\vec{\beta}|^2 + 3\beta_3^2\right)\right)\tilde{\kappa}_{o+}^{12}$$
$$+ \beta_3(2\tilde{\kappa}_{tr} - \tilde{\kappa}_{e-}^{33}) - \beta_1\tilde{\kappa}_{e-}^{13} - \beta_2\tilde{\kappa}_{e-}^{23}$$
$$+ \frac{3}{2}\beta_3\left(\beta_2\tilde{\kappa}_{o+}^{13} - \beta_1\tilde{\kappa}_{o+}^{23}\right), \tag{2.33}$$

$$\tilde{\kappa}_{o+}^{13}(\vec{\beta}) = \left(1 + \frac{1}{2}\left(|\vec{\beta}|^2 + 3\beta_2^2\right)\right)\tilde{\kappa}_{o+}^{13}$$
$$- \beta_2(2\tilde{\kappa}_{tr} - \tilde{\kappa}_{e-}^{22}) + \beta_1\tilde{\kappa}_{e-}^{12} + \beta_3\tilde{\kappa}_{e-}^{23}$$
$$+ \frac{3}{2}\beta_2\left(\beta_3\tilde{\kappa}_{o+}^{12} + \beta_1\tilde{\kappa}_{o+}^{23}\right), \tag{2.34}$$

$$\tilde{\kappa}_{o+}^{23}(\vec{\beta}) = \left(1 + \frac{1}{2}\left(|\vec{\beta}|^2 + 3\beta_1^2\right)\right)\tilde{\kappa}_{o+}^{23}$$
$$+ \beta_1(2\tilde{\kappa}_{tr} + \tilde{\kappa}_{e-}^{22} + \tilde{\kappa}_{e-}^{33}) - \beta_2\tilde{\kappa}_{e-}^{12} - \beta_3\tilde{\kappa}_{e-}^{13}$$
$$- \frac{3}{2}\beta_1\left(\beta_3\tilde{\kappa}_{o+}^{12} - \beta_1\tilde{\kappa}_{o+}^{13}\right). \tag{2.35}$$

The general form of the transformation valid to all orders in $\vec{\beta}$ is derived in Appendix A. It is important to note that the transformation law derived here and in Appendix A is not necessarily valid for boosts with extremely large Lorentz factors. The Standard Model Extension Lagrangian, like any effective field theory, should not be confused with its exact form at energies high enough that corrections to known low energy physics become significant. As a consequence, the relations presented here and in Appendix A should be considered accurate for boosts with both small and large γ, with the caveat that the energies of particles moving with Lorentz factor γ remain far below the level at which the details of physics at high energy scale become important [87].

2.4 Matter Sector

As noted in part 1.2, some forms of Lorentz symmetry violation in the physics of a given particle can only be detected by comparison with the Lorentz symmetries of another species. Such is the case for the non-birefringent $\tilde{\kappa}$'s in the photon sector of the SME, since they may be written, using (2.11) and (2.12), as the symmetric $(k_F)_\alpha{}^{\mu\alpha\nu}$ tensor coupled to the electromagnetic potentials. Tests of the non-birefringent $\tilde{\kappa}$'s must therefore be understood as constraints on differences in Lorentz-violating effects experienced by different particle species relative to one another, with the particular values of the SME coefficients in our model determined by the coordinates we choose to work in. It is sometimes convenient to choose to work in coordinate systems for which parts of the photon sector or those of a particular portion of the matter sector of the SME are manifestly Lorentz covariant. In part 3.3 of this thesis, we use coordinates such that $\tilde{\kappa}_{tr}$ is mapped into its corresponding fermion-sector coefficients, so as to facilitate a fully quantized representation of the photon-fermion interaction. We therefore review a selection of the Lorentz-violating terms in the matter sectors of the SME. The general form of the minimal SME Dirac fermion is given by [4,5]

$$
\mathcal{L} = i\frac{1}{2}\overline{\psi}\left(\gamma_\nu + c_{\mu\nu}\gamma^\mu + d_{\mu\nu}\gamma_5\gamma^\mu + e_\nu + if_\nu\gamma_5 + \frac{1}{2}g_{\lambda\mu\nu}\sigma^{\lambda\mu}\right)\overset{\leftrightarrow}{\partial^\nu}\psi
$$
$$
- \overline{\psi}\left(m + a_\mu\gamma^\mu + b_\mu\gamma_5\gamma^\mu + \frac{1}{2}H_{\mu\nu}\sigma^{\mu\nu}\right)\psi, \tag{2.36}
$$

where the 4×4 γ-matrices are as usual defined in terms of the 2×2 identity matrix I and the Pauli matrices σ_k as

$$
\gamma^0 = \begin{pmatrix} I & 0 \\ 0 & -I \end{pmatrix}, \qquad \gamma^k = \begin{pmatrix} 0 & \sigma_k \\ -\sigma_k & 0 \end{pmatrix}, \qquad \gamma^5 = i\gamma^0\gamma^1\gamma^2\gamma^3, \tag{2.37}
$$

and a_μ, b_μ, $c_{\mu\nu}$, $d_{\mu\nu}$, e_ν, f_ν, $g_{\lambda\mu\nu}$ and $H_{\mu\nu}$ parameterize violations of particle Lorentz covariance. Here, we focus on the properties of the $c_{\mu\nu}$ coupling in the non-relativistic limit. Like the photon-sector (k_F) couplings, the fermion $c_{\mu\nu}$ term is both C and CPT-even, and includes both parity-even and parity-odd interactions.

Since the $c_{\mu\nu}$, $d_{\mu\nu}$, e_ν, f_ν and $g_{\lambda\mu\nu}$ coefficients parameterize extra time-derivative couplings, the modified Dirac equation resulting from (2.36) has a number of non-

hermitian terms. Thus quantization of this theory must be preceded by a field re-definition $\psi = A\chi$, where A is a constant term selected so that the Euler-Lagrange equations for the evolution χ are Hermitian to leading order in $c_{\mu\nu}$ and other terms. From [68], the field redefinition is given by

$$A = 1 - \frac{1}{2}\gamma^0 c_{\mu 0}, \qquad \text{and} \qquad \overline{A} = 1 - \frac{1}{2}c_{\mu 0}\gamma^0. \qquad (2.38)$$

Note that since $A = A^\dagger$ and $A = A^{-1}$ to leading order in $c_{\mu 0}$, this field redefinition may also be understood as a redefinition of the inner product, or metric, on the Hilbert space of fermion states. Such changes in metric are commonly necessary to find Hermitian representations of theories with P-odd but PT-even couplings [88], and are also used in the quantization of the electromagnetic potentials [89, 90]. Considering only the $c_{\mu\nu}$ coefficients, this field redefinition maps the Lagrangian (2.36) into

$$\begin{aligned} \mathcal{L} &= i\bar{\chi}\overline{A}(\gamma_\nu + c_{\mu\nu}\gamma^\mu) \overleftrightarrow{\partial^\nu} A\chi - m\bar{\chi}\overline{A}A\chi \\ &\simeq i\bar{\chi}\gamma_0 \overleftrightarrow{\partial^0} \chi - m\bar{\chi}\chi + i\bar{\chi}\left([1 - c_{00}]\gamma_j + (c_{0j} + c_{j0})\gamma^0 + c_{kj}\gamma^k\right) \overleftrightarrow{\partial^j} \chi, \end{aligned} \qquad (2.39)$$

to leading order in $c_{\mu 0}$. The Euler-Lagrange equation

$$\frac{\partial \mathcal{L}}{\partial \chi} = \partial_\alpha \left(\frac{\partial \mathcal{L}}{\partial(\partial_\alpha \chi)}\right) \qquad (2.40)$$

then yields the form of the modified Dirac Hamiltonian:

$$i\partial_0 \chi^\dagger = -m\chi^\dagger \gamma^0 - i\partial_j \chi^\dagger \gamma^0 \left([1 - c^{00}]\gamma^j + (c^{0j} + c^{j0})\gamma_0 + c^{kj}\gamma_k\right). \qquad (2.41)$$

In the Lorentz-covariant theory of Dirac fermions, the non-relativistic Pauli Hamiltonian for the particle or antiparticle components of the fully relativistic Dirac Hamiltonian is obtained by a series of Foldy-Wouthuysen (FW) transformations [91]. The FW transformation can be understood as a series of unitary transformations that eliminate or suppress the particle-antiparticle interaction in terms of a transformed Hamiltonian operator equivalent to the Pauli Hamiltonian. In [68], a series of FW transformations is employed to obtain the relativistic free fermion Hamiltonian

$$H = \gamma m c^2(1 - c_{00}/\gamma) + (c_{0j} + c_{j0})p_j c - (c_{jl} + c_{00}\delta_{jl})\frac{p_j p_l}{\gamma m}, \qquad (2.42)$$

where γ is the fermion's Lorentz factor $(1-\beta^2)^{-1/2}$. Note that unlike the theory arising from the non-birefringent terms in the photon-sector of the SME, the Hamiltonian (2.42) can be straightforwardly quantized by identification of the momenta p_j as operators, and has been demonstrated to be both stable and causal under observer Lorentz transformations in some cases [68, 87].

2.5 Coordinate Redefinitions

As noted in part 1.2, our freedom to choose the system of coordinates in which we express the observer Lorentz covariant Lagrangian makes it impossible to define some forms of particle Lorentz symmetry violation for one sector of the SME independently of the others. Such is the case for the non-birefringent photon-sector (k_F) and the components of the matter-sector $c_{\mu\nu}$ interaction which contribute to the free particle Hamiltonian (2.42). Both the non-birefringent (k_F)'s and the fermion $c_{\mu\nu}$'s parameterize derivative couplings with forms similar to terms appearing in the fully covariant theory. As a consequence, they are susceptible to being eliminated to first order by a simple coordinate transformation. As an illustrative example, we consider the transformation which maps the non-birefringent (k_F)'s to zero. As previously noted [27, 28, 39, 79], this transformation is given by

$$x'^{\mu} = x^{\mu} - \frac{1}{2}(k_F)^{\alpha\mu}{}_{\alpha\nu}x^{\nu}, \tag{2.43}$$

which maps the derivatives according to

$$\partial'_{\mu} = \frac{\partial}{\partial x'^{\mu}} = \frac{\partial x^{\lambda}}{\partial x'^{\mu}}\partial_{\lambda} \tag{2.44}$$

or

$$\partial'_{\mu} = \left(\delta^{\mu}_{\lambda} - \frac{1}{2}(k_F)^{\alpha\mu}{}_{\alpha\nu}\delta^{\nu}_{\lambda}\right)\partial_{\lambda}. \tag{2.45}$$

Application of (2.43) to the photon-sector Lagrangian (2.3) and neglecting the birefringent terms in (k_F) and the (k_{AF}) term maps the Lorentz-violating theory into the fully covariant $-\frac{1}{4}F^2$ theory at leading order in (k_F), although some terms persist at second order. The effect of this transformation is perhaps more intuitively

understood when it is written explicitly in terms of $\tilde{\kappa}_{e-}$, $\tilde{\kappa}_{o+}$, and $\tilde{\kappa}_{tr}$. Defining $\vec{\kappa}_{o+} \equiv (\tilde{\kappa}_{o+}^{23}, \tilde{\kappa}_{o+}^{31}, \tilde{\kappa}_{o+}^{12})$, (2.43) becomes

$$
\begin{aligned}
t &= \left(1 - \frac{3}{4}\tilde{\kappa}_{tr}\right)t' - \frac{1}{2c}\vec{\kappa}_{o+} \cdot \vec{x'}, \\
\vec{x} &= \vec{x'} - \frac{1}{2}\left(\tilde{\kappa}_{e-} - \frac{1}{2}\tilde{\kappa}_{tr}\right) \cdot \vec{x'} + \frac{c}{2}\vec{\kappa}_{o+}t',
\end{aligned}
\tag{2.46}
$$

so that velocities are modified by

$$
\vec{v'} = \vec{v} - \frac{1}{2}\left(\tilde{\kappa}_{e-} - 2\tilde{\kappa}_{tr}\right) \cdot \vec{v} + c\vec{\kappa}_{o+} + \mathcal{O}\left((k_F)^2\right).
\tag{2.47}
$$

Comparison of (2.47) with (2.15) reveals that the speed of light is no longer anisotropic, but is instead always equal to c in the new coordinates. This can be also confirmed by examination of the transformed dispersion relation.

Although (2.43) eliminates most of the Lorentz violating physics from the photon sector, it does not leave the matter sector unaffected. Under this redefinition of coordinates, the matter-sector $c_{\mu\nu}$ coefficients are shifted to become $c'_{\mu\nu} = c_{\mu\nu} - \frac{1}{2}(k_F)^\alpha{}_{\mu\alpha\nu}$ [27,28,39,79]. For the case of an otherwise fully Lorentz covariant fermion, this mapping can be written as

$$
\begin{bmatrix}
c'_{00} & c'_{01} & c'_{02} & c'_{03} \\
c'_{10} & c'_{11} & c'_{12} & c'_{13} \\
c'_{20} & c'_{21} & c'_{22} & c'_{23} \\
c'_{30} & c'_{31} & c'_{32} & c'_{33}
\end{bmatrix}
= \frac{1}{2}
\begin{bmatrix}
-\frac{3}{2}\tilde{\kappa}_{tr} & \tilde{\kappa}_{o+}^{23} & \tilde{\kappa}_{o+}^{31} & \tilde{\kappa}_{o+}^{12} \\
\tilde{\kappa}_{o+}^{23} & \tilde{\kappa}_{e-}^{11} - \frac{1}{2}\tilde{\kappa}_{tr} & \tilde{\kappa}_{e-}^{12} & \tilde{\kappa}_{e-}^{13} \\
\tilde{\kappa}_{o+}^{31} & \tilde{\kappa}_{e-}^{12} & \tilde{\kappa}_{e-}^{22} - \frac{1}{2}\tilde{\kappa}_{tr} & \tilde{\kappa}_{e-}^{23} \\
\tilde{\kappa}_{o+}^{12} & \tilde{\kappa}_{e-}^{13} & \tilde{\kappa}_{e-}^{23} & \tilde{\kappa}_{e-}^{33} - \frac{1}{2}\tilde{\kappa}_{tr}
\end{bmatrix}.
\tag{2.48}
$$

The freedom to arbitrarily define the coordinates in which to analyze a given experiment, coupled with the consequences of this choice for the non-birefringent $\tilde{\kappa}$'s and $c_{\mu\nu}$ coefficients is a reflection of the fact that experimental measurements of the speed of light (or indeed the of the maximum attainable speed of any particle species) must always depend on the properties of the particles used to define a standard reference. This means that any constraint on the non-birefringent components of (k_F) is always more generally expressed as a constraint on the difference $(k_F)^\alpha{}_{\mu\alpha\nu} - 2c_{\mu\nu}^X$, where $c_{\mu\nu}^X$ is the SME c-coefficient for some species of fundamental particle, or an effective c-coefficient for some composite particle which may serve as a standard reference in the experiment it is derived from.

Many reported constraints on various terms in the SME are derived under the assumption that SME coefficients vanish for particles other than those targeted for investigation. This step is often justified when prior constraints on the neglected parameters rule out any significant contribution to the experimental observable, or when the term specifically constrained by the analysis would clearly dominate all other terms at the level to which it is ultimately constrained. Analyses in which the $c_{\mu\nu}$ for just one species *or* the non-birefringent (k_F) coefficients are arbitrarily set to zero are likewise unambiguous, as such assumptions are equivalent to specifying the coordinate system. Results derived from analyses that arbitrarily ignore the *c*-coefficients or other SME parameters in multiple species [44, 45] are typically not directly comparable to other experimental limits.

In addition to the convenience afforded by being able to arbitrarily set the matter-sector $c_{\mu\nu}$ coefficients of a particular species to zero [21], the freedom to choose coordinates is also used to zero the non-birefringent components of (k_F) whenever quantized descriptions of the SME are required. It should be noted that the geometry of an experiment is generally not left unaffected by this coordinate redefinition.

Chapter 3

New Constraints on Isotropic Violations of Lorentz Symmetry

We now turn to the subject of setting improved limits on isotropic violations of Lorentz symmetry for light. In part 3.1, we demonstrate that constraints on the RMS $\hat{\alpha}$ parameter (described in part 1.1.2) derived from Ives-Stilwell experiments are equivalent to constraints on the isotropic $\tilde{\kappa}_{tr}$ coefficient from the photon sector of the SME. This result is then used to set a baseline limit on any isotropic shift in the vacuum speed of light as being no larger than 66 m/s [8, 9] based on saturation spectroscopy of near-relativistic ions [23]. This limit was subsequently reduced to 25 m/s by an improved version of the same experiment [34]. We also propose several radically new forms of the Ives-Stilwell experiment with the potential to overcome some of the scaling limits closely approached by traditional experiments [34].

As we show in part 3.2, even tighter bounds on $\tilde{\kappa}_{tr}$ can be obtained from careful analysis of potential sidereal variations in the results of Michelson-Morley experiments. In particular, a reanalysis of the data from [6] yields the limit $|\tilde{\kappa}_{tr}| \leq 1.8 \times 10^{-8}$, limiting shifts in the speed of light to be no larger than about 5.3 m/s. This also marks the first time that a single Michelson-Morley experiment has provided new constraints on all nine of the non-birefringent $\tilde{\kappa}_{e-}$, $\tilde{\kappa}_{o+}$ and $\tilde{\kappa}_{tr}$ parameters.

Finally, in part 3.3, we show that the best constraints on isotropic violations of Lorentz symmetry for light may be obtained from collider physics. In particular, the

stability of high-energy (340 GeV and above) photons observed by the D0 collaboration at the Fermilab Tevatron, combined with the simple fact that center of mass energies in excess of 206 GeV were attained in e^+e^- collisions at CERN's LEP collider can be used to set the limit $-5.8 \times 10^{-12} \leq \tilde{\kappa}_{tr} \leq 1.2 \times 10^{-11}$. This is equivalent to the statement that the vacuum speed of light may be no more than 2 mm/s faster than the canonical value of c as defined by the maximum attainable speed of electrons, and no more than 4 mm/s slower [10, 92]. In the broader context of the SME, this limit may be more generally understood as a constraint on the difference $\tilde{\kappa}_{tr} - \frac{4}{3}c^e_{00}$, between the photon-sector $\tilde{\kappa}_{tr}$ and the fully timelike component of the electron-sector c^e_{00} tensor, and presently represents the best known constraint on this difference.

3.1   Ives-Stilwell and Clock Comparison Tests

An important class of Lorentz symmetry tests are the so-called "Ives-Stilwell" experiments, named for the first such experiment carried out and reported by H. Ives and G. Stilwell in 1938 [19]. These experiments compare the laboratory-frame frequency or wavelength of light emitted in a direction parallel to the motion of a rapidly moving source particle to that emitted counter to the particle's motion. The Doppler shift resulting from a boost between the moving and laboratory frames is different for light emitted in the two directions, and is compared with predictions from special relativity. When combined with other experiments demonstrating the isotropy of c, Ives-Stilwell measurements can directly measure the effects of time dilation on the frequency of emitted light, and can thus be characterized as a comparison of the rate of a moving clock (the atomic transition frequency) with that of a stationary one. If instead the measurements are combined with results indicating the universality of time-dilation, Ives-Stilwell tests can detect directional anisotropies in c.

As outlined in Figure 3.1, the goal of an Ives-Stilwell experiment is to simultaneously measure the relativistic Doppler shift for light traveling in opposite directions. In the absence of Lorentz-violating effects, light emitted by a particle moving with velocity $\vec{\beta}$ in a direction parallel to the motion is blueshifted, while light emitted in the direction anti-parallel to the particle velocity is redshifted. The emitted frequencies
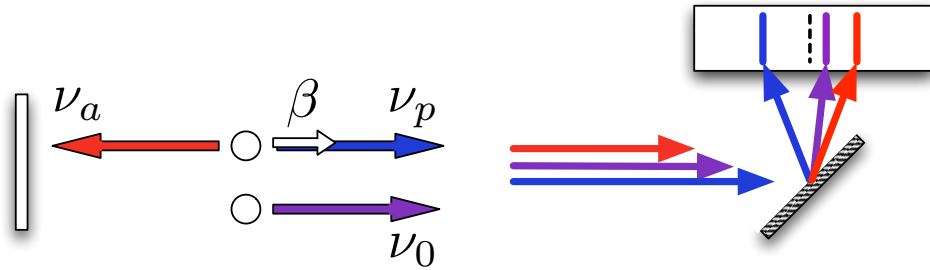
Figure 3.1: Schematic of the original Ives-Stilwell experiment. In the lab frame, an accelerated particle emits light in all directions. Light emitted parallel to the particle's motion is blue-shifted to ν_p and light emitted anti-parallel to the motion is red-shifted to ν_a relative to the transition frequency ν_0 that would be measured in the particle rest frame. Light emitted parallel and anti-parallel to the particle's motion is compared on a spectrometer. The shift of the centroid (dashed line) of the blue and red-shifted lines from the same transition is due to time-dilation for the moving atom.

are given by

$$\nu_p = \nu_0 \frac{1+\beta}{\sqrt{1-\beta^2}}, \qquad \text{and} \qquad \nu_a = \nu_0 \frac{1-\beta}{\sqrt{1-\beta^2}}. \qquad (3.1)$$

Once the frequencies of the light emitted parallel and anti-parallel to the particle velocity are known, the time dilation factor $1/\gamma = \sqrt{1-\beta^2}$ can be obtained directly from their average. In combination with the null results of the Michelson-Morley [14] and Kennedy-Thorndike [16] experiments, the Ives-Stilwell test not only made a direct measurement of relativistic time dilation, but also demonstrated that the relativistic length contraction required to explain the KT result occurs only along the direction of an object's motion, and not across it [19].

Modern Ives-Stilwell tests [23, 34, 93–95] essentially run the experiment in reverse. Moving atoms serve as frequency selective detectors of laboratory-generated light in the boosted frame. A pair of counter-propagating lasers is tuned into simultaneous resonance with a selected transition of a rapidly moving atom. The simultaneous resonance condition for the two beams is accompanied by a reduction, or Lamb dip [96] in fluorescent output as the transition is saturated. See also Figure 3.2. In terms of

the applied laser frequencies, the simultaneous resonance condition is simply

$$\frac{\nu_p \nu_a}{\nu_0^2} = 1 + \epsilon, \tag{3.2}$$

where $\epsilon = 0$ for the fully covariant theory. As originally noted in [8,9], anisotropies of
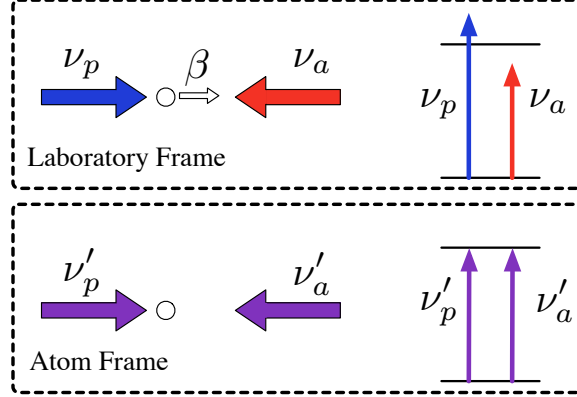
Figure 3.2: Schematic of a modern Ives-Stilwell experiment. In the lab frame, atoms are illuminated with light propagating parallel (with freq. ν_p) and anti-parallel (freq. ν_a) to their motion ($v = \beta c$). The frequencies of the applied fields are tuned to simultaneous resonance $\nu_p' = \nu_a'$ in the atoms' frame.

the speed of light in the laboratory frame will typically generate a nonzero ϵ. Using (2.10), we can respectively write the phase velocity of light in the directions parallel and anti-parallel to the atoms' motion as c_p and c_a, where

$$\begin{aligned} c_p &= \nu_p \lambda_p = c(1 + \rho_p) \\ c_a &= \nu_a \lambda_a = c(1 + \rho_a), \end{aligned} \tag{3.3}$$

where ρ_a and ρ_p are defined in equation (2.15). We can determine the frequency ν_p' and ν_a' that the moving atoms "see" by noting that in the laboratory frame, the rate at which an atom moving parallel to the wave ν_p and anti-parallel to ν_a passes through areas of peak field intensity is

$$\begin{aligned} \nu_p'' &= \nu_p - v/\lambda_p = \nu_p \left(1 - \beta \frac{c}{c_p} \right), \\ \nu_a'' &= \nu_a + v/\lambda_a = \nu_a \left(1 - \beta \frac{c}{c_a} \right). \end{aligned} \tag{3.4}$$

This can then be related to the frequency observed in the atoms' rest frame by applying the usual time-dilation factor γ, so that

$$\nu'_p = \nu_p \frac{1 - \beta(c/c_p)}{\sqrt{1 - \beta^2}}, \qquad\qquad \nu'_a = \nu_a \frac{1 - \beta(c/c_a)}{\sqrt{1 - \beta^2}}. \tag{3.5}$$

The simultaneous resonance condition that $\nu'_p = \nu'_a = \nu_0$ is then

$$\nu_p = \nu_0 \frac{\sqrt{1 - \beta^2}}{1 - \beta(c/c_p)}, \qquad \text{and} \quad \nu_a = \nu_0 \frac{\sqrt{1 - \beta^2}}{1 + \beta(c/c_a)}. \tag{3.6}$$

In terms of the Ives-Stilwell observable (3.2), this becomes

$$\frac{\nu_p \nu_a}{\nu_0^2} = \frac{1 - \beta^2}{\left(1 - \beta(c/c_p)\right)\left(1 + \beta(c/c_a)\right)}, \tag{3.7}$$

which to second order in β is

$$\frac{\nu_p \nu_a}{\nu_0^2} = 1 + \beta\left(\frac{c}{c_p} - \frac{c}{c_a}\right) + \beta^2\left(\frac{c^2}{c_a^2} + \frac{c^2}{c_p^2} - \frac{c^2}{c_a c_p} - 1\right) + \mathcal{O}\left(\beta^3\right). \tag{3.8}$$

Our purpose behind taking (3.8) to second order will shortly become apparent. From the form of the term proportional to β in (3.8) and equations (2.15) and (2.16), we immediately see that the Ives-Stilwell observable is dominated by the value of the parity-odd $\tilde{\kappa}_{o+}$ parameter in the laboratory frame. Similarly, the term proportional to β^2 will be dominated by the value of the parity-even $\tilde{\kappa}_{e-}$ and $\tilde{\kappa}_{tr}$ parameters, as must be the case given the parity of the scalar $\nu_p \nu_a / \nu_0^2$. We will assume, as will be justified after the fact, that all photon-sector SME parameters other than $\tilde{\kappa}_{tr}$ may be ignored. This means that the β^2 term is proportional to $\tilde{\kappa}_{tr}$. If only $\tilde{\kappa}_{tr}$ is nonzero in the SCCEF (defined in part 2.1), then the parity-odd $\tilde{\kappa}_{o+}$ in the laboratory frame is given by the relation $\vec{\kappa}_{o+} = 2\vec{\beta}_{lab}\tilde{\kappa}_{tr}$. Thus the Ives-Stilwell observable becomes [8,9]

$$\frac{\nu_p \nu_a}{\nu_0^2} = 1 + 2\tilde{\kappa}_{tr}\left(\beta^2 + 2\vec{\beta} \cdot \vec{\beta}_{lab}\right) + \mathcal{O}(\tilde{\kappa}_{tr}^2) + \mathcal{O}(\beta^3). \tag{3.9}$$

From (3.9), we see that for Ives-Stilwell tests, $\tilde{\kappa}_{tr}$ plays the same role as the RMS $\hat{\alpha}$ parameter, since the form of the Ives-Stilwell experimental observable using that kinematic framework is [23,97]

$$\frac{\nu_p \nu_a}{\nu_0^2} = 1 + 2\hat{\alpha}\left(\beta^2 + 2\vec{\beta} \cdot \vec{\beta}_{lab}\right). \tag{3.10}$$

This means that any reported constraint upon the RMS $\hat{\alpha}$ derived from an Ives-Stilwell test is tantamount to an identical bound on $\tilde{\kappa}_{tr}$, although it should be noted that in the context of some measurements of $\hat{\alpha}$, the standard reference frame is defined as the rest frame of the cosmic microwave background, and thus $\vec{\beta}_{lab}$ may sometimes be defined differently.

In [34], $|\frac{\nu_p \nu_a}{\nu_0^2} - 1|$ was experimentally measured to be no larger than 2×10^{-10}. Although this precision was insufficient to improve bounds on $\tilde{\kappa}_{e-}$ or $\tilde{\kappa}_{o+}$, (which at the time had been constrained to be no larger than 10^{-16} or 10^{-12}), it was sufficient to limit $|\tilde{\kappa}_{tr}| \leq 8.4 \times 10^{-8}$.

3.1.1   New Directions for Ives-Stilwell

The construction of the standard model extension has greatly aided the development of low energy experiments seeking to detect Lorentz violating physics by enabling direct comparison of a wide variety of effects [28]. In the photon sector of the SME, all but one of the Lorentz-violating coefficients have been constrained to be less (in many cases far less) than 10^{-11} [8, 28, 33]. The exception, $\tilde{\kappa}_{tr}$, has been limited to be no larger than the relatively loose bound of 8.4×10^{-8} [34]. Thus far, Ives-Stilwell experiments have offered the best measurements of $\tilde{\kappa}_{tr}$ [34].

Elements of the Ives-Stilwell experiment have seen significant improvement over the past seventy years [19, 23, 34, 93–95, 98], but the core has remained unchanged. All Ives-Stilwell experiments use continuous wave spectroscopy of fast-moving ($\vec{\beta}_{at} > \vec{\beta}_{lab}$) atoms to constrain the magnitude of anomalous Doppler shifts caused by violations of Lorentz invariance. The improved constraints that these experiments have most recently been able to place upon the isotropic $\tilde{\kappa}_{tr}$ parameter are largely the result of using the most highly relativistic particles ever employed in such tests [23, 34]. With particle velocities already in excess of 6% of the speed of light [34], relativistic Ives-Stilwell tests are fast approaching practical limits on the speeds at which atoms with one or more bound electrons may circulate in an accelerator without becoming fully ionized. Thus far, Ives-Stilwell tests using low-velocity atoms (*i.e.* those with $\vec{\beta}_{at} < \vec{\beta}_{lab}$) have not been performed since they have not been competitive with their

relativistic counterparts –whatever increased precision they might offer has not been sufficient to counterbalance their decreased intrinsic sensitivities to $\tilde{\kappa}_{tr}$[1]. Here, we outline a means by which low velocity experiments ($\beta_{at} \leq \beta_{lab}$) can approach their theoretical peak sensitivities, and propose the use of pulsed techniques to allow both high and low velocity experiments to beat the single-particle Fourier transform limit.

3.1.2 Scaling of Ives-Stilwell

Ives-Stilwell experiments are based on spectroscopy of moving atoms. Although the original Ives-Stilwell experiment analyzed the spectrum generated by the recombination of moving ions [19], modern techniques use atoms as frequency selective detectors of laboratory-generated light in the boosted frame [23, 34, 93, 99], outlined in Figure 3.1. The simultaneous resonance of the co- and counter-propagating fields ν_a and ν_p with an atomic transition of frequency ν_0 in the atoms' rest frame occurs when

$$\frac{\nu_p \nu_a}{\nu_0^2} = 1 + \epsilon \tag{3.11}$$

is satisfied. In the absence of anomalous Doppler shifts, $\epsilon = 0$, while for nonzero $\tilde{\kappa}_{tr}$, $\epsilon = 2\tilde{\kappa}_{tr} \left(\vec{\beta}_{at}^2 + 2\vec{\beta}_{at} \cdot \vec{\beta}_{lab} \right)$, from equation (3.9).

Variations of ϵ from 0 are reflected in fractional variation of the resonance frequencies ν_p, ν_a. The precision to which $\tilde{\kappa}_{tr}$ can be measured per interaction is thus given by

$$\delta\tilde{\kappa}_{tr} \propto \frac{\sqrt{\Gamma}/2}{\text{SNR}\sqrt{\tau} \left(\beta_{at}^2 + 2\vec{\beta}_{at} \cdot \vec{\beta}_{lab} \right)}, \tag{3.12}$$

where SNR is the measurement's signal to noise ratio, τ is the interaction time and Γ is the measured linewidth. The precision of a resultant measurement of $\tilde{\kappa}_{tr}$ over N interactions is then given by

$$\delta\tilde{\kappa}_{tr} \propto \frac{\sqrt{\Gamma}/2}{\text{SNR}\sqrt{N\tau} \left(\beta_{at}^2 + 2\vec{\beta}_{at} \cdot \vec{\beta}_{lab} \right)}. \tag{3.13}$$

For low velocity experiments (where $|\beta_{at}| < |\beta_{lab}|$), the precision to which $\tilde{\kappa}_{tr}$ can be measured improves with increasing $|\beta_{at}|$ until the measured linewidth Γ becomes

---

[1]or equivalently, the RMS framework $\hat{\alpha}$ parameter (see part 1.1.2)

interaction time limited –that is, when $\Gamma \simeq 1/\tau = |\beta_{at}|c/L$, where L is the length of the experiment's interaction region. For $\beta_{at} < \beta_{lab}$, the maximum sensitivity scales inversely with L, while the minimum velocity required to reach it is $\beta_{at} \geq \gamma L/c$ for transitions with natural (or minimally imhomogeneously broadened) linewidth γ. For modestly sized experiments ($L \sim 1$ m), with atoms for which $\beta_{at} = \beta_{lab}$, this limit is reached only if the width of the probed resonance is less than 30 kHz, while for atoms from thermal sources with $\beta_{at} \sim 10^{-6}$, the probed transition must be no more than 300 Hz wide. In both cases, the optimal bandwidths are far less than a typical optical transition linewidth.

For high velocity experiments, ($|\beta_{at}| \gg |\beta_{lab}|$), the attainable precision can be shown to scale as $1/\beta_{at}L$, with an overall improvement by a factor of β_{lab}/β_{at} upon experiments in the low velocity limit. Motivating the work described below is the fact that the the best Ives-Stilwell measurements of $\tilde{\kappa}_{tr}$ to date are derived from tests on relativistic Lithium ions with $|\beta_{at}| = 0.064$ (high velocity) over an interaction length L of approximately 1 meter [23,34]. Efforts to further increase β_{at} in such experiments are self-defeating in that one is soon left with stripped Lithium nuclei, whose energy levels are more difficult to address with commonly available laser systems. It is also unlikely that experiments with significantly larger interaction regions can be straightforwardly constructed, and funding for such projects is even less certain. Thus new approaches must be developed if Ives-Stilwell tests are to provide competitive measurements in the coming years.

To improve upon existing measurement techniques, two problems need to be solved. For low-velocity experiments to reach their full potential, we need experiments using narrow linewidths. More importantly, both high and low velocity tests will be enhanced if we can construct an experiment whose precision improves coherently over timescales longer than the atoms' time of flight through the apparatus. In what follows, we outline several methods by which such enhancements might be realized.

3.1.3   Two-Photon Tests with Metastable Atoms

Narrow optical transitions may be realized using two-photon transitions. For example, four-wave mixing processes (Figure 3.3) can be used to generate fields whose bandwidths scale inversely with the lifetime of the ground state coherence which generates them.
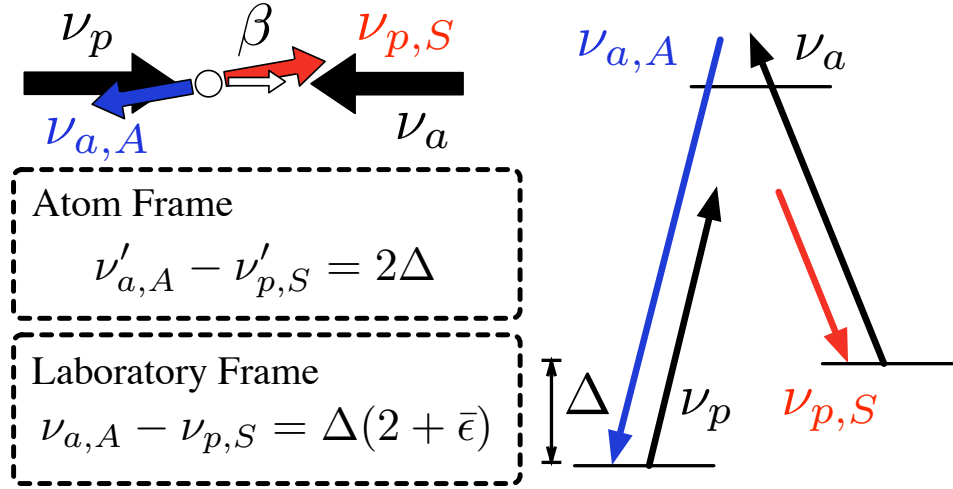
Figure 3.3: Ives-Stilwell using Four Wave Mixing. As in Figure 3.1, counter-propagating fields with frequencies ν_p and ν_a are applied to moving atoms. The three level Λ-system, with ground electronic state splitting Δ, generates an anti-stokes field $\nu_{a,A}$ propagating anti-parallel, and a stokes field $\nu_{p,S}$ propagating parallel to the atoms (angled for clarity). Generated fields are compared in the lab frame. Here, $\bar{\epsilon} \equiv \beta_{at}^2 \Delta + \Delta \left(2\beta_{at}^2 - 4\vec{\beta}_{at} \cdot \vec{\beta}_{lab} \right) \tilde{\kappa}_{tr}$.

The frequency of the emitted field in the atoms' rest frame is shifted by the ground state frequency difference $\pm\Delta$ from the applied field. Assuming the atoms' internal energy levels are frame-independent, the frequencies of the generated fields as measured in the laboratory frame are

$$\nu_{a,A} = \left(\nu_a \frac{1 + \beta_{at}c/c_a}{\sqrt{1 - \beta_{at}^2}} + \Delta \right) \frac{\sqrt{1 - \beta_{at}^2}}{1 + \beta_{at}c/c_a},$$

$$\nu_{p,S} = \left(\nu_p \frac{1 - \beta_{at}c/c_p}{\sqrt{1 - \beta_{at}^2}} - \Delta \right) \frac{\sqrt{1 - \beta_{at}^2}}{1 - \beta_{at}c/c_p}.$$

If $\nu_a = \nu_p$, the lab-frame difference between $\nu_{a,A}$ and $\nu_{p,S}$ is, to lowest order in $\tilde{\kappa}_{tr}$ and second order in β_{at},

$$\nu_{a,A} - \nu_{p,S} = 2\Delta + \beta_{at}^2 \Delta + \Delta \left(2\beta_{at}^2 - 4\vec{\beta}_{at} \cdot \vec{\beta}_{lab} \right) \tilde{\kappa}_{tr}. \qquad (3.14)$$

Using metastable states, we can generate fields with arbitrarily narrow-bandwidths, limited only by the interaction time, the scattering rate of the applied fields, and external sources of decoherence. Linewidths on the order of kHz are easily attainable [100], allowing low-velocity experiments to approach their $1/L$ limit. One limiting factor which should be considered, however, is that four-wave mixing is a nonlinear process relying upon the collective interaction of many atoms. Efficient production of the conjugate fields requires densities sufficient that many atoms lie inside the volume defined by the beams' transverse profile and the two-photon difference wavelength c/Δ. For thermal vapors near room temperature, this restricts us to systems with Δ no larger than several tens of GHz. Improved signal to noise ratios made possible by this experimental configuration may partially compensate for this restriction.

For an initial estimate of the sensitivity of such experiments, we consider an analysis of a thermal beam of ^{87}Rb atoms. Such atoms have a metastable ground state splitting of approximately 6.8 GHz, and have thermal velocities near room temperature of about $\beta = 10^{-6}$. Over a one meter interaction length, the interaction-time limited bandwidth of the emitted light would be about 300 Hz. Using (3.14), we find that the sensitivity to $\tilde{\kappa}_{tr}$ of an experiment using ^{87}Rb is $\nu_{a,A} - \nu_{p,S} \simeq 2.72\tilde{\kappa}_{tr}$. Significant improvements can be realized if the splitting between the involved metastable states is increased, as in ^{208}Pb. Lead 208 has a $6p^2(^3P_0)$ ground state and a metastable $6p^2(^3P_2)$ state which both couple to the short-lived $6p7s(^3P_1)$ or $6p9s(^3P_1)$ states. The frequency splitting between the ground and metastable states of ^{208}Pb is about 319 THz, and so even after accounting for a factor of $\sqrt{2}$ reduction in the mean thermal velocity of ^{208}Pb relative to ^{87}Rb, the overall sensitivity to $\tilde{\kappa}_{tr}$ is $\nu_{a,A} - \nu_{p,S} \simeq 9 \times 10^4 \tilde{\kappa}_{tr}$. If this frequency difference can be constrained to within 0.9 mHz, then constraints on $\tilde{\kappa}_{tr}$ at the level of 10^{-8} would be possible. Realization of such a continuous four-wave mixing process in ^{208}Pb might be challenging, however, as such nonlinear processes have as yet only been observed in pulsed experiments [101]. As we shall see, however,

working in the pulsed, rather than continuous-wave spectroscopy regime can prove to be advantageous.

3.1.4   Pulsed Experiments

Practical size constraints are likely to limit the further development of continuous wave spectroscopy based Ives-Stilwell experiments for the foreseeable future. To move forward, it is desirable to conceive of new methods of measuring anomalous Doppler shifts that do not rely on CW spectroscopy. With the development of extremely stable octave-spanning optical frequency combs [102], it is now possible to generate and measure extremely narrow resonances using many serially phase coherent pulses rather than the long pulse of a conventional CW spectroscopic measurement. By performing the same measurement repeatedly and coherently combining the results, we can use a very short interaction region to obtain linewidths that would require much larger experiments using CW spectroscopy.

3.1.5   Raman Comb Spectroscopy

One possible implementation of a pulsed anomalous Doppler shift experiment involves using a frequency comb to generate a train of Raman scattered pulses in an inverted atomic medium. Phase coherence between the generated pulses would give rise to a generated spectrum with features narrower than a single pulse's Fourier-transform limit. The short duration of each pulse means that only a small interaction length along the axis of the atoms' motion will be required.

Using an analysis similar to that presented previously, it can be shown that the frequency differences Δ_p and Δ_a of the Raman scattered fields relative to the frequencies of the applied driving fields ν_p and ν_a are, in the laboratory frame, given by

$$\Delta_p = \Delta \frac{\sqrt{1 - \beta_{at}^2}}{1 - \beta_{at} c/c_p} \tag{3.15}$$

$$\Delta_a = \Delta \frac{\sqrt{1 - \beta_{at}^2}}{1 + \beta_{at} c/c_a}. \tag{3.16}$$

To lowest order in β_{at}, and $\tilde{\kappa}_{tr}$, the sum of the frequency differences Δ_a and Δ_p are
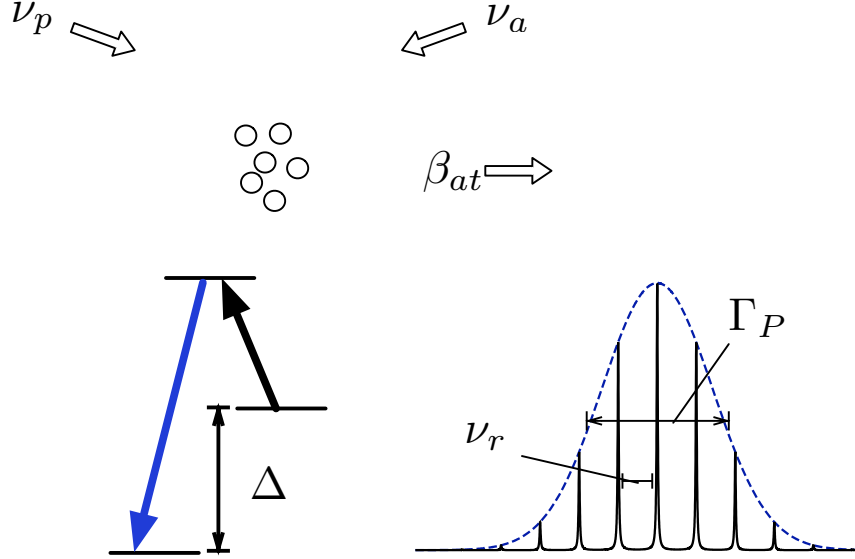
Figure 3.4: Pulsed Ives-Stilwell using a generated Raman comb. Atoms in a long-lived metastable state move at β_{at}, and interact with a frequency comb with repetition rate ν_r and comb-width Γ_P, generating a chain of anti-stokes Raman pulses. Anomalous Doppler shifts of the applied field from the lab frame to the boosted frame are preserved in the frequency of the generated Raman field in the lab frame, as described in the text. We expect individual comb line widths to be limited by velocity dispersion of the atomic beam (see text).

$$\Delta_p + \Delta_a = \frac{2\Delta}{\sqrt{1 - \beta_{at}^2}} + \Delta \left(2\beta_{at}^2 - 4\vec{\beta}_{at} \cdot \vec{\beta}_{lab} \right) \tilde{\kappa}_{tr}. \qquad (3.17)$$

Because the measured signal is a component of a generated frequency comb rather than the Fourier transform of a single pulse, the limiting precision of such an experiment is not a function of the interaction length, provided that length is sufficient to contain the atoms interacting with a single pulse. For example, for an octave-spanning frequency comb centered on 780 nm, each pulse might be approximately 3 femtoseconds in duration. In this instance, an interaction length of 1 micron would be sufficient for any possible β_{at}.

Sensitivity to $\tilde{\kappa}_{tr}$ for this system is likely to be limited by achievable signal to noise ratios, as well as the width of the atoms' velocity distribution about the selected

velocity $\vec{\beta}_{at}$. Departures from ideal monochromaticity of the atomic beam will lead to inhomogeneous Doppler broadening of the generated comb. As an example, we may consider two-photon scattering from the metastable $6p^2\,(^3P_2)$ state to the $6p^2\,(^3P_0)$ ground states of lead atoms, the two-photon detuning Δ is 319 THz. The width of the thermal velocity distribution for such atoms in a supersonic beam is roughly 200 m/s, leading to an inhomogeneous broadening of approximately 200 MHz. In order to pick out a single generated line, the pulse repetition rate must be larger than this inhomogeneous linewidth. As frequency combs with repetition rates of 1 GHz are available, this experiment may in fact be realizable with commercially available systems. Inhomogeneous broadening can also be significantly reduced by replacing the thermal beam with atoms allowed to fall under gravity after being cooled in a magneto-optical trap. Using the 10 m atom interferometer drop tower being constructed at Stanford, such atoms could reach velocities of up to 14 m/s [103, 104]. Provided that the inhomogeneous linewidth of the atomic sample can be reduced by more than the ratio of 14 m/s to the speeds available in thermal beams, such cold atom experiments could prove to be a useful way forward.

Our generated fields' bandwidth is set by the two-photon Doppler width, which is roughly 200 MHz in a thermal beam. By careful velocity class selection (at the ppm level) in a supersonic beam, a substantial linewidth reduction may be achieved, so that with an SNR of 1,000, a low β experiment could improve upon the relativistic ion bound [34] by a factor of 10.

Thus our scheme can place a competitive bound on $\tilde{\kappa}_{tr}$ on high β atoms in a relatively small space, granted a relatively mild signal to noise advantage. The linewidth of the generated comb resonances may be further reduced by cooling the atoms prior to their being loaded into the beam.

3.1.6 High Harmonic Generation

Another means to probe anomalous Doppler shifts uses the phenomenon of High Harmonic Generation (HHG), depicted in Figure 3.5. In the presence of extremely intense pulses of light, the binding energy of an atomic ground state electron can be
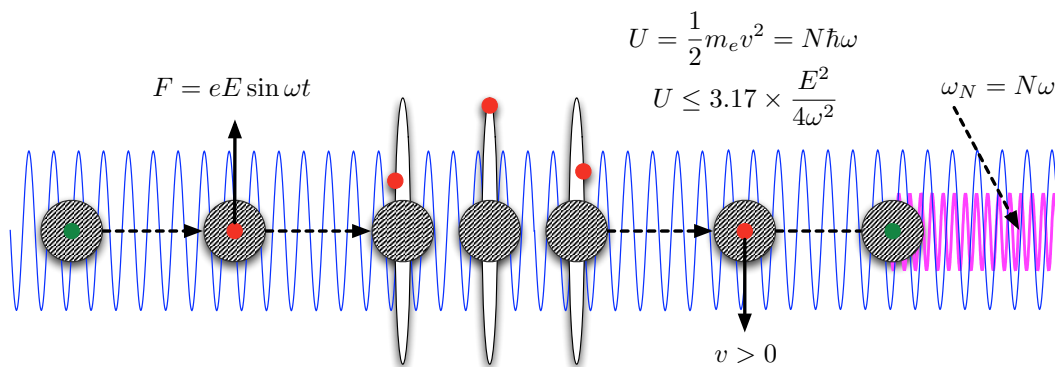
Figure 3.5: The process of High Harmonic Generation (HHG). When exposed to a very intense electromagnetic field, bound electrons (green dot at left) can tunnel into unbound states (red dot) and be accelerated directly by the oscillating field. After the first half optical cycle which the newly freed electron is accelerated, it passes over the source atom and can with high probability return to its original state, emitting the accumulated kinetic energy U as a photon at an odd harmonic of the driving field frequency.

small compared to its interaction with the applied field. Bound electrons can then tunnel into the ionization band, accumulate energy directly from the fields, and may then return to the ground state, giving up their energy in the form of light at higher harmonics of the applied field. Phase matching and diffusive constraints limit the energy accumulated by such returning electrons to no more than $I + 3.17U$, where I is the atomic ionization energy, and $U = E^2/(4\nu^2)$ is the ponderomotive energy supplied to free electrons by the field of frequency ν and amplitude E [105]. HHG schemes are quite compatible with frequency comb techniques. As demonstrated in [106], HHG driven by a frequency comb results in the production of correspondent frequency combs at harmonics of the driving comb.

Because the generated light appears only at odd harmonics of the applied field, and only up to a cutoff energy, the amplitudes of the generated harmonics can be used to measure the energy available per photon in the frame of moving atoms, and thus can be used to detect anomalous Doppler shifts. Any variation of the energy per photon in the atoms' rest frame will lead to amplitude modulation of the HHG fields, particularly near the the HHG cutoff energy (or indeed, near to any large variation of

the HHG fields tied to the satisfaction of a phase-matching condition). Such a HHG test could be implemented using the light generated by a chain of frequency comb pulses propagating parallel to a beam of atoms moving with velocity β_{at}, mounted upon a rotating table. $\tilde{\kappa}_{tr}$ gives rise to amplitude modulation of the HHG fields near the cutoff energy, according to the variation of the energy per Nth harmonic photon in the atoms' rest frame relative to the HHG cutoff energy. The former is given, to first order in $\tilde{\kappa}_{tr}$ by

$$E_{N\text{th harmonic}} = N\hbar\omega \left(\frac{1 - \beta_{at}}{\sqrt{1 - \beta_{at}^2}} + \frac{\beta_{at}}{\sqrt{1 - \beta_{at}^2}}\rho_p \right),$$

(3.18)

while the latter is

(a)   (b)
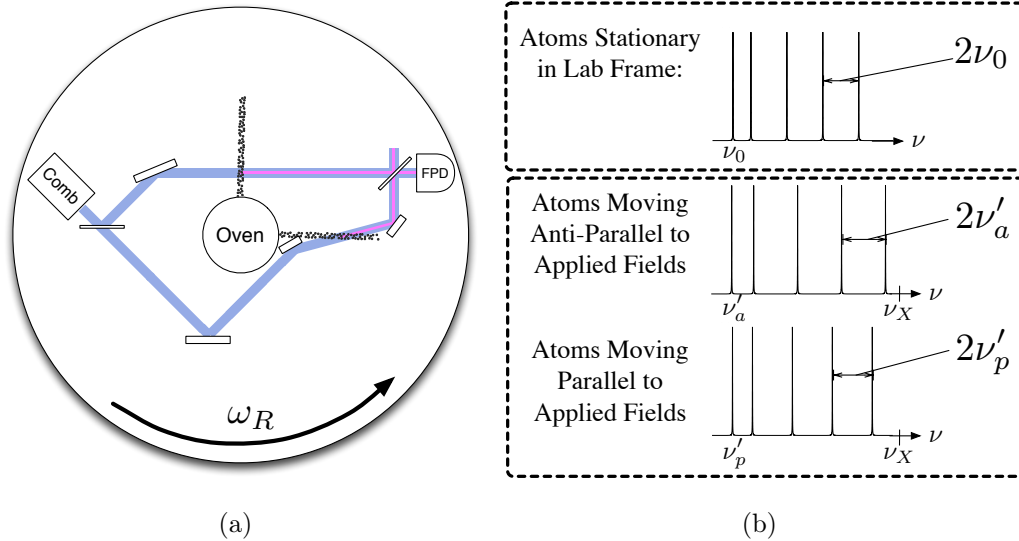
Figure 3.6: Ives-Stilwell using pulsed High Harmonic Generation (HHG). For nonzero $\tilde{\kappa}_{tr}$, frequency combs generated by HHG in moving atoms will be shifted according to the orientation of the atoms' motion relative to the boost from the SCCEF. The schematic in (a) depicts an experiment where two HHG combs are generated from the same source comb using atoms moving parallel and perpendicularly to the applied fields. Since the overall comb spacing is sensitive to anomalous Doppler shifts as indicated in (b), rotating the experiment in the laboratory frame should generate amplitude modulation sidebands at ω_R, detectable by interfering the two generated combs on a photodetector.

$$E_{\text{HHG cutoff}} = I + 3.17U \left(1 - \frac{2\beta_{at}\rho_p}{1 - \beta_{at}} \right), \tag{3.19}$$

and so the frame-dependent variation of the Nth harmonic energy relative to the cutoff energy is

$$\left(\frac{N\hbar\omega}{\sqrt{1 - \beta_{at}^2}} + \frac{6.34U}{1 - \beta_{at}} \right) \beta_{at}\rho_p. \tag{3.20}$$

When $I \ll U$, then for harmonics near the cutoff $N\hbar\omega \sim 3.17U$, so that the above reduces to $N\hbar\omega\beta_{at}\rho_p \left(\frac{1}{\sqrt{1-\beta_{at}^2}} + \frac{2}{1-\beta_{at}} \right)$. If the amplitude A of the generated fields drop off as $\frac{\partial A}{\partial E}$ near the cutoff, we find that $\tilde{\kappa}_{tr}$ will generate amplitude modulation sidebands about each frequency component of the generated comb with amplitude

$$N\hbar\omega \frac{\partial A}{\partial E} \left(\frac{1}{\sqrt{1 - \beta_{at}^2}} + \frac{2}{1 - \beta_{at}} \right) \beta_{at} \left(2\vec{\beta}_{at} \cdot \vec{\beta}_\oplus - 1 \right) \tilde{\kappa}_{tr}. \tag{3.21}$$

These sidebands can be detected by beating the generated fields against a reference comb, possibly also from HHG from stationary atoms. Systematics introduced by rotating the table can be suppressed by requiring sidereal variations of the phase of any measured beat-note, or by repeating the experiment with different β_{at}.

Ives-Stilwell tests using HHG are difficult to model in detail, as the magnitude of the generated signals is strongly dependent upon how sharp we can make the high-harmonic cutoff. Such experiments may offer relatively clean tests of local Lorentz violation for different particle species. Until now, all direct probes of anomalous Doppler shifts have been sensitive to differences in the degree of Lorentz-violation between the photon or electron sectors of the SME. Because HHG in the high energy limit is dominated by the free evolution of the charged electron in an applied field near a binding site, it provides a very clean photon-electron sector test. One could imagine using HHG with muonic hydrogen to constrain muon-specific SME parameters. The short lifetime of such exotic species might be compensated by the short interaction-time requirements of such experiments.

3.1.7 Summary

Modern Ives-Stilwell experiments are now closely approaching the fundamental limits of their sensitivity to anomalous Doppler shifts caused by anisotropies in the

vacuum phase velocity of light. This is a direct consequence of the manner in which the CW spectroscopy experiments' sensitivities scale with the size of and speeds achieved in the interaction volume. We have theoretically demonstrated that for experiments involving atoms moving more slowly than the Earth's orbital speed, the limiting sensitivity to anisotropies in the speed of light is determined by the linear dimension of the experiment alone, and proposed several "tabletop" experiments which take advantage of this fact. We have also outlined completely new forms of Ives-Stilwell test that beat the Fourier-transform limit of CW spectroscopy using optical frequency combs. In particular, searches for sidereal variations in the amplitude of optical combs produced via high harmonic generation may prove to be useful ways to constrain parameters in more exotic sectors of the SME.

3.2   Michelson-Morley and Optical Resonator Tests

Although Ives-Stilwell tests are in principle most sensitive to the parity-odd $\tilde{\kappa}_{o+}$ parameters, their precision as compared to that demonstrated by modern Michelson-Morley tests is not presently sufficient to place competitive limits on any SME parameter other than the isotropic $\tilde{\kappa}_{tr}$ coefficient. By way of comparison, the best sensitivity to $\tilde{\kappa}$ of any Ives-Stilwell experiment is that demonstrated by [34] at the level of 2×10^{-10} for the $\tilde{\kappa}_{o+}$ terms, whereas the leading Michelson-Morley experiments are sensitive to $\tilde{\kappa}_{e-}$ at the level of 10^{-16} or better [6,7,31,85]. As outlined in part 2.3, both experiments are sensitive to a term proportional to $\tilde{\kappa}_{tr}$ suppressed by two orders of β. For the relativistic ion Ives-Stilwell test, the suppression is $\beta_{at}^2 \simeq 4 \times 10^{-3}$, while for Michelson-Morley tests, $\tilde{\kappa}_{tr}$ appears proportional to $\beta_{\oplus}^2 \simeq 10^{-8}$. Despite the favorable boost of the ion in the storage ring [34], Michelson-Morley experiments which probe elements of $\tilde{\kappa}_{e-}$ at the level of 10^{-16} have the potential to set competitive limits on $\tilde{\kappa}_{tr}$. In this section, we describe a reanalysis of [6] which ultimately sets a new limit on isotropic violations of Lorentz symmetries for light: $|\tilde{\kappa}_{tr}| \leq 1.8 \times 10^{-8}$.

Modern Michelson-Morley experiments forgo the use of a Michelson interferometer in favor of a pair of optical or microwave resonators mounted perpendicularly to one another. Direction-dependent anisotropies in the speed of light cause correspondent

anisotropies in the wavelength of light at a given frequency, leading in turn to relative variations in the cavities' resonance frequencies. Because the resonance condition within a cavity depends upon the total phase accumulated during a round trip within it, the contribution of parity-odd anisotropies are canceled. Thus Michelson-Morley experiments are sensitive only to the value of the parity-even $\tilde{\kappa}_{e-}$ and $\tilde{\kappa}_{tr}$ parameters in their rest frame.

3.2.1 Characteristics and Observables of Michelson-Morley Experiments

Our bound comes from a reanalysis of data from an experiment performed at the University of Western Australia [6], which searched for variations in the resonance frequencies of two microwave frequency cryogenic sapphire oscillators (CSO) as a function of orientation and time. Previous analyses of this experiment focused on constraining the amplitude of sidereal variations generated by $\tilde{\kappa}_{e-}$ and by $\tilde{\kappa}_{o+}$ at leading order in the laboratory boost velocity $\vec{\beta}_{\oplus}$ due to the Earth's orbit about the Sun. In this reanalysis, we derive the form of the signals generated at second order in $\beta_{\oplus}$ by the isotropic $\tilde{\kappa}_{tr}$. As we will show, $\tilde{\kappa}_{tr}$ gives rise to signals which oscillate at the fundamental and first harmonic of the inverse sidereal day ($\omega_{\oplus}$ and $2\omega_{\oplus}$), and at harmonics of the inverse sidereal year $\Omega_{\oplus}$. Several of these signals are completely dominated by $\tilde{\kappa}_{tr}$, and can thus be used to set useful bounds on isotropic violations of Lorentz invariance.

Each CSO relied upon a high Q-factor ($\sim 2 \times 10^8$) sapphire loaded cylindrical resonant cavity, excited in the $WGH_{8,0,0}$ whispering gallery mode at approximately 10 GHz by a Pound stabilized loop oscillator circuit. The two resonators were mounted one above the other with their cylindrical axes perpendicular in the horizontal plane and orthogonal to one another. They were cooled in a cryogenic dewar using liquid helium, and their temperature controlled near to 6 Kelvin. The experiment was continuously rotated in the laboratory with a period of 18 seconds using a ring bearing rotation system. A more detailed description of this experiment and of CSOs in general has been reported elsewhere [6, 82, 85, 107].

When resonantly excited, the sapphire crystals support standing waves with the dominant electric and magnetic fields pointed in the axial and radial directions. For such whispering gallery modes, the Poynting vector is directed around the crystal circumference. The resonant frequency of each crystal is directly proportional to the integrated phase velocity of light, and is thus sensitive to Lorentz violation in the photon sector of the SME. The crystal resonance can also be modulated by Lorentz violation in the electron sector, but the contributing SME parameters for electrons have been constrained to the degree that they would not make significant contributions to our results [11, 33, 55][2], and so we assume that electrons are fully Lorentz-symmetric.

If any of the $\tilde{\kappa}$ parameters are nonzero, the difference in the resonance frequencies of the sapphire crystals will vary as the orientation of the laboratory reference frame is modulated with respect to the SCCEF (defined in part 2.1). In terms of the laboratory frame $\tilde{\kappa}$'s, the fractional difference between the resonance frequencies of two resonators oriented in the xy-plane at right angles to one another as they are rotated about the z-axis is given by [28, 85]

$$\frac{\delta\nu}{\nu} = S_e \left\{ [(\tilde{\kappa}_{e-})^{xx}_{\text{lab}} - (\tilde{\kappa}_{e-})^{yy}_{\text{lab}}] \cos 2\theta - 2(\tilde{\kappa}_{e-})^{xy}_{\text{lab}} \sin 2\theta \right\}, \tag{3.22}$$

where S_e is a sensitivity factor specific to the resonator materials and modes, and θ is the angle of the cavity axes relative to the x and y coordinate axes. This expression is valid for any pair of identical resonators, no matter what their geometry may be. To see this, consider the general form of the an expression yielding the resonant frequency of a vacuum-filled cavity in the presence of $\tilde{\kappa}_{e-}$ and $\tilde{\kappa}_{tr}$. To leading order, we must have

$$\nu = \nu_0 + f_{iso}\tilde{\kappa}_{tr} + f_x\tilde{\kappa}^{xx}_{e-} + f_y\tilde{\kappa}^{yy}_{e-} + f_z\tilde{\kappa}^{zz}_{e-} + f_{xy}\tilde{\kappa}^{xy}_{e-} + f_{xz}\tilde{\kappa}^{xz}_{e-} + f_{yz}\tilde{\kappa}^{yz}_{e-}, \tag{3.23}$$

where the f's are terms describing the cavities' orientation and geometry, and their resultant sensitivity to variations in the speed of light. Since $\tilde{\kappa}_{e-}$ is a real, symmetric matrix, then there exists a proper rotation which diagonalizes it. Thus we are free to either choose our axes such that $\tilde{\kappa}^{xy}_{e-} = \tilde{\kappa}^{yz}_{e-} = \tilde{\kappa}^{xz}_{e-} = 0$, or to orient the resonator such that f_{xy}, f_{yz}, and f_{xz} are zero. We are also free to make a rotation such that $\tilde{\kappa}^{xy}_{e-}$ is

---

[2]$c_{\mu\nu}$ coefficients that may be removed by a coordinate transformation are suppressed for clarity.

nonzero while holding $\tilde{\kappa}_{e-}^{yz}$ and $\tilde{\kappa}_{e-}^{xz}$ at zero. We may then declare that the resonator is aligned along the x-axis with

$$\nu_{0^\circ} = \nu_0 + f_{iso}\tilde{\kappa}_{tr} + f_x\tilde{\kappa}_{e-}^{xx} + f_y\tilde{\kappa}_{e-}^{yy} + f_z\tilde{\kappa}_{e-}^{zz} + f_{xy}\tilde{\kappa}_{e-}^{xy}. \tag{3.24}$$

Upon rotating the resonator about the z-axis by 90°, this becomes

$$\nu_{90^\circ} = \nu_0 + f_{iso}\tilde{\kappa}_{tr} + f_x\tilde{\kappa}_{e-}^{yy} + f_y\tilde{\kappa}_{e-}^{xx} + f_z\tilde{\kappa}_{e-}^{zz} - f_{xy}\tilde{\kappa}_{e-}^{xy}. \tag{3.25}$$

and so the difference must be

$$\nu_{0^\circ} - \nu_{90^\circ} = (f_x - f_y)\tilde{\kappa}_{e-}^{xx} - (f_x - f_y)\tilde{\kappa}_{e-}^{yy} + 2f_{xy}\tilde{\kappa}_{e-}^{xy}. \tag{3.26}$$

Recall that f_{xy} is generated from f_x and f_y by a rotation about the z-axis. We can therefore redefine the 0° orientation so as re-write this expression in terms of a rotation θ from that orientation about the z-axis:

$$\nu_{0^\circ} - \nu_{90^\circ} = (f_x - f_y)\left[(\tilde{\kappa}_{e-}^{xx} - \tilde{\kappa}_{e-}^{yy})\cos 2\theta - 2\tilde{\kappa}_{e-}^{xy}\sin 2\theta\right], \tag{3.27}$$

where we further infer the 2θ dependence from the fact that $\tilde{\kappa}_{e-}$ gives rise to parity-even effects. The form of (3.27) thus leads directly to (3.22).

Continuous measurements of $\delta\nu/\nu$ over extended periods can be used to extract limits on the values of $(\tilde{\kappa}_{e-})^{JK}$, $(\tilde{\kappa}_{o+})^{JK}$ or $\tilde{\kappa}_{tr}$ in the SCCEF. The orientation and boost of the lab relative to the SCCEF respectively vary periodically at the sidereal-day frequency $\omega_\oplus$ and the annual frequency $\Omega_\oplus$. The overall signal from the SCCEF-frame $\tilde{\kappa}$'s generates variations of $\delta\nu/\nu$ at the sum and difference frequencies of the fundamental and higher harmonics of ω_R, $\omega_\oplus$ and $\Omega_\oplus$, as previously derived to first order in $\beta_\oplus$ by [28]. Experimental limits on the amplitudes of several of these harmonics have been translated to limits on $(\tilde{\kappa}_{e-})^{JK}$ and $(\tilde{\kappa}_{o+})^{JK}$ [6, 31].

3.2.2   Sensitivity to $\tilde{\kappa}_{tr}$

Although we may use the second order analysis of part 2.3 to obtain the complete form of (3.22), its component proportional to the value of $\tilde{\kappa}_{tr}$ in the SCCEF can be obtained using simpler arguments based on observer Lorentz covariance. Since

(3.22) is the same up to the value of S_e for all Michelson-Morley experiments, we may simplify the problem by considering a pair of one-dimensional optical cavities aligned along the x- and y-axes in the laboratory frame, and rotated by an angle θ. The resonance frequencies of the resonators are then $\nu = \frac{mc_{\text{ph}}}{2L}$, where L is the length of the cavity, $m = 1, 2, 3, \ldots$, and $c_{\text{ph}} = (c_{\text{ph}}^+ + c_{\text{ph}}^-)/2$ is the average phase velocity of light moving back and forth along the cavity axis. Using (2.10) and (2.15), we can then write the frequency difference between the cavities due to Lorentz-violating variations in the speed of light as

$$\frac{\delta\nu_x}{\nu_x} - \frac{\delta\nu_y}{\nu_y} = \frac{1}{2}\left(\rho_{x+} + \rho_{x-} - \rho_{y+} - \rho_{y-}\right), \tag{3.28}$$

where ρ_{j+} (ρ_{j-}) is the fractional $\tilde{\kappa}$ induced shift in the speed of light parallel (antiparallel) to the j-axis in the laboratory frame. The problem can now be reduced to finding the mean speed of light along the laboratory x- and y-axes. Thus if we define

$$\vec{v} = c\vec{\beta} \qquad\qquad \vec{u} = \pm c(1 + \rho_{x\pm})\hat{x} \tag{3.29}$$

and

$$\vec{u}_{\parallel} = \frac{\vec{v} \cdot \vec{u}}{|v|^2}\vec{v} \qquad\qquad \vec{u}_{\perp} = \vec{u} - \vec{u}_{\parallel}, \tag{3.30}$$

then the velocity addition formula, which retains its standard form owing to observer Lorentz covariance, implies that if $\vec{u}$ is the speed of a beam of light moving along the x-axis in the laboratory, then the velocity $\vec{s}$ of that beam as measured in the SCCEF is

$$\vec{s}/c = \frac{\vec{v}/c + \vec{u}_{\parallel}/c + \vec{u}_{\perp}/(c\gamma)}{1 + \vec{v} \cdot \vec{u}/c^2}. \tag{3.31}$$

Since we are interested solely in the contribution of the SCCEF $\tilde{\kappa}_{tr}$ to our experiment, we may assume $\rho_{x\pm}$ and $\rho_{y\pm}$ are such that the speed of light in the SCCEF is isotropic and equal to $c(1 - \tilde{\kappa}_{tr})$. Thus the above formula yields

$$(1 - \tilde{\kappa}_{tr})^2 = \frac{\beta^2 - (1 + \rho_{x\pm})\left((1 + \rho_{x\pm})(\beta^2 - \beta_x^2 - 1) \mp 2\beta_x\right)}{\left(1 \pm \beta_x(1 + \rho_{x\pm})\right)^2}, \tag{3.32}$$

which to second order in β and first order in $\tilde{\kappa}_{tr}$, yields

$$\frac{1}{2}\left(\rho_{x+} + \rho_{x-}\right) = -\tilde{\kappa}_{tr} - (\beta^2 + \beta_x^2)\tilde{\kappa}_{tr}. \tag{3.33}$$

Similarly, we find that

$$\frac{1}{2}\left(\rho_{y+} + \rho_{y-}\right) = -\tilde{\kappa}_{tr} - (\beta^2 + \beta_y^2)\tilde{\kappa}_{tr}, \tag{3.34}$$

so that the dependence of $\delta\nu/\nu$ on $\tilde{\kappa}_{tr}$ is given by

$$\frac{\delta\nu_x}{\nu_x} - \frac{\delta\nu_y}{\nu_y} = \left(\beta_y^2 - \beta_x^2\right)\tilde{\kappa}_{tr}. \tag{3.35}$$

The detailed form of the boost $\vec{\beta}$ from the SCCEF as defined in the laboratory frame is

$$\vec{\beta} = R \begin{pmatrix} \beta_\oplus \sin\Omega_\oplus T \\ -\beta_\oplus \cos\eta \cos\Omega_\oplus T \\ -\beta_\oplus \sin\eta \cos\Omega_\oplus T \end{pmatrix}, \tag{3.36}$$

where we have neglected the contribution of the earth's rotation $\beta_L \simeq 10^{-6}$ to the boost vector, T is the time since the last vernal equinox, and the rotation R which reorients the SCCEF to align with the laboratory frame, with $\hat{z}$ pointing upwards and $\hat{x}$ pointing south, is given by

$$R = \begin{pmatrix} \cos\chi \cos\omega_\oplus T_\oplus & \cos\chi \sin\omega_\oplus T_\oplus & -\sin\chi \\ -\sin\omega_\oplus T_\oplus & \cos\omega_\oplus T_\oplus & 0 \\ \sin\chi \cos\omega_\oplus T_\oplus & \sin\chi \sin\omega_\oplus T_\oplus & \cos\chi \end{pmatrix}. \tag{3.37}$$

Here χ is the colatitude of the laboratory, η is the declination of the Earth's orbit relative to its spin, $\omega_\oplus$ and $\Omega_\oplus$ are the Earth's annual and sidereal frequencies, and $\beta_\oplus \simeq 10^{-4}$ is the Earth's orbital speed. The time $T_\oplus$ is not the same as T, and represents the time as measured in the SCCEF since the laboratory y-axis and the SCCEF Y-axis coincided [28]. We can account for the active rotation of the experiment [6] by redefining R so as to be aligned with the resonator axes:

$$R = \begin{pmatrix} \cos\omega_R T & -\sin\omega_R T & 0 \\ \sin\omega_R T & \cos\omega_R T & 0 \\ 0 & 0 & 1 \end{pmatrix} \cdot \begin{pmatrix} \cos\chi \cos\omega_\oplus T_\oplus & \cos\chi \sin\omega_\oplus T_\oplus & -\sin\chi \\ -\sin\omega_\oplus T_\oplus & \cos\omega_\oplus T_\oplus & 0 \\ \sin\chi \cos\omega_\oplus T_\oplus & \sin\chi \sin\omega_\oplus T_\oplus & \cos\chi \end{pmatrix}. \tag{3.38}$$

Insertion of $\vec{\beta}$ into (3.35) yields modulations of the form

$$\frac{\delta\nu_{x'}}{\nu_{x'}} - \frac{\delta\nu_{y'}}{\nu_{y'}} = S(T)\sin 2\omega_R T + C(T)\cos 2\omega_R T, \tag{3.39}$$

where

$$S(T) = (\tilde{\kappa}_{tr}) \times \sum_i \left[S_{S,i} \sin(\omega_i T) + S_{C,i} \cos(\omega_i T) \right], \tag{3.40}$$

$$C(T) = (\tilde{\kappa}_{tr}) \times \sum_i \left[C_{S,i} \sin(\omega_i T) + C_{C,i} \cos(\omega_i T) \right], \tag{3.41}$$

and $\omega_i \in \{\omega_\oplus T_\oplus, 2\omega_\oplus T_\oplus, \omega_\oplus T_\oplus \pm 2\Omega_\oplus T_\oplus, 2\omega_\oplus T_\oplus \pm 2\Omega_\oplus T_\oplus\}$. The complete form of the angular weights $C_{S,i}$ $C_{C,i}$, $S_{S,i}$ and $S_{C,i}$, proportional to each of these demodulated signals, along with the resulting numerical weights, are given in Table 3.1.

Table 3.1: Contributions of $\tilde{\kappa}_{tr}$, as defined in the SCCEF, to the amplitude of sidereal variations in the Michelson-Morley observable. Although $\tilde{\kappa}_{tr}$ does generate signals at $\omega_\oplus$ and $2\omega_\oplus$, the magnitude of such contributions is strongly suppressed relative to those from $\tilde{\kappa}_{e-}$ and $\tilde{\kappa}_{o+}$, and so the numerical weights for these frequencies are not shown. At all other frequencies, the signals from $\tilde{\kappa}_{e-}$ and $\tilde{\kappa}_{o+}$ are suppressed relative to $\tilde{\kappa}_{tr}$. This, combined with the far more stringent bounds set upon $\tilde{\kappa}_{e-}$ and $\tilde{\kappa}_{o+}$ from other experiments [33], allows us to ignore all but the contribution of $\tilde{\kappa}_{tr}$ to signals at $\omega_\oplus \pm 2\Omega_\oplus$ and $2\omega_\oplus \pm 2\Omega_\oplus$.

ω_i	C_{C,ω_i}	Num. Weight ($\times 10^{-10}$)	C_{S,ω_i}	Num. Weight ($\times 10^{-10}$)
$\omega_\oplus$	$\frac{-1}{2}\beta_\oplus^2\sin^2\eta(1+\cos^2\chi)$	-	-	
$2\omega_\oplus$	-		$\frac{1}{2}\beta_\oplus^2\sin 2\eta\sin 2\chi$	
$\omega_\oplus+2\Omega_\oplus$	-		$\frac{-1}{2}\beta_\oplus^2\sin 2\chi(1-\cos\eta)\sin\eta\tilde{\kappa}_{tr}$	-1.40
$\omega_\oplus-2\Omega_\oplus$	-		$\frac{1}{2}\beta_\oplus^2\sin 2\chi(1+\cos\eta)\sin\eta\tilde{\kappa}_{tr}$	33.7
$2\omega_\oplus+2\Omega_\oplus$	$\frac{1}{4}\beta_\oplus^2(1+\cos^2\chi)(1-\cos\eta)^2\tilde{\kappa}_{tr}$	0.202	-	
$2\omega_\oplus-2\Omega_\oplus$	$\frac{1}{4}\beta_\oplus^2(1+\cos^2\chi)(1+\cos\eta)^2\tilde{\kappa}_{tr}$	118	-	

ω_i	S_{C,ω_i}	Num. Weight ($\times 10^{-10}$)	S_{S,ω_i}	Num. Weight ($\times 10^{-10}$)
$\omega_\oplus$	$-\beta_\oplus^2\cos 2\eta\sin\chi$	-	-	
$2\omega_\oplus$	-		$-\beta_\oplus^2\sin^2\eta\cos\chi$	
$\omega_\oplus+2\Omega_\oplus$	$\beta_\oplus^2\sin\chi(1-\cos\eta)\tilde{\kappa}_{tr}$	6.74	-	
$\omega_\oplus-2\Omega_\oplus$	$-\beta_\oplus^2\sin\chi(1+\cos\eta)\tilde{\kappa}_{tr}$	-163	-	
$2\omega_\oplus+2\Omega_\oplus$	-		$\frac{1}{2}\beta_\oplus^2\cos\chi(1-\cos\eta)^2\tilde{\kappa}_{tr}$	0.167
$2\omega_\oplus-2\Omega_\oplus$	-		$\frac{1}{2}\beta_\oplus^2\cos\chi(1+\cos\eta)^2\tilde{\kappa}_{tr}$	97.7
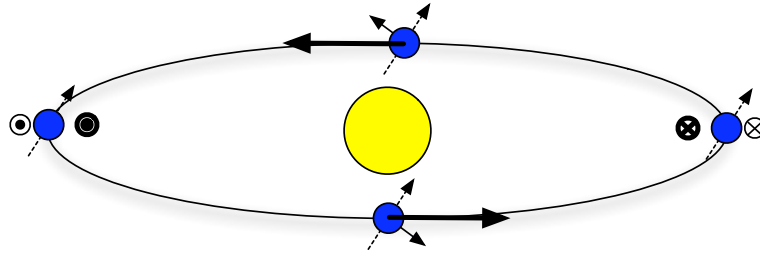
Figure 3.7: The variation of the maximal projection of a vector horizontal in the laboratory relative to the Earth's velocity in the SCCEF has a strong component at twice the annual frequency, since the period with which a fixed vector in the laboratory frame may coincide with $\vec{\beta}_{\oplus}$ is half a year. In contrast, the $(\tilde{\kappa}_{e-})^{JK}$ and $(\tilde{\kappa}_{o+})^{JK}$ terms do define preferred axes in the SCCEF, and so make contributions which depend upon the orientation and motion of the lab relative to these axes. The Earth's spin axis is denoted by a dashed line, while bold arrows indicate the Earth's orbital velocity. Arrows outside the orbit indicate the position at which a vector horizontal in the lab is most closely aligned with the orbital velocity.

A more detailed calculation of the total second order signal due to contributions from all the non-birefringent $\tilde{\kappa}$'s, presented in Appendix A, is readily shown to be consistent with this result. Note that this calculation predicts a comparatively strong signal from $\tilde{\kappa}_{tr}$ at the beat of first harmonic of the annual frequency $\Omega_{\oplus}$ with the fundamental and first harmonics of the sidereal frequency. This too can be intuited from the principle of observer Lorentz covariance, since the anisotropies that an SCCEF $\tilde{\kappa}_{tr}$ generates in the laboratory frame depend solely upon the alignment of the lab with respect to the lab's boost. Using our standard laboratory frame, we find (see Figure 3.7 that the daily maximum of the projection of the y-axis (which points east) onto the Earth's orbital velocity peaks at the summer and winter solstices, and is minimized during the equinoxes.

3.2.3 Summary and Conclusion

After removing the fixed offset and eliminating any linear drifts, the experimental data is demodulated with respect to $2\omega_R$ into two quadratures in blocks of 10 periods. The number of periods in each block was chosen to minimize the net effect of narrow

band noise (due to instabilities in systematics at $2\omega_R$) and broad band noise (due to oscillator frequency noise), approximating an optimal filter approach. This yields approximations to (3.40) and (3.41). Because $(\tilde{\kappa}_{e-})^{JK}$ and $(\tilde{\kappa}_{o+})^{JK}$ have been constrained by other experiments [6,31] to be far smaller than the limit we expect to set upon $\tilde{\kappa}_{tr}$, our experimental analysis attributes any signals at $\omega_i = \omega_\oplus \pm 2\Omega_\oplus, 2\omega_\oplus \pm 2\Omega_\oplus$ to $\tilde{\kappa}_{tr}$ alone. By fitting the measured quadratures to (3.40) and (3.41), we can obtain the value of $\tilde{\kappa}_{tr}$. From the sine term, we obtain $\tilde{\kappa}_{tr} = 3.5(3.0) \times 10^{-8}$ and from the cosine term, $\tilde{\kappa}_{tr} = 0.4(2.3) \times 10^{-8}$. The weighted average of the two results is $1.5(1.8) \times 10^{-8}$, yielding the new limit

$$|\tilde{\kappa}_{tr}| \leq 1.8 \times 10^{-8}. \tag{3.42}$$

This is an improvement of more than a factor of four over the existing limit, and marks the first time that a low energy experiment has been able to surpass the sensitivity of high energy ion spectroscopy tests [34]. In combination with previously reported limits [6], it also constitutes the first time that all nine non-birefringent photon sector coefficients in the SME have been competitively bounded by the same experiment.

3.3   Direct Constraints on $\tilde{\kappa}_{tr}$ From Collider Physics

Direct measurements of deviations of the speed of light from c are difficult due to a scarcity of independent references. Previous experimental limits on $\tilde{\kappa}_{tr}$ have been derived indirectly from tests for anisotropies of the speed of light. This is possible because $\tilde{\kappa}_{e-}^{jk}$, $\tilde{\kappa}_{o+}^{jk}$ and $\tilde{\kappa}_{tr}$ mix under boosts from one frame to another so as to preserve observer Lorentz covariance [28]. Thus optical resonator experiments [7] that set limits on the elements of $\tilde{\kappa}_{e-}^{jk}$ to be at the level of 10^{-17} can also constrain the magnitude of $\beta\tilde{\kappa}_{o+}^{jk}$, and indeed $\beta^2\tilde{\kappa}_{tr}$ to the same level, where β is the boost of the lab frame from the standard reference frame. Aside from the result derived below, the best experimental bound on $\tilde{\kappa}_{tr}$, with $|\tilde{\kappa}_{tr}| < 1.8 \times 10^{-8}$ is obtained indirectly from limits on $\tilde{\kappa}_{e-}^{jk}$ [6,86], as described in the previous section.

Here, we will consider direct measurements of $\tilde{\kappa}_{tr}$ [10,92]. In particular, we take advantage of the way non-zero $\tilde{\kappa}_{tr}$ modifies the kinematics of the electromagnetic

vertex. In contrast to the conventional situation, Lorentz-violating modifications to the fermion and photon dispersion relations can cause all three of the external legs of the vertex to go on shell together, permitting otherwise suppressed tree-level processes to go forth for particles above a certain energy threshold. As has been noted elsewhere [8,28], if the isotropic $\tilde{\kappa}_{tr} > 0$ then the phase velocity of light in the vacuum is reduced. Under such conditions, charged particles of sufficiently high-energy may actually exceed the speed of light in the vacuum, at which point the spontaneous emission of vacuum Cherenkov radiation

$$f \to f + \gamma \quad \text{for} \quad \tilde{\kappa}_{tr} > 0, \tag{3.43}$$

where γ denotes a photon and f a charged fermion, is kinematically allowed [54, 108]. By noting the absence of such Cherenkov emission from rapidly moving charged

(a) $\tilde{\kappa}_{tr} = 0$ (b) $\tilde{\kappa}_{tr} = 0.2$
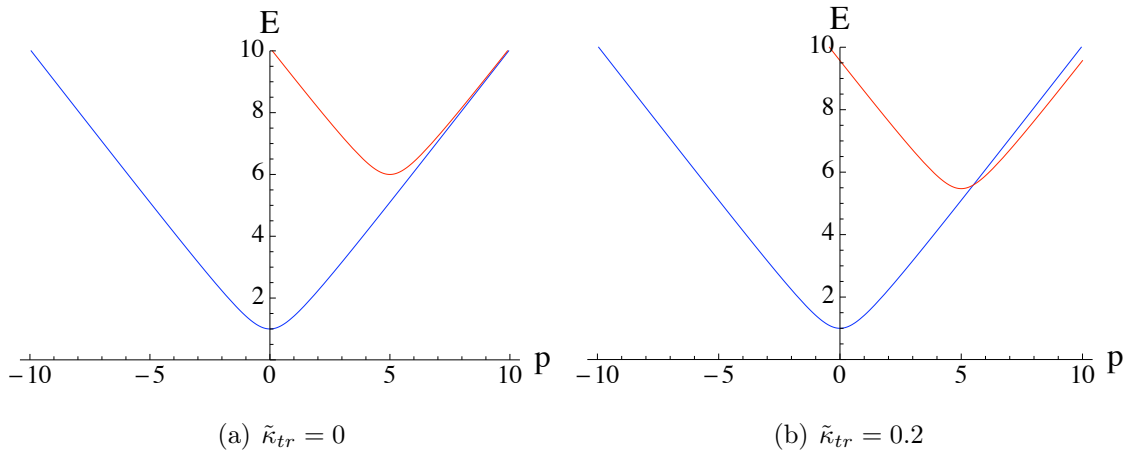
Figure 3.8: Dispersion Diagrams for Vacuum Cherenkov Radiation. For a fully Lorentz covariant theory, depicted by (a), the energy vs. momentum curve for a charged particle with unit mass (blue/lower curve in both plots) asymptotically approaches but can never intersect the energy curve of a charge+photon system with the same total momentum (red/upper curve). Conservation of energy and momentum thus suppresses moving charges from spontaneously emitting photons. If $\tilde{\kappa}_{tr} > 0$, however, the energy vs. momentum curve for the photon becomes shallower, so that now the dispersion curves for the two systems can intersect as shown in (b), and vacuum Cherenkov radiation becomes possible for sufficiently fast-moving charges.

particles, we can infer that they must not be traveling in excess of the speed of light.

This realization can be used to set a lower limit on the speed of light in the vacuum, and hence an upper bound on $\tilde{\kappa}_{tr}$. Similarly, if the fermion and photon dispersion relations are such that the limiting velocity for fermions is less than the speed of light, tree-level decays of sufficiently high energy photons into fermion–antifermion pairs, *i.e.*

$$\gamma \to f + \overline{f} \quad \text{for} \quad \tilde{\kappa}_{tr} < 0, \tag{3.44}$$

where $\overline{f}$ represents the antiparticle for f, are kinematically possible [54, 56]. We demonstrate that this decay is efficient, and use it to set a complementary bound on the magnitude of $\tilde{\kappa}_{tr} < 0$.

Note that the Lorentz-violating theory also allows vacuum Cherenkov radiation to occur for antifermions, and that even more unconventional processes, such as fermion–antifermion annihilation into a single photon, are possible. In addition, more conventional two-photon emission and absorption processes, synchrotron radiation, and inverse Compton processes can also be modified. Some of these effects have been employed in astrophysical contexts to extract general bounds on $\frac{\Delta c}{c}$ down to the 10^{-16} level [54–56].

In what follows, we will exploit the fact that Nature does not seem to support the reactions (3.43) and (3.44) to infer bounds on $\tilde{\kappa}_{tr}$. This approach has been used in earlier estimates of the degree to which the speed of light may deviate from c [44, 109, 110], primarily in the context of kinematic tests of dispersion relations [111, 112]. Here, we use the underlying SME Lagrangian to consider the overall rate at which the otherwise forbidden reactions (3.43) and (3.44) proceed. Such dynamical considerations are often necessary to obtain convincing and conservative results [113–116].

The dispersion relations governing the conditions under which the transitions (3.43) or (3.44) go on shell are also affected by SME coefficients other than $\tilde{\kappa}_{tr}$. The effects of such coefficients can be safely ignored so long as the scale of their contribution to the physics is small compared to the ultimate bound obtained on $\tilde{\kappa}_{tr}$. The other relevant coefficients are those impacting the fermion f, the other $\tilde{\kappa}$ matrices, and the (k_{AF}) coefficient in the photon-sector Lagrangian (2.3). Since we will focus on cases

where f is an electron, the relevant fermion coefficients are the b_e^μ, $c_e^{\mu\nu}$, $d_e^{\mu\nu}$, and $H^{\mu\nu}$ terms. This means that the relevant scale $\mathcal{S}$ is given by

$$\mathcal{S} \equiv \max\left(\tilde{\kappa}_{e-}, \tilde{\kappa}_{e+}, \tilde{\kappa}_{o+}, \tilde{\kappa}_{o-}, \frac{(k_{AF})}{m_e}, \frac{b_e}{m_e}, c_e, d_e, \frac{H_e}{m_e}\right), \qquad (3.45)$$

where the absolute values of the individual components of the SME coefficients are implied, and m_e denotes the electron mass.

To properly evaluate the scale $\mathcal{S}$, certain subtleties must be taken into account. One such is that elements of the electron's $c^{\mu\nu}$ coefficient can be expressed in terms of the non-birefringent $\tilde{\kappa}$ parameters by a coordinate redefinition (given in general form in part 2.5). This means that only the anisotropic piece of $c^{\mu\nu}$ should enter the determination of $\mathcal{S}$, and that our ultimate constraint upon $\tilde{\kappa}_{tr}$ is, strictly speaking, a constraint upon the linear combination $\tilde{\kappa}_{tr} - \frac{4}{3}c_e^{00}$. These issues are discussed in Appendix A.4. For electrons, we find that the scale $\mathcal{S}$ is presently about 10^{-13}, dominated by the $\tilde{\kappa}_{o+}$ matrix coefficient. Since we will ultimately derive limits on $\tilde{\kappa}_{tr}$ at the level of 10^{-12}, we may safely ignore other types of Lorentz violation in the present context.

3.3.1 Vacuum Cherenkov Radiation

In the absence of other contributing Lorentz-violating effects, vacuum Cherenkov emission can only occur for positive $\tilde{\kappa}_{tr}$. To leading order, the modified dispersion relation for a photon with wave vector $p^\mu \equiv (E_\gamma, \vec{p})$ is [27, 28]

$$E_\gamma^2 - (1 - \tilde{\kappa}_{tr})\vec{p}^{\,2} = 0 . \qquad (3.46)$$

In our chosen set of coordinates, the fermion dispersion relation is conventional, so that $c_e^{\mu\nu} = 0$. Energy–momentum conservation for the process (3.43) then yields a threshold energy E_{VCR},

$$E_{\text{VCR}} = \frac{1 - \tilde{\kappa}_{tr}}{\sqrt{(2 - \tilde{\kappa}_{tr})\tilde{\kappa}_{tr}}}m = \frac{1}{\sqrt{2\tilde{\kappa}_{tr}}}m + \mathcal{O}\left(\sqrt{\tilde{\kappa}_{tr}}\right) , \qquad (3.47)$$

corresponding to the kinetic energy of a fermion with mass m moving as fast as photons obeying (3.46) in the vacuum [108]. For charges with energies above E_{VCR}, vacuum Cherenkov radiation is kinematically allowed.

We would now like to infer an upper bound on $\tilde{\kappa}_{tr}$ from the absence of vacuum Cherenkov radiation from highly relativistic electrons. To do this, however, we must show that in addition to being kinematically allowed, the Cherenkov radiation process is efficient enough to be observable. Close to the threshold energy E_{VCR}, the dominant process is single-photon emission such that the charge falls below threshold. The estimated rate for this process is [108]:

$$\Gamma_{\text{VCR}} = \alpha\, Z^2 m^2\, \frac{(E_f - E_{\text{VCR}})^2}{2E_f^3} \ , \tag{3.48}$$

where α is the fine-structure constant, Z the charge measured in multiples of the elementary charge, and E_f the fermion energy. This shows the effect is undoubtedly efficient: for example, a 104.5 GeV electron with an energy of 1% above the threshold (3.47) would reach sub-luminal speeds after traveling an average distance of 23 cm. We therefore conclude that limits on $\tilde{\kappa}_{tr}$ can indeed be established from the absence of the vacuum Cherenkov effect for low-mass charges at the highest possible energies.

Cosmic Ray Constraints

Ultrahigh-energy cosmic rays (UHECRs) have the potential to yield the tightest limits on positive values of $\tilde{\kappa}_{tr}$, as they have energies orders of magnitude above those available in any laboratory. Unfortunately, efforts to use observations of UHECRs to constrain Lorentz violation in the photon sector [44,110] are beleaguered by a number of interpretational difficulties. Chief among them is a lack of certainty as to the composition of UHECR primaries, due to the relatively small number of reconstructed events at the highest energy scales. Although the observed UHECR primaries are believed to be single protons [44, 110], the possibility that the observations could be due to the scattering of more massive nuclei, high energy photons, or Lorentz-violating particles exhibiting no or a qualitatively different Cherenkov effect, such as stable neutral pions or neutrons, cannot yet be excluded [109]. This uncertainty will likely be ameliorated in coming years with continued observations.

As discussed in Appendix A.4, experimental limits on $\tilde{\kappa}_{tr}$ based on the vacuum Cherenkov effect actually measure the speed of light relative to that of the radiating

particle, or $\tilde{k}^{\mu\nu} - 2c_x^{\mu\nu}$, where $c_x^{\mu\nu}$ are SME coefficients modifying the dispersion relation for particles of species x. If the observed UHECRs are single protons, then the analysis of [44, 110], which uses coordinates in which the proton $c_p^{\mu\nu}$ coefficients are zero, would provide a one-sided bound on positive $\tilde{\kappa}_{tr}$ at the level of 10^{-22}, and two-sided constraints on the magnitude of the other non-birefringent $\tilde{\kappa}$'s at the level of 10^{-21}. These bounds would be consistent with the results of Cs-fountain clock experiments, which as noted in Appendix A.4, limit the parity-even $\tilde{\kappa}_{e-}$ to the level of 10^{-25}, and the parity-odd $\tilde{\kappa}_{o+}$ to 10^{-21}. In such a scenario, the UHECR studies would provide a new constraint upon $\tilde{\kappa}_{tr} - \frac{4}{3}c_p^{00}$.

If the UHECR primaries are atomic nuclei such as He, ^{12}C, or even ^{56}Fe nuclei, as assumed in [44, 110], we note that actual observation of vacuum Cherenkov emission could be used to set joint constraints upon $\tilde{\kappa}$ and the neutron c-coefficients. The *absence* of vacuum Cherenkov radiation from nuclei at a given energy, however, can only be used to constrain $\tilde{\kappa}$ if the neutron $c_n^{\mu\nu}$ coefficients are already known to be zero, or at least such that the limiting velocity of neutrons is larger than any resulting constraint on the speed of light. If this condition is not satisfied, then E_{VCR} for any composite particle containing neutrons is effectively infinite. To date, many components of $c_n^{\mu\nu}$ are unconstrained, so it is impossible to draw conclusions about Lorentz violation in the photon sector from composite UHECRs. We note, however, that previous experiments [117–119] constraining the magnitude of parity-even c_n^{JK} coefficients at the level of 10^{-27} may be sensitive enough to limit all $c_n^{\mu\nu}$ coefficients to the level of 10^{-19}. If further observations confirm that ^{56}Fe nuclei with EeV scale energies are striking the Earth's atmosphere, such $c_n^{\mu\nu}$ constraints may be sufficient to constrain $\tilde{\kappa}$ at the levels reported in [44, 110]. More stringent limits on $c_n^{\mu\nu}$ would be required if the UHECR primaries prove to be lighter neutron-containing nuclei.

Bounds from Collider Experiments

Although the energy scales attainable in terrestrial collider experiments are several orders of magnitude below those of cosmic rays, studies of vacuum Cherenkov induced braking in the LEP collider are attractive for a number of reasons. Common

to all analyses of collider experiments is a precise knowledge of the species and energy of the potential vacuum Cherenkov emitter. As a result, we can immediately determine that measurements of E_{VCR} derived from the LEP e^+e^- beams will constrain $\tilde{k}^{\mu\nu} - 2c_e^{\mu\nu}$, independent of Lorentz violating effects for other particles. At present, the LEP experiment provides the best compromise between a charge's mass vs. its energy for terrestrial Cherenkov constraints. Finally, as shown in Appendix A.4, for the energies attained at LEP (~ 100 GeV), $\tilde{\kappa}_{tr} - \frac{4}{3}c_e^{00}$ is the only SME coefficient combination that can contribute to vacuum Cherenkov radiation, permitting a significantly simplified analysis. An analysis of LEP data has the potential to yield rigorous one-sided improvements upon previous laboratory constraints on $\tilde{\kappa}_{tr}$.

The LEP collider was a circular particle accelerator approximately 27 km in circumference. This accelerator was an exquisitely precise and carefully controlled device with a relative uncertainty in the center-of-mass energy $\Delta E_{\mathrm{CM}}/E_{\mathrm{CM}}$ less than 2.0×10^{-4} [80]. To keep the uncertainty at this level, minute effects such as Earth tides, variations in the pressure of the local water table, and even seasonal variations in the volume of the nearby lake needed to be taken into account [80]. The highest laboratory-frame energy attained at LEP was $E_{\mathrm{LEP}} = 104.5$ GeV. We can obtain a first estimate for a limit on $\tilde{\kappa}_{tr}$ by arbitrarily setting $E_{\mathrm{VCR}} = 100$ GeV. Under such conditions, 104.5 GeV electrons or positrons would fall below threshold after traveling approximately 1.2 cm. This length is far shorter than the distance between RF cavities at LEP or even the dimensions (5.8 m) of each of the dipole bending magnets [80], so that such an effect should have been observable. However, this was not the case, implying $E_{\mathrm{VCR}} > 100$ GeV. Together with equation (3.47) one would then obtain the bound $0 \le \tilde{\kappa}_{tr} \le 1.3 \times 10^{-11}$.

We can do slightly better by considering the total energy budget at LEP. At $E_{\mathrm{LEP}} = 104.5$ GeV, energy losses due to conventional synchrotron radiation were $U_0 = 3.486$ GeV per electron or positron per turn [80]. Since LEP had a circumference of 26 659 m we find that the mean energy loss per distance traveled around the ring must be

$$\frac{dE_{\mathrm{syn}}}{dL} = 2.580 \times 10^{-20} \, \mathrm{GeV}^2 \,. \tag{3.49}$$

One of the three energy-calibration methods at LEP relied upon the dependence of the synchrotron tune on the energy loss. Thus it was extremely important that these losses be precisely determined. Deviations from (3.49) arise through parasitic-mode losses, finite beam size and other quadrupole effects, and losses in the corrector dipoles. The sum of these contributions was conservatively estimated to be 0.5 MeV per turn per particle with at most a 20% uncertainty [80]. This implies that

$$\frac{dE_{\text{Cher}}}{dL} \leq 10^{-4} \frac{dE_{\text{syn}}}{dL} \; , \tag{3.50}$$

where dE_{Cher}/dL denotes the energy loss per distance traveled due to vacuum Cherenkov radiation.

We may now determine a lower bound for E_{VCR} such that both (3.50) and value (3.49) are satisfied. To this end, recall that for charges near E_{VCR} the dominant Cherenkov process for reaching sub-threshold energies proceeds via single-photon emission (3.48). The energy loss per Cherenkov event must therefore be greater than $E - E_{\text{VCR}}$. The average distance L traversed by an electron before Cherenkov emission occurs is $1/\Gamma_{\text{VCR}}$. With equation (3.48), this yields

$$\frac{dE_{\text{Cher}}}{dL} \geq \alpha \, m_e^2 \, \frac{(E_{\text{LEP}} - E_{\text{VCR}})^3}{2E_{\text{LEP}}^3} \; , \tag{3.51}$$

where $m_e = 5.11 \times 10^{-4}$ GeV denotes the electron mass, as before. It follows that E_{VCR} must be no more than 1.5 MeV below $E_{\text{LEP}} = 104.5$ GeV. With equation (3.47), we then obtain

$$0 \leq \tilde{\kappa}_{tr} \leq 1.2 \times 10^{-11} \; . \tag{3.52}$$

The above reasoning also shows that the uncertainty in the bound (3.52) is primarily determined by the accuracy of the electron-energy measurement. As this limit is still much larger than the scale $\mathcal{S}$ defined in equation (3.45), other photon- or electron-sector coefficients are not further constrained by this reasoning. At the same time, this provides the justification for dropping these additional coefficients from our analysis.

3.3.2   Photon Decay

This section considers the case of a negative $\tilde{\kappa}_{tr}$, which means that the phase speed of light is now greater than unity [3]. Vacuum Cherenkov radiation is then forbidden and cannot be used to set experimental limits. However, the kinematics of the electromagnetic vertex now allows photon decay into a fermion–antifermion pair (3.44). The dispersion relation (3.46) remains valid and establishes that photons with energies

$$E_{\text{pair}} = \frac{2m}{\sqrt{\tilde{\kappa}_{tr}(\tilde{\kappa}_{tr} - 2)}} = \sqrt{\frac{2}{-\tilde{\kappa}_{tr}}}\, m + \mathcal{O}\left(\sqrt{\tilde{\kappa}_{tr}}\right) \qquad (3.53)$$

or above are unstable. As before, m is the fermion mass. The derivation of the corresponding tree-level decay rate (A.106) is presented in Appendix A.5. At leading order in $\tilde{\kappa}_{tr}$, this result gives

$$\Gamma_{\text{pair}} = \frac{2}{3}\, \alpha\, E_\gamma\, \frac{m^2}{E_{\text{pair}}^2} \sqrt{1 - \frac{E_{\text{pair}}^2}{E_\gamma^2}} \left(2 + \frac{E_{\text{pair}}^2}{E_\gamma^2}\right) \; . \qquad (3.54)$$

Here, E_γ denotes the photon energy and α is again the fine-structure constant[4]. The efficiency of this photon decay can be established by example: a $40\,\text{GeV}$ photon with energy 1% above threshold would decay after traveling an average distance of about $15\,\mu\text{m}$.

The above results show that we may obtain limits on negative values of $\tilde{\kappa}_{tr}$ from the existence of long-lived photons with high energies. As for the Cherenkov analysis, cosmic-ray observations provide the potential for the best reach in sensitivity. For example, primary photons from the Crab nebula with energies up to $80\,\text{TeV}$ have been reported by HEGRA [121]. Equation (3.53) then implies that one-sided limits on $\tilde{\kappa}$ coefficients at the 10^{-16} level would be possible. In addition to some of the non-birefringent $\tilde{\kappa}$ matrices, certain SME coefficients in the electron sector can no longer be neglected at these scales. In view of the small event sample for TeV gamma rays, the extraction of comprehensive and clean bounds on this potentially large number

---

[3]This does not necessarily constitute a means to violate causality [87, 120]. For example, we remain free to redefine the coordinate system such that photons move at or below the speed of light c and the maximum attainable speed of massive fermions is distinctly lower than c. In the new coordinate system, both fields obey causality.

[4]Note that a similar investigation of photon decay for negative $\tilde{\kappa}_{tr}$ may be found in [45]

of SME coefficients appears unlikely at the present time. Estimates for limits from astrophysical TeV gamma rays would certainly be useful, but such an analysis lies outside the scope of the present study.

We focus instead on high-energy photons generated in Earth-based laboratories. As for vacuum Cherenkov radiation, the superior experimental control allows cleaner, more conservative limits at the cost of a somewhat diminished sensitivity. In this context, LEP becomes again one possible experiment to consider: studies of quark-to-photon fragmentation involved a careful analysis of final-state photons in LEP scattering events. In such analyses, photons with energies up to 42 GeV have been studied at OPAL [122]. Equation (3.53) then allows limits at the level $-3 \times 10^{-10} \lesssim \tilde{\kappa}_{tr} \leq 0$. Other LEP studies at the L3 [123] and OPAL [124] detectors, which were optimized for QED precision tests, have measured pair annihilation $e^+ e^- \to \gamma\gamma$ at center-of-mass energies up to 209 GeV. This would yield an even better bound of $-5 \times 10^{-11} \lesssim \tilde{\kappa}_{tr} \leq 0$.

Nevertheless, the highest energies at terrestrial accelerators are not reached with electrons but with hadrons. For example, Fermilab's Tevatron $p\bar{p}$ collider reached center-of-mass energies up to 1.96 TeV and offers therefore an excellent potential for producing high-energy photons. One particular process, namely isolated-photon production with an associated jet, is of importance for QCD studies and has therefore been investigated with the D0 detector. In this context, photons of energies up to 442 GeV have been observed [125]. This value implies an estimate of $-3 \times 10^{-12} \lesssim \tilde{\kappa}_{tr} \leq 0$. However, the small number of events observed at this energy did not warrant inclusion into these QCD investigations.

Our analysis uses only D0 photon data at lower energies, where comparisons to QCD predictions were made. With this conservative restriction, photon-energy bins up to 340.5 GeV are at our disposal [126]. For these measurements, the aforementioned jet-plus-photon production was measured as a function of E_γ in four angular regions. These four directional configurations were characterized by the photon and jet pseudorapidities y^γ and y^{jet}. The largest deviations between experiment and QCD theory in the 340.5 GeV energy bin occurred in the $\{|y^{\text{jet}}| < 0.8, y^\gamma y^{\text{jet}} < 0\}$ angular region [126]. The measured cross section was about 52% of the QCD prediction. The relative uncertainties in the experimental value were 46.1% statistical, 12.9% sys-

tematic, and a 7.8% normalization error [126]. To account for theory uncertainties, the employed theoretical scales were varied by a factor of two, which led to a relative spread of about 11% for theoretical predictions [126]. Combining these errors in quadrature yields an overall relative uncertainty of about 50%. The experiment-to-theory ratio in the 340.5 GeV energy bin is therefore 0.52±0.26 for the selected angular configuration. We can thus estimate that at least 26% of the produced photons have reached the detector.

The layout of the D0 detector implies that measured photons traverse a minimum distance of $l_{\min} \simeq 78$ cm: they have to travel through various drift chambers and the transition-radiation detector before they interact and are detected in the central calorimeter [127]. With the above photon-flux estimate, we then obtain

$$\exp\left(-\Gamma_{\mathrm{pair}}\, l_{\min}\right) \geq 0.26 \ . \tag{3.55}$$

The 340.5 GeV energy bin extended from 300 GeV to 400 GeV. We will therefore conservatively take $E_\gamma = 300$ GeV in the final part of our analysis. With equation (3.54), we then find that E_{pair} cannot be more than about 0.1 keV below E_γ. We therefore conclude

$$-5.8 \times 10^{-12} \leq \tilde{\kappa}_{tr} \leq 0 \ . \tag{3.56}$$

This argument also establishes that the uncertainty in the constraint (3.56) is essentially determined by the accuracy of the photon-energy measurement. As for the Cherenkov bound, the limit (3.56) is larger than the scale $\mathcal{S}$, so other photon- or electron-sector coefficients are not further constrained by this argument. At the same time, this justifies the exclusion of these additional coefficients from our study.

3.3.3   Summary and Outlook

In this chapter, we have considered new physical effects arising from a Lorentz-violating CPT-even deviation of the phase speed of light c_{ph} from its conventional value c. At the theoretical level, such a deviation is controlled by the $\tilde{\kappa}_{tr}$ coefficient of the SME. This coefficient is defined with respect to the Sun-centered celestial equatorial coordinate system, in which the phase-speed deviation is isotropic. At

the phenomenological level, a positive value for $\tilde{\kappa}_{tr}$ would lead to vacuum Cherenkov radiation (3.43) at the rate (3.48) for charges with energies above the threshold (3.47); whereas a negative value would cause photon decay (3.44) at the rate (3.54) for photons with energies above the threshold (3.53).

We have exploited the fact that both phenomena are efficient threshold effects to extract constraints on $\tilde{\kappa}_{tr}$ from the non-observation of vacuum Cherenkov radiation and photon decay. In particular, the absence of the Cherenkov effect at LEP leads to the bound (3.52), and from the stability of photons at the Tevatron the constraint (3.56) can be inferred. These results give the combined conservative limit [10, 92]

$$-5.8 \times 10^{-12} \leq \tilde{\kappa}_{tr} \leq 1.2 \times 10^{-11} \ . \tag{3.57}$$

This limit represents an improvement of previous laboratory bounds by 3–4 order of magnitude.

There are various ways to obtain complementary or improved bounds on $\tilde{\kappa}_{tr}$. For instance, future low-energy laboratory tests with present-day technology could reach a level of 10^{-11} or better [8, 9]. Another idea is to exploit photon triple splitting, as it is known that the amplitude for this effect is nonzero in the presence of $c^{\mu\nu}$ Lorentz violation [128]. This effect does not involve a threshold, and so high energies are not necessarily required.

Other future terrestrial bounds could proceed along the line of reasoning of this work employing the absence of vacuum Cherenkov radiation and photon decay at even higher energies than the ones considered here. One example would be the prospective International Linear Collider (ILC). If we take the laboratory-frame energy to be $500 \, \mathrm{GeV}$, the ILC gives a projected one-sided Cherenkov limit of $0 \leq \tilde{\kappa}_{tr} \leq 5.2 \times 10^{-13}$. Similarly, the Large Hadron Collider (LHC) will reach about seven times the energy of the Tevatron. Under the assumption that the energy of produced photons scales by the same factor, the limit (3.56) can be tightened by a factor of 50. Other improvements of the photon-decay bound would be possible with a dedicated D0 (or possibly LHC) analysis: Ultrahigh-energy events not considered for QCD tests could be used because the statistics of such events is not of primary importance for photon-

decay studies. Moreover, the end of the photon-energy spectrum could be exploited more efficiently by avoiding large energy bins.

Ultimately, the best limits on the $\tilde{\kappa}$ coefficients are likely to be derived from improved UHECR studies [44, 45, 110]. Given a more reliable identification of the UHECR primary particle, the prospect of observing still higher-energy events, a more complete coverage of the sky with more events, and a full analysis allowing for the possibility of Lorentz violation in both the primary scatterer as well as its decay products, cosmic ray studies may yet produce an impressive array of limits on Lorentz symmetry violation. The chief limit on the experimental reach of such surveys arises only because the universe becomes opaque to cosmic rays above certain threshold energies, due to processes like GZK suppression or pair creation with IR photons. Until then, however, high-precision experiments carried out in terrestrial laboratories will continue to provide competitive tests of Lorentz symmetry in Nature.

Chapter 4

Quantization of Light in the SME

Most experimental and theoretical investigations of (k_F) to date have treated the electromagnetic fields classically, as happens in analyses of Michelson-Morley tests, or semiclassically with the assumption that the excitations of the quantized fields satisfy the classical dispersion relation, as in Ives-Stilwell experiments. Generally speaking, whenever a fully quantum treatment of both non-birefringent electromagnetism and the coupled charges is necessary, quantization is preceded by a coordinate redefinition which maps $(k_F)^{\alpha}_{\ \mu\alpha\nu} \rightarrow 0$, and the matter-sector $c_{\mu\nu}$ coefficients to $c^X_{\mu\nu} \rightarrow c^X_{\mu\nu} - \frac{1}{2}(k_F)^{\alpha}_{\ \mu\alpha\nu}$. The added complication these steps introduce to the analysis of a physical system is warranted by concerns regarding the stability and causality of the Lorentz-violating quantized theory. For cases involving spontaneous Lorentz violation, the stability and causality of a massive fermion with Lorentz-violating interactions has been explicitly demonstrated [87]. Thus transforming the coordinates such that the non-birefringent components of (k_F) appear in the matter-sector $c_{\mu\nu}$ coefficients maps the question of stability and causality for the electromagnetic theory into the form of a solved problem in the matter sector. To date, there exists no similar explicit demonstration of causality and stability for the photon-sector of the SME.

The downside to this state of affairs is that tractability concerns regarding a given analysis of observational or experimental tests of Lorentz invariance often leads researchers to begin with the arbitrary assumption that the SME coefficients vanish in one or more sectors of the theory [44]. This practice can greatly complicate efforts

to make rigorous comparisons of the results from different experiments. For any given analysis, the equivalence of the theory under coordinate redefinitions permits us to arbitrarily choose to set either the $c_{\mu\nu}^X$ for a single species X or the non-birefringent (k_F) parameters to zero. That is, we are free to use any given particle species, or light, as our reference against which any Lorentz-violating effects will be measured. If the analysis rests on the quantized description of light, this choice is made for us. Thus any analysis of the Ives-Stilwell experiments described in Chapter 3 in terms of $\tilde{\kappa}_{tr}$ is formally incorrect, despite being entirely consistent with the results of a derivation in coordinates such that $\tilde{\kappa}_{tr}$ is mapped onto the $c_{\mu\nu}$ coefficients.

Our goal in this chapter is to make the first steps towards deriving a fully quantized Hamiltonian representation of electrodynamics in the photon sector of the SME. Since the Earth is evidently in a concordant[1] frame [87] with respect to any of the (k_F) coefficients, we focus on proving that the free field theory can be stably quantized in an arbitrary concordant inertial frame. We demonstrate that the Hamiltonian that results from the photon-sector Lagrangian is Hermitian; and further that it leaves the subspace of states that correspond to solutions of the Lorentz-violating Maxwell equations invariant. Thus we demonstrate that the free field Hamiltonian is at least physically consistent within a given inertial frame.

Although we do not explicitly consider questions of stability and causality in arbitrary frames, we do find that the quantized modes reproduce the dispersion relation obtained from the classical Lorentz-violating theory [5]. At the end of 4.2, we find the explicit form of the unitary transformation that diagonalizes the Lorentz-violating Hamiltonian operator in terms of the normal modes of the fully covariant theory. As this transformation is frame-dependent, this is consistent with the observation made in [78] that the vacuum in one inertial frame may not be equivalent to that in another inertial frames, much as happens in when comparing the vacua of the covariant theory in an inertial frame with one in an accelerated frame [129, 130].

In the process of our derivation, we also discover that the subsidiary gauge con-

---

[1]Where by "concordant", we mean a frame in which the parameters describing Lorentz-violation are sufficiently small as to avoid issues of stability and causality in the effective theory, without the need to refer to the details of an underlying high-energy theory. Current experience suggests that any frame moving slowly relative to the Earth-Sun system must be concordant [87].

dition used by Gupta and Bleuler [89] in quantizing the electromagnetic potential of the fully covariant theory is incorrect when applied to the entirety of the quantized Hilbert space. Although the consequences of imposing an overly broad subsidiary condition are negligible to the fully covariant theory, they are severe for the Lorentz-violating model. We therefore replace the subsidiary condition with a weaker Lorenz gauge condition in part 4.3.4.

Finally, in part 4.4, we consider the form of the transverse potentials in terms of the free-field eigenmode operators. The unitary transformation derived at the end of 4.2 is shown to lead to anisotropic scaling as well as mixing between the transverse potentials. This suggests that the "non-birefringent" components of (k_F) could lead to a birefringent coupling between light and an isotropic medium it passes through. Although the present result is not conclusive, the existence of a similar effect arising from the electron $c_{\mu\nu}$ coefficients in a dielectric medium has been postulated [61].

4.1   The Lagrangian

We begin with the photon-sector free-field Lagrangian density

$$\mathcal{L} = -\frac{1}{4}F_{\mu\nu}F^{\mu\nu} - \frac{1}{4}(k_F)_{\kappa\lambda\mu\nu}F^{\kappa\lambda}F^{\mu\nu}, \tag{4.1}$$

where $F_{\mu\nu} = \partial_\nu A_\mu - \partial_\mu A_\nu$, and we have assumed $(k_{AF}) = 0$ (see part 2.2). Direct canonical quantization of the potential A_μ using (4.1) is impossible since observer Lorentz invariance requires the commutator between the quantized fields to be a Lorentz scalar, and the momentum π^0 conjugate to the scalar potential A^0 is given by

$$\pi^0 = \frac{\partial \mathcal{L}}{\partial \dot{A}^0} = 0. \tag{4.2}$$

This is a reflection of the fact that the scalar potential is not a physical observable. This problem can be addressed by quantizing an observable like $\vec{E}$, in place of the physically unobservable vector potential A^μ, but taking such a step at this stage would complicate the form of the interaction with charges, and obscure the Lorentz covariance of the F^2 component of the Lagrangian. Our first step is therefore to find

an alternative Lagrangian which produces the same physics. The equations of motion which result from (4.1) are

$$\partial^\alpha \frac{\partial \mathcal{L}}{\partial(\partial^\alpha A^\gamma)} = \partial^\alpha F_{\alpha\gamma} + \partial^\alpha (k_F)_{\alpha\gamma} F^{\mu\nu} = 0. \tag{4.3}$$

In terms of the potentials, taking into account that (k_F) has the symmetries of the Riemann tensor (see B.1), we obtain the modified Maxwell equations

$$\Box A_\gamma - \partial_\gamma(\partial^\alpha A_\alpha) - 2(k_F)_{\alpha\gamma\mu\nu}\partial^\alpha\partial^\nu A^\mu = 0. \tag{4.4}$$

Proceeding in a fashion similar to those employed in quantizing the field potentials in the covariant theory [131], we introduce the SME Fermi Lagrangian

$$\begin{aligned}
\mathcal{L} = & -\frac{1}{2}(\partial_\nu A_\mu)(\partial^\nu A^\mu) - \frac{1}{4}(k_F)_{\kappa\lambda\mu\nu}F^{\kappa\lambda}F^{\mu\nu} \\
= & -\frac{1}{2}(\partial_\nu A_\mu)(\partial^\nu A^\mu) - (k_F)_{\kappa\lambda\mu\nu}(\partial^\lambda A^\kappa)(\partial^\nu A^\mu),
\end{aligned} \tag{4.5}$$

which, like the fully Lorentz covariant Fermi Lagrangian used to quantize the covariant theory, has a nonzero momentum π^0 conjugate to A^0. The equations of motion resulting from (4.5) are then

$$\Box A_\gamma - 2(k_F)_{\alpha\gamma\mu\nu}(\partial^\alpha\partial^\nu A^\mu) = 0, \tag{4.6}$$

which are equivalent to (4.4), provided that we enforce the Lorenz gauge condition

$$\partial^\alpha A_\alpha = 0. \tag{4.7}$$

Separating the spatial and time-derivatives in the Lagrangian, we obtain

$$\begin{aligned}
\mathcal{L} = & -\frac{1}{2}\left[(\partial_0 A_\mu)(\partial^0 A^\mu) + (\partial_p A_\mu)(\partial^p A^\mu)\right] - (k_F)_{\kappa 0\mu 0}(\partial^0 A^\kappa)(\partial^0 A^\mu) \\
& - (k_F)_{\kappa p\mu 0}(\partial^p A^\kappa)(\partial^0 A^\mu) - (k_F)_{\kappa 0\mu q}(\partial^0 A^\kappa)(\partial^q A^\mu) - (k_F)_{\kappa p\mu q}(\partial^p A^\kappa)(\partial^q A^\mu)
\end{aligned} \tag{4.8}$$

The full Lagrangian is obtained by integrating $\mathcal{L}$ over all space, so we may use the Parseval-Plancherel identity to obtain the reciprocal-space Lagrangian density

$$\begin{aligned}
\widetilde{\mathcal{L}} = & -\frac{1}{2}\left[(\partial_0\mathcal{A}_\mu(\vec{k}))(\partial^0\mathcal{A}^\mu(\vec{k}))^* + k_p k^p \mathcal{A}_\mu(\vec{k})\mathcal{A}^\mu(\vec{k})^*\right] \\
& - (k_F)_{\kappa 0\mu 0}(\partial^0\mathcal{A}^\kappa(\vec{k}))(\partial^0\mathcal{A}^\mu(\vec{k}))^* + ik^p(k_F)_{\kappa p\mu 0}(\mathcal{A}^\kappa(\vec{k}))(\partial^0\mathcal{A}^\mu(\vec{k}))^* \\
& - ik^q(k_F)_{\kappa 0\mu q}(\partial^0\mathcal{A}^\kappa(\vec{k}))(\mathcal{A}^\mu(\vec{k}))^* - k^p k^q(k_F)_{\kappa p\mu q}(\mathcal{A}^\kappa(\vec{k}))(\mathcal{A}^\mu(\vec{k}))^*,
\end{aligned} \tag{4.9}$$

from which the full Lagrangian may be recovered by integrating over all $\vec{k}$. Because the potentials are real, we have

$$\mathcal{A}^\mu(\vec{k}) = \mathcal{A}^\mu(-\vec{k})^*, \tag{4.10}$$

which permits us to write the full Lagrangian as an integral over only half of reciprocal space of the Lagrangian density $\widetilde{\mathcal{L}}_R$,

$$
\begin{aligned}
\widetilde{\mathcal{L}}_R = &- \left[(\partial_0 \mathcal{A}_\mu(\vec{k}))(\partial^0 \mathcal{A}^\mu(\vec{k}))^* + k_p k^p \mathcal{A}_\mu(\vec{k}) \mathcal{A}^\mu(\vec{k})^* \right] \\
&- (k_F)_{\kappa 0 \mu 0}(\partial^0 \mathcal{A}^\kappa(\vec{k}))(\partial^0 \mathcal{A}^\mu(\vec{k}))^* - (k_F)_{\kappa 0 \mu 0}(\partial^0 \mathcal{A}^\kappa(\vec{k}))^*(\partial^0 \mathcal{A}^\mu(\vec{k})) \\
&+ ik^p (k_F)_{\kappa p \mu 0}(\mathcal{A}^\kappa(\vec{k}))(\partial^0 \mathcal{A}^\mu(\vec{k}))^* - ik^p (k_F)_{\kappa p \mu 0}(\mathcal{A}^\kappa(\vec{k}))^*(\partial^0 \mathcal{A}^\mu(\vec{k})) \\
&- ik^q (k_F)_{\kappa 0 \mu q}(\partial^0 \mathcal{A}^\kappa(\vec{k}))(\mathcal{A}^\mu(\vec{k}))^* + ik^q (k_F)_{\kappa 0 \mu q}(\partial^0 \mathcal{A}^\kappa(\vec{k}))^*(\mathcal{A}^\mu(\vec{k})) \\
&- k^p k^q (k_F)_{\kappa p \mu q}(\mathcal{A}^\kappa(\vec{k}))(\mathcal{A}^\mu(\vec{k}))^* - k^p k^q (k_F)_{\kappa p \mu q}(\mathcal{A}^\kappa(\vec{k}))^*(\mathcal{A}^\mu(\vec{k})).
\end{aligned}
\tag{4.11}
$$

Taking $\mathcal{A}^\gamma(\vec{k})$ as our coordinates, we find that the conjugate momenta are given by (using $\pi_\gamma(\vec{k}) = (1/c)\partial\widetilde{\mathcal{L}}_R/\partial(\partial^0\mathcal{A}^\gamma(\vec{k})^*)$):

$$c\pi_\gamma(\vec{k}) = -(\partial_0\mathcal{A}_\gamma(\vec{k})) - 2(k_F)_{\gamma 0 \kappa 0}(\partial^0\mathcal{A}^\kappa(\vec{k})) + 2ik^p(k_F)_{\gamma 0 \kappa p}\mathcal{A}^\kappa(\vec{k}). \tag{4.12}$$

This can be solved to leading order in (k_F) for $(\partial_0\mathcal{A}_\gamma(\vec{k}))$ as

$$\partial_0\mathcal{A}_\gamma(\vec{k}) = -c\pi_\gamma(\vec{k}) + 2c(k_F)_{\gamma 0 \kappa 0}\pi^\kappa(\vec{k}) + 2ik^p(k_F)_{\gamma 0 \kappa p}\mathcal{A}^\kappa(\vec{k}) + \mathcal{O}\left((k_F)^2\right). \tag{4.13}$$

By substituting the leading order expansion (4.13) for $(\partial_0\mathcal{A}_\gamma(\vec{k}))$ in (4.11), we exchange the exact Lagrangian for one which is equivalent to first order in (k_F) at the cost of adding additional unphysical terms at second order. We seek a leading order expansion, and so shall ignore all second order and higher couplings. This leads to the approximate Lagrangian density

$$
\begin{aligned}
\widetilde{\mathcal{L}}_R = -\Big(& c^2(g_{\kappa\mu} - 2(k_F)_{\kappa 0 \mu 0})\pi^\kappa(\vec{k})\pi^\mu(\vec{k})^* \\
& + (g_{\kappa\mu}g_{pq} + 2(k_F)_{\kappa p \mu q})k^p k^q(\mathcal{A}^\kappa(\vec{k}))(\mathcal{A}^\mu(\vec{k}))^* \Big),
\end{aligned}
\tag{4.14}
$$

where $g_{\mu\nu}$ is the Minkowski metric: $g_{\mu\nu} = \mathrm{diag}\,(1, -1, -1, -1)$.

4.2   The Hamiltonian

The Hamiltonian density is given by

$$\widetilde{\mathcal{H}}_R = c(\pi^\gamma(\vec{k}))(\partial_0 \mathcal{A}_\gamma(\vec{k}))^* + c(\partial_0 \mathcal{A}_\gamma(\vec{k}))(\pi^\gamma(\vec{k}))^* - \widetilde{\mathcal{L}}_R, \tag{4.15}$$

and so using (4.13) and (4.14), $\widetilde{\mathcal{H}}_R$ becomes

$$\widetilde{\mathcal{H}}_R = \left((g_{\kappa\mu}g_{pq} + 2(k_F)_{\kappa p\mu q})k^p k^q (\mathcal{A}^\kappa(\vec{k}))(\mathcal{A}^\mu(\vec{k}))^* - c^2 (g_{\kappa\mu} - 2(k_F)_{\kappa 0\mu 0})\pi^\kappa(\vec{k})\pi^\mu(\vec{k})^* \right) \\ - 2ick^p (k_F)_{\gamma 0\kappa p} \left[(\pi^\gamma(\vec{k}))(\mathcal{A}^\kappa(\vec{k}))^* - (\mathcal{A}^\kappa(\vec{k}))(\pi^\gamma(\vec{k}))^* \right]. \tag{4.16}$$

Since this theory is a perturbation of the fully Lorentz covariant theory, we expect the normal modes that result to be perturbations of the fully covariant normal modes. These standard normal modes can be written in terms of $\mathcal{A}^\mu(\vec{k})$ and $\pi^\mu(\vec{k})$, so that

$$\alpha^\mu(\vec{k}) = \sqrt{\frac{c^2}{2\hbar\omega_k}} \left[\frac{\omega_k}{c^2} \mathcal{A}^\mu(\vec{k}) + i\pi^\mu(\vec{k}) \right] \tag{4.17}$$

$$\alpha^\mu(\vec{k})^* = \sqrt{\frac{c^2}{2\hbar\omega_k}} \left[\frac{\omega_k}{c^2} \mathcal{A}^\mu(-\vec{k}) - i\pi^\mu(-\vec{k}) \right] \tag{4.18}$$

$$\alpha^\mu(-\vec{k}) = \sqrt{\frac{c^2}{2\hbar\omega_k}} \left[\frac{\omega_k}{c^2} \mathcal{A}^\mu(-\vec{k}) + i\pi^\mu(-\vec{k}) \right] \tag{4.19}$$

$$\alpha^\mu(-\vec{k})^* = \sqrt{\frac{c^2}{2\hbar\omega_k}} \left[\frac{\omega_k}{c^2} \mathcal{A}^\mu(\vec{k}) - i\pi^\mu(\vec{k}) \right], \tag{4.20}$$

where we have made use of the reality of the potentials and their conjugate momenta (4.10). Note that insofar as choosing a set of variables to write the Hamiltonian in terms of, we are free to make use of any linear combination of $\mathcal{A}^\mu(\vec{k})$ and $\pi^\mu(\vec{k})$ that yield an acceptable commutator. We have chosen $\omega_k = |\vec{k}|c$, as is usual for the fully covariant theory. As a consequence of our choosing an ω_k that does not necessarily satisfy the Lorentz-violating dispersion relation, there will be terms coupling the forward propagating modes to those propagating backwards in the Hamiltonian. At the end of our derivation, these and other similar terms will be eliminated by a transformation of the mode operators, diagonalizing $\widetilde{\mathcal{H}}_R$, and which can be interpreted

in part as changing ω_k to satisfy the appropriate dispersion relation. Proceeding using this set of (approximately) normal modes, we then find that

$$\mathcal{A}^\mu(\vec{k}) = \sqrt{\frac{\hbar c^2}{2\omega_k}} \left(\alpha^\mu(\vec{k}) + \alpha^\mu(-\vec{k})^* \right) \tag{4.21}$$

$$\pi^\mu(\vec{k}) = -i\sqrt{\frac{\hbar \omega_k}{2c^2}} \left(\alpha^\mu(\vec{k}) - \alpha^\mu(-\vec{k})^* \right). \tag{4.22}$$

We can quantize this theory by identifying $\mathcal{A}^\mu(\vec{k})$ and $\pi^\nu(\vec{k})$ as operators with the canonical commutation relation

$$\left[\mathcal{A}^\mu(\vec{k}), \overline{\pi^\nu}(\vec{k'}) \right] = i\hbar g^{\mu\nu} \delta(\vec{k} - \vec{k'}), \tag{4.23}$$

where $\overline{A}$ represents the adjoint of an operator A. We use this peculiar form so as to be consistent with the notation of [90], and to distinguish the properties of the adjoint in the canonically quantized metric from those of the adjoint in the "physical" metric used to define a basis in Hilbert space, as discussed in more detail in section 4.3. The (approximately) normal modes $\alpha(\vec{k})$ now become operators $a(\vec{k})$, whose non-vanishing commutators are, from (4.23)

$$\left[a_r(\vec{k}), \overline{a}_s(\vec{k'}) \right] = \zeta_r \delta_{rs} \delta(\vec{k} - \vec{k'}), \tag{4.24}$$

where $\zeta_r = \{-1, 1, 1, 1\}$ for $r = \{0, 1, 2, 3\}^2$. In what follows, it will be useful to distinguish between the scalar, transverse, and longitudinal modes associated with a given $\vec{k}$. Thus we take the $\{a_0(\vec{k}), \overline{a}_0(\vec{k})\}$ to act on the scalar modes, $\{a_3(\vec{k}), \overline{a}_3(\vec{k})\}$ to act on longitudinal modes, and the $\{a_1(\vec{k}), \overline{a}_1(\vec{k})\}$ and $\{a_2(\vec{k}), \overline{a}_2(\vec{k})\}$ operators to act on the transverse modes for fields propagating parallel to $\vec{k}$. We can then write $\mathcal{A}$ and π as

$$\mathcal{A}^\mu(\vec{k}) = \sqrt{\frac{\hbar c^2}{2\omega_k}} \sum_r \epsilon_r^\mu(\vec{k}) \left(a_r(\vec{k}) + \overline{a}_r(-\vec{k}) \right) \tag{4.25}$$

$$\pi^\nu(\vec{k}) = -i\sqrt{\frac{\hbar \omega_k}{2c^2}} \sum_s \epsilon_s^\nu(\vec{k}) \left(a_s(\vec{k}) - \overline{a}_s(-\vec{k}) \right). \tag{4.26}$$

---

[2]To be consistent with the notation of [131], we have departed from our usual convention that reserves roman indices for 3-vectors, as r now denotes the scalar ($r = 0$), transverse ($r = 1, 2$) and longitudinal ($r = 3$) modes for a given wavevector $\vec{k}$, rather than the components of a 3 or 4-vector.

The newly introduced $\epsilon_s^\nu(\vec{k})$ tensor is responsible for keeping track of which time-spatial components of A^μ are excited by the mode operators. Following [131], and as defined in part 2.2 $\epsilon_0^\nu(\vec{k}) = (-1, 0, 0, 0)$, while the spatial components $\vec{\epsilon}_j(\vec{k})$ form a set of mutually orthogonal polarization vectors for each $\vec{k}$. Specifically, we choose $\vec{\epsilon}_p(\vec{k}) \times \vec{\epsilon}_q(\vec{k}) = \epsilon_{pqr}\vec{\epsilon}_r(\vec{k})$, with $\vec{\epsilon}_1(\vec{k}) = \vec{\epsilon}_1(-\vec{k})$, $\vec{\epsilon}_2(\vec{k}) = -\vec{\epsilon}_2(-\vec{k})$, and $\vec{\epsilon}_3(\vec{k}) = \hat{k} = -\vec{\epsilon}_3(-\vec{k})$. With these definitions, (4.24) is easily shown to be consistent with (4.23). Note that at this point, we can immediately infer that the form of the fields' conserved momentum operator is unchanged from its form in the fully covariant theory, since the conserved momentum density is given by

$$\mathcal{P}^j(\vec{k}) = \pi_\gamma(\vec{k})\left(-i\vec{k}^j\mathcal{A}^\gamma(\vec{k})\right)^* + \pi_\gamma(\vec{k})^*\left(i\vec{k}^j\mathcal{A}^\gamma(\vec{k})\right), \tag{4.27}$$

which does not depend upon (k_F). Substituting (4.25) and (4.26) into (4.16), we find

$$\begin{aligned}
\widetilde{\mathcal{H}}_R = {}& \hbar\omega_k \left(-\epsilon_{r,\mu}(\vec{k})\epsilon_s^\mu(\vec{k})\right)\left(a_r(\vec{k})\bar{a}_s(\vec{k}) + \bar{a}_r(-\vec{k})a_s(-\vec{k})\right) \\
&+ \hbar\omega_k \left(\epsilon_r^\kappa(\vec{k})\epsilon_s^\mu(\vec{k})\right)\left((k_F)_{\kappa p\mu q}\hat{k}^p\hat{k}^q + (k_F)_{\kappa 0\mu 0} - (k_F)_{\mu 0\kappa p}\hat{k}^p\right)\left[a_r(\vec{k})\bar{a}_s(\vec{k})\right] \\
&+ \hbar\omega_k \left(\epsilon_r^\kappa(\vec{k})\epsilon_s^\mu(\vec{k})\right)\left((k_F)_{\kappa p\mu q}\hat{k}^p\hat{k}^q + (k_F)_{\kappa 0\mu 0} + (k_F)_{\mu 0\kappa p}\hat{k}^p\right)\left[\bar{a}_r(-\vec{k})a_s(-\vec{k})\right] \\
&+ \hbar\omega_k \left(\epsilon_r^\kappa(\vec{k})\epsilon_s^\mu(\vec{k})\right)\left((k_F)_{\kappa p\mu q}\hat{k}^p\hat{k}^q - (k_F)_{\kappa 0\mu 0} + (k_F)_{\mu 0\kappa p}\hat{k}^p\right)\left[a_r(\vec{k})a_s(-\vec{k})\right] \\
&+ \hbar\omega_k \left(\epsilon_r^\kappa(\vec{k})\epsilon_s^\mu(\vec{k})\right)\left((k_F)_{\kappa p\mu q}\hat{k}^p\hat{k}^q - (k_F)_{\kappa 0\mu 0} - (k_F)_{\mu 0\kappa p}\hat{k}^p\right)\left[\bar{a}_r(-\vec{k})\bar{a}_s(\vec{k})\right] \\
&- \hbar\omega_k\hat{k}^p(k_F)_{\mu 0\kappa p}\left(\epsilon_r^\kappa(\vec{k})\epsilon_s^\mu(\vec{k})\right)\left[a_s(\vec{k})\bar{a}_r(\vec{k}) - \bar{a}_s(-\vec{k})a_r(-\vec{k})\right] \\
&- \hbar\omega_k\hat{k}^p(k_F)_{\mu 0\kappa p}\left(\epsilon_r^\kappa(\vec{k})\epsilon_s^\mu(\vec{k})\right)\left[a_s(\vec{k})a_r(-\vec{k}) - \bar{a}_s(-\vec{k})\bar{a}_r(\vec{k})\right].
\end{aligned} \tag{4.28}$$

Note that the first line of the above expression for $\widetilde{\mathcal{H}}_R$ is that of the covariant free-field, and the terms that follow represent the Lorentz-violating perturbation. Making use of the identity (B.7) in Appendix B.1, we note that

$$\begin{aligned}
(k_F)_{\kappa 0\mu 0}\epsilon_r^\kappa(\vec{k})\epsilon_s^\mu(\vec{k}) &= (k_F)_{\kappa\lambda\mu\nu}\epsilon_r^\kappa(\vec{k})\delta_{\lambda 0}\epsilon_s^\mu(\vec{k})\delta_{\nu 0} \\
&= -\frac{1}{2}\left[\vec{\epsilon}_r(\vec{k}) \cdot (\tilde{\kappa}_{e-} + I\tilde{\kappa}_{tr}) \cdot \vec{\epsilon}_s(\vec{k})\right],
\end{aligned} \tag{4.29}$$

$$\epsilon_r^\kappa(\vec{k})\epsilon_s^\mu(\vec{k})(k_F)_{\kappa p\mu q}\hat{k}^p\hat{k}^q = (k_F)_{\kappa p\mu q}\epsilon_r^\kappa(\vec{k})\hat{k}^p\epsilon_s^\mu(\vec{k})\hat{k}^q$$

$$= -\frac{1}{2}\epsilon_r^0(\vec{k})\epsilon_s^0(\vec{k})\left(\left[\hat{k}\right]\cdot(\tilde{\kappa}_{e-} + I\tilde{\kappa}_{tr})\cdot\left[\hat{k}\right]\right)$$

$$-\frac{1}{2}\left(\left[\epsilon_r^0\hat{k}\right]\cdot\tilde{\kappa}_{o+}\cdot\left[\vec{\epsilon}_s(\vec{k})\times\hat{k}\right] + \left[\epsilon_s^0\hat{k}\right]\cdot\tilde{\kappa}_{o+}\cdot\left[\vec{\epsilon}_r(\vec{k})\times\hat{k}\right]\right)$$

$$-\frac{1}{2}\left(\left[\vec{\epsilon}_r(\vec{k})\times\hat{k}\right]\cdot(\tilde{\kappa}_{e-} + I\tilde{\kappa}_{tr})\cdot\left[\vec{\epsilon}_s(\vec{k})\times\hat{k}\right]\right)$$

$$= -\frac{1}{2}\Bigg\{\epsilon_r^0(\vec{k})\epsilon_s^0(\vec{k})\left[\vec{\epsilon}_3(\vec{k})\cdot(\tilde{\kappa}_{e-} + I\tilde{\kappa}_{tr})\cdot\vec{\epsilon}_3(\vec{k})\right]$$

$$+ \epsilon_{s3m}\epsilon_r^0(\vec{k})\left[\vec{\epsilon}_3(\vec{k})\cdot\tilde{\kappa}_{o+}\cdot\vec{\epsilon}_m(\vec{k})\right]$$

$$+ \epsilon_{r3m}\epsilon_s^0(\vec{k})\left[\vec{\epsilon}_3(\vec{k})\cdot\tilde{\kappa}_{o+}\cdot\vec{\epsilon}_m(\vec{k})\right]$$

$$+ \epsilon_{r3n}\epsilon_{s3m}\left[\vec{\epsilon}_n(\vec{k})\cdot(\tilde{\kappa}_{e-} + I\tilde{\kappa}_{tr})\cdot\vec{\epsilon}_m(\vec{k})\right]\Bigg\},$$

$$(4.30)$$

and

$$\epsilon_r^\kappa(\vec{k})\epsilon_s^\mu(\vec{k})(k_F)_{\mu 0\kappa p}\hat{k}^p = (k_F)_{\kappa p\mu 0}\epsilon_r^\kappa(\vec{k})\hat{k}^p\epsilon_s^\mu(\vec{k})$$

$$= \frac{1}{2}\left(\left[\epsilon_r^0(\vec{k})\hat{k}\right]\cdot(\tilde{\kappa}_{e-} + I\tilde{\kappa}_{tr})\cdot\left[\vec{\epsilon}_s(\vec{k})\right]\right)$$

$$+ \frac{1}{2}\left(\left[\vec{\epsilon}_s(\vec{k})\right]\cdot\tilde{\kappa}_{o+}\cdot\left[\vec{\epsilon}_r(\vec{k})\times\hat{k}\right]\right)$$

$$= \frac{1}{2}\Bigg(\epsilon_r^0(\vec{k})\left[\vec{\epsilon}_s(\vec{k})\cdot(\tilde{\kappa}_{e-} + I\tilde{\kappa}_{tr})\cdot\vec{\epsilon}_3(\vec{k})\right]$$

$$+ \epsilon_{r3m}\left[\vec{\epsilon}_s(\vec{k})\cdot\tilde{\kappa}_{o+}\cdot\vec{\epsilon}_m(\vec{k})\right]\Bigg). \qquad (4.31)$$

By substituting the above three expressions into the Hamiltonian (4.28), and taking full advantage of the symmetry of the $\tilde{\kappa}_{e-}$ matrix and the antisymmetry of $\tilde{\kappa}_{o+}$; for which the scalar product with two vectors $\vec{v}_1$ and $\vec{v}_2$ obey

$$\vec{v}_1\cdot\tilde{\kappa}_{e-}\cdot\vec{v}_2 = \vec{v}_2\cdot\tilde{\kappa}_{e-}\cdot\vec{v}_1 \qquad (4.32)$$

$$\vec{v}_1\cdot\tilde{\kappa}_{o+}\cdot\vec{v}_2 = -\vec{v}_2\cdot\tilde{\kappa}_{o+}\cdot\vec{v}_1, \qquad (4.33)$$

we can write the Hamiltonian density in five parts.

$$\widetilde{\mathcal{H}}_R = \widetilde{\mathcal{H}}_T + \widetilde{\mathcal{H}}_{\pm,T} + \widetilde{\mathcal{H}}_{LS} + \widetilde{\mathcal{H}}_{+,T,LS} + \widetilde{\mathcal{H}}_{-,T,LS}, \qquad (4.34)$$

where $\widetilde{\mathcal{H}}_T$ includes products of transverse mode operators with the same wavevector $\vec{k}$, $\widetilde{\mathcal{H}}_{\pm,T}$ contains products of the transverse mode operators with opposing wavevectors $-\vec{k}$, $\widetilde{\mathcal{H}}_{LS}$ includes terms involving only the longitudinal and scalar modes, and the couplings between the "positive" and "negative" transverse modes with the longitudinal and scalar degrees of freedom are expressed in $\widetilde{\mathcal{H}}_{+,T,LS}$ and $\widetilde{\mathcal{H}}_{-,T,LS}$. To simplify the expression for $\widetilde{\mathcal{H}}_T$, we write the fractional shift in the speed of light moving parallel to $\vec{k}$ due to the Lorentz-violating terms as

$$\delta(\vec{k}) = \left[\vec{\epsilon}_1(\vec{k}) \cdot \tilde{\kappa}_{o+} \cdot \vec{\epsilon}_2(\vec{k})\right] - \frac{1}{2}\sum_{r=1}^{2}\left[\vec{\epsilon}_r(\vec{k}) \cdot (\tilde{\kappa}_{e-} + I\tilde{\kappa}_{tr}) \cdot \vec{\epsilon}_r(\vec{k})\right]. \tag{4.35}$$

Recalling that the Hamiltonian density $\widetilde{\mathcal{H}}_R$ is only summed over half of reciprocal space, we obtain

$$\begin{aligned}
\widetilde{\mathcal{H}}_T = \ &\hbar\omega_k\left[1 + \delta(\vec{k})\right]\left(a_1(\vec{k})\bar{a}_1(\vec{k}) + a_2(\vec{k})\bar{a}_2(\vec{k})\right) \\
&+ \hbar\omega_k\left[1 + \delta(-\vec{k})\right]\left(\bar{a}_1(-\vec{k})a_1(-\vec{k}) + \bar{a}_2(-\vec{k})a_2(-\vec{k})\right).
\end{aligned} \tag{4.36}$$

This shows that the leading order shift to the energy of photons with wavevector $\vec{k}$ is consistent with the dispersion relation derived from the Lagrangian [5, 28]. The remaining $\widetilde{\mathcal{H}}_{\pm,T}$, $\widetilde{\mathcal{H}}_{+,T,LS}$, and $\widetilde{\mathcal{H}}_{-,T,LS}$ terms, as well as the cross couplings between scalar and longitudinal modes in $\widetilde{\mathcal{H}}_{LS}$, can be attributed to the differences between the normal modes of the covariant theory and those of the Lorentz-violating model.

$$\begin{aligned}
\widetilde{\mathcal{H}}_{\pm,T} = \frac{\hbar\omega_k}{2}\Bigg\{ &\left(\left[\vec{\epsilon}_1(\vec{k}) \cdot (\tilde{\kappa}_{e-} + I\tilde{\kappa}_{tr}) \cdot \vec{\epsilon}_1(\vec{k})\right] - \left[\vec{\epsilon}_2(\vec{k}) \cdot (\tilde{\kappa}_{e-} + I\tilde{\kappa}_{tr}) \cdot \vec{\epsilon}_2(\vec{k})\right]\right) \times \\
&\left(a_1(\vec{k})a_1(-\vec{k}) + \bar{a}_1(-\vec{k})\bar{a}_1(\vec{k}) - a_2(\vec{k})a_2(-\vec{k}) - \bar{a}_2(-\vec{k})\bar{a}_2(\vec{k})\right) \\
&+ \left(2\left[\vec{\epsilon}_1(\vec{k}) \cdot (\tilde{\kappa}_{e-} + I\tilde{\kappa}_{tr}) \cdot \vec{\epsilon}_2(\vec{k})\right]\right)\left(a_1(\vec{k})a_2(-\vec{k}) + \bar{a}_2(-\vec{k})\bar{a}_1(\vec{k})\right) \\
&+ \left(2\left[\vec{\epsilon}_1(\vec{k}) \cdot (\tilde{\kappa}_{e-} + I\tilde{\kappa}_{tr}) \cdot \vec{\epsilon}_2(\vec{k})\right]\right)\left(a_2(\vec{k})a_1(-\vec{k}) + \bar{a}_1(-\vec{k})\bar{a}_2(\vec{k})\right)\Bigg\}.
\end{aligned} \tag{4.37}$$

$$\widetilde{\mathcal{H}}_{LS} = \hbar\omega_k \left(a_3(\vec{k})\bar{a}_3(\vec{k}) + \bar{a}_3(-\vec{k})a_3(-\vec{k}) \right) - \left(a_0(\vec{k})\bar{a}_0(\vec{k}) + \bar{a}_0(-\vec{k})a_0(-\vec{k}) \right)$$

$$- \frac{\hbar\omega_k}{2} \left[\vec{\epsilon}_3(\vec{k}) \cdot (\tilde{\kappa}_{e-} + I\tilde{\kappa}_{tr}) \cdot \vec{\epsilon}_3(\vec{k}) \right] \left\{ a_3(\vec{k})\bar{a}_3(\vec{k}) + \bar{a}_3(-\vec{k})a_3(-\vec{k}) \right.$$

$$+ a_0(\vec{k})\bar{a}_0(\vec{k}) + \bar{a}_0(-\vec{k})a_0(-\vec{k}) + a_0(\vec{k})a_0(-\vec{k}) + \bar{a}_0(-\vec{k})\bar{a}_0(\vec{k})$$

$$+ a_3(\vec{k})a_0(-\vec{k}) + \bar{a}_0(-\vec{k})\bar{a}_3(\vec{k}) - a_0(\vec{k})a_3(-\vec{k}) - \bar{a}_3(-\vec{k})\bar{a}_0(\vec{k})$$

$$- a_3(\vec{k})a_3(-\vec{k}) - \bar{a}_3(-\vec{k})\bar{a}_3(\vec{k}) + a_0(\vec{k})\bar{a}_3(\vec{k}) + a_3(\vec{k})\bar{a}_0(\vec{k})$$

$$\left. - \bar{a}_0(-\vec{k})a_3(-\vec{k}) - \bar{a}_3(-\vec{k})a_0(-\vec{k}) \right\} \tag{4.38}$$

$$\widetilde{\mathcal{H}}_{+,T,LS} = \frac{-\hbar\omega_k}{2} \left\{ \left(\left[\vec{\epsilon}_1(\vec{k}) \cdot (\tilde{\kappa}_{e-} + I\tilde{\kappa}_{tr}) \cdot \vec{\epsilon}_3(\vec{k}) \right] - \left[\vec{\epsilon}_3(\vec{k}) \cdot \tilde{\kappa}_{o+} \cdot \vec{\epsilon}_2(\vec{k}) \right] \right) \times \right.$$

$$\left(a_0(\vec{k})\bar{a}_1(\vec{k}) + a_1(\vec{k})\bar{a}_0(\vec{k}) + a_3(\vec{k})\bar{a}_1(\vec{k}) + a_1(\vec{k})\bar{a}_3(\vec{k}) \right.$$

$$\left. + a_1(\vec{k})a_0(-\vec{k}) + \bar{a}_0(-\vec{k})\bar{a}_1(\vec{k}) - a_1(\vec{k})a_3(-\vec{k}) - \bar{a}_3(-\vec{k})\bar{a}_1(\vec{k}) \right)$$

$$+ \left(\left[\vec{\epsilon}_2(\vec{k}) \cdot (\tilde{\kappa}_{e-} + I\tilde{\kappa}_{tr}) \cdot \vec{\epsilon}_3(\vec{k}) \right] + \left[\vec{\epsilon}_3(\vec{k}) \cdot \tilde{\kappa}_{o+} \cdot \vec{\epsilon}_1(\vec{k}) \right] \right) \times$$

$$\left(a_0(\vec{k})\bar{a}_2(\vec{k}) + a_2(\vec{k})\bar{a}_0(\vec{k}) + a_3(\vec{k})\bar{a}_2(\vec{k}) + a_2(\vec{k})\bar{a}_3(\vec{k}) \right.$$

$$\left. \left. + a_2(\vec{k})a_0(-\vec{k}) + \bar{a}_0(-\vec{k})\bar{a}_2(\vec{k}) - a_2(\vec{k})a_3(-\vec{k}) - \bar{a}_3(-\vec{k})\bar{a}_2(\vec{k}) \right) \right\}$$

$$\tag{4.39}$$

$$\widetilde{\mathcal{H}}_{-,T,LS} = \frac{\hbar\omega_k}{2} \left\{ \left(\left[\vec{\epsilon}_1(\vec{k}) \cdot (\tilde{\kappa}_{e-} + I\tilde{\kappa}_{tr}) \cdot \vec{\epsilon}_3(\vec{k}) \right] + \left[\vec{\epsilon}_3(\vec{k}) \cdot \tilde{\kappa}_{o+} \cdot \vec{\epsilon}_2(\vec{k}) \right] \right) \times \right.$$

$$\left(\bar{a}_0(-\vec{k})a_1(-\vec{k}) + \bar{a}_1(-\vec{k})a_0(-\vec{k}) - \bar{a}_3(-\vec{k})a_1(-\vec{k}) - \bar{a}_1(-\vec{k})a_3(-\vec{k}) \right.$$

$$\left. + a_0(\vec{k})a_1(-\vec{k}) + \bar{a}_1(-\vec{k})\bar{a}_0(\vec{k}) + a_3(\vec{k})a_1(-\vec{k}) + \bar{a}_1(-\vec{k})\bar{a}_3(\vec{k}) \right)$$

$$+ \left(\left[\vec{\epsilon}_2(\vec{k}) \cdot (\tilde{\kappa}_{e-} + I\tilde{\kappa}_{tr}) \cdot \vec{\epsilon}_3(\vec{k}) \right] - \left[\vec{\epsilon}_3(\vec{k}) \cdot \tilde{\kappa}_{o+} \cdot \vec{\epsilon}_1(\vec{k}) \right] \right) \times$$

$$\left(\bar{a}_0(-\vec{k})a_2(-\vec{k}) + \bar{a}_2(-\vec{k})a_0(-\vec{k}) - \bar{a}_3(-\vec{k})a_2(-\vec{k}) - \bar{a}_2(-\vec{k})a_3(-\vec{k}) \right.$$

$$\left. \left. + a_0(\vec{k})a_2(-\vec{k}) + \bar{a}_2(-\vec{k})\bar{a}_0(\vec{k}) + a_3(\vec{k})a_2(-\vec{k}) + \bar{a}_2(-\vec{k})\bar{a}_3(\vec{k}) \right) \right\}.$$

$$\tag{4.40}$$

The Hamiltonian can be further simplified by expressing the scalar and longitudinal operators in terms of

$$a_d(\vec{k}) = \frac{i}{\sqrt{2}}\left(a_3(\vec{k}) - a_0(\vec{k})\right) \tag{4.41}$$

$$a_g(\vec{k}) = \frac{1}{\sqrt{2}}\left(a_3(\vec{k}) + a_0(\vec{k})\right), \tag{4.42}$$

so that

$$\begin{aligned}
\widetilde{\mathcal{H}}_{LS} =\ & i\hbar\omega_k\left(a_d(\vec{k})\overline{a}_g(\vec{k}) - a_g(\vec{k})\overline{a}_d(\vec{k}) + \overline{a}_g(-\vec{k})a_d(-\vec{k}) - \overline{a}_d(-\vec{k})a_g(-\vec{k})\right) \\
& - \hbar\omega_k\left[\vec{\epsilon}_3(\vec{k})\cdot(\tilde{\kappa}_{e-} + I\tilde{\kappa}_{tr})\cdot\vec{\epsilon}_3(\vec{k})\right]\left(a_g(\vec{k})\overline{a}_g(\vec{k}) + \overline{a}_d(-\vec{k})a_d(-\vec{k})\right) \\
& - i\hbar\omega_k\left[\vec{\epsilon}_3(\vec{k})\cdot(\tilde{\kappa}_{e-} + I\tilde{\kappa}_{tr})\cdot\vec{\epsilon}_3(\vec{k})\right]\left(a_g(\vec{k})a_d(-\vec{k}) - \overline{a}_d(-\vec{k})\overline{a}_g(\vec{k})\right)
\end{aligned} \tag{4.43}$$

$$\begin{aligned}
\widetilde{\mathcal{H}}_{+,T,LS} = \frac{-\hbar\omega_k}{\sqrt{2}}\Bigg\{ & \left(\left[\vec{\epsilon}_1(\vec{k})\cdot(\tilde{\kappa}_{e-} + I\tilde{\kappa}_{tr})\cdot\vec{\epsilon}_3(\vec{k})\right] - \left[\vec{\epsilon}_3(\vec{k})\cdot\tilde{\kappa}_{o+}\cdot\vec{\epsilon}_2(\vec{k})\right]\right)\times \\
& \left(a_1(\vec{k})\left[\overline{a}_g(\vec{k}) + ia_d(-\vec{k})\right] + \left[a_g(\vec{k}) - i\overline{a}_d(-\vec{k})\right]\overline{a}_1(\vec{k})\right) \\
& + \left(\left[\vec{\epsilon}_2(\vec{k})\cdot(\tilde{\kappa}_{e-} + I\tilde{\kappa}_{tr})\cdot\vec{\epsilon}_3(\vec{k})\right] + \left[\vec{\epsilon}_3(\vec{k})\cdot\tilde{\kappa}_{o+}\cdot\vec{\epsilon}_1(\vec{k})\right]\right)\times \\
& \left(a_2(\vec{k})\left[\overline{a}_g(\vec{k}) + ia_d(-\vec{k})\right] + \left[a_g(\vec{k}) - i\overline{a}_d(-\vec{k})\right]\overline{a}_2(\vec{k})\right)\Bigg\},
\end{aligned} \tag{4.44}$$

$$\begin{aligned}
\widetilde{\mathcal{H}}_{-,T,LS} = \frac{\hbar\omega_k}{\sqrt{2}}\Bigg\{ & \left(\left[\vec{\epsilon}_1(\vec{k})\cdot(\tilde{\kappa}_{e-} + I\tilde{\kappa}_{tr})\cdot\vec{\epsilon}_3(\vec{k})\right] + \left[\vec{\epsilon}_3(\vec{k})\cdot\tilde{\kappa}_{o+}\cdot\vec{\epsilon}_2(\vec{k})\right]\right)\times \\
& \left(\left[a_g(\vec{k}) - i\overline{a}_d(-\vec{k})\right]a_1(-\vec{k}) + \overline{a}_1(-\vec{k})\left[\overline{a}_g(\vec{k}) + ia_d(-\vec{k})\right]\right) \\
& + \left(\left[\vec{\epsilon}_2(\vec{k})\cdot(\tilde{\kappa}_{e-} + I\tilde{\kappa}_{tr})\cdot\vec{\epsilon}_3(\vec{k})\right] - \left[\vec{\epsilon}_3(\vec{k})\cdot\tilde{\kappa}_{o+}\cdot\vec{\epsilon}_1(\vec{k})\right]\right)\times \\
& \left(\left[a_g(\vec{k}) - i\overline{a}_d(-\vec{k})\right]a_2(-\vec{k}) + \overline{a}_2(-\vec{k})\left[\overline{a}_g(\vec{k}) + ia_d(-\vec{k})\right]\right)\Bigg\}.
\end{aligned} \tag{4.45}$$

To leading order in $\tilde{\kappa}$, the interactions between the transverse modes contained in $\widetilde{\mathcal{H}}_{\pm,T}$ can be eliminated by performing the unitary transformation

$$e^{\Xi_1 + \Xi_2}\,\widetilde{\mathcal{H}}_R\,e^{-\Xi_1 - \Xi_2}, \tag{4.46}$$

where

$$\Xi_1 = \sum_{\vec{k}} \frac{1}{4} \left(\left[\vec{\epsilon}_1(\vec{k}) \cdot (\tilde{\kappa}_{e-} + I\tilde{\kappa}_{tr}) \cdot \vec{\epsilon}_1(\vec{k}) \right] - \left[\vec{\epsilon}_2(\vec{k}) \cdot (\tilde{\kappa}_{e-} + I\tilde{\kappa}_{tr}) \cdot \vec{\epsilon}_2(\vec{k}) \right] \right) \times$$

$$\left(\overline{a}_1(\vec{k})\overline{a}_1(-\vec{k}) - a_1(-\vec{k})a_1(\vec{k}) - \overline{a}_2(\vec{k})\overline{a}_2(-\vec{k}) + a_2(-\vec{k})a_2(\vec{k}) \right)$$

$$\Xi_2 = \sum_{\vec{k}} \frac{1}{2} \left[\vec{\epsilon}_1(\vec{k}) \cdot (\tilde{\kappa}_{e-} + I\tilde{\kappa}_{tr}) \cdot \vec{\epsilon}_2(\vec{k}) \right] \times$$

$$\left(\overline{a}_1(\vec{k})\overline{a}_2(-\vec{k}) - a_1(\vec{k})a_2(-\vec{k}) + \overline{a}_2(\vec{k})\overline{a}_1(-\vec{k}) - a_2(\vec{k})a_1(-\vec{k}) \right).$$

$$(4.47)$$

Thus we may write the free field Hamiltonian in terms of (4.36), (4.43), (4.44), and (4.45) as

$$e^{\Xi_1 + \Xi_2} \widetilde{\mathcal{H}}_R \, e^{-\Xi_1 - \Xi_2} = \widetilde{\mathcal{H}}_T + \widetilde{\mathcal{H}}_{LS} + \widetilde{\mathcal{H}}_{+,T,LS} + \widetilde{\mathcal{H}}_{-,T,LS}. \qquad (4.48)$$

As will be demonstrated in part 4.3.5, the remaining $\widetilde{\mathcal{H}}_{LS}$ and $\widetilde{\mathcal{H}}_{\pm,T,LS}$ terms do not contribute to physical observables, and do not affect the evolution of the free fields at leading order. Thus the similarity transform (4.46) has effectively diagonalized the free-field Hamiltonian. We note that at second order in $\tilde{\kappa}$, the $\widetilde{\mathcal{H}}_{\pm,T,LS}$ terms can generate vacuum birefringence via an intermediate coupling to the scalar and longitudinal modes (*i.e. d-* and *g-*modes). This is qualitatively consistent with the solution to the Lagrangian equations of motion (4.6) taken to second order in $\tilde{\kappa}_{e-}$, $\tilde{\kappa}_{o+}$, and $\tilde{\kappa}_{tr}$, although a rigorous treatment would require the inclusion of numerous second order terms (all of which are suppressed by at least a factor of 10^{12} relative to the leading order effects) which were discarded in the course of this derivation. The $\widetilde{\mathcal{H}}_{LS}$ and $\widetilde{\mathcal{H}}_{\pm,T,LS}$ components of the Hamiltonian are also critically important in any fully quantum treatment of electro- and magneto-statics in the photon sector of the SME.

4.3 The Indefinite Metric

While the Hamiltonian (4.48) is self-adjoint in the sense that $\widetilde{\mathcal{H}}_R = \overline{\widetilde{\mathcal{H}}_R}$, this fact alone does not establish that eigenstates of $\widetilde{\mathcal{H}}_R$ will satisfy the Lorenz condition, and thus represent solutions to the modified Maxwell equations. In contrast to the

fully covariant theory, (4.48) includes a variety of terms coupling the physically per-
mitted transverse modes to the unphysical scalar and longitudinal modes. Here, we
demonstrate that these terms do not couple states that are consistent with Maxwells
equations to states that are not; and that (4.48) is the operator of a well defined ob-
servable which can act as the generator of translations in time. To do this, we follow
the usual process by which the potentials of the fully covariant theory are quantized,
and choose to define a basis for the quantized fields' Hilbert space in a metric other
than the one induced by (4.23).

We first review the properties of the inner product, or metric, that covariant
quantization imposes on the Hilbert space, and recapitulate the procedure by which
the metric is redefined to permit the construction of a basis for the Hilbert space
comprised of states with non-negative (if not strictly positive definite) norm. For the
fully covariant theory, this process is sufficient to completely isolate a subspace S of
states satisfying the Lorenz condition and that have positive norm from those that
do not. In the Lorentz-violating theory, however, the $\widetilde{\mathcal{H}}_{\pm,T,LS}$ terms do not leave the
subspace S invariant. Fortunately, as we will show in part 4.3.5, the Lorentz-violating
theory leaves the larger subspace $S_{LV} \supset S$ invariant. Although the metric on states in
S_{LV} is not strictly positive, we demonstrate that every $|\psi\rangle \in S_{LV}$ is a solution of the
modified Maxwell equations (4.4). In so doing, we demonstrate that the form of the
Lorenz condition used in the course of covariant quantization of the fully covariant
theory is stronger than is strictly required, and develop a minimal "weak" Lorenz
condition to define S_{LV}. Finally, we show that to leading order in $\tilde{\kappa}$, states in S_{LV}
outside of S can be ignored, and the metric can again be treated as if it were strictly
positive.

4.3.1   Origins of the Indefinite Metric

In the process of covariant quantization, we made two fateful decisions. First, we
chose to quantize the *potentials* A^μ and their conjugate momenta, rather than use the
physically observable electric and magnetic fields. This choice makes the interaction
of the quantized field with Dirac fermions particularly straightforward, but inserts

an additional unphysical degree of freedom into our system, associated with gauge invariance. Next, in order to obtain a fully covariant commutation relation between the coordinate potentials and their conjugate momenta, we had to use a variant of the Fermi Lagrangian to induce a nonvanishing momentum for the time-component of the potential, inserting another degree of freedom. This means that where we once had a system that admitted only transverse solutions of the free-field wave equation, we now have a representation of that system for which, in the absence of the appropriate constraints, scalar and longitudinal modes are permitted[3]. These unphysical degrees of freedom cause the Hilbert space of the quantized fields to include wavefunctions that are not solutions of (4.4). This problem can be addressed in more detail once we have constructed a suitable basis in part 4.3.3. Specifying that basis in terms of the normal mode operators defined in (4.25) and (4.26) is complicated by the covariant commutation relation between the potentials and their conjugate momenta:

$$[A^\mu(\vec{r}, t), \pi^\nu(\vec{r}', t')] = i\hbar g^{\mu\nu} \delta(t - t') \delta(\vec{r} - \vec{r}'). \tag{4.49}$$

As stated in (4.24), this gives rise to the equal time commutation relation between the normal modes in reciprocal space

$$\left[a_r(\vec{k}), \overline{a}_s(\vec{k}') \right] = \zeta_r \delta_{rs} \delta(\vec{k} - \vec{k}'), \tag{4.50}$$

with $\zeta_r = \{-1, 1, 1, 1\}$ for $r = \{0, 1, 2, 3\}$. Because $[a_0(\vec{k}), a_0^\dagger(\vec{k})] = -1$, respectively identifying $a_0^\dagger$ and a_0 as creation and annihilation operators leads to states with negative norm. If the vacuum is normalized such that $\langle 0|0 \rangle = 1$, then one such negative norm state is that with a single scalar-mode photon

$$\langle 1_0 | 1_0 \rangle = \langle 0|a_0 a_0^\dagger|0 \rangle = -\langle 0|0 \rangle + \langle 0|a_0^\dagger a_0|0 \rangle = -1. \tag{4.51}$$

This is a direct consequence of quantizing the potentials of the Fermi Lagrangian, which has led to a Hilbert space with an *indefinite* (rather than strictly positive) inner product, or metric.

---

[3]Note that this statement applies to the classical as well as the quantum theory. Differences in the derivation of the classical covariant field representation as compared to their quantum representation arise in how the Lorenz gauge condition is applied.

4.3.2   Properties of the Indefinite Metric

Paralleling the discussion in [90], we can define a new metric with respect to an existing Hilbert space (whose elements are denoted as $|\psi\rangle$) in terms of an operator M, hermitian on all $|\psi\rangle$, such that $M = M^\dagger = M^{-1}$. Using this *metric operator M*, we can then define a new metric on the Hilbert space in terms of $|\psi\rangle$ and the original metric by

$$\subset \psi | \phi \supset = \langle \psi | M | \phi \rangle, \tag{4.52}$$

where $| \supset$ and $\subset |$ are isomorphic to the physical states according to

$$|\psi \supset = |\psi\rangle, \text{ and } \subset \psi | = \langle \psi | M. \tag{4.53}$$

This implies that

$$\subset \psi | \phi \supset = \langle \psi | M | \phi \rangle = \left(\langle \phi | M^\dagger | \psi \rangle \right)^* = (\subset \phi | \psi \supset)^*. \tag{4.54}$$

As was the case in the original metric, the product $\subset \psi | \phi \supset$ is linear in $|\phi \supset$ and antilinear in $\subset \psi|$. Even though we may initially choose $\langle \psi | \psi \rangle$ to be positive definite, $\subset \psi | \psi \supset$ need not be, since

$$\subset \psi | \psi \supset = \langle \psi | M | \psi \rangle = \langle \psi | \left(\sum_j m_j | m_j \rangle \langle m_j | \right) | \phi \rangle = \sum_j m_j |\langle \psi | m_j \rangle|^2, \tag{4.55}$$

and the eigenvalues m_j of M can be ± 1, leading to the possibility of states with vanishing or negative norm. If the original metric is positive definite, then metrics derived from that metric by a metric operator M with one or more negative eigenvalues are termed *indefinite*. The freedom to choose M permits us to define a new adjoint $\bar{A}$ such that

$$\subset \psi | A | \phi \supset = \left(\subset \phi | \bar{A} | \psi \supset \right)^* \tag{4.56}$$

is satisfied. The new adjoint can be related to the old adjoint via

$$\subset \psi | A | \phi \supset = \langle \psi | M A | \phi \rangle = \langle \psi | \bar{A}^\dagger M^\dagger | \phi \rangle = \left(\langle \phi | M \bar{A} | \psi \rangle \right)^* = \left(\subset \phi | \bar{A} | \psi \supset \right)^*, \tag{4.57}$$

which implies $A^\dagger M^\dagger = M \bar{A}$. Since $M = M^\dagger$ and $M^2 = I$, we have that the new adjoint is given by

$$\bar{A} = M A^\dagger M. \tag{4.58}$$

The mean value of an operator A in the new metric is given by

$$\subset A \supset_\psi = \frac{\subset \psi|A|\psi \supset}{\subset \psi|\psi \supset}.$$

(4.59)

If the operator is hermitian in the new metric $(A = \bar{A})$, the mean value $\subset A \supset_\psi$ can easily be shown to coincide with the mean $\langle A \rangle_\psi$ in the original metric, provided that $A = A^\dagger$. Finally, for an orthonormal basis $|\varphi_j\rangle$, the closure relation becomes

$$1 = \sum_j |\varphi_j\rangle\langle\varphi_j| = \sum_j |\varphi_j \supset \subset \varphi_j|M.$$

(4.60)

4.3.3 Construction of Hilbert Space and the Metric Operator

As noted above in 4.3, quantizing the potentials of the Fermi Lagrangian yields a Hilbert space of states with an indefinite metric. Following [90], we will denote the adjoint of an operator A as $\bar{A}$ in this metric, reserving the $A^\dagger$ adjoint for the transformed "physical metric" used in the fully covariant theory to isolate the unphysical modes. Since we would like to perform calculations in a Hilbert space of coupled harmonic oscillators with positive-definite metric, we need to change the sign of (4.50) for $r = 0$. Assuming that such a metric exists, it must be related to the original indefinite metric operators by a metric operator M such that

$$M a_{0,1,2,3}(\vec{k})M = a_{0,1,2,3}(\vec{k}) \qquad M \bar{a}_{1,2,3}(\vec{k})M = a^\dagger_{1,2,3}(\vec{k}),$$

(4.61)

and

$$M \bar{a}_0(\vec{k})M = -a^\dagger_0(\vec{k}).$$

(4.62)

With this transformation of the field operators, the covariant commutation relations (4.50) become

$$[a_r(\vec{k}), a^\dagger_s(\vec{k})] = \delta_{rs}\delta(\vec{k} - \vec{k}').$$

(4.63)

It is then straightforward to use these operators to define a well-behaved basis for the scalar polarization modes for each $\vec{k}$ in terms of the transformed operators as

$$|n_0\rangle = \frac{(a^\dagger_0)^{n_0}}{\sqrt{n_0!}}|0\rangle,$$

(4.64)

where the dependence on $\vec{k}$ is suppressed. Because the scalar mode commutator (4.63) matches that of the conventional harmonic oscillator, the usual ladder operator relations apply in this basis, and *all* states have positive norm ($\langle n_0 | n_0 \rangle = 1$). On this basis, we can now explicitly write M as [90]

$$M|n_0\rangle = (-1)^{n_0}|n_0\rangle. \tag{4.65}$$

This form of M can easily be shown to satisfy (4.62) on the chosen basis, and is self-evidently hermitian in the new or "physical" metric. In particular, since $|\psi \supset = |\psi\rangle$ and $\subset \psi| = \langle \psi|M$, we have

$$\subset n_0 | n'_0 \supset = \langle n_0 | M | n'_0 \rangle = (-1)^{n'_0}\delta_{n_0,n'_0}, \tag{4.66}$$

demonstrating that the combination of the chosen basis (4.64) with M is consistent with the properties of the norm in (4.51), derived by canonical quantization of the potentials.

A basis for the Hilbert space can be defined in the new metric as

$$|n_1, n_2, n_3, n_0\rangle = \frac{(a_1^\dagger)^{n_1}(a_2^\dagger)^{n_2}(a_3^\dagger)^{n_3}(a_0^\dagger)^{n_0}}{\sqrt{n_1! n_2! n_3! n_0!}}|0\rangle, \tag{4.67}$$

although the subspace of states satisfying the modified Maxwell equations given in (4.4) is necessarily smaller. To apply the Lorenz gauge condition (4.7) to isolate the physical subspace, we must keep in mind that it is defined in the indefinite metric

$$\subset \psi|\partial_\alpha A^\alpha|\psi \supset = 0. \tag{4.68}$$

Because it is not possible to form a basis in which $\partial_\alpha A^\alpha|\psi \supset = 0$, the Lorenz condition is typically expressed in terms of the weaker condition due to Gupta and Bleuler [89]

$$\left(a_3(\vec{k}) - a_0(\vec{k})\right)|\psi \supset = 0 \qquad \text{and} \qquad 0 = \subset \psi| \left(\bar{a}_3(\vec{k}) - \bar{a}_0(\vec{k})\right). \tag{4.69}$$

Note that in general, expressions given in terms of operators acting on states $|\psi \supset$ in one metric do not necessarily have the same form when expressed in terms of operators acting on the corresponding states $|\psi\rangle$ in another metric. In the present

case, however, $|\psi\rangle = |\psi \supset$, and M does not alter the annihilation operators, so $(a_3 - a_0)|\psi \supset = (a_3 - a_0)|\psi\rangle$. It is therefore convenient to work in the modified basis

$$|n_1, n_2, n_d, n_g\rangle = \frac{(a_1^\dagger)^{n_1}(a_2^\dagger)^{n_2}(a_d^\dagger)^{n_d}(a_g^\dagger)^{n_g}}{\sqrt{n_1!n_2!n_d!n_g!}}|0\rangle, \tag{4.70}$$

where the d-photon and g-photon operators are given by

$$a_d = \frac{i}{\sqrt{2}}(a_3 - a_0), \qquad \text{and} \qquad a_g = \frac{1}{\sqrt{2}}(a_3 + a_0), \tag{4.71}$$

which obey the usual bosonic commutation relations with respect to the physical (where the adjoint of A is $A^\dagger$) metric. This permits us to express the Lorenz condition (4.69) in the compact form $a_d|\psi\rangle = 0$.

Note that although the Maxwell equations are satisfied by $|\psi\rangle$ for which $a_d|\psi\rangle = a_d|\psi \supset = 0$, the $\langle\psi|$ which satisfy the Maxwell equations are *not* necessarily those for which $\langle\psi|a_d^\dagger = 0$. The Lorenz condition of Gupta and Bleuler, properly expressed in terms of the indefinite metric, is

$$a_d|\psi \supset = 0, \qquad \text{and} \qquad \subset \psi|\bar{a}_d = 0, \tag{4.72}$$

where

$$\bar{a}_d = -\frac{i}{\sqrt{2}}(\bar{a}_3 - \bar{a}_0) = -ia_g^\dagger, \qquad \text{and} \qquad \bar{a}_g = \frac{1}{\sqrt{2}}(\bar{a}_3 + \bar{a}_0) = ia_d^\dagger. \tag{4.73}$$

Thus we see that the Lorenz condition on $\langle\psi|$ is $\subset \psi|\bar{a}_d = \langle\psi|M(-ia_g^\dagger) = 0$. In what follows, we will find it more convenient to use the indefinite metric to pick out the physical $\langle\psi|$. The physical subspace that satisfies (4.69) is now completely defined by [90]

$$|n_1, n_2, 0_d, n_g\rangle = \frac{(a_1^\dagger)^{n_1}(a_2^\dagger)^{n_2}(a_g^\dagger)^{n_g}}{\sqrt{n_1!n_2!n_g!}}|0\rangle. \tag{4.74}$$

Application of the Lorenz condition in both the indefinite metric on $|\psi \supset$ as well the physical metric on $|\psi\rangle$ explicitly restricts one of the unphysical degrees of freedom. At this point, we may be tempted to treat the so-called physical metric as if it were the "real" metric, and that expectation values calculated in the underlying indefinite metric should be judged according to whether they are sensible in the metric on $|\psi\rangle$.

Such an approach would be misguided. If we consider only the $|\psi\rangle$ Hilbert space, then since the norm

$$\langle n_1, n_2, 0_d, n_g | n'_1, n'_2, 0_d, n'_g \rangle = \delta_{n_1,n'_1} \delta_{n_2,n'_2} \delta_{n_g,n'_g} \tag{4.75}$$

is positive for any n_g, it might then appear that the unphysical g-photon mode could yield quantum-mechanically valid observables that are nevertheless entirely decoupled from the transverse modes, and indeed decoupled from the state of any other field. This interpretation would make it a practical necessity to trace over the g-modes when calculating expectation values. This is no problem for the covariant theory, as the energy associated with each g-photon is zero, and there is no way for g-photons to couple to the transverse modes. A trace over the unphysical modes would leave a pure state of the physically observed fields unchanged. For the Lorentz-violating theory, the effects of a trace over such modes is potentially much more troubling, due to the existence of terms proportional to $(a_g^\dagger)^2$ in the Hamiltonian. This question of interpretation is immediately resolved if the observables are defined strictly according to their hermiticity in the underlying indefinite metric. There, we find

$$\subset n_1, n_2, 0_d, n_g | n'_1, n'_2, 0_d, n'_g \supset = \langle n_1, n_2, 0_d, n_g | M | n'_1, n'_2, 0_d, n'_g \rangle$$
$$= \delta_{n_1,n'_1} \delta_{n_2,n'_2} \delta_{n_g,0} \delta_{n'_g,0}, \tag{4.76}$$

since the action of M on a state with n d-photons and m g-photons is, using the definitions (4.71) and (4.62),

$$M|n_d, m_g\rangle = i^{m-n}|m_d, n_g\rangle. \tag{4.77}$$

From (4.76), we see that the norm of any state satisfying (4.72) with $n_g > 0$ must vanish, implying that such states cannot contribute to the eigenvalue of any observable operator. This also implies that if a state $|\psi\rangle$ satisfying the Lorenz condition of Gupta and Bleuler can be written $|\psi\rangle = |\psi\rangle_T \otimes |\phi\rangle_g$; where $|\psi\rangle_T$ represents the state of the transverse modes, and $|\phi\rangle_g$ is the state of the g-photon mode; then the mean value of any physical observable A must be

$$\frac{\subset \psi|A|\psi \supset}{\subset \psi|\psi \supset} = \frac{_T\langle\psi|A|\psi\rangle_T}{_T\langle\psi|\psi\rangle_T}, \tag{4.78}$$

since A can only act on the transverse degrees of freedom. The underlying indefinite metric formally eliminates the need to trace over g-modes, simplifying the interpretation of both the covariant theory as well as the Lorentz-violating theory [4].

4.3.4 The Weak Lorenz Condition

The preceding discussion suggests that the Lorenz condition (4.69) of Gupta and Bleuler may itself be stronger than is strictly necessary to satisfy (4.68). We are motivated by the general form of (4.76), which is

$$\subset n_1, n_2, n_d, n_g | n_1', n_2', n_d', n_g' \supset = i^{n_g' - n_d'} \delta_{n_1, n_1'} \delta_{n_2, n_2'} \delta_{n_g, n_d'} \delta_{n_g', n_d}. \tag{4.79}$$

This means that we can write down states (*e.g.* , $|n_1, n_2, 4_d, 0_g \supset$) that do not satisfy (4.69), but which simultaneously have zero norm. If $\subset \varphi | \varphi \supset = 0$, then the contribution of $|\varphi \supset$ to the expectation of any physical observable must also vanish, since an operator corresponding to a physical observable cannot depend or act upon the unphysical d or g modes. That is, given a state $|\psi \supset$ which is orthogonal to $|\varphi \supset$, has nonzero norm, and which satisfies (4.69), then the states $|\phi_1 \supset = |\psi \supset$ and $|\phi_2 \supset = c_1 |\psi \supset + c_2 |\varphi \supset$ are experimentally indistinguishable from one another, since for any operator A corresponding to a physical observable,

$$\langle A \rangle = \frac{\subset \phi_1 | A | \phi_1 \supset}{\subset \phi_1 | \phi_1 \supset} = \frac{\subset \psi | A | \psi \supset}{\subset \psi | \psi \supset}$$
$$= \frac{\subset \psi | A | \psi \supset}{\subset \psi | \psi \supset} + \frac{\subset \varphi | A | \varphi \supset}{\subset \psi | \psi \supset} = \frac{\subset \phi_2 | A | \phi_2 \supset}{\subset \phi_2 | \phi_2 \supset}. \tag{4.80}$$

Note that the validity of this expression is dependent upon the orthogonality of $|\psi \supset$ with $|\varphi \supset$ with respect to the *indefinite metric*, and not the metric suggested by (4.75). In particular, if we take $|\varphi \supset = |0_1, 0_2, n_d, 0_g \supset$, then $|\psi \supset$ must not have a $|0_1, 0_2, 0_d, n_g \supset$ component, since this would lead to a nonvanishing cross term proportional to the real part of $c_1 c_2^*(i)^n$ in (4.80). A diagram of the relative orthogonality and norm of the d- and g-mode subspace for fixed $\vec{k}$ is given in Figure 4.1.

---

[4]We could have arrived at an expression similar to (4.76), and thus derived (4.78) purely in terms of the $|\psi\rangle$ metric, using the properly transformed adjoint of the Lorenz condition $\langle \psi | M(-ia_g^\dagger) = 0$. This would show that $\langle n_g \neq 0|$ does not belong to the subspace satisfying (4.69) on the larger Hilbert space. The problem is somewhat easier to address both mathematically and conceptually in the indefinite metric.

If the observed field configuration in state $|\phi_1 \supset$ is indistinguishable from that in state $|\phi_2 \supset$, then since the configuration due to $|\phi_1 \supset$ is consistent with the (modified) Maxwell equations (4.4), the field configuration represented by $|\phi_2 \supset$ must *also* be a solution to (4.4). Thus the conventional formulation of the Lorenz gauge condition of Gupta and Bleuler is overly restrictive; it excludes states that are consistent with the Maxwell equations. We are therefore led to restate the Lorenz condition in the less restrictive form:

$$\text{For all } |\psi \supset \text{ such that } \subset \psi|\psi \supset \neq 0: \quad \left(a_d|\psi \supset = 0 \text{ and } \subset \psi|\bar{a}_d = 0 \right). \quad (4.81)$$

Just as happened with respect to the g-photon modes in part 4.3.3, the difference between the weak Lorenz condition (4.81) and the stronger condition of Gupta and Bleuler is relatively unimportant to the development of the fully covariant theory. States $|\varphi \supset$ with one or more d-photons such that $\subset \varphi|\varphi \supset = 0$ are, like the states with one or more g-photons, entirely decoupled from the transverse modes as $(k_F) \rightarrow 0$. The distinction is however critically important to the development of the Lorentz-violating theory, as the Hamiltonian (4.48), in the $\widetilde{\mathcal{H}}_{LS}$ and $\widetilde{\mathcal{H}}_{\pm,T,LS}$ terms, includes couplings between states that satisfy (4.69) and states that do not. In what follows, we demonstrate that the Lorentz-violating Hamiltonian $\widetilde{\mathcal{H}}_R$ does in fact leave the space of states that satisfy the weak Lorenz condition invariant, and therefore represents a generator of unitary time translations that is fully consistent with the modified Maxwell equations.

4.3.5   Lorentz-Violating Hamiltonian in the Indefinite Metric

At the conclusion of part 4.2, we stated that the effects of $\widetilde{\mathcal{H}}_{LS}$, $\widetilde{\mathcal{H}}_{+,T,LS}$, and $\widetilde{\mathcal{H}}_{-,T,LS}$ could be ignored at leading order in $\tilde{\kappa}$. In the limit that $(k_F) \rightarrow 0$, these terms pose no special problem: the $\widetilde{\mathcal{H}}_{\pm,T,LS}$ terms vanish, and $\widetilde{\mathcal{H}}_{LS}$ reduces to $\widetilde{\mathcal{H}}_{LS}^0$, where we have explicitly made the division

$$\widetilde{\mathcal{H}}_{LS} = \widetilde{\mathcal{H}}_{LS}^0 + \widetilde{\mathcal{H}}_{LS}^{LV}, \quad (4.82)$$

with

$$\widetilde{\mathcal{H}}_{LS}^0 = i\hbar\omega_k \left(a_d(\vec{k})\bar{a}_g(\vec{k}) - a_g(\vec{k})\bar{a}_d(\vec{k}) + \bar{a}_g(-\vec{k})a_d(-\vec{k}) - \bar{a}_d(-\vec{k})a_g(-\vec{k}) \right) \quad (4.83)$$
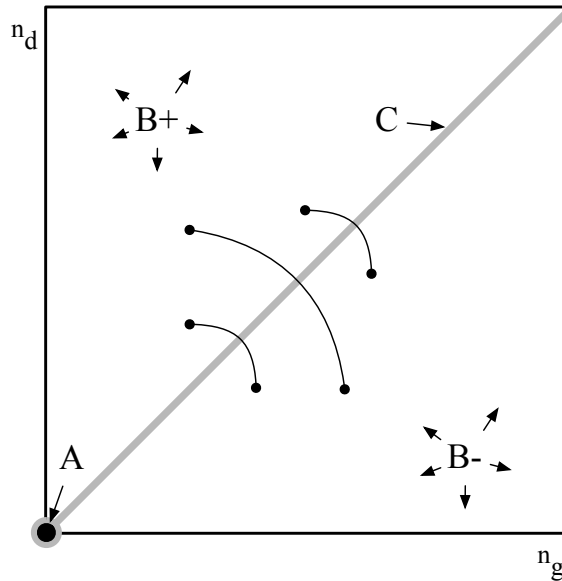
Figure 4.1: A partition of Hilbert space into four sets according to their indefinite metric inner product. All states within each set have a vanishing inner product with any other state in the same set. Set A contains only the $n_d = n_g = 0$ state with nonzero norm permitted by the Maxwell equations. Set C contains all states that are not consistent with the Maxwell equations and have nonzero norm, while states in sets B+ and B- have varying numbers of d and g-photons but have vanishing norm. Each state in set B+ has a corresponding state in set B- with which it has a finite inner product. Three such pairings are indicated by arcs. States in sets A and C are orthogonal to states in all other sets. A wavefunction $|\psi \supset$ is consistent with the weak Lorenz condition (4.81) if it is made up of a superposition of mutually orthogonal states drawn from sets A, B+, and B-.

which becomes $\hbar\omega_k \left(a_d(\vec{k})a_d^\dagger(\vec{k}) + a_g(\vec{k})a_g^\dagger(\vec{k}) + a_d^\dagger(-\vec{k})a_d(-\vec{k}) + a_g^\dagger(-\vec{k})a_g(-\vec{k}) \right)$ when expressed in the physical metric, and

$$
\begin{aligned}
\widetilde{\mathcal{H}}_{LS}^{LV} = \ & -\hbar\omega_k \left[\vec{\epsilon}_3(\vec{k}) \cdot (\tilde{\kappa}_{e-} + I\tilde{\kappa}_{tr}) \cdot \vec{\epsilon}_3(\vec{k}) \right] \left(a_g(\vec{k})\overline{a}_g(\vec{k}) + \overline{a}_d(-\vec{k})a_d(-\vec{k}) \right) \\
& - i\hbar\omega_k \left[\vec{\epsilon}_3(\vec{k}) \cdot (\tilde{\kappa}_{e-} + I\tilde{\kappa}_{tr}) \cdot \vec{\epsilon}_3(\vec{k}) \right] \left(a_g(\vec{k})a_d(-\vec{k}) - \overline{a}_d(-\vec{k})\overline{a}_g(\vec{k}) \right).
\end{aligned}
\tag{4.84}
$$

Using the commutation relation for $[a_r(\vec{k}), \overline{a}_s(\vec{k'})]$ and the definition of $a_d(\vec{k})$ and $a_g(\vec{k})$, we may derive the commutators for $a_g(\vec{k})$, $a_d(\vec{k})$ and their adjoints:

$$[a_g(\vec{k}), \overline{a}_g(\vec{k'})] = 0 \tag{4.85a}$$

$$[a_d(\vec{k}), \overline{a}_d(\vec{k'})] = 0 \tag{4.85b}$$

$$[a_d(\vec{k}), \overline{a}_g(\vec{k'})] = i\delta(\vec{k} - \vec{k'}) \tag{4.85c}$$

$$[a_g(\vec{k}), \overline{a}_d(\vec{k'})] = i\delta(\vec{k} - \vec{k'}). \tag{4.85d}$$

Using these commutation relations, it is straightforward to demonstrate that $\widetilde{\mathcal{H}}_{LS}^{LV}$, $\widetilde{\mathcal{H}}_{+,T,LS}$, and $\widetilde{\mathcal{H}}_{-,T,LS}$ all commute with one another, as do the individual operators in $\widetilde{\mathcal{H}}_{LS}^{LV}$. To get a sense for the action of $\widetilde{\mathcal{H}}_{LS}^{LV}$ on an arbitrary wavefunction, we must write it in terms of the "physical" metric, where we have defined our basis. Using (4.73), we obtain

$$
\begin{aligned}
\widetilde{\mathcal{H}}_{LS}^{LV} = \ & -i\hbar\omega_k \left[\vec{\epsilon}_3(\vec{k}) \cdot (\tilde{\kappa}_{e-} + I\tilde{\kappa}_{tr}) \cdot \vec{\epsilon}_3(\vec{k}) \right] \left(a_g(\vec{k})a_d^\dagger(\vec{k}) - a_g^\dagger(-\vec{k})a_d(-\vec{k}) \right) \\
& - i\hbar\omega_k \left[\vec{\epsilon}_3(\vec{k}) \cdot (\tilde{\kappa}_{e-} + I\tilde{\kappa}_{tr}) \cdot \vec{\epsilon}_3(\vec{k}) \right] \left(a_g(\vec{k})a_d(-\vec{k}) - a_g^\dagger(-\vec{k})a_d^\dagger(\vec{k}) \right).
\end{aligned}
\tag{4.86}
$$

Note that while $\widetilde{\mathcal{H}}_{LS}^{LV}$ is manifestly self-adjoint with respect to the indefinite metric, it is not with respect to the physical metric. Fortunately, the properties of the inner product are such that although $\widetilde{\mathcal{H}}_{LS}^{LV}$ does represent a non-hermitian Hamiltonian coupling to states with different numbers of unphysical d- and g-photons, the evolution of the wavefunction with respect to physical observables (including $\widetilde{\mathcal{H}}$) remains unitary. As we now demonstrate, if a state $|\varphi \supset$ is coupled by $\widetilde{\mathcal{H}}_{LS}^{LV}$ to a state $|\psi \supset$ with nonzero norm that also satisfies the weak Lorenz condition (4.81), then $|\varphi \supset$ must also satisfy (4.81), and thus $\subset \varphi|\varphi \supset = 0$. For fixed $\vec{k}$, $\widetilde{\mathcal{H}}_{LS}^{LV}$ can either create a d-photon in mode $\vec{k}$ while removing a g-photon from that mode, create a g-photon in mode $-\vec{k}$ while removing a d-photon from that mode, annihilate a g-photon from mode $\vec{k}$ along

with a d-photon in mode $-\vec{k}$, or create a g-photon in mode $-\vec{k}$ along with a d-photon in mode $\vec{k}$. The action of $\left(\widetilde{\mathcal{H}}_{LS}^{LV}\right)^N$ on an arbitrary state $|\psi\rangle = |n_d, n_g\rangle_{\vec{k}}|n'_d, n'_g\rangle_{-\vec{k}}$ can yield superpositions of the states $|\varphi\rangle = |m_d, m_g\rangle_{\vec{k}}|m'_d, m'_g\rangle_{-\vec{k}}$, where

$$m_d = n_d + w + z$$
$$m_g = n_g - w - y$$
$$m'_d = n'_d - x - y \qquad (4.87)$$
$$m'_g = n'_g + x + z$$
$$N = w + x + y + z.$$

For $\subset \varphi|\varphi \supset \neq 0$, we must have $m_d = m_g$ and $m'_d = m'_g$, or

$$m_d - m_g = n_d - n_g + w - x + N = 0$$
$$m'_d - m'_g = n'_d - n'_g + w - x - N = 0. \qquad (4.88)$$

If $\subset \psi|\psi \supset \neq 0$, then $n_d = n_g$ and $n'_d = n'_g$. We then see that (4.88) can only be satisfied for the trivial case $N = 0$, and thus no power of $\widetilde{\mathcal{H}}_{LS}^{LV}$ can couple a state $|\psi \supset$ that satisfies the weak Lorenz condition (4.81) to one that does not. Furthermore, it cannot couple two different states with nonzero norm to one another. This means that the presence of $\widetilde{\mathcal{H}}_{LS}^{LV}$ does not contribute to the expectation value of $\widetilde{\mathcal{H}}$, and indeed cannot affect the expectation value of the operator for any physical observable constructed from the transverse mode operators.

We now apply a similar analysis to the $\widetilde{\mathcal{H}}_{\pm,T,LS} = \widetilde{\mathcal{H}}_{+,T,LS} + \widetilde{\mathcal{H}}_{-,T,LS}$ terms. In the physical metric, these terms take the form

$$\widetilde{\mathcal{H}}_{\pm,T,LS} = \left(\delta_1 a_1(\vec{k}) + \delta_2 a_2(\vec{k}) + \delta_3 a_1^\dagger(-\vec{k}) + \delta_4 a_2^\dagger(-\vec{k})\right)\left[ia_d^\dagger(\vec{k}) + ia_d(-\vec{k})\right]$$
$$+ \left[a_g(\vec{k}) - a_g^\dagger(-\vec{k})\right]\left(\delta_1 a_1^\dagger(\vec{k}) + \delta_2 a_2^\dagger(\vec{k}) + \delta_3 a_1(-\vec{k}) + \delta_4 a_2(-\vec{k})\right), \qquad (4.89)$$

where δ_1, δ_2, δ_3 and δ_4 are terms of order $\tilde{\kappa}$. The action of $\left(\widetilde{\mathcal{H}}_{\pm,T,LS}\right)^N$ on an arbitrary state $|\psi\rangle = |n_d, n_g\rangle_{\vec{k}}|n'_d, n'_g\rangle_{-\vec{k}}$ can yield superpositions of states $|\varphi\rangle =$

$|m_d, m_g\rangle_{\vec{k}}|m'_d, m'_g\rangle_{-\vec{k}}$, where

$$
\begin{aligned}
m_d &= n_d + w \\
m_g &= n_g - y \\
m'_d &= n'_d - x \\
m'_g &= n'_g + z \\
N &= w + x + y + z.
\end{aligned}
\tag{4.90}
$$

Thus if $\subset \psi|\psi \supset \neq 0$, then if $\subset \varphi|\varphi \supset \neq 0$, then both

$$
\begin{aligned}
m_d - m_g &= n_d - n_g + w - y = 0 \\
m'_d - m'_g &= n'_d - n'_g + N - 2x - w - y = 0.
\end{aligned}
\tag{4.91}
$$

If $w = y$, then this is satisfied for $N = 2x$, provided that $n'_d \geq x$ and $n_g \geq y$. If $|\psi \supset$ has nonzero norm and satisfies the weak Lorenz condition (4.81), then $n_g = n'_d = 0$, which in turn requires the $w = x = y = 0$, and that $N = 0$ if we are to have $\subset \varphi|\varphi \supset \neq 0$.

Finally, it is interesting to consider the effect of taking the actions of both $\widetilde{\mathcal{H}}^{LV}_{LS}$ and $\widetilde{\mathcal{H}}_{\pm,T,LS}$ together. We then find that the state $|\psi\rangle = |n_d, n_g\rangle_{\vec{k}}|n'_d, n'_g\rangle_{-\vec{k}}$ may be coupled to $|\varphi\rangle = |m_d, m_g\rangle_{\vec{k}}|m'_d, m'_g\rangle_{-\vec{k}}$ provided that

$$
\begin{aligned}
m_d &= n_d + w_1 + z_1 + w_2 \\
m_g &= n_g - w_1 - y_1 - y_2 \\
m'_d &= n'_d - x_1 - y_1 - x_2 \\
m'_g &= n'_g + x_1 + z_1 + z_2 \\
N_1 &= w_1 + x_1 + y_1 + z_1 \\
N_2 &= w_2 + x_2 + y_2 + z_2.
\end{aligned}
\tag{4.92}
$$

If $|\varphi\rangle$ has a nonzero norm, then we must have

$$
\begin{aligned}
m_d - m_g &= n_d - n_g + w_1 - x_1 + N_1 + w_2 - y_2 = 0 \\
m'_d - m'_g &= n'_d - n'_g + w_1 - x_1 - N_1 + N_2 - 2x_2 - w_2 - y_2 = 0.
\end{aligned}
\tag{4.93}
$$

If $|\psi \supset$ satisfies (4.81), then $w_1 = y_1 = y_2 = y_1 = x_1 = x_2 = 0$, and the above reduces to

$$m_d - m_g = n_d - n_g + N_1 + w_2 = 0$$
$$m_d' - m_g' = n_d' - n_g' - N_1 + N_2 - w_2 = 0, \tag{4.94}$$

which cannot be satisfied for any $N_1 > 0$ or $N_2 > 0$. Taking the subspace S_{LV} as that generated by $\widetilde{\mathcal{H}}_R$ on the subspace S of states with no d- or g-mode excitations, we may now say that every $|\psi \supset \in S_{LV}$ satisfies the weak Lorenz condition (4.81). This means that $\widetilde{\mathcal{H}}_R$ leaves the space of solutions of the modified Maxwell equations (4.4) invariant. Furthermore, we have shown that the apparently non-hermitian form of $\widetilde{\mathcal{H}}_{LS}^{LV}$ and $\widetilde{\mathcal{H}}_{\pm,T,LS}$ in terms of the physical metric operators does not lead to non-unitary evolution in time, since all states coupled by such terms have vanishing norm.

4.4 Effects on Transverse Mode Couplings

Although this work focuses on the free-field evolution, it is worthwhile to consider the form of the transverse potentials when expressed in terms of the free-field eigenmodes. From (4.25), we find that the transverse components of the potential

$$\mathcal{A}_{\perp,1}(\vec{k}) = \sqrt{\frac{\hbar c^2}{2\omega_k}} \left(a_1(\vec{k}) + \bar{a}_1(-\vec{k}) \right) \tag{4.95}$$

$$\mathcal{A}_{\perp,2}(\vec{k}) = \sqrt{\frac{\hbar c^2}{2\omega_k}} \left(a_2(\vec{k}) + \bar{a}_2(-\vec{k}) \right) \tag{4.96}$$

become

$$e^{\Xi_1 + \Xi_2} \, \mathcal{A}_{\perp,1}(\vec{k}) \, e^{-\Xi_1 - \Xi_2} = (1 - \delta_1) \, \mathcal{A}_{\perp,1}(\vec{k}) - \delta_2 \mathcal{A}_{\perp,2}(\vec{k}) \tag{4.97}$$

$$e^{\Xi_1 + \Xi_2} \, \mathcal{A}_{\perp,2}(\vec{k}) \, e^{-\Xi_1 - \Xi_2} = (1 + \delta_1) \, \mathcal{A}_{\perp,2}(\vec{k}) - \delta_2 \mathcal{A}_{\perp,1}(\vec{k}) \tag{4.98}$$

where

$$\delta_1 = \frac{1}{4} \left(\left[\vec{\epsilon}_1(\vec{k}) \cdot (\tilde{\kappa}_{e-} + I\tilde{\kappa}_{tr}) \cdot \vec{\epsilon}_1(\vec{k}) \right] - \left[\vec{\epsilon}_2(\vec{k}) \cdot (\tilde{\kappa}_{e-} + I\tilde{\kappa}_{tr}) \cdot \vec{\epsilon}_2(\vec{k}) \right] \right) \tag{4.99}$$

$$\delta_2 = \frac{1}{2} \left[\vec{\epsilon}_1(\vec{k}) \cdot (\tilde{\kappa}_{e-} + I\tilde{\kappa}_{tr}) \cdot \vec{\epsilon}_2(\vec{k}) \right]. \tag{4.100}$$

In particular, for a wave propagating in the $+\hat{z}$ direction, with the two orthogonal polarizations respectively lying along the $\hat{x}$ and $\hat{y}$ directions, its transverse potentials are

$$e^{\Xi_1 + \Xi_2}\, \mathcal{A}_{\perp,1}(\vec{k})\, e^{-\Xi_1 - \Xi_2} = \left(1 - \frac{\tilde{\kappa}_{e-}^{xx} - \tilde{\kappa}_{e-}^{yy}}{4}\right) \mathcal{A}_{\perp,1}(\vec{k}) - \frac{\tilde{\kappa}_{e-}^{12}}{2}\mathcal{A}_{\perp,2}(\vec{k}) \quad (4.101)$$

$$e^{\Xi_1 + \Xi_2}\, \mathcal{A}_{\perp,2}(\vec{k})\, e^{-\Xi_1 - \Xi_2} = \left(1 + \frac{\tilde{\kappa}_{e-}^{xx} - \tilde{\kappa}_{e-}^{yy}}{4}\right) \mathcal{A}_{\perp,2}(\vec{k}) - \frac{\tilde{\kappa}_{e-}^{12}}{2}\mathcal{A}_{\perp,1}(\vec{k}). \quad (4.102)$$

A more complete treatment of Lorentz-violating QED would yield additional mixing between the transverse modes and the scalar and longitudinal components from the $\widetilde{\mathcal{H}}_{\pm,T,LS}$ and $\widetilde{\mathcal{H}}_{LS}$ terms. Nevertheless, equations (4.101) and (4.102) have important consequences for the interaction $\vec{p} \cdot \vec{A}$. In particular, to leading order in $\tilde{\kappa}$, they imply that the interaction of an electromagnetic wave with charges depends upon the orientation of the transverse polarization. Thus although the SME parameters under consideration do not cause the vacuum to become birefringent, they can in general cause otherwise isotropic media to be become birefringent. This suggests that a Michelson-Morley test could be performed with two different polarizations of light propagating within a single dielectric cavity, rather than two separate cavities. Indeed, an experimental search for similar effects resulting from the electron $c_{\mu\nu}$ coefficients has been proposed [61], although a full analysis of the magnitude of such birefringence has not yet been completed. An extension of the derivation presented here incorporating the interaction of the potentials with charged particles would likely aid in such analyses, and will be the subject of future work.

Part II

Coherent Phenomena in Anti-Relaxation Coated Cells and New Ways to Stabilize Atomic Frequency Standards

Chapter 5

Classical Transport of Coherence in Anti-Relaxation Coated Cells

Electromagnetically induced transparency (EIT) is a key component of a wide range of technologies. In the realm of atomic frequency standards, where it is known as coherent population trapping (CPT), EIT is used to generate the highly stable resonance required of an atomic frequency standard [132–136]. When established between a set of states that are sensitive to the local magnetic field, the EIT resonance forms the basis of a high-precision magnetometer [137–140]. In recent years, EIT has even formed the basis for proposed experimental tests of Lorentz invariance [141]. EIT can also be used to manipulate the coherent propagation of light [142–144]. By dynamically varying the width of the resonance, EIT can be used to coherently control the group velocity and even stop the propagation of light within its bandwidth [144, 145]. The slow and stored light phenomena thus demonstrated has a number of promising applications to both classical and quantum information processing [146–152].

Although optimizing a particular EIT medium for slow and stored light applications is generally a complex task [153], the lifetime of the EIT medium's metastable coherence is known to be a significant limiting factor. Following the deleterious effects of local magnetic field gradients, which can typically be suppressed by the use of straightforward magnetic shielding techniques, the largest single source of loss in EIT

media based on the metastable states of warm atomic vapors is due to atoms leaving the field interaction volume. To some extent, this loss can be mitigated by the introduction of an auxiliary inert buffer gas of atoms which do not interact with the fields or the internal states of the EIT medium, but such techniques have thus far yielded $1/e$ storage lifetimes of no more than a several hundreds of microseconds [153, 154]. This has prompted many researchers to focus their attention on EIT in systems of cold and even bose-condensed atoms [155–161], or on the use of ensembles of rare-earth ions trapped within yttrium orthosilicate crystals [162–168].

Another approach which has been explored forgoes the use of an inert buffer gas in favor of a thin paraffin coating on the inside of the pyrex vapor cell enclosing a warm (40 to 70 °C) gas of Rb atoms [169, 170]. Although the surface physics of the Rb-paraffin interaction has chiefly been studied empirically, these coatings effectively reduce the surface binding potential to the extent that Rb atoms may collide with the paraffin many times before their internal states depolarize due to interactions with the surface [171–176]. Paraffin coatings have been used to good effect in conjunction with EIT for precision magnetometry [137, 176–180], and to demonstrate slow light with group velocities as low as 8 m/s [181].

A striking consequence of the extended lifetime of atoms' metastable coherence in paraffin coated cells is the dual structure of the EIT resonance, illustrated in Figure 5.1. Such cells have demonstrated $1/e$ stored light lifetimes of up to 4 ms [153]. In this chapter, we present a model of electromagnetically induced transparency in cells with anti-relaxation coatings. This model can be viewed as the infinite pulse limit of the Ramsey pulse sequence model developed for EIT in buffer gas cells by [182, 183], and describes the effects of random classical transport of the atomic ensemble throughout the cell. Note that the related problem of describing magneto-optical rotation in paraffin coated cells treated in [184–186] shares some features in common with the model developed here. Then, in section 5.3, we explore basic theoretical issues related to coherently coupling two distinct transverse modes to one another using EIT in anti-relaxation coated cells.
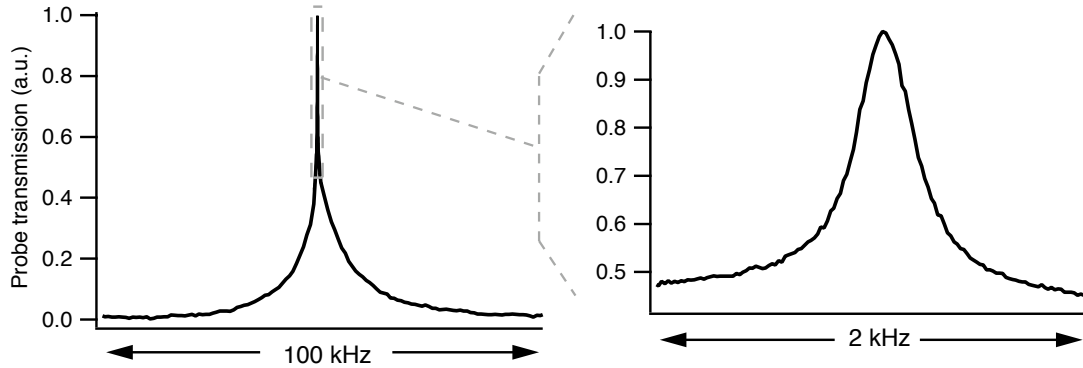
Figure 5.1: Measured EIT transmission spectrum in an anti-relaxation coated cell with control field intensity 3.5 mW/cm^2, or $\Omega_c \simeq 3.8$ MHz, at temperature $T = 48$ °C. Note that the vertical axis has been scaled so that the full spectrum has unit amplitude. The full width of the broad structure (at left) is approximately 13 kHz, while that of the narrow structure (inset at right) is power-broadened to 350 Hz.

5.1   Electromagnetically Induced Transparency

The potential to exhibit electromagnetically induced transparency (EIT) exists within many physical systems, ranging from the metastable states of atoms in warm[1] atomic vapors [143,145,187–190], to ultra-cold [155,156] and bose-condensed gases [157–161], and rare-earth ion impurities in Yttrium orthosilicate crystals [162–168]. Although the complexity of these systems varies widely, the basic physics of EIT is comparatively simple. Generally speaking, EIT can be established for any quantum system with a set of two or more metastable states[2] that can be coherently coupled to a single common state, often an unstable electronically excited state. If this condition is satisfied, then EIT can be established by driving the system into a superposition of the metastable states which does not couple to the common excited state. The simplest system which can exhibit EIT is the three level Λ-system atom depicted in Figure 5.2(a), with both of the applied fields Ω_c and Ω_p tuned to simultaneous

---

[1]where by "warm", we mean temperatures which vary from room temperature to 100 °C for Rubidium vapors, on up to more than 600 °C for vapors composed of Lead atoms...

[2]These states typically belong to different Zeeman or Hyperfine sublevels of a single electronic ground state manifold.

resonance with their respective transitions. Under these circumstances, we can easily determine that the ground state superposition $|-\rangle$, where

$$|-\rangle = \frac{\Omega_p|a\rangle - \Omega_c|b\rangle}{\sqrt{\Omega_c^2 + \Omega_p^2}}, \qquad\qquad |+\rangle = \frac{\Omega_c|a\rangle + \Omega_p|b\rangle}{\sqrt{\Omega_c^2 + \Omega_p^2}}, \qquad (5.1)$$

is not coupled by the combination of Ω_c and Ω_p to the excited state $|e\rangle$, due to destructive interference. In this case, spontaneous emission and the fields themselves tend to drive atoms into the so-called "dark state". Thus an otherwise opaque medium made up of a large number of Λ-systems can be rendered transparent by applying a suitable combination of electromagnetic fields. Although the basic properties of EIT physics have been derived elsewhere [191–194], we reprise the derivation of the essential details of EIT phenomena below for the sake of clarity and consistency of notation.
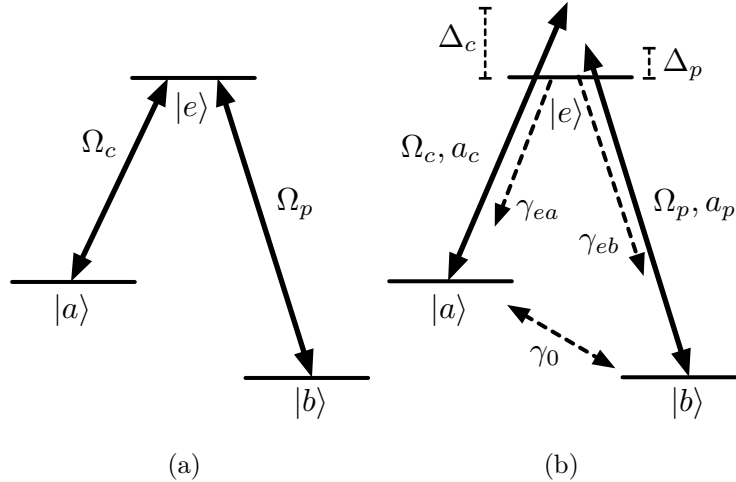
Figure 5.2: Electromagnetically induced transparency in three-level atom. (a) Resonant EIT. (b) General schematic of EIT in a three-level Λ-system.

The interaction of a pair of mutually phase coherent single mode laser fields with the three-level Λ-system indicated in Figure 5.2(b) can be described, in the electric dipole representation [90], by the equations generated by the Hamiltonian

$$H = H_0 + H_I, \qquad (5.2)$$

with

$$H_0 = \hbar\omega_c a_c^\dagger a_c + \hbar\omega_p a_p^\dagger a_p + E_a|a\rangle\langle a| + E_b|b\rangle\langle b| + E_e|e\rangle\langle e|, \qquad (5.3)$$

$$H_I = -g_c a_c|e\rangle\langle a| - g_c^* a_c^\dagger|a\rangle\langle e| - g_p a_p|e\rangle\langle b| - g_p^* a_p^\dagger|b\rangle\langle e|, \qquad (5.4)$$

where g_c and g_p are respectively the electric dipole matrix elements for the $a \leftrightarrow e$ and $b \leftrightarrow e$ transitions, and $a^\dagger$ and a represent creation and annihilation operators for the normal modes of the electric field operator. Note that we have already taken the rotating-wave approximation. Thus we ignore the contribution of terms such as $g_c a_c^\dagger|e\rangle\langle a|$ which appear in the exact Hamiltonian in the electric dipole representation. This approximation is justified by the observation that the optical frequencies ω_c and ω_p are far larger than any other frequencies that shall arise in our subsequent analyses. These terms primarily generate small shifts in the effective energies of the atomic states, which for our purposes we will assume to be accounted for in the definitions of E_a, E_b, and E_e. They will have no significant effect on the more slowly evolving steady-state solutions which we study. The above Hamiltonian may be simplified via the unitary transformation into the interaction picture,

$$\begin{aligned}
H_{int} = e^{-iH_0 t} H_I e^{iH_0 t} = &-g_c a_c|e\rangle\langle a|e^{i\omega_c t - i(E_e - E_a)t} - g_c^* a_c^\dagger|a\rangle\langle e|e^{-i\omega_c t + i(E_e - E_a)t} \\
&- g_p a_p|e\rangle\langle b|e^{i\omega_p t - i(E_e - E_b)t} - g_p^* a_p^\dagger|p\rangle\langle e|e^{-i\omega_p t + i(E_e - E_b)t},
\end{aligned} \qquad (5.5)$$

or

$$H_{int} = -g_c a_c e^{i\Delta_c t}|e\rangle\langle a| - g_c^* a_c^\dagger e^{-i\Delta_c t}|a\rangle\langle e| - g_p a_p e^{i\Delta_p t}|e\rangle\langle b| - g_p^* a_p^\dagger e^{-i\Delta_p t}|b\rangle\langle e|. \quad (5.6)$$

The explicit time-dependence of this operator can be suppressed by redefining the ground states $|a\rangle$ and $|b\rangle$ as

$$|\tilde{a}\rangle = e^{i\Delta_c t}|a\rangle \qquad\qquad |\tilde{b}\rangle = e^{i\Delta_p t}|b\rangle, \qquad (5.7)$$

In terms of these states, the interaction Hamiltonian can be written as

$$H_{int} = -\hbar\Delta_c|\tilde{a}\rangle\langle\tilde{a}| - \hbar\Delta_p|\tilde{b}\rangle\langle\tilde{b}| - \left(g_c a_c|e\rangle\langle\tilde{a}| + g_p a_p|e\rangle\langle\tilde{b}| + h.c.\right), \qquad (5.8)$$

or, by choosing the zero of energy appropriately,

$$H_{int} = -\hbar\delta|\tilde{b}\rangle\langle\tilde{b}| - \left(g_c a_c|e\rangle\langle\tilde{a}| + g_p a_p|e\rangle\langle\tilde{b}| + h.c.\right), \qquad (5.9)$$

where $\delta \equiv \Delta_p - \Delta_c$. We may then write the equations of motion

$$\dot{\rho} = \partial_t \rho = -(i/\hbar)[H, \rho] \tag{5.10}$$

for the Heisenberg density-matrix operator $\rho_{j,k} \equiv |j\rangle\langle k|$ in time-independent form as

$$\dot{\rho}_{\tilde{a},\tilde{a}} = -\gamma_0(\rho_{\tilde{a},\tilde{a}} - \rho_{\tilde{b},\tilde{b}}) + \gamma_{ea}\rho_{ee} - \left(i\frac{g_c a_c}{\hbar}\rho_{e,\tilde{a}} + h.c.\right) \tag{5.11a}$$

$$\dot{\rho}_{\tilde{b},\tilde{b}} = -\gamma_0(\rho_{\tilde{b},\tilde{b}} - \rho_{\tilde{a},\tilde{a}}) + \gamma_{eb}\rho_{ee} + \left(i\frac{g_p^* a_p^\dagger}{\hbar}\rho_{\tilde{b},e} + h.c.\right) \tag{5.11b}$$

$$\dot{\rho}_{e,e} = -(\gamma_{ea} + \gamma_{eb})\rho_{ee} + \left(i\frac{g_c a_c}{\hbar}\tilde{\rho}_{e,\tilde{a}} - i\frac{g_p^* a_p^\dagger}{\hbar}\rho_{\tilde{b},e} + h.c.\right) \tag{5.11c}$$

$$\dot{\rho}_{e,\tilde{a}} = -\frac{1}{2}(\gamma_0 + \gamma_{ea} + \gamma_{eb} + i2\Delta_c)\rho_{e,\tilde{a}} + i\frac{g_c^* a_c^\dagger}{\hbar}(\rho_{\tilde{a},\tilde{a}} - \rho_{e,e}) + i\frac{g_p^* a_p^\dagger}{\hbar}\rho_{\tilde{b},\tilde{a}} \tag{5.11d}$$

$$\dot{\rho}_{\tilde{b},e} = -\frac{1}{2}(\gamma_0 + \gamma_{ea} + \gamma_{eb} - i2\Delta_p)\rho_{\tilde{b},e} - i\frac{g_p a_p}{\hbar}(\rho_{\tilde{b},\tilde{b}} - \rho_{e,e}) - i\frac{g_c a_c}{\hbar}\rho_{\tilde{b},\tilde{a}} \tag{5.11e}$$

$$\dot{\rho}_{\tilde{b},\tilde{a}} = -(\gamma_0 - i\delta)\rho_{\tilde{b},\tilde{a}} + i\frac{g_p a_p}{\hbar}\rho_{e,\tilde{a}} - i\frac{g_c^* a_c^\dagger}{\hbar}\rho_{\tilde{b},e}, \tag{5.11f}$$

where γ_0, γ_{ea}, and γ_{eb} describe the system's coupling to an external reservoir whose maximally mixed quantum state is not measured before, during, or after our experiments. Similarly, the evolution of the field operators $a_c^\dagger$ and a_p is given by

$$(\partial_t - c\partial_z)\,a_c^\dagger = i(g_c/\hbar)\rho_{e,\tilde{a}} \tag{5.12}$$

$$(\partial_t - c\partial_z)\,a_p = -i(g_p^*/\hbar)\rho_{\tilde{b},e}, \tag{5.13}$$

where the above advection equations are obtained from the full wave equation by taking the slowly varying envelope approximation, *i.e.* , by assuming that the overall field amplitudes do not change appreciably on the scale of the optical wavelength. In the semiclassical limit, where one or both of these fields may be treated classically, but where we wish to retain the quantum properties of the Λ-system, we may replace the field couplings in (5.11) with the generalized complex Rabi frequencies

$$\Omega_c \equiv \frac{g_c\langle a_c\rangle}{\hbar} = \frac{g_c E_c^+}{\hbar}, \qquad \text{and} \qquad \Omega_p \equiv \frac{g_p\langle a_p\rangle}{\hbar} = \frac{g_p E_p^+}{\hbar}, \tag{5.14}$$

where E_c^+ and E_p^+ formally represent the expectation values of the positive frequency components of the electric fields. If the applied fields are not sufficient to saturate

either of the Λ-system's optical transitions, we may take the approximation $\rho_{e,e} \simeq 0$, and allow the optical coherence $\rho_{e,\tilde{a}}$ to adiabatically follow the ground state populations $\rho_{\tilde{a},\tilde{a}}$, $\rho_{\tilde{b},\tilde{b}}$ and the ground state coherence $\rho_{\tilde{b},\tilde{a}}$, reducing (5.11) to

$$\dot{\rho}_{\tilde{a},\tilde{a}} = -\gamma_0(\rho_{\tilde{a},\tilde{a}} - \rho_{\tilde{b},\tilde{b}}) - \left(i\frac{g_c a_c}{\hbar}\rho_{e,\tilde{a}} + h.c.\right) \tag{5.15a}$$

$$\dot{\rho}_{\tilde{b},\tilde{b}} = -\gamma_0(\rho_{\tilde{b},\tilde{b}} - \rho_{\tilde{a},\tilde{a}}) + \left(i\frac{g_p^* a_p^\dagger}{\hbar}\rho_{\tilde{b},e} + h.c.\right) \tag{5.15b}$$

$$\dot{\rho}_{\tilde{b},e} = -\tfrac{1}{2}(\gamma_0 + \gamma_{ea} + \gamma_{eb} - i2\Delta_p)\rho_{\tilde{b},e} - i\frac{g_p a_p}{\hbar}\rho_{\tilde{b},\tilde{b}} - i\frac{g_c a_c}{\hbar}\rho_{\tilde{b},\tilde{a}} \tag{5.15c}$$

$$\dot{\rho}_{\tilde{b},\tilde{a}} = -\left(\gamma_0 - i\delta\right)\rho_{\tilde{b},\tilde{a}} + i\frac{g_p a_p}{\hbar}\rho_{e,\tilde{a}} - i\frac{g_c^* a_c^\dagger}{\hbar}\rho_{\tilde{b},e}, \tag{5.15d}$$

with

$$\rho_{e,\tilde{a}} = \frac{i}{\hbar}\frac{g_c^* a_c^\dagger \rho_{\tilde{a},\tilde{a}} + g_p^* a_p^\dagger \rho_{\tilde{b},\tilde{a}}}{(\gamma_0 + \gamma_{ea} + \gamma_{eb})/2 + i\Delta_c}. \tag{5.16}$$

Taking the semiclassical limit for Ω_c, with $|\Omega_c|^2 \gg \frac{|g_p|^2\langle a_p^\dagger a_p\rangle}{\hbar^2}$, and Δ_c and γ_0 small enough that $\rho_{\tilde{a},\tilde{a}} \simeq 0$ and $\rho_{\tilde{b},\tilde{b}} \simeq 1$, this further reduces to

$$\dot{\rho}_{\tilde{b},e} = -(\Gamma - i\Delta_p)\rho_{\tilde{b},e} - i\frac{g_p a_p}{\hbar} - i\Omega_c\rho_{\tilde{b},\tilde{a}} \tag{5.17a}$$

$$\dot{\rho}_{\tilde{b},\tilde{a}} = -\left(\tilde{\gamma}_0 - i\tilde{\delta}\right)\rho_{\tilde{b},\tilde{a}} - i\Omega_c^*\rho_{\tilde{b},e}, \tag{5.17b}$$

where

$$\Gamma = \gamma_0 + \gamma_{ea} + \gamma_{eb}, \qquad \tilde{\gamma}_0 = \gamma_0 + \frac{|\Omega_c|^2\Gamma/2}{\Gamma^2/4 + \Delta_p^2}, \qquad \tilde{\delta} = \delta - \frac{|\Omega_c|^2\Delta_p}{\Gamma^2/4 + \Delta_p^2}, \tag{5.18}$$

Generally speaking, the fields Ω_c and a_p are not coupled to a single three level atom, but rather to an large ensemble of such atoms with density N. Taking this into account, we extend the single system results above to the ensemble coupling by defining the collective operators

$$S(\vec{r},t) \equiv \frac{1}{\sqrt{Z_S}}\sum_{n=1}^{N}\alpha_n\rho_{\tilde{b},\tilde{a}}^n$$

$$P_{\tilde{b},e}(\vec{r},t) \equiv \frac{1}{\sqrt{Z_{P,\tilde{b}}}}\sum_{n=1}^{N}\beta_{n,p}\rho_{\tilde{b},e}^n \tag{5.19}$$

$$P_{e,\tilde{a}}(\vec{r},t) \equiv \frac{1}{\sqrt{Z_{P,\tilde{a}}}}\sum_{n=1}^{N}\beta_{n,c}\rho_{e,\tilde{a}}^n,$$

where $\rho_{j,k}^n = |j\rangle_n\langle k|_n$ for the nth atom in a small unit volume centered on $\vec{r}$; α_n, $\beta_{n,p}$, $\beta_{n,c}$ are coupling constants of order unity which account for variations in the phase and magnitude of the field-atom coupling over the full ensemble; and where

$$Z_S = \sum_n \alpha_n \qquad\qquad Z_{P,\tilde{b}} = \sum_n \beta_{n,p} \qquad\qquad Z_{P,\tilde{a}} = \sum_n \beta_{n,c}. \qquad (5.20)$$

As shown by [150, 194], for $\alpha_n = \beta_{n,p} = \beta_{n,c} = 1$ and $N \gg \langle a_p^\dagger a_p\rangle$, we may substitute $\{S(\vec{r},t), P_{\tilde{b},e}(\vec{r},t), P_{e,\tilde{a}}(\vec{r},t)\}$ for $\{\rho_{\tilde{b},\tilde{a}}, \rho_{\tilde{b},e}, \rho_{e,\tilde{a}}\}$ in the above equations to describe the fields' interaction with the entire ensemble.

5.1.1   Dispersive Properties of EIT

Substituting $\Delta_c = 0$, and taking the limit that $\rho_{\tilde{b},\tilde{b}} \simeq 1$ and $\tilde{\delta} \simeq \delta$, the steady-state solution of the semiclassical equations (5.17) is

$$\rho_{\tilde{b},\tilde{a}} = \frac{-i\Omega_c^*}{\tilde{\gamma}_0 - i\delta}\rho_{\tilde{b},e}, \qquad \text{so that} \qquad \rho_{\tilde{b},e} = \frac{-i\Omega_p(\gamma_0 + i\delta)}{(\Gamma - i\delta)(\gamma_0 - i\delta) + |\Omega_c|^2}. \qquad (5.21)$$

As shown in Figure 5.3, for $\delta \ll |\Omega_c|^2/\Gamma$, the semiclassical susceptibility χ of the

(a) Absorption Spectrum   (b) Dispersion Spectrum
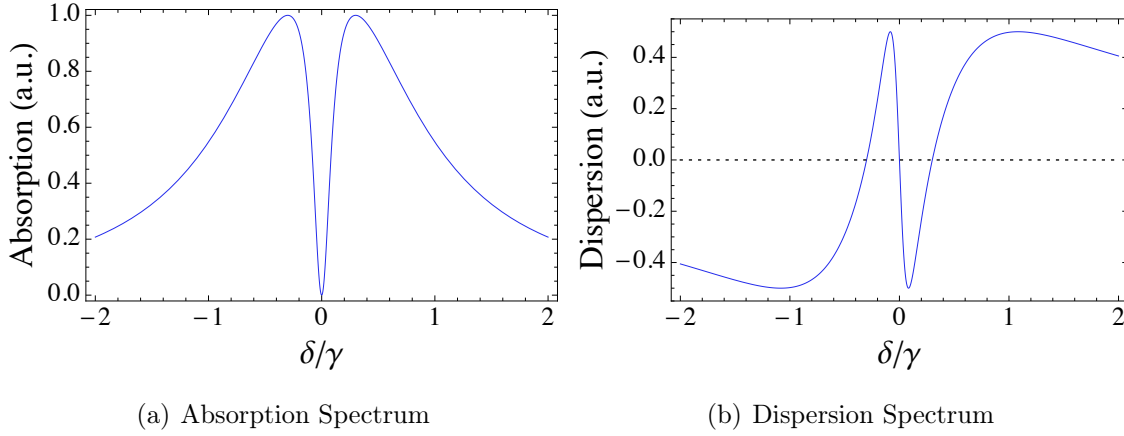
Figure 5.3: Characteristic absorption (a) and dispersion (b) spectrum of an EIT resonance. The absorption is proportional to $\mathcal{I}m(\chi)$, and the dispersion to $\mathcal{R}e(\chi)$ in (5.22). Here $\Omega_c = 0.3\gamma$, $\gamma_0 = 10^{-6}\gamma$, and $|g_p|^2 N = 1$.

medium as felt by the Ω_p field is

$$\chi = -|g_p|^2 N \frac{-i(\gamma_0 + i\delta)}{(\Gamma - i\delta)(\gamma_0 - i\delta) + |\Omega_c|^2} \qquad (5.22)$$

such that the medium becomes transparent in a narrow bandwidth centered about $\delta = 0$. This narrow transmission resonance comes with a steep dispersion, responsible for the dramatic reduction in the group velocity of a narrow-bandwidth pulse of the a_p field. Semiclassically, the group velocity of a narrow-bandwidth pulse propagating in a dispersive medium with $\mathbf{Re}(\chi) \propto |g_p|^2 N / |\Omega_c|^2$, as happens in a narrow bandwidth about $\delta = 0$, is given by

$$v_g = \frac{c|\Omega_c|^2}{|\Omega_c|^2 + |g_p^2|N}. \tag{5.23}$$

This result may also be obtained for the propagation of single photons using the dark state polariton representation [194].

5.2 Modeling EIT in Anti-Relaxation Coated Cells

In this section, we introduce a formal method of calculating the steady-state EIT spectra in coated cells. As has been noted in [178, 182], whenever atoms can make several separate passages through the laser fields before they decohere, the evolution of their internal degrees of freedom may be calculated by solving the equivalent problem of the atomic state after an arbitrary sequence of Ramsey pulses. In the steady-state, the EIT spectrum is determined by the average atomic state after a sequence of Ramsey pulses of varying duration, delays between pulses, and effective frequency due to factors such as the distribution of atomic velocities and the geometry of the system. An illustration of the problem is shown in Figure 5.4. To determine the steady-state density matrix for the atomic ensemble in the beam, we trace the atoms' trajectories backwards in time and take an appropriate average over all possible paths.

We begin by adopting the Bloch vector representation for the state of a Λ system developed by [195], which has also been used in [182]. Here, we begin with a three level Λ-system, depicted in Figure 5.5(a). The two ground states $|a\rangle$ and $|b\rangle$ are semi-classically coupled to the excited state $|e\rangle$ respectively by the "control" Ω_c and "probe" Ω_p fields. The behavior of this system can be more clearly understood by

(a) Sample Atomic Trajectory

(b) Three Random Ramsey Pulse Sequence
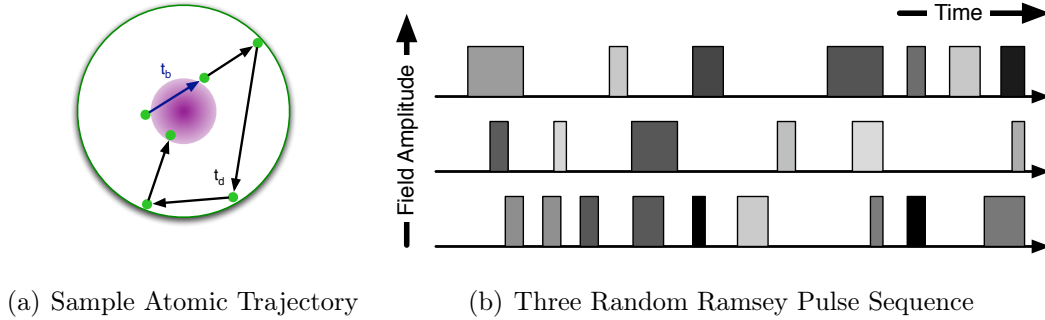
Figure 5.4: (a) Illustration of an atomic trajectory relevant in determining the state of the atomic ensemble in anti-relaxation coated cells. (b) Representation of three different interaction histories from the full set which must be summed over to obtain the density matrix. Time spent inside the beam is represented as a shaded box, with darker boxes representing interactions with reduced axial Doppler shifts, and hence stronger couplings than those indicated by lighter boxes, (see part 5.2.2).

redefining the ground state basis so that

$$|-\rangle = \cos\theta|\tilde{a}\rangle - \sin\theta|\tilde{b}\rangle, \qquad\qquad |+\rangle = \sin\theta|\tilde{a}\rangle + \cos\theta|\tilde{b}\rangle, \qquad (5.24)$$

and hence

$$|\tilde{a}\rangle = \sin\theta|+\rangle + \cos\theta|-\rangle, \qquad\qquad |\tilde{b}\rangle = \cos\theta|+\rangle - \sin\theta|-\rangle, \qquad (5.25)$$

where

$$\sin\theta \equiv \frac{\Omega_p}{\Omega_{\mathrm{EIT}}}, \qquad \cos\theta \equiv \frac{\Omega_c}{\Omega_{\mathrm{EIT}}}, \qquad \text{and} \qquad \Omega_{\mathrm{EIT}} \equiv \sqrt{|\Omega_p|^2 + |\Omega_c|^2} \qquad (5.26)$$

This transforms the semiclassical version of the bare-state basis Hamiltonian (5.8) into

$$H_{int} = -\hbar\left(\delta_1 + \frac{\delta}{2}\right)(|+\rangle\langle+| + |-\rangle\langle-|) - \hbar\frac{C\delta}{2}(|+\rangle\langle+| - |-\rangle\langle-|) \qquad (5.27)$$

$$- \hbar\frac{S\delta}{2}(|-\rangle\langle+| + |+\rangle\langle-|) - \hbar S\left(\Omega_{\mathrm{EIT}}|e\rangle\langle+| + \Omega_{\mathrm{EIT}}^*|+\rangle\langle e|\right) \qquad (5.28)$$

with

$$S = \sin(2\theta), \qquad\qquad C = \cos(2\theta), \qquad\qquad \delta = \delta_1 - \delta_2. \qquad (5.29)$$

(a) Bare State Basis   (b) Dark State Basis
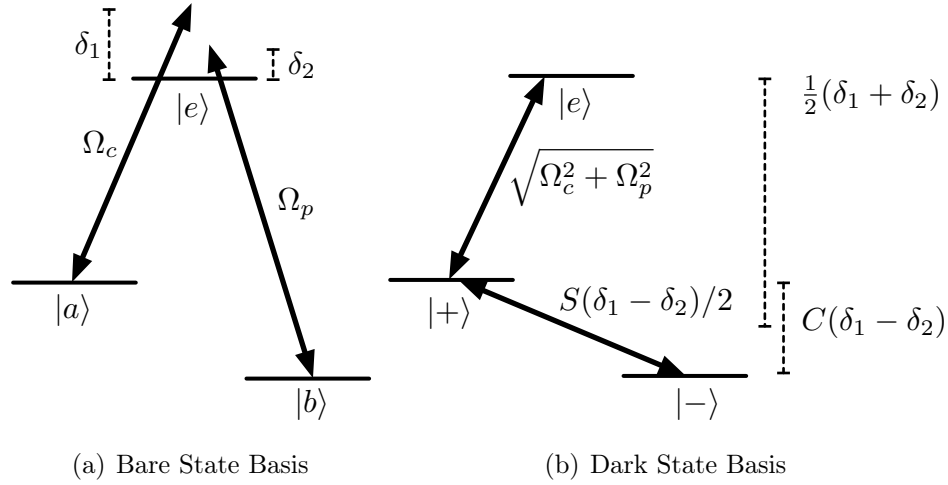
Figure 5.5: Atomic energy level diagram exhibiting electromagnetically induced transparency (EIT) in a three level atom. (a) depicts the "bare state" representation, where two fields Ω_c and Ω_p coherently couple the states $|a\rangle$ and $|b\rangle$ to the same excited state $|e\rangle$. As noted in the text, some superposition states of $|a\rangle$ and $|b\rangle$ are not coupled to $|e\rangle$ by the fields. In (b), the same system is shown in the "dark state" basis, where the fields couple solely to the bright state $|+\rangle$ which can mix with the dark state $|-\rangle$ for nonzero two-photon detuning $\delta = \delta_1 - \delta_2$.

In this representation, we clearly see that the dark state $|-\rangle$ is not directly coupled to $|e\rangle$ by the applied fields. For nonzero two-photon detuning δ, however, the dark state finds itself effectively coupled to the bright state. This occurs because for $\delta \neq 0$, the relative phase accumulation rate between the fields Ω_c and Ω_p will be different than the rate of relative phase accumulation between the $|a\rangle$ and $|b\rangle$ ground states. Thus dark states may become bright states and vice versa simply by the passage of a sufficient amount of time.

To further simplify this model, we can reduce it to an effective two-level system by adiabatically eliminating the excited state as in [195]. This two level system is composed of the dark state $|-\rangle$ and a radiatively damped bright state $|+\rangle$. We then construct the Bloch vector representation $\mathbf{R}$ of the atomic density matrix ρ in this basis state basis with

$$\frac{1}{2}(R_1 + iR_2) = \rho_{-+}, \qquad \text{and} \qquad R_3 = \rho_{--} - \rho_{++}, \qquad (5.30)$$

whose evolution is given by

$$\frac{d\mathbf{R}}{dt} = \mathbf{Q} \times \mathbf{R} - (\alpha + \gamma_0)\mathbf{R} + \alpha\hat{\mathbf{e}}_3, \tag{5.31}$$

where the precession vector $\mathbf{Q}$ is given by

$$\mathbf{Q} = -S\delta\hat{\mathbf{e}}_1 + (\beta - C\delta)\hat{\mathbf{e}}_3, \tag{5.32}$$

where γ_0 is the "intrinsic" relaxation rate of the atomic ground state coherence, including the effects of stray magnetic field gradients and any dephasing due to many collisions with the wall, and

$$\alpha = \frac{|\Omega_{\mathrm{EIT}}|^2\Gamma/2}{\Gamma^2 + 4\Delta^2} \qquad\qquad \beta = \frac{|\Omega_{\mathrm{EIT}}|^2\Delta}{\Gamma^2 + 4\Delta^2}, \tag{5.33}$$

where Γ is the radiative relaxation rate of the excited state. Taking $\beta' = \beta - C\delta$, this can be written in matrix form as

$$\begin{bmatrix} \dot{R}_1 \\ \dot{R}_2 \\ \dot{R}_3 \end{bmatrix} = \begin{bmatrix} -(\alpha + \gamma_0) & -\beta' & 0 \\ \beta' & -(\alpha + \gamma_0) & S\delta \\ 0 & -S\delta & -(\alpha + \gamma_0) \end{bmatrix} \begin{bmatrix} R_1 \\ R_2 \\ R_3 \end{bmatrix} + \begin{bmatrix} 0 \\ 0 \\ \alpha \end{bmatrix}. \tag{5.34}$$

For constant fields, (5.34) can be integrated to yield

$$\mathbf{R}(t) = A(t)\mathbf{R}_0 + (I - A(t))\mathbf{R}_s \tag{5.35}$$

where $\mathbf{R}_0$ is the Bloch vector at $t = 0$, and $\mathbf{R}_s$ is the steady-state solution of (5.34).

$$\mathbf{R}_s = \frac{\alpha}{(\alpha + \gamma_0)((\alpha + \gamma_0)^2 + \Omega^2)} \begin{bmatrix} -S\delta\beta' \\ S\delta(\alpha + \gamma_0) \\ (\alpha + \gamma_0)^2 + \beta'^2 \end{bmatrix}, \tag{5.36}$$

where $\Omega = \sqrt{S^2\delta^2 + \beta'^2}$. Note that the above is the general form of the solution to the equations of motion both inside and outside the beam. Inside the beam, $A(t) = A_b(t)$:

$$A_b(t) = e^{-(\alpha + \gamma_0)t} \times \begin{bmatrix} \frac{S^2\delta^2 + \beta'^2\cos(t\Omega)}{\Omega^2} & -\frac{\beta'\sin(t\Omega)}{\Omega} & -\frac{S\delta\beta'(1 - \cos(t\Omega))}{\Omega^2} \\ \frac{\beta'\sin(t\Omega)}{\Omega} & \cos(t\Omega) & \frac{S\delta\sin(t\Omega)}{\Omega} \\ -\frac{S\delta\beta'(1 - \cos(t\Omega))}{\Omega^2} & -\frac{S\delta\sin(t\Omega)}{\Omega} & \frac{\beta'^2 + S^2\delta^2\cos(t\Omega)}{\Omega^2} \end{bmatrix}. \tag{5.37}$$

Outside the beam, the steady state solution is $\mathbf{R}_s = \mathbf{0}$, and $A(t) = A_d(t)$:

$$A_d(t) = e^{-\gamma_0 t} \times \begin{bmatrix} S^2 + C^2 \cos(t\delta) & C\sin(t\delta) & SC(1 - \cos(t\delta)) \\ -C\sin(t\delta) & \cos(t\delta) & S\sin(t\delta) \\ SC(1 - \cos(t\delta)) & -S\sin(t\delta) & C^2 + S^2 \cos(t\delta) \end{bmatrix}. \tag{5.38}$$

We determine the steady-state of the ensemble by averaging over all possible Ramsey pulse sequences the atoms may experience. We assume that atoms' external degrees of freedom completely thermalize upon contact with the wall, and that we may treat the selection of atoms' speeds and trajectories after each wall-collision as the result of a Markovian process. The average state of an initially unpolarized atom that has completed one passage across the beam and is about to re-enter the beam (after any number of cell crossings that missed the beam) is given by two iterations of (5.35):

$$\langle \mathbf{R}_1 \rangle = (\langle A_d \rangle - \langle A_d A_b \rangle) \, \mathbf{R}_s, \tag{5.39}$$

where $\mathbf{R}_s$ is the steady-state Bloch vector in the beam. Formally, the average $\langle A_d A_b \rangle$ is taken over the distribution of time spent in the beam and in the dark before re-entering the beam, and thus depends upon the detailed trajectory the atom follows as it travels from the wall to the beam.

To simplify our analysis, we will take the approximation $\langle A_d A_b \rangle \simeq \langle A_d \rangle \langle A_b \rangle$. This approximation works best when atoms cross the cell several times between beam interactions. Treating the vacuum cell as an infinite cylinder, the mean number of times an atom must cross a cell of diameter D before encountering a beam of diameter d is D/d (see part C.1.1). Choosing $D/d \gg 1$, we may treat τ_d (the time spent in the dark) as if it were independent of τ_b (the time spent crossing the beam). After N passages,

$$\langle \mathbf{R}_N \rangle = \langle A_d \rangle \sum_{k=1}^{N} (-\langle A_b \rangle \langle A_d \rangle)^k \, \mathbf{R}_s. \tag{5.40}$$

Taking $N \to \infty$, we obtain the steady-state distribution of the atomic ensemble. Equation (5.40) has the form of a power series, and is readily solvable once we know $\langle A_d \rangle \langle A_b \rangle$.

Because the time-dependent terms in $A_b(t)$ and $A_d(t)$ are of the form $e^{-\gamma t}\sin(\eta t)$ and $e^{-\gamma t}\cos(\eta t)$, we need only find the form of $\langle e^{-(\gamma - i\eta)t}\rangle$ to determine the matrix averages. The exact probability density function (p.d.f.) governing the distribution of times spent in the beam and in the dark yields an expression which is difficult to evaluate (see Appendix C.1). For small d/D, we approximate the beam (dark) interaction time p.d.f. for an atom with mean beam interaction (dark time) $\tau = \tau_b$ ($\tau = \tau_d$) as an exponential:

$$g_{b,d}(t) = \frac{\sqrt{\pi}}{\tau_{b,d}\sqrt{2}}e^{-\sqrt{\frac{\pi}{2}}\frac{t}{\tau_{b,d}}}. \tag{5.41}$$

As shown in Appendix C.1, these exponential approximations of $g_b(t)$ and $g_d(t)$ produce better results when $d/D \ll 1$, in the small beam limit.

5.2.1 Weak Field Limit, no Doppler Averaging

In the weak field limit $\Omega_p \ll \Omega_c$, and when the average one-photon detuning $\Delta = 0$, $A_b(t)$ and $A_d(t)$ differ only by a factor of $e^{-\alpha t}$. Taking the average over the exponential time distributions $g_b(t)$ and $g_d(t)$, we define

$$X(\delta) = \langle e^{-(\alpha + \gamma_0 - i\delta)t}\rangle_{g_b} = \frac{1/\tau_b}{(1/\tau_b + \alpha + \gamma_0) - i\delta} \tag{5.42}$$

$$Y(\delta) = \langle e^{-(\gamma_0 - i\delta)t}\rangle_{g_d} = \frac{1/\tau_d}{(1/\tau_d + \gamma_0) - i\delta}. \tag{5.43}$$

Setting

$$Z(\delta) = \sum_{n=0}^{\infty}(X(\delta)Y(\delta))^n(1 - X(\delta)) = \frac{1 - X(\delta)}{1 - X(\delta)Y(\delta)}, \tag{5.44}$$

the steady-state Bloch vector is

$$\langle \mathbf{R}\rangle = \begin{bmatrix} C^2\mathbf{Re}(Z(\delta)) & C\mathbf{Im}(Z(\delta)) & -\mathbf{Re}(Z(\delta)) \\ -C\mathbf{Im}(Z(\delta)) & \mathbf{Re}(Z(\delta)) & S\mathbf{Im}(Z(\delta)) \\ -\mathbf{Re}(Z(\delta)) & -S\mathbf{Im}(Z(\delta)) & +S^2\mathbf{Re}(Z(\delta)) \end{bmatrix}\mathbf{R}_s$$

$$+ \begin{bmatrix} S^2 Z(0) & 0 & SCZ(0) \\ 0 & 0 & 0 \\ SCZ(0) & & C^2 Z(0) \end{bmatrix}\mathbf{R}_s. \tag{5.45}$$

Using (5.24), (5.30), and (5.33), we then find that the optical coherence $\rho_{e,b}$, probed by Ω_p, is given by

$$\rho_{e,b} = \left(\frac{i\alpha - \beta}{\Omega_{\text{EIT}}^2}\right)\left[\Omega_p(1 - R_3) - \Omega_c(R_1 - iR_2)\right]. \qquad (5.46)$$

Figure 5.6 shows a typical probe absorption spectrum derived from (5.45) and (5.46). When the applied fields have a nonzero two-photon detuning, the bare ground states have different effective energies (in the rotating frame), and so the atomic states nutate (from the perspective of the fields) between the bright and dark states at a rate $S\delta/2$. This nutation causes the absorption spectrum to develop Ramsey fringes, as the probe absorption increases when $t\delta$ is such that atoms tend to return in the bright state, and decreases when they tend to return in the dark state.

Because the distribution of time spent in the dark before returning to the beam has a nonzero variance, the spectra from different atoms interfere with each other and wipe out the fringe pattern everywhere except in the vicinity of $\delta = 0$. A similar effect has been observed by [182] for EIT in buffer gas cells. Near two-photon resonance, all fringes have an absorption minimum (since atoms prepared in the dark state cannot nutate into the bright state if $\delta = 0$), and constructively interfere.

Calculations plotted in Figure 5.7 demonstrate that the ultra-narrow transmission feature of the EIT spectrum is due to atomic coherence accumulating a relative phase in the dark. Increasing the diameter of the beam relative to the cell reduces the amount of time atoms can spend in the dark. This in turn reduces the fraction of atoms present in the beam which have just returned from evolution in the dark, and reduces the contrast of the Ramsey-narrowed transmission peak. Because the fraction of atoms in the beam being actively pumped into the dark state increases, so too does the overall transparency.

As happens with EIT systems involving stationary atoms, we expect the width of the Ramsey-narrowed EIT transmission peak to increase with increasing field intensity. The stronger the applied fields, the faster atoms are optically pumped into the dark state, and the fewer passes through the beam are necessary to cause atoms to "forget" their accumulated phase and be reset into the dark state. In contrast to the stationary EIT result, however, this increase in the Ramsey-narrowed EIT
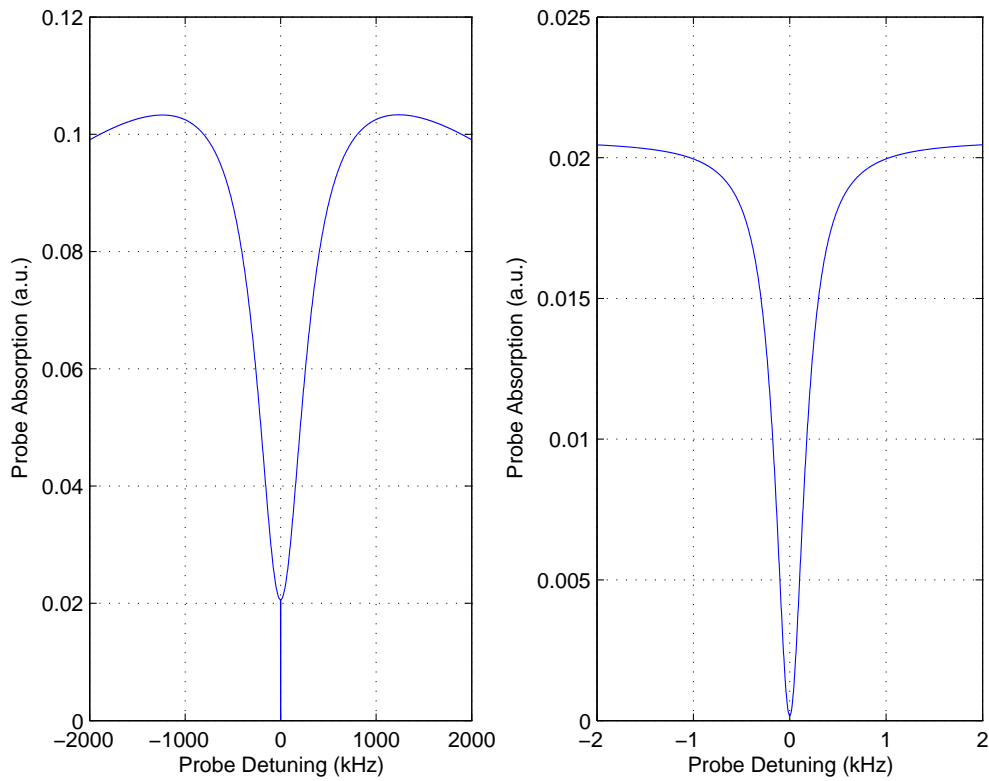
Figure 5.6: Left: Typical calculated probe absorption as a function of probe detuning from resonance. Right: Blow-up of left absorption spectrum showing the neighborhood of two-photon resonance more clearly.
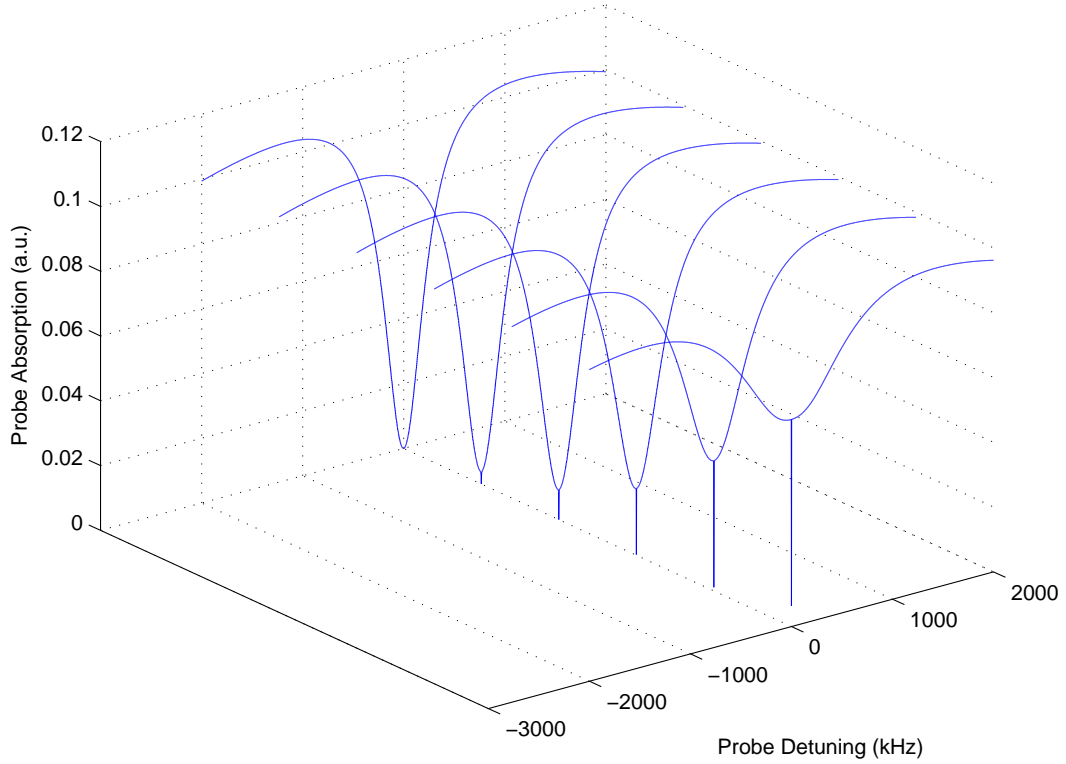
Figure 5.7: Calculated probe absorption as a function of probe detuning, for beams with equal intensity, but varying diameters ($\frac{r}{R} = .01, \ldots, 1$). For small beam diameters, the EIT spectrum is well described by a model with ground state decoherence determined by the finite atomic transit time, except in the neighborhood of two-photon resonance, where the Ramsey-narrowed absorption minima resides. As the beam diameter increases, more and more atoms in the beam at any given time are pumped into the dark state, decreasing the contrast of the narrowed feature, until all atoms spend all their time in the beam, and the ground state lifetime is limited by the coating. These calculations were performed with $\Omega_p = \Omega_c = 1$ MHz, cell diameter $R = 2.54$ cm, and T = 43 °C with negligible intrinsic ground state decoherence γ_0.
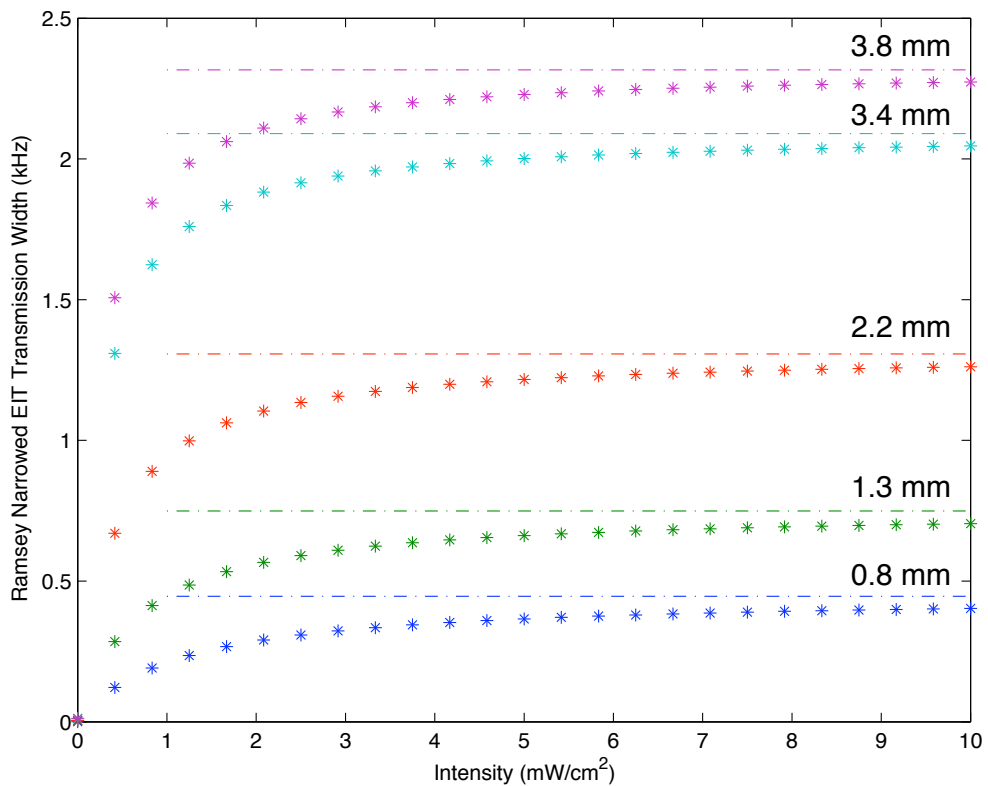
Figure 5.8: Lorentzian fits to calculated Ramsey-Narrowed EIT transmission bandwidth as a function of applied field intensities for various beam radii. As illustrated in the figure above, the bandwidth increases until it approaches a "saturated" value determined by the rate at which atoms re-enter the beam. *'s represent fits to calculations, while like-colored dashed lines illustrate the asymptotic bandwidth of $2/\tau_d$. Cell diameter is 2.54 cm, and T = 43 °C.

bandwidth should reach a maximum when the intensity is such that most atoms are pumped into the dark state in a single pass through the beam. Beyond this point, increasing the field intensity does nothing to the Ramsey-narrowed EIT bandwidth, but simply reduces the contrast of the transmission peak, as shown in Figure 5.8. This EIT bandwidth "saturation" takes place because atoms are guaranteed a minimum coherence lifetime equal to the time atoms spend in the dark. Note that Figure 5.8 demonstrates another unique feature of the ultra-narrow resonance, in that increasing the beam diameter serves to *increase* the ultra-narrow EIT linewidth. This happens because the increased beam diameters increases the probability that atoms interact with the beam, and thus reduces the mean time atoms spend in the dark.

5.2.2   Doppler Broadening

Experimental measurements of the Ramsey-narrowed EIT transmission peaks are narrower than the theoretical predictions of section 5.2.1. This discrepancy can be attributed to Doppler effects. Atoms with large one-photon detunings do not couple to the fields as strongly as those near one-photon resonance, and so Doppler broadening increases the lifetime of the atomic coherence, when that lifetime is limited by the optical pumping rate (*i.e.*, in the power broadened limit).

For EIT between pair of energy-degenerate ground states, such as when EIT is established between two degenerate Zeeman sublevels, Doppler broadening simply narrows the Ramsey-narrowed transmission bandwidth, as we will show below. For EIT established across two non-degenerate states, however, Doppler broadening decreases the Ramsey-narrowed transmission peak contrast. Because the dark state is sensitive to the relative phase of the applied fields, rethermalization on the cell wall can effectively rotate the Bloch vector (relative to the fields) by virtue of the $\Delta k v$ two-photon Doppler shift on δ. This random rotation of the Bloch vector between each passage through the beam washes out the contrast of the Ramsey fringes. As the lifetime of an individual atom's coherence increases, the stronger this inhomogeneous dephasing becomes, and so we find that the contrast of the Ramsey-narrowed peak actually increases with increasing field intensity.

Zeeman EIT

To incorporate the effects of Doppler broadening, note that the Bloch vector $\mathbf{R}$ is actually made up of many sub-ensembles of atoms with different axial velocities. Atoms in different velocity classes couple differently to the applied fields, and so we must consider the formation of Bennett structures [196] in the atomic vapor. Let us examine the evolution of the Bloch vector for the sub-ensemble with velocity v, given by $\mathbf{R}(v)$. We note the three different processes that atoms in this sub-ensemble undergo: interaction with the beam, evolution in the dark, and contact with subsequent desorption on the wall.

Given an input distribution $\mathbf{R}_{in}(v)$, interaction with the beam for a time t_1 results in an output distribution

$$\mathbf{R}_{out}(v) = A_b(t_1, v)\mathbf{R}_{in}(v) + (I - A_b(t_1, v))\mathbf{R}_s(v). \tag{5.47}$$

Given an initial distribution $\mathbf{R}_{in}(v)$, evolution in the dark for a time t_2 results in

$$\mathbf{R}_{out}(v) = A_d(t_2)\mathbf{R}_{in}(v), \tag{5.48}$$

since $\mathbf{R}_s = \mathbf{0}$ in the dark, and A_d is independent of the atomic Doppler shift.

Finally, interaction with the cell coating re-thermalizes the atoms, yielding the output distribution

$$\mathbf{R}_{out}(v) = \int_{-\infty}^{\infty} dv' f(v')\mathbf{R}_{in}(v'), \tag{5.49}$$

where $f(v')$ is the axial velocity distribution for the atomic gas.

Linearity implies that the operations of eqs (5.48) and (5.49) commute with one another. We also note that two applications of (5.49) are equivalent to one application, and so we may model the sequence of evolution in the dark, followed by collision with the cell coating, followed by further evolution in the dark by first applying eq (5.49) and then eq (5.48) for the full period the atoms spend in the dark.

Depolarized atoms are represented by $\mathbf{R} = \mathbf{0}$ regardless of their velocity class, so we may drop the velocity dependence from $\mathbf{R}_{in}$ in eq (5.47) since atoms never re-enter the beam without first re-thermalizing on the cell coating. In light of these considerations, we may take the average over all axial velocities immediately upon

atoms' exiting the beam. The expression for the Doppler-averaged Bloch vector after interaction for a time t_b in the beam is given by

$$\mathbf{R}(t_b) = B(t_b)\mathbf{R}_{in} + \mathbf{C}(t_b) \tag{5.50}$$

where

$$
\begin{aligned}
B(t_b) &= \int_{-\infty}^{\infty} dv f(v) A_b(t_b, v) \\
\mathbf{C}(t_b) &= \int_{-\infty}^{\infty} f(v) \left[\mathbf{R}_s(v) - A_b(t_b, v)\mathbf{R}_s(v) \right].
\end{aligned}
$$

Evolution in the dark is as simple as it was in section 5.2.1, as $\mathbf{R}(t_d) = A_d(t_d)\mathbf{R}_{in}$. We now take the averages over t_b and t_d to obtain

$$
\begin{aligned}
\langle A \rangle &= \int_0^{\infty} dt\, \frac{\sqrt{\pi}e^{-\sqrt{\frac{\pi}{2}}\frac{t}{\tau_d}}}{\sqrt{2}\tau_d} A_d(t) \\
\langle B \rangle &= \int_0^{\infty} dt\, \frac{\sqrt{\pi}e^{-\sqrt{\frac{\pi}{2}}\frac{t}{\tau_b}}}{\sqrt{2}\tau_b} B(t) \\
\langle \mathbf{C} \rangle &= \int_0^{\infty} dt\, \frac{\sqrt{\pi}e^{-\sqrt{\frac{\pi}{2}}\frac{t}{\tau_b}}}{\sqrt{2}\tau_b} \mathbf{C}(t).
\end{aligned}
$$

The Doppler-averaged steady state Bloch vector immediately prior to interaction with the beam is then given by

$$\mathbf{R}_{ss} = \langle A \rangle \sum_{n=0}^{\infty} \left(\langle B \rangle \langle A \rangle \right)^n \langle \mathbf{C} \rangle. \tag{5.51}$$

This can be written in closed form by finding the eigenvector matrix P and the eigenvalues $\lambda_{1,2,3}$ of $\langle B \rangle \langle A \rangle$, and then summing over n to obtain

$$\mathbf{R}_{ss} = \langle A \rangle P \begin{bmatrix} \frac{1}{1-\lambda_1} & 0 & 0 \\ 0 & \frac{1}{1-\lambda_2} & 0 \\ 0 & 0 & \frac{1}{1-\lambda_3} \end{bmatrix} P^{-1}\langle \mathbf{C} \rangle. \tag{5.52}$$

To finally determine the distribution $\mathbf{R}$ in the beam at any given time, we apply

$$\mathbf{R}(v) = \int_0^{\infty} dt_b r_b e^{-r_b t} A_b(t_b, v)\mathbf{R}_{ss} + \left[I - \int_0^{\infty} dt_b r_b e^{-r_b t} A_b(t_b, v) \right] \mathbf{R}_s(v) \tag{5.53}$$

The measured optical coherence is then obtained by using (5.24), (5.30) and (5.33), and by averaging over v:

$$\rho_{e,b} = \int_{-\infty}^{\infty} dv \frac{e^{-\frac{v^2}{2\sigma_v}}}{\sigma_v \sqrt{2\pi}} \left(\frac{i\alpha(v) - \beta(v)}{\Omega_{\text{EIT}}^2} \right) \times$$

$$[\Omega_p(1 - R_{ss,3}(v)) - \Omega_c(R_{ss,1}(v) - iR_{ss,2}(v))]. \tag{5.54}$$

Although there is no closed analytic form for (5.52) and (5.54), they can be evaluated numerically. For example, using the known experimental parameters as an input, the results of these calculations are compared with measurements in Figure 5.9.
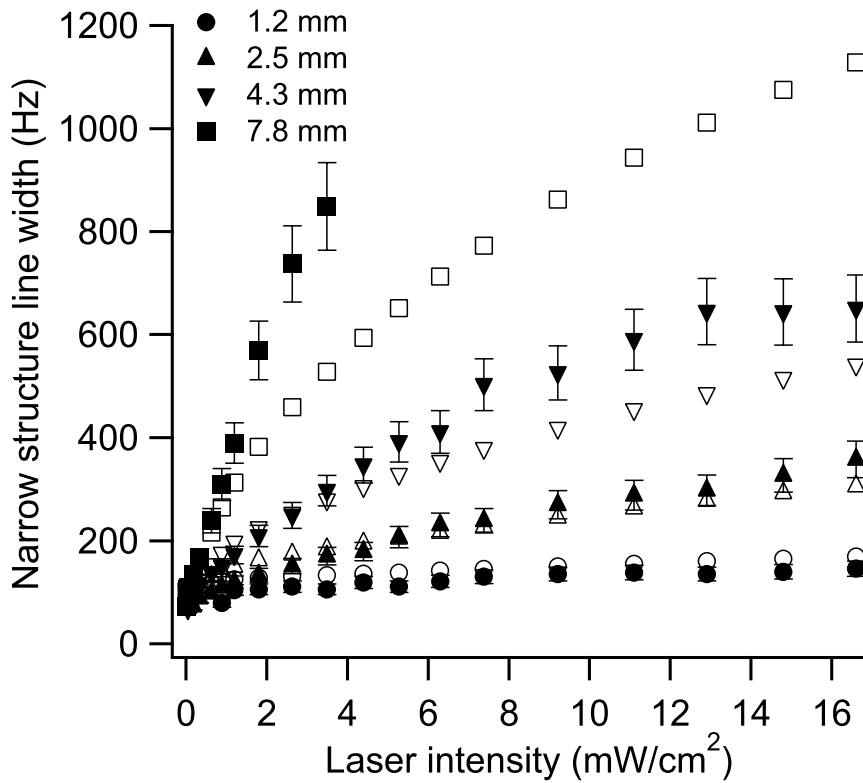
Figure 5.9: Measured (solid symbols) vs predicted (open symbols) ultra-narrow EIT linewidths in a cell with 2.54 cm diameter and various beam diameters with T = 45 °C. Note that this result is obtained with no fit parameters.

Note that although we have good quantitative agreement for the smallest beam di-

ameters, our calculated Ramsey-narrowed bandwidths deviate from the experimental results as the beam diameter and the applied field intensities increase. This remaining discrepancy results from our choosing to approximate the beam interaction time distribution with an exponential. While the exponential distribution has nice algebraic properties, it reaches a maximum at $t = 0$, while the actual time distribution's p.d.f. falls to zero at $t = 0$. This causes our model to underestimate the time atoms spend interacting with the beam, and thus we overestimate the effective lifetime of the atomic coherence. Longer estimated coherence times in turn result in narrower EIT bandwidths. This artifact becomes more pronounced as the beam size is increased and our model more drastically underestimates the fraction of optically pumped atoms exiting the beam, although the approximate model's predictions converge with the exact solution as the narrow transmission peak approaches saturation. Although our limited laser power prevented us from fully saturating the Ramsey-narrowed transmission peak for any but the smallest beams, we expect our model to show better agreement with experiment at higher intensities provided that the beams do not become so large as to produce significant correlations between time spent in the dark and time spent in the beam. (as occurs when $R/r \simeq 1$).

Hyperfine EIT

Doppler effects on Hyperfine EIT can be treated similarly to Zeeman EIT, save that the two-photon Doppler shift must be accounted for. Again, we divide the atomic ensemble into a set of sub-ensembles of atoms in different velocity classes. The internal degrees of freedom evolve as before, but now the basis in which each sub-ensemble is represented is a function of the atomic velocity. Rethermalization on the cell wall mixes these velocity classes, and so the technique described above needs some modification.

To obtain the average Bloch vector after rethermalization on the cell walls, we must express the state of atoms belonging to different velocity classes in a common basis. We choose the $v = 0$ velocity class basis as this common basis. In the spirit of the above treatment, we transform into the specific velocity class basis just before

atoms enter the beam, and transform back into the common basis when they exit. The necessary transformation matrix is given by

$$Q(t,v) = \begin{bmatrix} S^2 + C^2\cos(t\Delta kv) & C\sin(t\Delta kv) & SC\left[1 - \cos(t\Delta kv)\right] \\ -C\sin(t\Delta kv) & \cos(t\Delta kv) & S\sin(t\Delta kv) \\ SC\left[1 - \cos(t\Delta kv)\right] & -S\sin(t\Delta kv) & C^2 + S^2\cos(t\Delta kv) \end{bmatrix}, \quad (5.55)$$

which is simply the evolution matrix $A_d(t)$ with no loss and Δkv standing in for the two-photon detuning, where Δkv is the two-photon Doppler shift. After interacting with the beam for time t_1, the rotation necessary to convert to the $v = 0$ basis is supplied by $Q(t_1, -v)$. To transform into the appropriate Doppler-shifted basis after evolution in the dark for time t_2, we need only apply $Q(t_2, v)$. To calculate the steady state of the atomic ensemble immediately after exiting the beam, we adapt equation (5.51):

$$\mathbf{R}_{ss} = \sum_{n=0}^{\infty} \left[\int_{-\infty}^{\infty} dv \langle B(v)\rangle \langle A(v)\rangle \right]^n \int_{-\infty}^{\infty} dv' \langle \mathbf{C}(v')\rangle, \quad (5.56)$$

where

$$\langle A(v)\rangle = \int_0^{\infty} dt\, \frac{\sqrt{\pi}e^{-\sqrt{\frac{\pi}{2}}\frac{t}{\tau_d}}}{\sqrt{2}\tau_d} Q(t,v)A_d(t) \quad (5.57)$$

$$\langle B(v)\rangle = \int_0^{\infty} dt\, \frac{\sqrt{\pi}e^{-\sqrt{\frac{\pi}{2}}\frac{t}{\tau_b}}}{\sqrt{2}\tau_b} Q(t,-v)A_b(t,v) \quad (5.58)$$

$$\langle \mathbf{C}(v)\rangle = \int_0^{\infty} dt\, \frac{\sqrt{\pi}e^{-\sqrt{\frac{\pi}{2}}\frac{t}{\tau_b}}}{\sqrt{2}\tau_b} Q(t,-v) \times \left[I - A_b(t,v)\right] \mathbf{R}_s(v). \quad (5.59)$$

Equation (5.56) can be evaluated by finding the eigenvector matrix P and the eigenvalues $\lambda_{1,2,3}$ of $\int_{-\infty}^{\infty} dv \langle B(v)\rangle \langle A(v)\rangle$, as was done in equation (5.52). We obtain the distribution of states within the beam from

$$\mathbf{R}(v) = \langle B(v)\rangle \langle A(v)\rangle \mathbf{R}_{ss} + \langle \mathbf{C}(v)\rangle. \quad (5.60)$$

The optical coherence is obtained from this distribution by application of equation (5.54). Owing to the drastically reduced contrast of ultra-narrow hyperfine EIT resonances, due in part to the effective dephasing mechanism described above, relevant experimental tests of the hyperfine EIT resonance analogous to those presented in Figure 5.9 have not yet been completed.

5.3   A Coated Cell Beamsplitter

Inspired by this understanding of the properties of EIT in anti-relaxation coated cells, a recent experiment [170] demonstrated that coherent slow light excitations can be controllably transferred between two distinct transverse modes defined by a pair of control laser fields passing through the same wall-coated Rb vapor cell (see Figure 5.10).   In this section, we address the question as to whether anti-relaxation coated cells, in the idealized limit, may perform the same function as an ordinary beamsplitter. That is, whether the quantum state of an arbitrary input field can be controllably and reversibly mapped into the same superposition state produced by passing a similar field through a partially-reflecting mirror. If so, then future advances in anti-relaxation coating technology could lead to the development of all-optically reconfigurable routers and interferometers for quantum states of light. Such devices would greatly improve the efficiency with which highly entangled states could be generated [197,198], and would vastly reduce the number of optical components necessary to carry out certain probabilistic quantum computation schemes [199–203]. We use an analytic model in conjunction with Monte-Carlo simulations to demonstrate that a cell with an idealized anti-relaxation coating can in principle mimic the action of a conventional beamsplitter, provided that the atoms pass through a region in which their coherence may rapidly accumulate an extra phase as they travel from one beam to another. We show that this added phase is necessary if all of the input light is to be split equally between two output modes while preserving unitarity. In the idealized limit that photons propagate through the cell more slowly than the atoms can move from one transverse mode to another, we present one-photon Monte-Carlo simulations involving up to $N = 10,000$ spins demonstrating these effects.

5.3.1   The Beamsplitter Map

Before we turn to the physics of anti-relaxation coated cells, we first briefly summarize the important properties of a conventional beamsplitter. As can be straightforwardly demonstrated in the classical limit [204], the phase of an electromagnetic
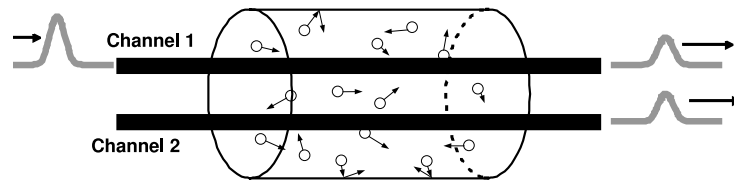
(a) Schematic of coated cell slow light beamsplitter
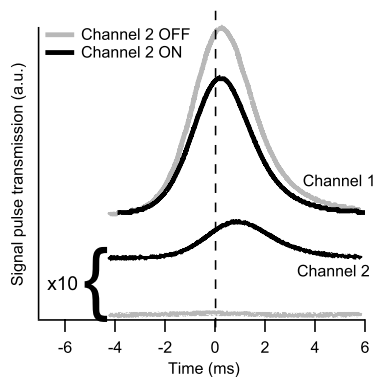
(b) Examples of signal pulse output in the two channels with Ch. 2 control beam on and off
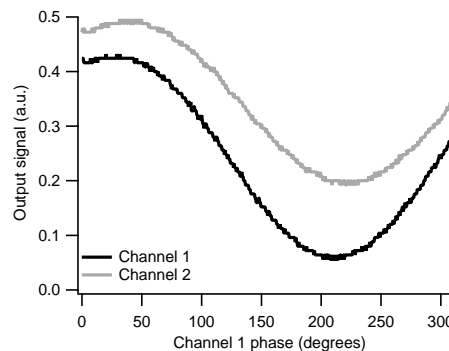
(c) Demonstration of phase coherence between signal pulse output in the two channels

Figure 5.10: (a) Representation of an anti-relaxation coated cell beamsplitter. Two input/output modes are established by a pair of mutually phase coherent "control" fields with identical polarizations. A weak "probe" pulse with orthogonal polarization is introduced along one of these input modes, coherently coupled to the atomic ensemble in the coated cell by EIT, and ultimately split between both outputs by classical transport of the atoms' coherence throughout the cell. Also shown are measurements demonstrating transfer (b) of a slow light pulse from one optical channel to another in an anti-relaxation coated cell, and (c) demonstrating that the relative phase between the signal field in channel 2 and the channel 2 control field is controlled by the phase between the signal field in channel 1 relative to the channel 1 control field. [Y. Xiao, M. Klein, M. Hohensee, L. Jiang, D. F. Phillips, and R. L. Walsworth, *Phys. Rev. Lett.* **101**, 043601 (2008) ©2008 by the American Physical Society]

wave reflected from a dielectric surface is in general different than the phase of the transmitted component. This phase shift extends to the quantum limit, where we may write the input–output operator relations for an ideal, 50/50 beamsplitter as

$$a_{1,\text{out}} = \frac{1}{\sqrt{2}}(a_{1,\text{in}} + ia_{2,\text{in}})$$
$$a_{2,\text{out}} = \frac{1}{\sqrt{2}}(a_{2,\text{in}} + ia_{1,\text{in}}).$$

(5.61)

These relations give rise to the well known photon-bunching effect. Given an input superposition state of photons $|1_{1,\text{in}}, 1_{2,\text{in}}\rangle = a_1^\dagger a_2^\dagger |0\rangle$, we may use (5.61) to find that the output state becomes

$$a_{1,\text{in}}^\dagger a_{2,\text{in}}^\dagger |0\rangle \rightarrow \frac{1}{2}(a_{1,\text{out}}^\dagger + ia_{2,\text{out}}^\dagger)(a_{2,\text{out}}^\dagger + ia_{1,\text{out}}^\dagger)$$
$$= \frac{i}{\sqrt{2}}\left(|2_{1,\text{out}}, 0_{2,\text{out}}\rangle + |0_{1,\text{out}}, 2_{2,\text{out}}\rangle\right).$$

(5.62)

Note that this phenomenon is closely related to the relative phase between the transmitted and reflected components of the incident light, as well as the coherent nature of the interaction. In what follows, we shall see that merely demonstrating coherent interactions between a pair of optical modes in a coated-cell "beamsplitter" is not itself sufficient for the system to mimic the action of a true beamsplitter. We will find that even in the idealized limit, obtaining good balanced transmission efficiency and the proper output phase relation depends strongly on our ability to control the phase accumulation rate of the atomic ensemble *between* interactions with the optical modes.

5.3.2 Single Photon Model

We begin with an ensemble of N three-level Λ-systems, coupled by two fields Ω_c and $\mathcal{E}$, as shown in Figure 5.11. Assuming that the field Ω_c is sufficiently strong to optically pump all atoms in state $|a\rangle$ into $|b\rangle$, that $\mathcal{E} \ll \Omega_c$, and that the fields evolve adiabatically, we may treat Ω_c semiclassically, while the atoms and the probe field $\mathcal{E}$ retain their characteristics as quantum operators. We begin with an idealized version of the coupling of the dark state polariton $\mathcal{E}$ to the atomic ensemble $S = \sum_j \sigma_{a,b}^j$

$$H(\vec{\alpha}) = -S^\dagger(\vec{\alpha})\mathcal{E} - \mathcal{E}^\dagger S(\vec{\alpha}),$$

(5.63)
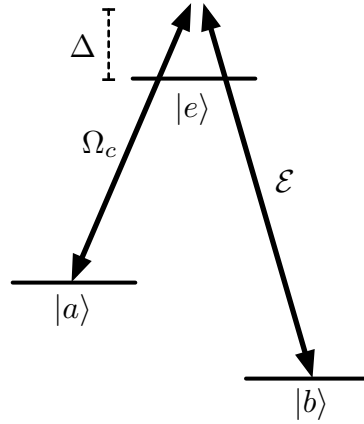
Figure 5.11: The three-level system under consideration for realizing an anti-relaxation coated cell beamsplitter. A strong field Ω_c couples the grond state $|a\rangle$ to the excited state $|e\rangle$, while a weaker probe field $\mathcal{E}$ couples to the $|b\rangle \leftrightarrow |e\rangle$ transition. The Ω_c field is treated semiclassically, while the weaker $\mathcal{E}$ field is treated quantum mechanically in the absence of dissipative losses. Both fields are assumed to be equally detuned by Δ from the one-photon resonance.

where

$$\left[\mathcal{E}, \mathcal{E}^\dagger\right] = 1, \qquad S^\dagger(\vec{\alpha}) = \sum_{j=1}^{N} \alpha_j^* \sigma_{a,b}^j \qquad S(\vec{\alpha}) = \sum_{j=1}^{N} \alpha_j \sigma_{b,a}^j, \qquad (5.64)$$

with $\sigma_{a,b}^j = |a\rangle\langle b|$ for the jth atom, and $|\vec{\alpha}|^2 = d_0|\Omega_c|^2/\Delta^2$, where d_0 is the optical thickness of the atomic ensemble to the $\mathcal{E}$ field. This Hamiltonian may be derived from (5.6) by adiabatic elimination of the optical coherences in the unsaturated limit. The anti-relaxation coating preserves the coherence of the atomic ground states over long periods of time and hence across many interactions with the fields. Thus a faithful representation of the system requires us to take note of the fact that only a fraction of the total ensemble is coupled to the fields at any given time, and that the assemblage of atoms making up that fraction changes randomly in time. These dynamics are captured by the coupling vector $\vec{\alpha}$, which is nonzero only for those indices corresponding to atoms inside the field interaction volume. This is in contrast to the usual situation in which all N atoms in the ensemble are assumed to couple to the fields at the same time and in the same way for the duration of the experiment.

5.3.3   Evolution For a Single Optical Mode

To determine the system's time evolution, we need to evaluate

$$U^\dagger(\vec{\alpha}, t)\mathcal{E}U(\vec{\alpha}, t), \qquad \text{and} \qquad U^\dagger(\vec{\alpha}, t)S(\vec{\beta})U(\vec{\alpha}, t), \qquad (5.65)$$

where $U(\vec{\alpha}, t) = e^{-iH(\vec{\alpha})t}$. Note that the rapid (compared to the field evolution) redistribution of the atomic ensemble within the anti-relaxation coated cell makes it necessary to calculate the effects of (5.63) on arbitrary $S(\vec{\beta})$. Using the Campbell-Baker-Hausdorff (CBH) theorem [205],

$$e^{-\lambda G}Ae^{\lambda G} = \sum_{n=0}^{\infty} \frac{\lambda^n}{n!}C_n, \quad \text{where} \quad C_n = [G, C_{n-1}], \quad \text{and} \quad C_0 = A, \quad (5.66)$$

we can determine the unitary evolution of the Heisenberg operators $\mathcal{E}$ and $S(\vec{\alpha})$. The relevant commutators are given by

$$[H(\vec{\alpha}), \mathcal{E}] = S(\vec{\alpha}), \quad \text{and} \quad [H(\vec{\alpha}), S(\vec{\alpha})] = -\left[S^\dagger(\vec{\alpha}), S(\vec{\alpha})\right]\mathcal{E} = |\vec{\alpha}|^2\mathcal{E}, \quad (5.67)$$

where we have assumed that the vast majority of the atoms are in state $|b\rangle$ and that $N \gg \langle\mathcal{E}^\dagger\mathcal{E}\rangle$, so that we may ignore finite-size effects [206]. Using the CBH theorem, we note that if $\lambda = -it$, and $C_0 = \mathcal{E}$, then

$$\begin{aligned}
C_1 &= S(\vec{\alpha}) & C_2 &= |\vec{\alpha}|^2\mathcal{E} \\
C_3 &= |\vec{\alpha}|^2 S(\vec{\alpha}) & C_4 &= |\vec{\alpha}|^4\mathcal{E} \\
C_{n,\text{odd}} &= |\vec{\alpha}|^{n-1}S(\vec{\alpha}) & C_{n,\text{even}} &= |\vec{\alpha}|^n\mathcal{E},
\end{aligned} \qquad (5.68)$$

so that

$$U^\dagger(\vec{\alpha}, t)\mathcal{E}U(\vec{\alpha}, t) = \left(\sum_{n,\text{even}} \frac{(-it|\vec{\alpha}|)^n}{n!}\mathcal{E}\right) + \left(\frac{1}{|\vec{\alpha}|}\sum_{n,\text{odd}} \frac{(-it|\vec{\alpha}|)^n}{n!}S(\vec{\alpha})\right). \qquad (5.69)$$

For the evolution of the atomic ensemble, we take $C_0 = S(\vec{\beta})$, and then evaluate

$$\left[H(\vec{\alpha}), S(\vec{\beta})\right] = -\mathcal{E}\left(\sum_j \alpha_j^* \sigma_{a,b}^j \sum_k \beta_k \sigma_{b,a}^k\right), \qquad (5.70)$$

which reduces to

$$\mathcal{E}\sum_{j,k} \alpha_j^* \beta_k \left(\sigma_{b,b}^j - \sigma_{a,a}^j\right)\delta_{j,k} = (\vec{\alpha}^* \cdot \vec{\beta})\mathcal{E}, \qquad (5.71)$$

where we have again neglected the contributions of state $|a\rangle$. Thus for $C_0 = S(\vec{\beta})$, we find that for $n \geq 1$,

$$C_{n,\text{odd}} = |\vec{\alpha}|^{n-1}(\vec{\alpha}^* \cdot \vec{\beta})\mathcal{E} \qquad C_{n,\text{even}} = |\vec{\alpha}|^{n-2}(\vec{\alpha}^* \cdot \vec{\beta})S(\vec{\alpha}). \qquad (5.72)$$

Therefore

$$U^\dagger(\vec{\alpha},t)S(\vec{\beta})U(\vec{\alpha},t) = S(\vec{\beta}) - \frac{\vec{\alpha}^* \cdot \vec{\beta}}{|\vec{\alpha}|^2}S(\vec{\alpha}) + \frac{\vec{\alpha}^* \cdot \vec{\beta}}{|\vec{\alpha}|^2}\left(\sum_{n,\text{even}}\frac{(-it|\vec{\alpha}|)^n}{n!}\right)S(\vec{\alpha})$$
$$+ \frac{\vec{\alpha}^* \cdot \vec{\beta}}{|\vec{\alpha}|}\left(\sum_{n,\text{odd}}\frac{(-it|\vec{\alpha}|)^n}{n!}\right)\mathcal{E}. \qquad (5.73)$$

From the definition of $S(\vec{\alpha})$, we note that

$$S(\vec{\alpha}) + S(\vec{\beta}) = S(\vec{\alpha} + \vec{\beta}), \qquad \eta S(\vec{\alpha}) = S(\eta\vec{\alpha}), \qquad \text{and} \quad \eta^* S^\dagger(\vec{\alpha}) = S^\dagger(\eta\vec{\alpha}). \qquad (5.74)$$

Using (5.74), the action of the evolution operator reduces to

$$U^\dagger(\vec{\alpha},t)\mathcal{E}U(\vec{\alpha},t) = \mathcal{E}\cos(|\vec{\alpha}|t) - i\frac{\sin(|\vec{\alpha}|t)}{|\vec{\alpha}|}S(\vec{\alpha}) \qquad (5.75)$$

$$U^\dagger(\vec{\alpha},t)S(\vec{\beta})U(\vec{\alpha},t) = S\left(\vec{\beta} - \vec{\alpha}\frac{\vec{\alpha}^* \cdot \vec{\beta}}{|\vec{\alpha}|^2}[1 - \cos(|\vec{\alpha}|t)]\right) - i\frac{\vec{\alpha}^* \cdot \vec{\beta}}{|\vec{\alpha}|}\frac{\sin(|\vec{\alpha}|t)}{}\mathcal{E}. \qquad (5.76)$$

5.3.4   Generalization to Multiple Optical Modes

This result can easily be generalized to an arbitrary number of separated fields passing through the coated cell, *e.g.* $\mathcal{E}_1$, $\mathcal{E}_2$, ..., $\mathcal{E}_n$. Since the nonzero components of the coupling vectors $\vec{\alpha}_1$, $\vec{\alpha}_2$, ..., $\vec{\alpha}_n$ describe disjoint sets provided that the various transverse modes are non-overlapping, $\vec{\alpha}_j \cdot \vec{\alpha}_k = |\vec{\alpha}_j|^2\delta_{j,k}$. This means that the commutators of the multi-mode interaction Hamiltonian given by

$$H(\{\vec{\alpha}_p\}) = \sum_p H(\vec{\alpha}_p), \qquad (5.77)$$

are

$$[H(\{\vec{\alpha}_p\}), S(\vec{\alpha}_k)] = [H(\vec{\alpha}_k), S(\vec{\alpha}_k)], \qquad (5.78)$$

so that the unitary evolution of the system operators is given by

$$U^\dagger\left(\{\vec{\alpha}_p\}, t\right)\mathcal{E}_j\, U\left(\{\vec{\alpha}_p\}, t\right) = \mathcal{E}_j\cos(|\vec{\alpha}_j|t) - i\frac{\sin(|\vec{\alpha}_j|t)}{|\vec{\alpha}_j|}S(\vec{\alpha}_j) \tag{5.79}$$

$$U^\dagger\left(\{\vec{\alpha}_p\}, t\right)S(\vec{\beta})\, U\left(\{\vec{\alpha}_p\}, t\right) = S\left(\vec{\beta} - \sum_p\left[\vec{\alpha}_p\frac{\vec{\alpha}_p^* \cdot \vec{\beta}}{|\vec{\alpha}_p|^2}\left[1 - \cos(|\vec{\alpha}_p|t)\right]\right]\right)$$
$$- i\sum_p\frac{\left(\vec{\alpha}_p^* \cdot \vec{\beta}\right)\sin(|\vec{\alpha}_p|t)}{|\vec{\alpha}_p|}\mathcal{E}_p. \tag{5.80}$$

5.3.5   Monte-Carlo Simulations

We are now equipped to investigate whether the input-output relations for the anti-relaxation coated cell "beamsplitter" can be made to mimic those of a conventional beamsplitter (recall equation (5.61)). In the limit that all atoms have a chance to interact with the fields many times over the fields' characteristic evolution timescale, we expect an input photon to be mapped onto the coherence of the entire ensemble, which then couples symmetrically to both output modes. Thus we might naively expect that the anti-relaxation coated cell could simulate a balanced beamsplitter if the control fields defining the two coupled modes are $\phi = \pi/2$ out of phase with one another. This turns out to be false, since such a situation would imply

$$a^\dagger_{1,\text{in}} \rightarrow \frac{1}{\sqrt{2}}\left(a^\dagger_{1,\text{out}} + e^{i\phi}a^\dagger_{2,\text{out}}\right)$$
$$a^\dagger_{2,\text{in}} \rightarrow \frac{1}{\sqrt{2}}\left(a^\dagger_{2,\text{out}} + e^{-i\phi}a^\dagger_{1,\text{out}}\right) =\rightarrow \frac{e^{-i\phi}}{\sqrt{2}}\left(a^\dagger_{1,\text{out}} + e^{i\phi}a^\dagger_{2,\text{out}}\right), \tag{5.81}$$

so that the beamsplitter produces the same output, up to a global phase, for two different input states. This would violate unitarity, and is thus clearly impossible. In actuality, as is demonstrated by the simulation depicted in Figure 5.12, we find that the balanced output condition only occurs if the final state of the fields is not fully separable from that of the ensemble, so that

$$a^\dagger_{1,\text{in}} \rightarrow \frac{1}{2}\left(a^\dagger_{1,\text{out}} + e^{i\phi}a^\dagger_{2,\text{out}}\right) + \frac{ie^{i\phi}}{\sqrt{2}}S^\dagger$$
$$a^\dagger_{2,\text{in}} \rightarrow \frac{1}{2}\left(a^\dagger_{2,\text{out}} + e^{-i\phi}a^\dagger_{1,\text{out}}\right) - \frac{ie^{-i\phi}}{\sqrt{2}}S^\dagger, \tag{5.82}$$
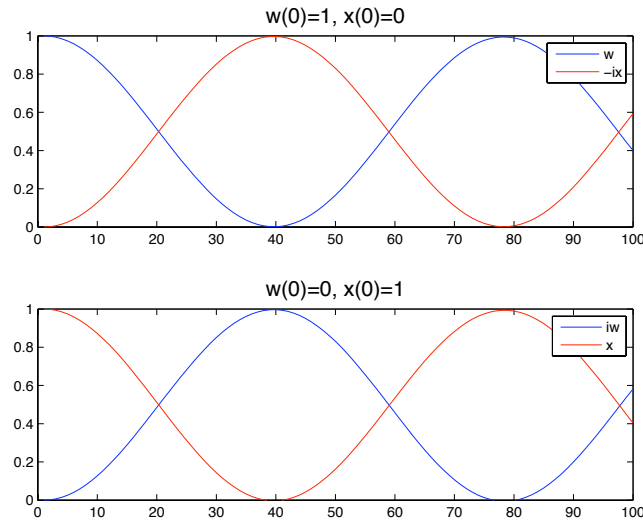
Figure 5.12: Simulation of the photon mode amplitudes $w(t)$ and $x(t)$ in the evolution of the quantum state $|\psi\rangle = \left(w(t)a_1^\dagger + x(t)a_2^\dagger + S^\dagger(\vec{\eta}(t)) \right)|0\rangle$. Here, $N = 1,000$ atoms couple to two optical modes, each of which couples to an average of ~ 22 atoms at a time, with mean coupling strength $\langle|\vec{\alpha}_{j=1,2}|\rangle = 4.6$ Hz. Note that the total probability for an input excitation to be in the optical modes is only 50% when the probability to be in either optical mode is equalized.

where $S^\dagger = \sum_j \sigma_{a,b}^j$ represents the collective spin of the entire atomic ensemble.

This problem can be remedied by the introduction of an additional phase shift applied to atoms while they are between field interactions. Depending upon the cell geometry, such a shift may be produced by the application of a small localized magnetic field gradient, or by light-shifts induced by application of a third, far off-resonant laser to a volume not occupied by the two control fields. The effect of such phase accumulation "in the dark" can be understood in two ways. First, it provides a "one-way" phase shift for photons transferred from one mode to another. As illustrated in Figure 5.13, this more closely mirrors the action of a conventional beamsplitter, which always imparts the same phase of $\pi/2$ to reflected photons. After a sufficiently large one-way phase θ has been accumulated, the amplitude of the ensemble spin excitation may vanish for balanced field outputs without violating
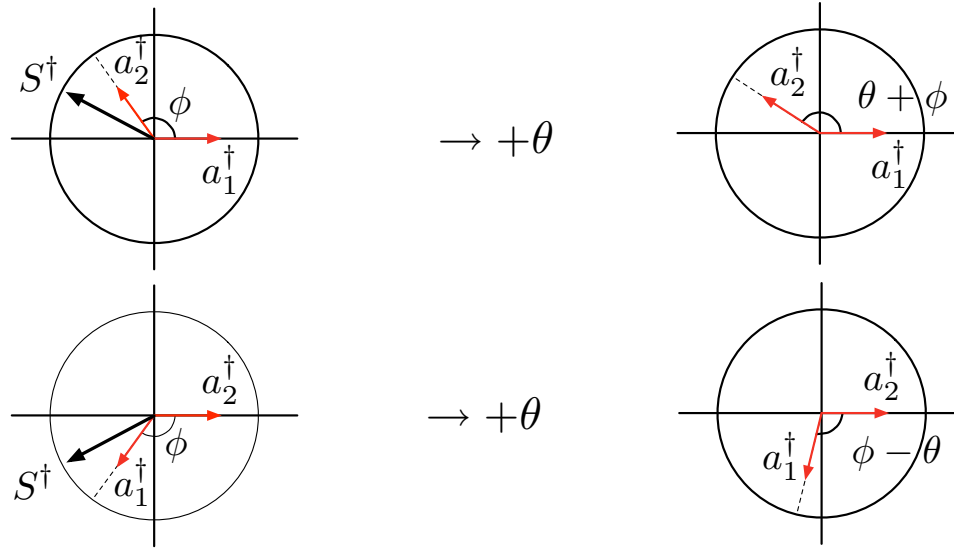
Figure 5.13: Phasor Diagram of Coated Cell Beamsplitter Mode Amplitudes. Left: In the absence of a one-way phase shift for photons transferred between modes by the atomic ensemble, the amplitudes of the output fields balance when the total spin of the atomic ensemble is maximized, as is necessary to preserve unitarity. Right: By adding a mechanism for the atoms to accumulate a phase θ as they travel between the two optical modes, the growth of the $S^\dagger$ amplitude is suppressed. Furthermore, the field component of the system's wavefunction may differ according to which mode was initially excited, so that unitarity may be satisfied for balanced fields which are fully decoupled from the atomic ensemble.

unitarity. The action of the dark phase accumulation can also be understood as a means to suppress spin excitations. As shown in Figure 5.14, the growth of the collective spin excitation is checked as its phase changes relative to that of the driving photon amplitudes. Figure 5.14 also shows that as the dark phase accumulation rate is increased, the phasor plots of the field amplitudes become circularized to the point that the amplitude of the collective spin excitation nearly vanishes. In this limit, the two optical modes behave as if they are directly coupled to one another. Note that these results apply to a very idealized limit. The zero-dimensional simulation shown in Figure 5.14 presumes coherences will survive $> 500,000$ wall-interactions, a figure far in excess of the best performing wall coatings [176]. Future work which extends this zero-dimensional model into one or two-dimensions will be required to properly

(a) $\theta = \frac{7}{10}\pi$

(b) $\theta = \frac{9}{5}\pi$

(c) $\theta = 5\pi$
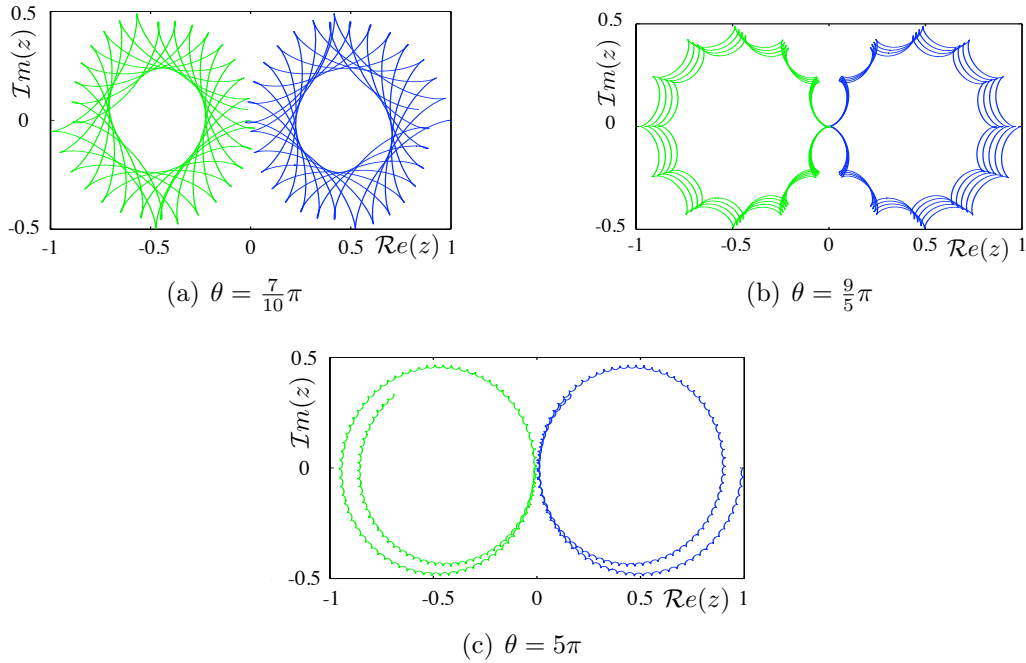
Figure 5.14: Time evolution of the field amplitudes $z(t) = w(t)$ (blue/dark grey on right) and $z(t) = x(t)$ (green/light grey on left) in the complex plane for varying rates of phase accumulation in the dark. All atoms not interacting with the fields accumulate an average phase at rate θ. Initially, $w(0) = 1$ and $x(0) = 0$ for all simulations. $N = 10,000$, with each mode interacting with ~ 250 atoms at any given time, so that $\langle|\vec{\alpha}|\rangle \simeq 125$ Hz, with the mean time atoms spend in the beam equal to 1 ms. Total simulated time: 500 s, equivalent to approximately $500,000$ "passages" across the confining vapor cell.

determine the conditions under which a coated-cell beamsplitter may practically be realized.

This system also displays an intrinsic inhomogeneous dephasing due to variations in the amount of time that each atom spends interacting with the fields and in the dark, as indicated in Figure 5.15. Although the Rabi oscillations of the spin excitation are suppressed by increasing θ, the mean rate of inhomogeneous dephasing is not. The impact of this particular dephasing mechanism may be worth considering in future work on optimizing anti-relaxation coated cells for use as quantum memories, optical routers, or interferometers.

5.4   Conclusion

We have developed a model of electromagnetically induced transparency in warm atomic vapors in anti-relaxation coated cells. Our model correctly accounts for the classical motion of the atoms and the resulting effects on the collective atomic coherence established and probed by the applied fields, and shows good quantitative agreement with experimental observations for EIT laser fields much smaller than the cell diameter. We have developed a simplified model of how classical motions of an atomic ensemble could be used to coherently couple two distinct transverse optical modes in a manner functionally identical to a conventional optical beamsplitter. This model demonstrates that anti-relaxation coated cells can in principle be used as deterministic optical switches or as interferometers. Both the specific set of coupled modes and the manner in which they are coupled can be controlled all-optically, permitting the path of a coherent state of light through an experimental apparatus to be reconfigured during a single experiment. Note that all-optically configurable optical routers based on anti-relaxation coated cells can be controlled by turning arbitrary sets of control fields on and off, and through control of the rate of the atomic ensemble's phase accumulation in the dark. Although present-day paraffin coatings have do not preserve the atomic coherence of a warm atomic vapor long enough to realize such devices, future improvements in cell coatings may one day change this. If so, then coated cell beamsplitters may be used to significantly enhance the scaling of probabilistic quantum information processing schemes based on linear optics.

(a) $\theta = \frac{7}{10}\pi$

(b) $\theta = \frac{9}{5}\pi$

(c) $\theta = 5\pi$
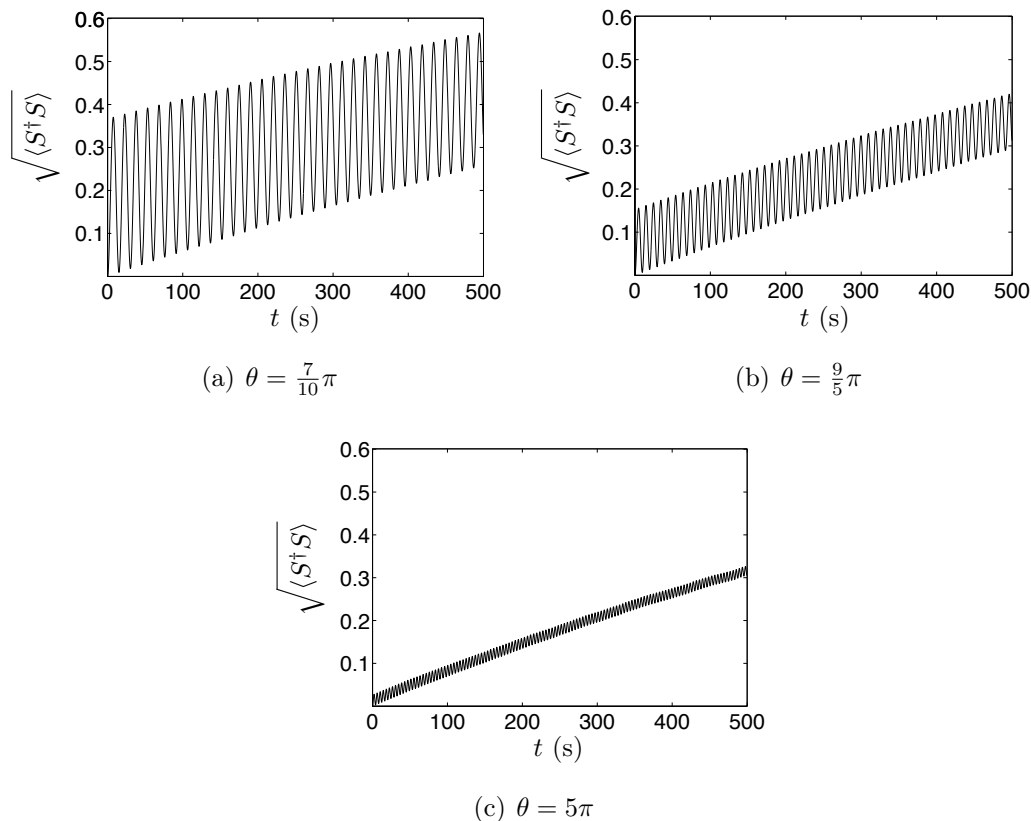
Figure 5.15: Total excitation amplitude $\sqrt{\langle S^\dagger S \rangle}$ of the atomic ensemble as a function of time under conditions identical to those described in Figure 5.14. Coherent couplings between the ensemble and the optical fields drive rabi-oscillations in the total excitation of the ensemble. Although the amplitude of these oscillations is suppressed by increasing the rate at which the ensemble accumulates phase in the dark, the mean ensemble excitation monotonically increases. This residual dephasing is a consequence of the finite variance in the atoms' interaction and return times.

Chapter 6

Novel Means of Stabilizing Compact Atomic Clocks

The widespread adoption of GPS and high-speed wireless communications networks has created significant demand for portable, high precision and high stability clocks. The use of a more precise clock can translate directly into more accurate position readings in GPS applications, or in the case of wireless networks, improved synchronization between nodes and thus the potential for higher communications bandwidth. Improving clock stability would allow precise geolocation in areas in which acquiring the signals from many GPS satellites is problematic, and would be a benefit to high speed wireless communications between mobile base stations in such environments. In either situation, the portability of such systems is of significant importance. These requirements are largely satisfied by modern atomic clocks referenced to a coherent population trapping (CPT) resonance. Such clocks have demonstrated stabilities of up to 10^{-11} at up to 1000 seconds [207], and since they do not require the use of a resonant cavity, can be as made as small as permitted by their supporting electronics [208].

The excellent short term stability exhibited by CPT standards is made possible by the unique symmetries of the CPT resonance. Despite the generally high sensitivity of the CPT resonance to the properties of the driving laser, there exists a fairly broad volume of parameter space in which the manifold laser-induced light shifts cancel

with one another [209]. As a result, random fluctuations of the laser about any given point in the light-shift cancelation regime have minimal impact on the clock frequency, permitting the short-term clock stability to exceed that of the driving laser. Nevertheless, the medium- to long-term stability of such clocks is limited by the degree to which slow drifts in the laser parameters can be constrained. In this study, we examine a potentially useful way to use the CPT resonance itself to limit slow laser fluctuations without compromising the short term clock stability.

Although the light-shift cancelation limit derived by Vanier *et al.* [209] is well known, it is commonly unappreciated that the wide breath of the parameter space suitable for CPT clock operation is due to an additional symmetry [133] between a multitude of individual CPT and asymmetric, 3-photon transitions known as N-resonances [210] excited by sidebands of the interrogating laser. As we experimentally demonstrate, these individual resonances are generally quite sensitive to the properties of the laser, including within the Vanier light shift cancelation regime. In particular, we find that the individual sideband resonances can in some cases coincide with the clock resonance. This means that it should be possible to obtain a clock signal which is insensitive to small laser fluctuations, while simultaneously preventing such fluctuations from developing into long-term drifts by measuring the comparatively sensitive sideband resonance. These early results could provide the basis for the development of CPT clocks with good short- and long-term stabilities.

6.1 Theoretical Background

Coherent population trapping (CPT) is simply another term describing the phenomenon of electromagnetically induced transparency (EIT), as introduced in part 5.1 of this thesis. Although the EIT system is generally isolated from externally varying magnetic fields by multiple layers of magnetic shielding, most atomic frequency standards are based upon the CPT resonance involving only the $m = 0$ ground states shown in Figure 6.1. This is advantageous because the energy difference between these states is insensitive, at first order, to the local magnetic field.
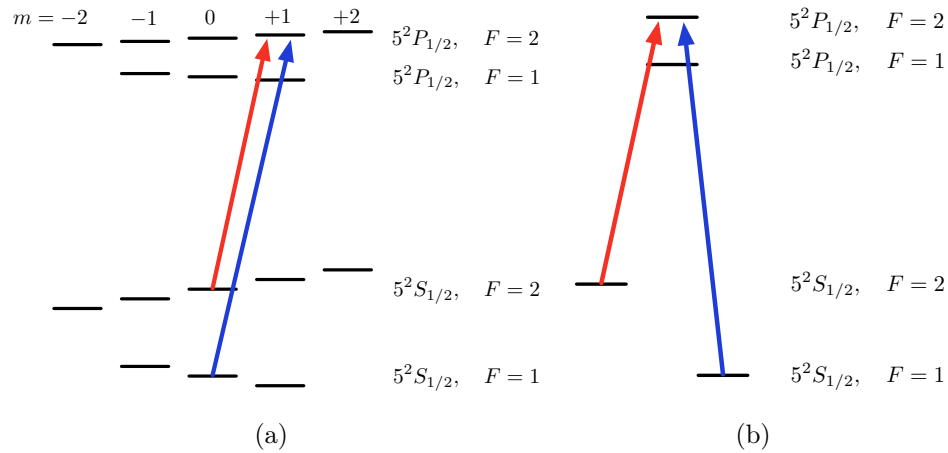
Figure 6.1: Level Diagram of the D_1 Line of ^{87}Rb. The full D_1 line (a) is composed of the optical transitions between the eight $5^2S_{1/2}$ ground states of ^{87}Rb and the eight states in the $5^2P_{1/2}$ excited state manifold. Application of a uniform magnetic field along the quantization axis lifts the three- and five-fold degeneracy of the ground state, isolating transitions involving the $m = 0$ ground states from all others, reducing the system to that depicted in (b).

6.1.1 Operation of an Optical Atomic Clock

As outlined in Figure 6.2, an atomic clock consists of an electronic oscillator whose operating frequency is stabilized by comparing it with the frequency of an atomic transition. The means by which this comparison is made can be simply illustrated by analogy to a clock referenced to the transition of a two-level atom. In such situations, the oscillator is stabilized to the atomic transition frequency ω_0. The output of the oscillator is used to set the frequency of a generated laser field, which is then phase modulated at a much lower frequency ω_1. This phase modulation generates a pair of sidebands with equal amplitude and opposite phase, separated from the carrier by ω_1. This can be understood mathematically by considering the effect of phase modulating a field with carrier frequency ω_0 on the spectrum of the modulated field. Using the Jacobi-Anger Bessel identity, this is

$$E(t) = E_0 e^{i(\omega_0 t + m \cos \omega_1 t)} = E_0 e^{i\omega_0 t} \sum_{n=-\infty}^{\infty} i^n J_n(m) e^{in\omega_1 t}, \tag{6.1}$$
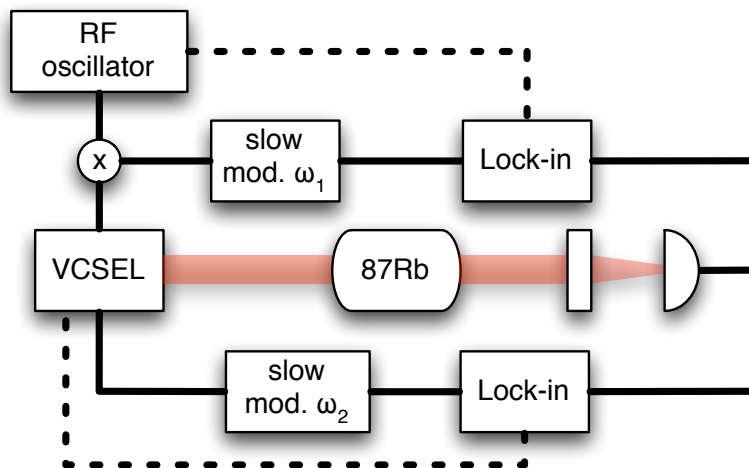
Figure 6.2: Schematic diagram of a passive frequency standard based on a CPT resonance in ^{87}Rb. The output of a radio-frequency (RF) oscillator tuned to ground-state hyperfine splitting of ^{87}Rb is used to phase modulate the output of a Vertical Cavity Surface Emitting Laser (VCSEL). This output light is then used to interrogate a CPT resonance in a warm ^{87}Rb vapor before being collected on a photodetector. Slow ($\omega_1 \lesssim 1$ kHz) modulation of the signal input to the VCSEL from the RF oscillator is mapped by interaction with the CPT resonance into a corresponding amplitude modulation of the observed light, the amplitude and phase of which can be used as an error signal for short-term stabilization of the RF oscillator. The total intensity of the light collected on the photodetector can also be used to stabilize other degrees of freedom for the VCSEL, such as the total power output or one-photon detuning.

where $J_n(m)$ is the nth Bessel function of the first kind, and m is known as the modulation index. This situation is graphically illustrated for $n = 0, \pm 1$ in Figure 6.3(a). The deviation of the oscillator frequency from ω_0 can then be determined by the amplitude and phase of any amplitude modulation which may be detected in the fields after interaction with the two level resonance. Because the relative phase of the two sidebands is π, the beat signal generated by interference between the lower sideband and the carrier is initially canceled by that generated by interference between the carrier and the upper sideband, as must be the case for a signal with no amplitude modulation. This can be inferred formally from (6.1), since the beat is

proportional to the real part of

$$\frac{E(t)E(t)^*}{|E_0|^2} = \sum_{n_1=-\infty}^{\infty} \sum_{n_2=-\infty}^{\infty} i^{n_1-n_2} J_{n_1}(m) J_{n_2}(m) e^{i(n_1-n_2)\omega_1 t}, \tag{6.2}$$

which, taking only the contribution of the $J_1(m)$ and $J_0(m)$ terms to signals at ω_1 into account is

$$
\begin{aligned}
\frac{E(t)E(t)^*}{|E_0|^2} &\simeq \left(-iJ_{-1}(m)e^{-i\omega_1 t} + J_0(m) + iJ_1(m)e^{i\omega_1 t}\right) \\
&\quad \times \left(iJ_{-1}(m)e^{i\omega_1 t} + J_0(m) - iJ_1(m)e^{-i\omega_1 t}\right) \\
&\simeq \left(\frac{J_0(m)^2}{2} + J_1(m)^2 - i\left(J_{-1}(m) + J_1(m)\right)J_0(m)e^{-i\omega_1 t}\right) + h.c.
\end{aligned}
\tag{6.3}
$$

Since the amplitude of the -1 sideband is proportional to $J_{-1}(m)$, and that of the $+1$ sideband is proportional to $J_1(m)$, and $J_{-n}(m) = (-1)^n J_n(m)$, we see that there is no net amplitude modulation at ω_1 in this signal. When such fields are used to probe the absorption resonance of a two level atom as in Figure 6.3(b), the transmitted amplitudes of the two sidebands are reduced. In particular, if the carrier is blue-detuned from the ω_0 resonance, as in Figure 6.3(c), the lower sideband experiences greater absorption than the upper sideband. The result of this absorption imbalance is a net amplitude modulation of the output light at ω_1, since the beat between the upper sideband and the carrier can no longer be fully canceled by that between the carrier and the lower sideband. The same thing happens when the carrier is red-detuned, although the phase of the amplitude modulation will be shifted by π. If the carrier is exactly on the ω_0 resonance, the amplitudes of both sidebands are reduced equally, yielding zero net amplitude modulation, as before. Thus an error signal which can be used to stabilize the frequency of the electronic oscillator to ω_0 is obtained by monitoring the amplitude and phase of any amplitude modulation in the transmitted fields with frequency ω_1.

For clocks referenced to a CPT resonance, the situation is slightly different. In this case, the oscillator output is used to rapidly phase modulate a laser tuned to the D_1 line of an alkali vapor, in this case ^{87}Rb. The carrier frequency is tuned midway between the transitions to the $5^2P_{1/2}, F = 2$ excited state from the $5^2S_{1/2}, F = 1$
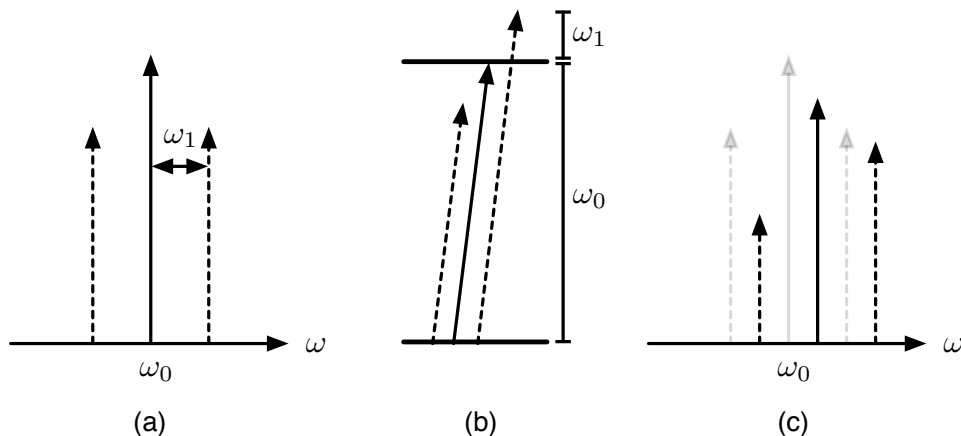
Figure 6.3: (a) First order phase modulated spectrum of a field with carrier frequency ω_0 Note that the vertical axis denotes field amplitude, but not phase, and that the lower (leftmost) sideband is π out of phase with the carrier and the upper (rightmost) sideband. When such modulated fields are used to probe the transition of a two-level system (b), differential absorption of the two sidebands maps the phase modulation into an easily detected amplitude modulation (c).

and $F = 2$ ground states, as illustrated in Figure 6.1(b). As before, this phase modulation generates sidebands around the carrier, shown in Figure 6.4(a) out to second order, separated from the carrier by ω_{rf}. In particular, this generates a pair of first order sidebands separated by $2\omega_{rf} = 6834.68261$ MHz, or roughly the ground state hyperfine splitting of ^{87}Rb. Together, these fields probe the CPT transmission resonance indicated in Figure 6.1(b).

As for our two-level example, deviations of $2\omega_{rf}$ from the CPT resonance are detected by mixing a slower modulation signal at ω_1 with the ω_{rf} output of the clock oscillator, and using the resulting total to phase modulate the laser. Any deviation of $2\omega_{rf}$ from the hyperfine splitting of ^{87}Rb translates into a nonzero two-photon detuning for the CPT system, leading to differential absorption of the slow modulation sidebands, and thus a slow-modulation beatnote whose amplitude and phase may be used to correct ω_{rf}. The detailed properties of CPT resonance atomic frequency standards have been the subject of extensive investigations [207, 209, 211–213].

6.1.2 Stability of CPT Clocks

As shown in [209], the CPT resonance frequency is subject to a variety of external influences. In particular, the sidebands generated by phase modulating the laser can each contribute AC Stark, or light shifts on the CPT resonance. In general, this makes the resonance condition a sensitive function of both the laser's power output and the detuning of the laser's carrier frequency from the one-photon resonance. Fortunately, there exists an operating regime in which the light shift is insensitive to small variations in laser power and detuning. As demonstrated in [207, 209, 213], this regime is reached when the modulation index (m in (6.1)) of the ω_{rf} phase modulation is approximately 1.9. CPT clocks which operate in this regime are thus insensitive to small fluctuations in the laser's power and carrier frequency, and consequently have good stability in the short term. Over longer timescales, however, slow drifts in these parameters cause the lock frequency ω_{rf} to vary, so that regular comparisons with high-accuracy atomic references such as Cesium beam tube clocks, become necessary.

Although CPT clocks have enjoyed good short term stability properties by virtue of operating in the Vanier regime, it is less commonly appreciated that this success is also due to the unique manner in which the slow modulation signal is generated. In contrast to the comparatively simple two-level picture, the CPT clock signal is derived from beats of the slow modulation sidebands arranged about every one of the fast modulation sidebands shown in Figure 6.4(a). This means that the CPT clock signal is the coherent sum of the beat signals generated by probing each of the multi-photon resonances outlined in Figure 6.4(c), which are in general quite asymmetric. These asymmetries are, however, systematically canceled by the overall symmetry of the CPT system: The asymmetric, 3-photon transition known as an N-resonance [210] formed by the carrier, -2 and +1 sidebands is balanced by the resonance formed by the carrier with the +2 and -1 sidebands, etc. Such resonances have also been proposed as the basis of compact atomic clocks [214, 215], and their detailed properties of these resonances can be calculated in a number of ways, two of which are outlined in [216]. For our purposes, we simply note that these asymmetries permit us to experimentally find a stable CPT clock operation regime. This comes

(a) Phase-Modulated CPT Clock Spectrum   (b) Idealized CPT   (c) Realistic CPT
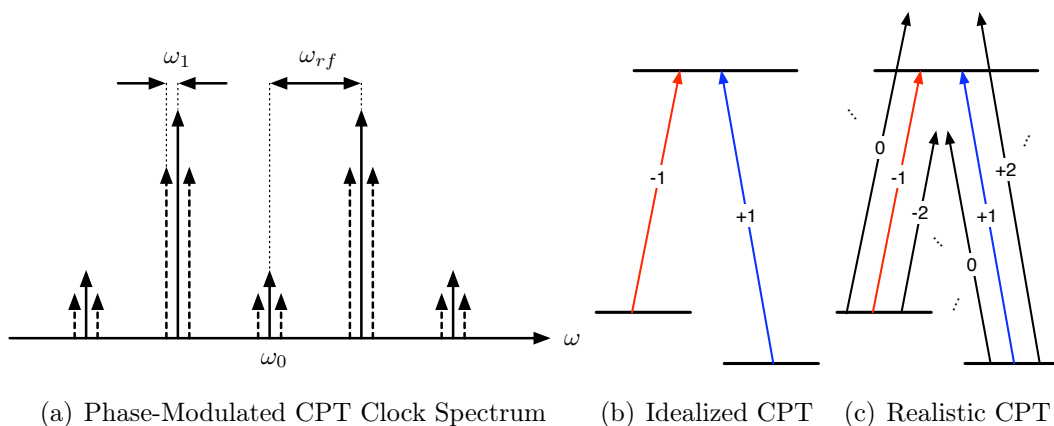
Figure 6.4: Illustration of the field spectrum (a) and simplified atomic level diagrams relevant to the operation of an atomic frequency standard based on a CPT resonance.

despite the inevitable admixture of small amounts of amplitude modulation at ω_{rf} due to imperfections of the VCSEL, which causes the applied amplitudes of the $+1$ and -1 sidebands to be unequal. An example of a simulated Fabry-Perot scan of the spectrum of a phase modulated VCSEL with 0.1% of the total output power derived from amplitude modulation at the same frequency is shown in Figure 6.5.

6.1.3   Isolated Sidebands

Even though we obtain a clock signal by operating in the Vanier stability regime, the detailed source of that clock signal holds out the possibility that by isolating the signal generated by an individual fast modulation sideband, we may obtain useful information about the overall drift in the laser's output power or detuning. An illustration of what these signals may look like is shown in Figure 6.6. This is easily accomplished by passing a portion of the light transmitted through the atomic ensemble through a spectral filter. In particular, we expect that the error signals contributed by the $+1$ and -1 sidebands will vary significantly vs laser detuning and intensity, although their total contribution to the clock signal will be comparatively insensitive, as indicated in Figure 6.7.
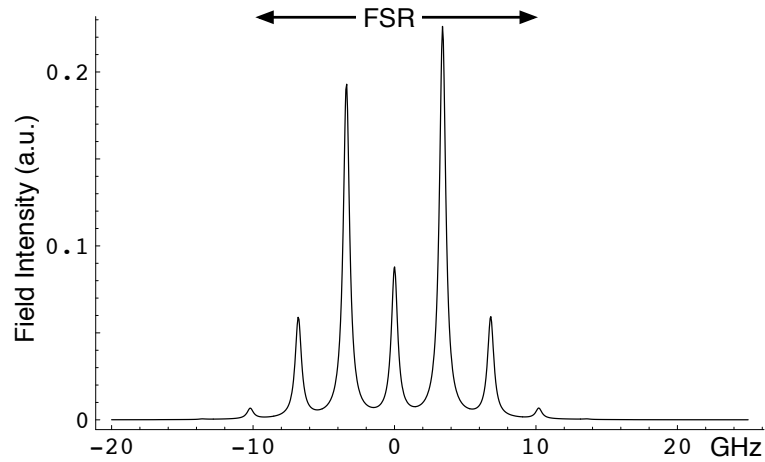
Figure 6.5: Simulated spectrum of a realistically phase-modulated VCSEL, neglecting any slow ω_1 modulation. A fraction of the RF power used to phase modulate the central carrier also gives rise to a small amount of amplitude modulation. In this case, the phase modulation index is 1.8, and the fractional power of the amplitude-modulated component is 0.1%. Superimposed is the 20 GHz free spectral range (FSR) of the temperature stabilized etalon used to isolate individual sidebands, as described in the text.

6.2   Description of Apparatus

As shown in Figure 6.8, the apparatus used to measure the properties of the CPT clock signal is quite similar to what would be required to construct an actual atomic clock. Our experimental setup mainly lacks the final feedback link between the generated clock error signal and the RF oscillator. Instead, we calibrate our oscillators with the external frequency reference provided by a Hydrogen maser. This greatly simplifies the interpretation of our generated error signals.

6.2.1   Oscillator and Signal Generation

The 3417.34584 MHz RF signal is generated by an HP 83732 frequency synthesizer, referenced to the 10 MHz output of a Hydrogen maser. This signal is modulated by the comparatively low-frequency (800 Hz) output of a SR 830 lock-in amplifier, itself referenced to the 10 MHz maser signal, before being used to modulate the laser. The

(a) Sideband Resonances

(b) Sideband Resonances and Clock Resonance
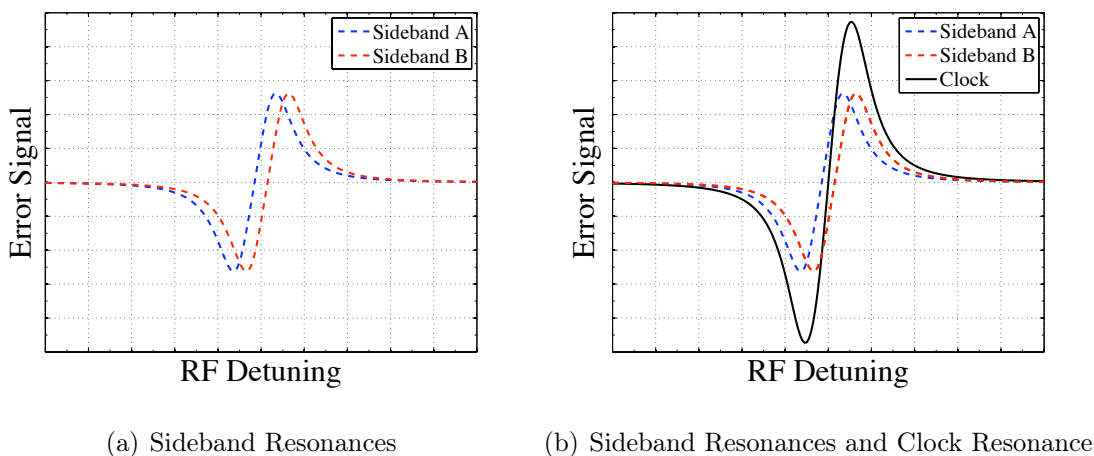
Figure 6.6: Representation of (a) the expected beat-note signals generated by probes of the two sideband resonances (for sidebands A and B), and the shape of the resultant "clock" signal formed from their sum. Provided that the two sidebands are shifted in opposite directions by any given perturbation of the applied laser's properties, the center frequency of the clock resonance can remain unaffected.

laser fields are generated by a vertical-cavity surface-emitting laser (VCSEL) diode of only slightly questionable provenance which emits a field at 795 nm with 100 MHz bandwidth, and a peak power output of approximately 0.5 mW. The carrier frequency emitted by the VCSEL is extremely sensitive to the diode temperature. To maintain a fixed carrier frequency output, we use a dichroic atomic-vapor laser lock (DAVLL) loop [217] to control the power delivered to a combination peltier cooler and resistive heater built into the circuit board housing the VCSEL. The DAVLL is constructed using a passively heated vacuum cell containing a natural abundance mixture of ^{87}Rb and ^{85}Rb. The error signal produced by the DAVLL is fed into a Linear Research 130 temperature controller which in turn drives the VCSEL temperature control system.

6.2.2 Magnetic Shields, Bias Solenoid, and Vapor Cell

The atomic reference consists of a pyrex vapor cell containing a small amount of isotopically pure ^{87}Rb along with 22 Torr of Ne serving as a buffer gas. The cell is housed within three cylindrical high permeability magnetic shields. These shields
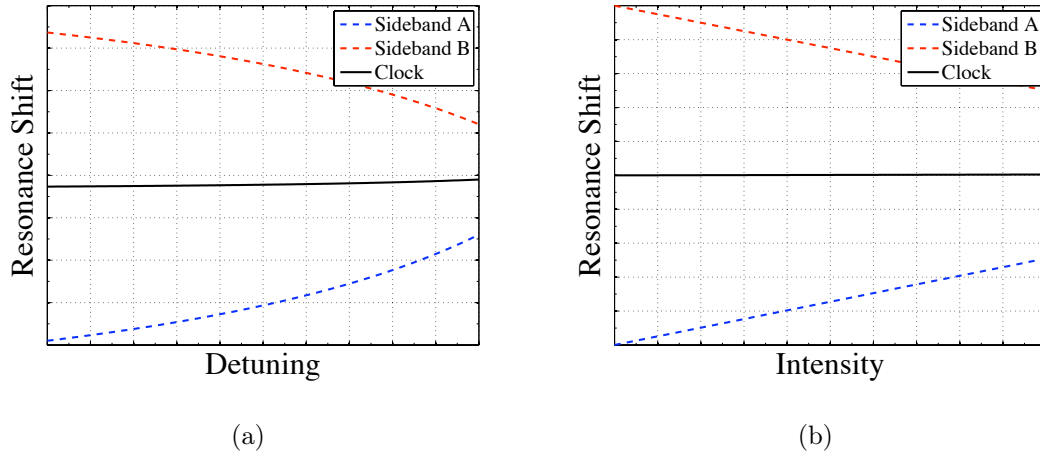
Figure 6.7: Illustration of the expected variation of the sideband resonances vs. carrier detuning (a) and overall field intensity (b). In each case, information about the detuning or field intensity can be obtained from the behavior of the sideband resonances in regimes where the clock signal is comparatively insensitive to such variations.

are made of metal with high magnetic permeability. The magnetic domains of these shields easily align counter to the local magnetic fields generated by the Earth and nearby equipment, and effectively cancel the effects of such fields in the volume the shields enclose. Despite the comparative mobility of these magnetic domains, the shields must be degaussed after significant changes in the local field environment have occurred, after experiencing large temperature variations, or otherwise mechanically disturbed. This is accomplished by sending large amounts of electric current ($\sim$ 200 A) through a cable passing through the innermost set of shields, and smoothly reducing this current to zero.

The cell temperature is regulated by a resistive heater in the form of a counter-wound solenoid placed about the innermost magnetic shield in conjunction with a resistance thermometer (RTD) affixed to the side of the vapor cell. Any magnetic fields generated by the heating solenoid are thus limited by both its counter-wound geometry and the innermost shield. An approximately uniform magnetic field is generated by a solenoid located immediately inside the innermost magnetic shield. The uniformity of the field generated by this solenoid in the vicinity of the vapor
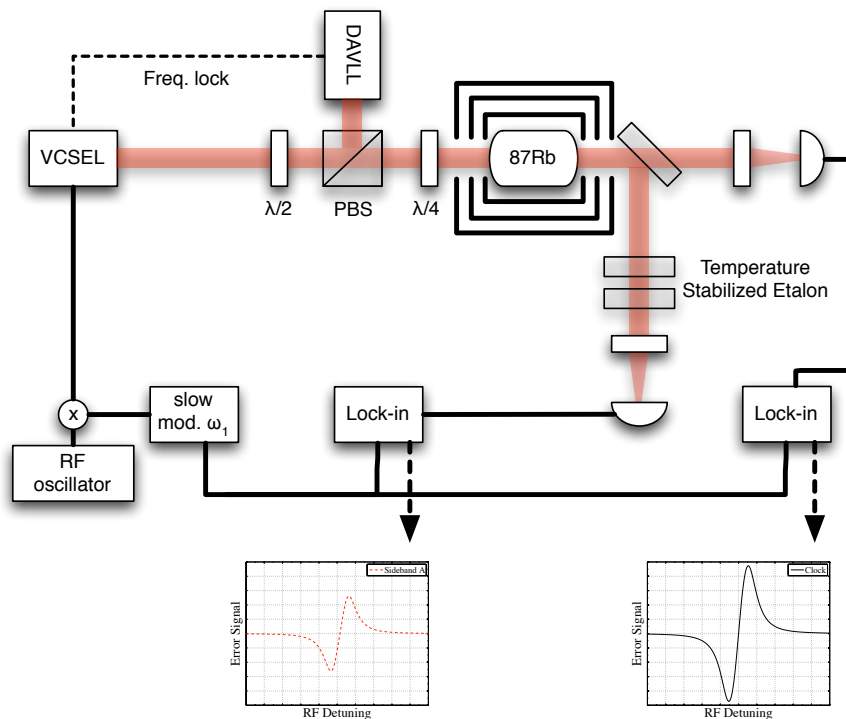
Figure 6.8: Experimental apparatus for simultaneous measurement of the properties of arbitrary sideband or full CPT clock resonances.

cell is improved by the field generated by an additional pair of smaller coils located at either end of the main solenoid. For all measurements reported here, the current through the solenoids was selected so as to separate the $m = 0$ resonance from the $m = \pm 1$ resonances by approximately 30 kHz.

6.2.3   Temperature Stabilized Etalon

To isolate the signals generated by individual sidebands, we pass a portion of the light that has interacted with the atomic ensemble through a temperature stabilized etalon. This is comprised of a 5 mm disc of glass mounted in the center of a cylindrical aluminum frame, and protected from direct contact with the outside atmosphere by a pair of anti-reflection coated windows at each end of the cylinder. The cylinder rests upon a thermo-electric cooler used to control its overall temperature, and is surrounded by felt insulation. The etalon temperature is measured by an RTD mounted

in a hole drilled in the edge of the cylinder. This yields an etalon with a free spectral range (FSR) of approximately 20 GHz, with a finesse of about 30. As indicated on Figure 6.5, the 20 GHz FSR is larger than the modulated spectrum of the VSCEL, greatly simplifying our experimental analysis. Note that the 670 MHz bandwidth of the etalon resonance is broad compared with the 100 MHz VCSEL linewidth, reducing the impact of any fluctuations in the etalon resonance due to temperature or vibrational disturbances.

6.3   Results

For our first measurements, we used a beam with an approximately gaussian profile which was approximately 2 mm in diameter. This beam size was selected as being both small enough to allow sufficient intensity for significant power broadening of the CPT resonance, and large enough to avoid the undesirable effects of steep transverse intensity gradients [218]. As shown in Figures 6.9(a) and 6.9(b), we find that both the $+1$ and -1 sideband resonances (*i.e.* , the zero crossings) are offset from one another and from the clock resonance. The variation of the center frequencies of these resonances with input laser power shown in Figure 6.10 is particularly striking. In particular, we notice that both of the sideband resonances trend towards the overall clock resonance with increasing laser power. Figure 6.11 portrays the shifts in the sideband and clock resonances as the amount of power driving the VCSEL's phase modulation is varied.

In an effort to determine how closely these resonances approach the clock resonance, or even whether they may overlap at some point, we reduced the beam diameter to 1 mm so as to explore the resonances at higher intensities. As shown in Figure 6.12, we observe the same sort of behavior here as in the 2 mm beam, although the distorted shape of the entire error signal resonance observed here is indicative of our approach to the "peaky" EIT regime described in [183, 218]. As the applied laser power is increased, we find that there are indeed intensities at which the ± 1 sideband resonances individually coincide with the clock resonance, as shown in FIgure 6.12. This coincidence is possible because the clock signal is derived from contributions

(a) Clock Resonance

(b) ±1 Sideband Resonances
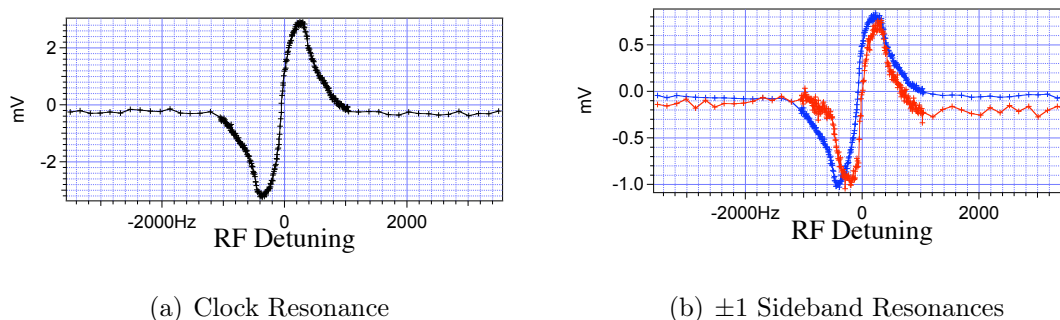
Figure 6.9: (a) The error signal derived from the CPT resonance in a regime typical of where CPT clocks operate *i.e.* with modulation index ~ 2 and with intensity sufficient to moderately power-broaden the resonance. (b) Measured error signal resonance for the -1 sideband (red/lighter grey) and the $+1$ sideband (blue/darker grey) under the same conditions, with the $+1$ sideband taken simultaneously with the data in (a). RF detuning is measured relative to 3417.34584 MHz. Total power $= 120$ μW, in ^{87}Rb vapor cell with 22 Torr of Ne buffer gas at 51 °C, corresponding to a ^{87}Rb density of approximately 1.1×10^{11} cm^{-3}.

from *all* fast modulation sideband resonances (*e.g.* , ± 2, ± 3, . . .), and not merely the sum of the ± 1 sidebands. We note that the overlaps between the sideband and clock resonances shown in Figure 6.13 occur at lower overall laser powers as the phase modulation is increased. This occurs because in our particular operating regime, higher phase modulation translates to a larger proportion of the incident laser power being diverted into the higher order sidebands, making the overall clock signal more dependent on their contributions, and proportionately less dependent on the sum of the ± 1 sidebands.

6.4   Summary

We have experimentally demonstrated that the isolated sideband resonances which contribute to the total error signal of a CPT clock are generally quite sensitive to the properties of the driving laser, despite the fact that the total sum of such signals can be comparatively insensitive. Although further work will be required to use these phenomena to stabilize an actual clock, these early results are quite promising.

(a) −1 Sideband Resonance

(b) +1 Sideband Resonance
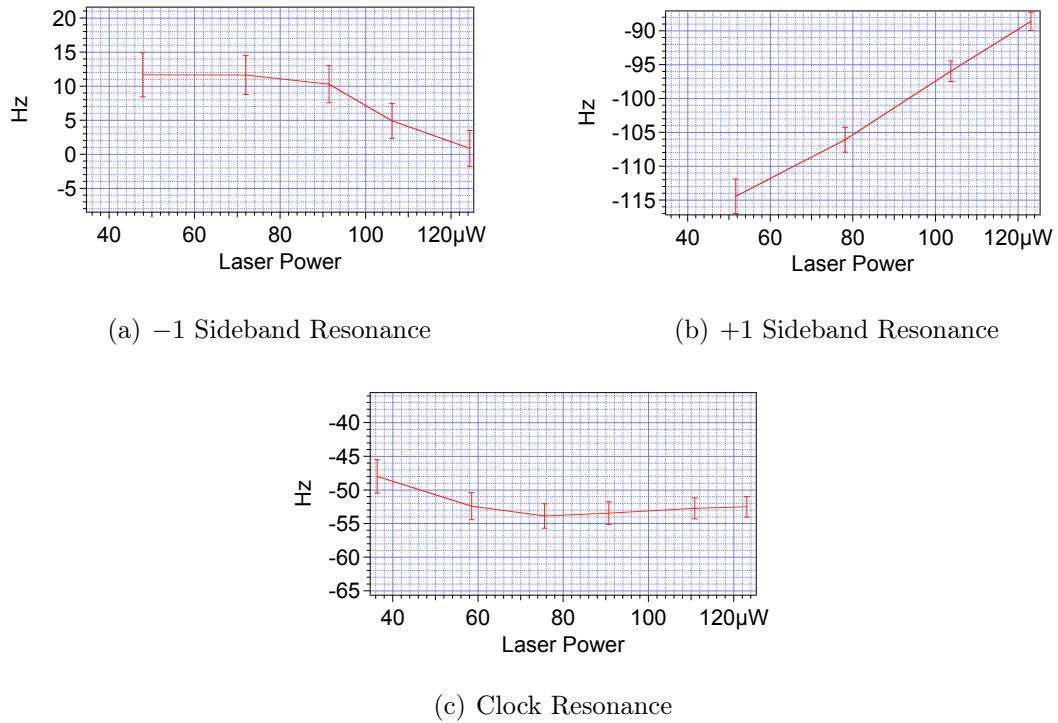
(c) Clock Resonance

Figure 6.10: Measured resonance shifts for ±1 sidebands and CPT clock resonance vs. laser power at modulation index ∼ 2. Data taken with a 2 mm beam, in a ^{87}Rb vapor cell with 22 Torr of Ne buffer gas at 51 °C, corresponding to a ^{87}Rb density of approximately 1.1×10^{11} cm^{-3}. Higher power RF signals correspond to higher modulation indices.

In particular, the observed crossing of the +1 sideband resonance with the overall clock resonance suggests a good operating point at which both resonances may be simultaneously locked.
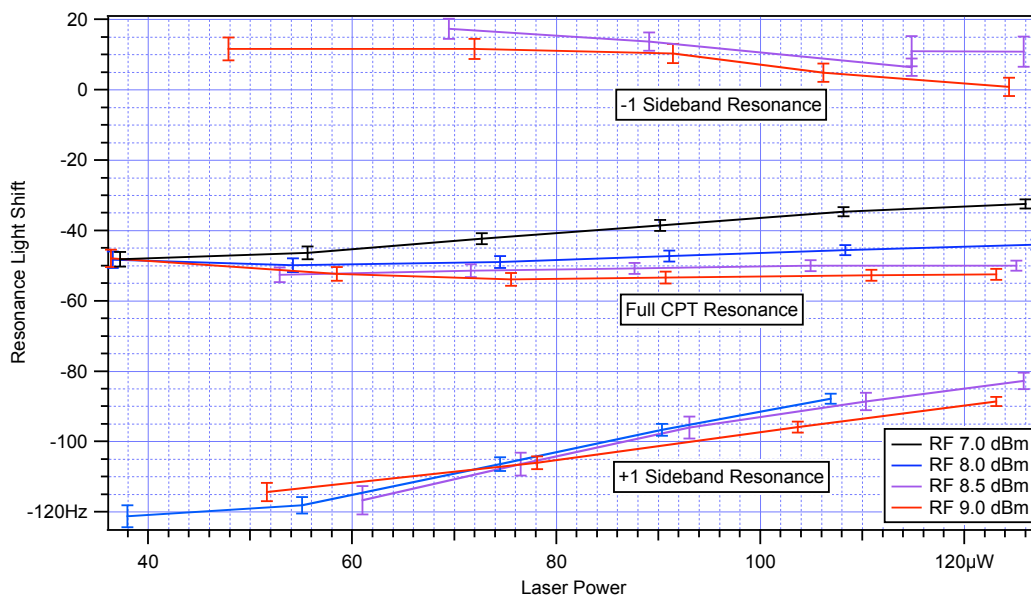
Figure 6.11: Measured shift in the clock and sideband resonances vs laser power, as the sidebands' modulation index is varied by changing the amplitude of the phase modulation signal. All data taken with a 2 mm beam in a ^{87}Rb vapor cell with 22 Torr of Ne buffer gas at 51 °C, corresponding to a ^{87}Rb density of approximately 1.1×10^{11} cm^{-3}. Higher power RF signals correspond to higher modulation indices.
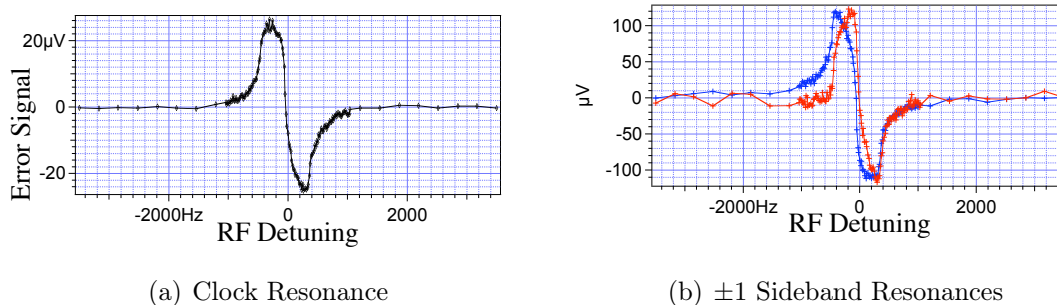
(a) Clock Resonance

(b) ± 1 Sideband Resonances

Figure 6.12: (a) Clock signal obtained with 1 mm beam diameter, to obtain higher intensities. Also shown in (b) is the associated signal from the -1 sideband (red/light grey) and $+1$ sideband (blue/dark grey). Total power $=$ 37.6 μW, 1 mm beam, in ^{87}Rb vapor cell with 22 Torr of Ne buffer gas at 51 °C, corresponding to a ^{87}Rb density of approximately 1.1×10^{11} cm^{-3}.
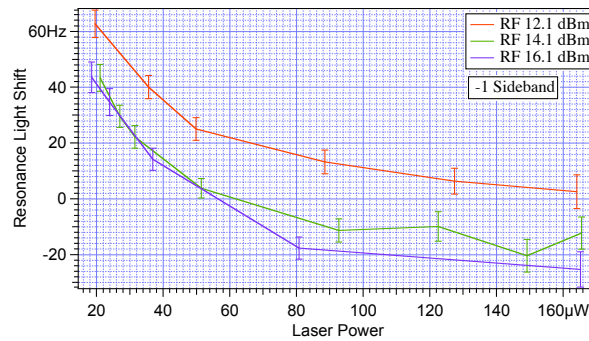
(a) −1 Sideband Resonance
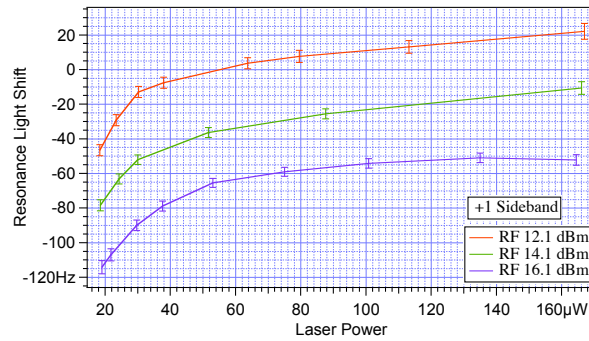
(b) +1 Sideband Resonance
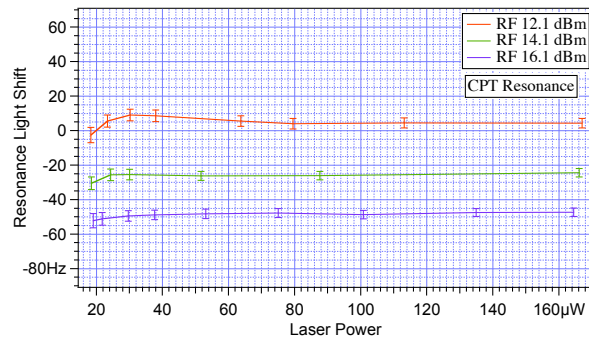
(c) Clock Resonance

Figure 6.13: Measured resonance shifts for ±1 sidebands and CPT clock resonance vs. laser power at higher intensities. Data taken with a 1 mm beam, in ^{87}Rb vapor cell with 22 Torr of Ne buffer gas at 51 °C, corresponding to a ^{87}Rb density of approximately 1.1×10^{11} cm^{-3}. Higher power RF signals correspond to higher modulation indices.

Appendix A

Appendices to Chapters 2 and 3

A.1 Second Order $\tilde{\kappa}$ Transformation

Lorentz violation in the photon sector modifies Maxwell's equations and can be seen as giving the vacuum a frame-dependent electric and magnetic polarizability. Thus the electromagnetic field may be understood in terms of the solution to Maxwell's equations in a medium, where

$$\begin{pmatrix} \vec{D} \\ \vec{H} \end{pmatrix} = \begin{pmatrix} (1 + \kappa_{DE}) & \kappa_{DB} \\ \kappa_{HE} & (1 + \kappa_{HB}) \end{pmatrix} \begin{pmatrix} \vec{E} \\ \vec{B} \end{pmatrix}. \tag{A.1}$$

The κ matrixes are fully determined by 19 coefficients, to wit, four traceless tensors and one scalar:

$$(\tilde{\kappa}_{e+})^{jk} = \frac{1}{2} (\kappa_{DE} + \kappa_{HB})^{jk} \tag{A.2}$$

$$(\tilde{\kappa}_{e-})^{jk} = \frac{1}{2} (\kappa_{DE} - \kappa_{HB})^{jk} - \delta^{jk} \tilde{\kappa}_{tr} \tag{A.3}$$

$$(\tilde{\kappa}_{o+})^{jk} = \frac{1}{2} (\kappa_{DB} + \kappa_{HE})^{jk} \tag{A.4}$$

$$(\tilde{\kappa}_{o-})^{jk} = \frac{1}{2} (\kappa_{DB} - \kappa_{HE})^{jk} \tag{A.5}$$

$$\tilde{\kappa}_{tr} = \frac{1}{3} (\kappa_{DE})^{ll}. \tag{A.6}$$

The SME-modified Lagrangian for the electromagnetic field is, in the standard reference frame:

$$\mathcal{L} = \frac{1}{2}\left(\vec{E}^2 - \vec{B}^2\right) + \frac{1}{2}\vec{E}\cdot(\kappa_{DE})\cdot\vec{E} - \frac{1}{2}\vec{B}\cdot(\kappa_{HB})\cdot\vec{B} + \vec{E}\cdot(\kappa_{DB})\cdot\vec{B}, \qquad (A.7)$$

or, in terms of the independent parameters:

$$\begin{aligned}
\mathcal{L} = \frac{1}{2}&\left((1+\tilde{\kappa}_{tr})|\vec{E}|^2 - (1-\tilde{\kappa}_{tr})|\vec{B}|^2\right) \\
&+ \frac{1}{2}\vec{E}\cdot(\tilde{\kappa}_{e+}+\tilde{\kappa}_{e-})\cdot\vec{E} - \frac{1}{2}\vec{B}\cdot(\tilde{\kappa}_{e+}-\tilde{\kappa}_{e-})\cdot\vec{B} + \vec{E}\cdot(\tilde{\kappa}_{o+}+\tilde{\kappa}_{o-})\cdot\vec{B}.
\end{aligned} \qquad (A.8)$$

The action must be invariant, so by replacing the fields with their values in a boosted frame, we can gather like terms to obtain the properties of the vacuum in those boosted frames.

$$\begin{aligned}
\mathcal{L} = \mathcal{L}' = \frac{1}{2}&\left((1+\tilde{\kappa}_{tr}')|\vec{E}'|^2 - (1-\tilde{\kappa}_{tr}')|\vec{B}'|^2\right) + \frac{1}{2}\vec{E}'\cdot\left(\tilde{\kappa}_{e+}'+\tilde{\kappa}_{e-}'\right)\cdot\vec{E}' \\
&- \frac{1}{2}\vec{B}'\cdot\left(\tilde{\kappa}_{e+}'-\tilde{\kappa}_{e-}'\right)\cdot\vec{B}' + \vec{E}'\cdot\left(\tilde{\kappa}_{o+}'+\tilde{\kappa}_{o-}'\right)\cdot\vec{B}'.
\end{aligned} \qquad (A.9)$$

To obtain the properties of the vacuum in boosted frames (in our case, along the x-axis, we transform $\vec{E}$ and $\vec{B}$ as in special relativity to obtain $\vec{E}' = E_x\hat{x}+\gamma\left(E_y + \beta B_z\right)\hat{y}+\gamma\left(E_z - \beta B_y\right)\hat{z}$ and $\vec{B}' = B_x\hat{x} + \gamma\left(B_y - \beta E_z\right)\hat{y} + \gamma\left(B_z + \beta E_y\right)\hat{z}$. We then insert the transformed fields into the Lagrangian and collect terms to discover how the $\tilde{\kappa}$ parameters transform under a boost. In this analysis, we want to determine how LV in the photon sector might affect the operation of synchrotrons, and so we are interested in κ_{DE} and κ_{DB} under the condition that $\tilde{\kappa}_{tr}$ and possibly $\tilde{\kappa}_{e-}$ and $\tilde{\kappa}_{o+}$ are the only nonzero $\tilde{\kappa}$ parameters. By matching coefficients from the reference-frame Lagrangian

to the boosted Lagrangian, we obtain the following system of equations

$$E_1^2 \quad : \quad \frac{1}{2}(1 + \tilde{\kappa}'_{tr} - \tilde{\kappa}'^{22}_{e-} - \tilde{\kappa}'^{33}_{e-} - \tilde{\kappa}'^{22}_{e+} - \tilde{\kappa}'^{33}_{e+}) = \frac{1}{2}(1 + \tilde{\kappa}_{tr} - \tilde{\kappa}^{22}_{e-} - \tilde{\kappa}^{33}_{e-}) \quad \text{(A.10)}$$

$$E_2^2 \quad : \quad \frac{1}{2}\left(1 + (2\gamma^2 - 1)\tilde{\kappa}'_{tr} + \gamma^2(\tilde{\kappa}'^{22}_{e-} + \tilde{\kappa}'^{22}_{e+}) + (\gamma^2 - 1)(\tilde{\kappa}'^{33}_{e-} - \tilde{\kappa}'^{33}_{e+})\right) \quad \text{(A.11)}$$

$$+2\beta\gamma^2(\tilde{\kappa}'^{23}_{o+} + \tilde{\kappa}'^{23}_{o-})) = \frac{1}{2}(1 + \tilde{\kappa}_{tr} + \tilde{\kappa}^{22}_{e-}) \quad \text{(A.12)}$$

$$E_3^2 \quad : \quad \frac{1}{2}\left(1 + (2\gamma^2 - 1)\tilde{\kappa}'_{tr} + \gamma^2(\tilde{\kappa}'^{33}_{e-} + \tilde{\kappa}'^{33}_{e+}) + (\gamma^2 - 1)(\tilde{\kappa}'^{22}_{e-} - \tilde{\kappa}'^{22}_{e+})\right) \quad \text{(A.13)}$$

$$+2\beta\gamma^2(\tilde{\kappa}'^{23}_{o+} - \tilde{\kappa}'^{23}_{o-})) = \frac{1}{2}(1 + \tilde{\kappa}_{tr} + \tilde{\kappa}^{33}_{e-}) \quad \text{(A.14)}$$

$$B_1^2 \quad : \quad \frac{-1}{2}\left(1 - \tilde{\kappa}'_{tr} + \tilde{\kappa}'^{22}_{e-} + \tilde{\kappa}'^{33}_{e-} - \tilde{\kappa}'^{22}_{e+} - \tilde{\kappa}'^{33}_{e+}\right) = \frac{-1}{2}\left(1 - \tilde{\kappa}_{tr} + \tilde{\kappa}^{22}_{e-} + \tilde{\kappa}^{33}_{e-}\right) \quad \text{(A.15)}$$

$$B_2^2 \quad : \quad \frac{-1}{2}\left(1 - (2\gamma^2 - 1)\tilde{\kappa}'_{tr} - \gamma^2(\tilde{\kappa}'^{22}_{e-} - \tilde{\kappa}'^{22}_{e+}) - (\gamma^2 - 1)(\tilde{\kappa}'^{33}_{e-} + \tilde{\kappa}'^{33}_{e+})\right) \quad \text{(A.16)}$$

$$-2\beta\gamma^2(\tilde{\kappa}'^{23}_{o+} - \tilde{\kappa}'^{23}_{o-})) = \frac{1}{2}(1 - \tilde{\kappa}_{tr} - \tilde{\kappa}^{22}_{e-}) \quad \text{(A.17)}$$

$$B_3^2 \quad : \quad \frac{-1}{2}\left(1 - (2\gamma^2 - 1)\tilde{\kappa}'_{tr} - \gamma^2(\tilde{\kappa}'^{33}_{e-} - \tilde{\kappa}'^{33}_{e+}) - (\gamma^2 - 1)(\tilde{\kappa}'^{22}_{e-} + \tilde{\kappa}'^{22}_{e+})\right) \quad \text{(A.18)}$$

$$-2\beta\gamma^2(\tilde{\kappa}'^{23}_{o+} + \tilde{\kappa}'^{23}_{o-})) = \frac{1}{2}(1 - \tilde{\kappa}_{tr} - \tilde{\kappa}^{33}_{e-}) \quad \text{(A.19)}$$

$$E_1 E_2 \quad : \quad \gamma\left(\beta(\tilde{\kappa}'^{13}_{o+} + \tilde{\kappa}'^{13}_{o-}) + \tilde{\kappa}'^{12}_{e-} + \tilde{\kappa}'^{12}_{e+}\right) = \tilde{\kappa}^{12}_{e-} \quad \text{(A.20)}$$

$$E_1 E_3 \quad : \quad \gamma\left(-\beta(\tilde{\kappa}'^{12}_{o+} + \tilde{\kappa}'^{12)}_{o-}) + \tilde{\kappa}'^{13}_{e-} + \tilde{\kappa}'^{13}_{e+}\right) = \tilde{\kappa}^{13}_{e-} \quad \text{(A.21)}$$

$$E_2 E_3 \quad : \quad \beta\gamma^2(\tilde{\kappa}'^{33}_{o-} - \tilde{\kappa}'^{22}_{o-}) + (2\gamma^2 - 1)\tilde{\kappa}^{23}_{e+} + \tilde{\kappa}'^{23}_{e-} = \tilde{\kappa}^{23}_{e-} \quad \text{(A.22)}$$

$$B_1 B_2 \quad : \quad \gamma\left(\beta(\tilde{\kappa}'^{13}_{o+} - \tilde{\kappa}'^{13}_{o-}) + \tilde{\kappa}'^{12}_{e-} - \tilde{\kappa}'^{12}_{e+}\right) = \tilde{\kappa}^{12}_{e-} \quad \text{(A.23)}$$

$$B_1 B_3 \quad : \quad \gamma\left(\beta(\tilde{\kappa}'^{12}_{o-} - \tilde{\kappa}'^{12}_{o+}) + \tilde{\kappa}'^{13}_{e-} - \tilde{\kappa}'^{13}_{e+}\right) = \tilde{\kappa}^{13}_{e-} \quad \text{(A.24)}$$

$$B_2 B_3 \quad : \quad \gamma^2\left(\beta(\tilde{\kappa}'^{22}_{o-} - \tilde{\kappa}'^{33}_{o-}) - 2\tilde{\kappa}'^{2,3}_{e+}\right) + \tilde{\kappa}'^{23}_{e+} + \tilde{\kappa}'^{23}_{e-} = \tilde{\kappa}^{23}_{e-} \quad \text{(A.25)}$$

and the EB terms are

$$E_1B_1 \quad : \quad -(\tilde{\kappa}_{o-}'^{22} + \tilde{\kappa}_{o-}'^{33}) = 0 \tag{A.26}$$

$$E_1B_2 \quad : \quad \gamma\left(\tilde{\kappa}_{o-}'^{12} + \tilde{\kappa}_{o+}'^{12} - \beta(\tilde{\kappa}_{e-}'^{13} + \tilde{\kappa}_{e+}'^{13})\right) = \tilde{\kappa}_{o+}^{12} \tag{A.27}$$

$$E_1B_3 \quad : \quad \gamma\left(\tilde{\kappa}_{o-}'^{13} + \tilde{\kappa}_{o+}'^{13} + \beta(\tilde{\kappa}_{e-}'^{12} + \tilde{\kappa}_{e+}'^{12})\right) = \tilde{\kappa}_{o+}^{13} \tag{A.28}$$

$$E_2B_1 \quad : \quad \gamma\left(\tilde{\kappa}_{o-}'^{12} - \tilde{\kappa}_{o+}'^{12} + \beta(\tilde{\kappa}_{e-}'^{13} - \tilde{\kappa}_{e+}'^{13})\right) = -\tilde{\kappa}_{o+}^{12} \tag{A.29}$$

$$E_2B_2 \quad : \quad \gamma^2\left(\tilde{\kappa}_{o-}'^{22} - \beta^2\tilde{\kappa}_{o-}'^{33} - 2\beta\tilde{\kappa}_{e+}'^{2,3}\right) = 0 \tag{A.30}$$

$$E_2B_3 \quad : \quad \gamma^2\left((1+\beta^2)(\tilde{\kappa}_{o-}'^{23} + \tilde{\kappa}_{o+}'^{23}) + \beta(2\tilde{\kappa}_{tr}' + \tilde{\kappa}_{e-}'^{22} + \tilde{\kappa}_{e-}'^{33} + \tilde{\kappa}_{e+}'^{22} - \tilde{\kappa}_{e+}'^{33})\right) = \tilde{\kappa}_{o+}^{23} \tag{A.31}$$

$$E_3B_1 \quad : \quad \gamma\left((\tilde{\kappa}_{o-}'^{13} - \tilde{\kappa}_{o+}'^{13}) + \beta(\tilde{\kappa}_{e+}'^{12} - \tilde{\kappa}_{e-}'^{12})\right) = -\tilde{\kappa}_{o+}^{13} \tag{A.32}$$

$$E_3B_2 \quad : \quad (2\gamma^2 - 1)(\tilde{\kappa}_{o-}'^{23} - \tilde{\kappa}_{o+}'^{23}) - \gamma^2\beta(2\tilde{\kappa}_{tr}' + \tilde{\kappa}_{e-}'^{22} + \tilde{\kappa}_{e-}'^{33} + \tilde{\kappa}_{e+}'^{33} - \tilde{\kappa}_{e+}'^{22}) = -\tilde{\kappa}_{o+}^{23} \tag{A.33}$$

$$E_3B_3 \quad : \quad \gamma^2\left(\tilde{\kappa}_{o-}'^{33} - \beta^2\tilde{\kappa}_{o-}'^{22} + 2\beta\tilde{\kappa}_{e+}'^{23}\right) = 0 \tag{A.34}$$

Solving these equations yields

$$\tilde{\kappa}_{tr}' = \left(1 + \frac{\beta^2}{3}\right)\gamma^2\tilde{\kappa}_{tr} - \frac{2}{3}\beta\gamma^2\left(2\tilde{\kappa}_{o+}^{23} - \beta(\tilde{\kappa}_{e-}^{22} + \tilde{\kappa}_{e-}^{33})\right) \tag{A.35}$$

$$\tilde{\kappa}_{e-}'^{12} = \gamma\left(\tilde{\kappa}_{e-}^{12} - \beta\tilde{\kappa}_{o+}^{13}\right) \tag{A.36}$$

$$\tilde{\kappa}_{e-}'^{13} = \gamma\left(\tilde{\kappa}_{e-}^{13} + \beta\tilde{\kappa}_{o+}^{12}\right) \tag{A.37}$$

$$\tilde{\kappa}_{e-}'^{23} = \tilde{\kappa}_{e-}^{23} \tag{A.38}$$

$$\tilde{\kappa}_{e-}'^{22} = \frac{1}{3}\left(2 + \gamma^2\right)\tilde{\kappa}_{e-}^{22} + \frac{1}{3}\beta^2\gamma^2\tilde{\kappa}_{e-}^{33} + \frac{2}{3}\gamma^2\beta^2\tilde{\kappa}_{tr} - \frac{2}{3}\gamma^2\beta\tilde{\kappa}_{o+}^{23} \tag{A.39}$$

$$\tilde{\kappa}_{e-}'^{33} = \frac{1}{3}\left(2 + \gamma^2\right)\tilde{\kappa}_{e-}^{33} + \frac{1}{3}\beta^2\gamma^2\tilde{\kappa}_{e-}^{22} + \frac{2}{3}\gamma^2\beta^2\tilde{\kappa}_{tr} - \frac{2}{3}\gamma^2\beta\tilde{\kappa}_{o+}^{23} \tag{A.40}$$

$$\tilde{\kappa}_{e+}'^{jk} = 0 \tag{A.41}$$

$$\tilde{\kappa}_{o-}'^{jk} = 0 \tag{A.42}$$

$$\tilde{\kappa}_{o+}'^{12} = \gamma\left(\tilde{\kappa}_{o+}^{12} + \beta\tilde{\kappa}_{e-}^{13}\right) \tag{A.43}$$

$$\tilde{\kappa}_{o+}'^{13} = \gamma\left(\tilde{\kappa}_{o+}^{13} - \beta\tilde{\kappa}_{e-}^{12}\right) \tag{A.44}$$

$$\tilde{\kappa}_{o+}'^{23} = (2\gamma^2 - 1)\tilde{\kappa}_{o+}^{23} - \beta\gamma^2\left(2\tilde{\kappa}_{tr} + \tilde{\kappa}_{e-}^{22} + \tilde{\kappa}_{e-}^{33}\right). \tag{A.45}$$

In the limit that only $\tilde{\kappa}_{tr}$ is significant the only nonzero terms are

$$\tilde{\kappa}'_{tr} = \left(1 + \frac{\beta^2}{3}\right)\gamma^2\tilde{\kappa}_{tr} \tag{A.46}$$

$$\tilde{\kappa}'^{23}_{o+} = -2\beta\gamma^2\tilde{\kappa}_{tr} \tag{A.47}$$

$$\tilde{\kappa}'^{22}_{e-} = \frac{2}{3}\gamma^2\beta^2\tilde{\kappa}_{tr} \tag{A.48}$$

$$\tilde{\kappa}'^{33}_{e-} = \frac{2}{3}\gamma^2\beta^2\tilde{\kappa}_{tr}. \tag{A.49}$$

From the definitions of these four terms, we find that

$$\kappa'_{DE} = \begin{pmatrix} \tilde{\kappa}'_{tr} + \tilde{\kappa}'^{11}_{e-} & 0 & 0 \\ 0 & \tilde{\kappa}'_{tr} + \tilde{\kappa}'^{22}_{e-} & 0 \\ 0 & 0 & \tilde{\kappa}'_{tr} + \tilde{\kappa}'^{33}_{e-} \end{pmatrix} \tag{A.50}$$

$$= \begin{pmatrix} \tilde{\kappa}_{tr} & 0 & 0 \\ 0 & (1+\beta^2)\gamma^2\tilde{\kappa}_{tr} & 0 \\ 0 & 0 & (1+\beta^2)\gamma^2\tilde{\kappa}_{tr} \end{pmatrix} \tag{A.51}$$

$$\kappa'_{DB} = \begin{pmatrix} 0 & 0 & 0 \\ 0 & 0 & \tilde{\kappa}'^{23}_{o+} \\ 0 & -\tilde{\kappa}'^{23}_{o+} & 0 \end{pmatrix} = \begin{pmatrix} 0 & 0 & 0 \\ 0 & 0 & -2\beta\gamma^2\tilde{\kappa}_{tr} \\ 0 & 2\beta\gamma^2\tilde{\kappa}_{tr} & 0 \end{pmatrix} \tag{A.52}$$

$$\kappa'_{HB} = \begin{pmatrix} -\tilde{\kappa}_{tr} & 0 & 0 \\ 0 & -(1+\beta^2)\gamma^2\tilde{\kappa}_{tr} & 0 \\ 0 & 0 & -(1+\beta^2)\gamma^2\tilde{\kappa}_{tr} \end{pmatrix}. \tag{A.53}$$

A.2 General Transformation

$$\mathcal{L} = \frac{1}{2}\left((1 + \tilde{\kappa}_{tr})|\vec{E}|^2 - (1 - \tilde{\kappa}_{tr})|\vec{B}|^2\right) + \frac{1}{2}\vec{E}\cdot(\tilde{\kappa}_{e+} + \tilde{\kappa}_{e-})\cdot\vec{E}$$
$$-\frac{1}{2}\vec{B}\cdot(\tilde{\kappa}_{e+} - \tilde{\kappa}_{e-})\cdot\vec{B} + \vec{E}\cdot(\tilde{\kappa}_{o+} + \tilde{\kappa}_{o-})\cdot\vec{B}. \tag{A.54}$$

The action must be invariant, so by replacing the fields with their values in a boosted frame, we can gather like terms to obtain the properties of the vacuum in those boosted frames.

$$\mathcal{L} = \mathcal{L}' = \frac{1}{2}\left((1 + \tilde{\kappa}'_{tr})|\vec{E}'|^2 - (1 - \tilde{\kappa}'_{tr})|\vec{B}'|^2\right) + \frac{1}{2}\vec{E}'\cdot(\tilde{\kappa}'_{e+} + \tilde{\kappa}'_{e-})\cdot\vec{E}'$$
$$-\frac{1}{2}\vec{B}'\cdot(\tilde{\kappa}'_{e+} - \tilde{\kappa}'_{e-})\cdot\vec{B}' + \vec{E}'\cdot(\tilde{\kappa}'_{o+} + \tilde{\kappa}'_{o-})\cdot\vec{B}'. \tag{A.55}$$

In what follows, we neglect entirely the contribution of $\tilde{\kappa}_{o-}$ and $\tilde{\kappa}_{e+}$ to either $\mathcal{L}$ or $\mathcal{L}'$. These terms give rise to birefringence of the vacuum, a phenomena which has been thoroughly excluded in any frame concordant [87] with the standard Sun-centered reference frame. Dropping these terms greatly simplifies our task. For an arbitrary boost $\vec{\beta}$, the electric and magnetic fields transform according to

$$\vec{E}' = \gamma(\vec{E} + \vec{\beta}\times\vec{B}) - \frac{\gamma^2}{\gamma + 1}\vec{\beta}(\vec{\beta}\cdot\vec{E})$$

$$\vec{B}' = \gamma(\vec{B} - \vec{\beta}\times\vec{E}) - \frac{\gamma^2}{\gamma + 1}\vec{\beta}(\vec{\beta}\cdot\vec{B})$$

Examination of $\mathcal{L}$ in the unprimed frame reveals that the sum of the coefficients of E_1^2, E_2^2, and E_3^2 is $3/2(1 + \tilde{\kappa}_{tr})$. The form of $\tilde{\kappa}'_{tr}$ is easily obtained by the sum of the coefficients of E_1^2, E_2^2, and E_3^2 in the primed frame after substitution of $\vec{E}$ and $\vec{B}$ for $\vec{E}'$ and $\vec{B}'$, and is given by

$$\tilde{\kappa}'_{tr} = \left(1 + \frac{|\beta|^2}{3}\right)\gamma^2\tilde{\kappa}_{tr} + \frac{2}{3}\gamma^2\left[(\beta_1^2 - \beta_2^2)\tilde{\kappa}_{e-}^{22} + (\beta_1^2 - \beta_3^2)\tilde{\kappa}_{e-}^{33}\right]$$
$$-\frac{4}{3}\gamma^2\left[\beta_1\beta_2\tilde{\kappa}_{e-}'^{12} + \beta_1\beta_3\tilde{\kappa}_{e-}'^{13} + \beta_2\beta_3\tilde{\kappa}_{e-}'^{23} - \beta_3\tilde{\kappa}_{o+}'^{12} + \beta_2\tilde{\kappa}_{o+}'^{13} - \beta_1\tilde{\kappa}_{o+}'^{23}\right]. \tag{A.56}$$

We can find $\tilde{\kappa}_{e-}'^{22}$ in a similar fashion, noting that if we define $a = \text{coef}(E_1^2)$, $b = \text{coef}(E_2^2)$, and $c = \text{coef}(E_3^2)$ in the unprimed frame, the weighted sum $(4/3)(b - a/2 -$

$c/2$) is equal to $\tilde{\kappa}_{e-}^{22}$. Taking the same linear combination of primed-frame coefficients after substitution, and switching the sign of $\vec{\beta}$, we find that

$$\tilde{\kappa}_{e-}'^{22} = \frac{2}{3}\left[(1 - 3\beta_2^2)\gamma^2 - 1\right]\tilde{\kappa}_{tr} + \frac{(\beta_1^2 - \beta_3^2)\gamma^2}{3(\gamma + 1)^2}\left[1 + \gamma(2 - \gamma(3\beta_2^2 - 1))\right]\tilde{\kappa}_{e-}^{33}$$
$$+ \left[\frac{1}{3}(2 + (1 - \beta_3^2)\gamma^2) + \frac{\beta_2^2(\beta_2^2 - \beta_1^2)\gamma^4}{(\gamma + 1)^2} - \frac{2\beta_2^2\gamma^2(\gamma - 2)}{3(\gamma + 1)}\right]\tilde{\kappa}_{e-}^{22}$$
$$+ \frac{2\gamma^2(2 + \gamma + (3\beta_2^2 - 1)\gamma^2)}{3(\gamma + 1)^2}\left[\beta_1\beta_2\tilde{\kappa}_{e-}^{12} + \beta_1\beta_3\tilde{\kappa}_{e-}^{13} + \beta_2\beta_3\tilde{\kappa}_{e-}^{23}\right] \qquad \text{(A.57)}$$
$$- \frac{2\beta_1\beta_3\gamma^2}{\gamma + 1}\tilde{\kappa}_{e-}^{13}$$
$$+ \frac{2}{3}\gamma^2\left(1 - \frac{3\beta_2^2\gamma}{\gamma + 1}\right)\left[\beta_3\tilde{\kappa}_{o+}^{12} - \beta_2\tilde{\kappa}_{o+}^{13} + \beta_1\tilde{\kappa}_{o+}^{23}\right] + 2\beta_2\gamma\tilde{\kappa}_{o+}^{13}.$$

Similarly, we find the expression for $\tilde{\kappa}_{e-}'^{33}$:

$$\tilde{\kappa}_{e-}'^{33} = \frac{2}{3}\left[(1 - 3\beta_3^2)\gamma^2 - 1\right]\tilde{\kappa}_{tr} + \frac{(\beta_1^2 - \beta_2^2)\gamma^2}{3(\gamma + 1)^2}\left[1 + \gamma(2 - \gamma(3\beta_3^2 - 1))\right]\tilde{\kappa}_{e-}^{22}$$
$$+ \left[\frac{1}{3}(2 + (1 - \beta_2^2)\gamma^2) + \frac{\beta_3^2(\beta_3^2 - \beta_1^2)\gamma^4}{(\gamma + 1)^2} - \frac{2\beta_3^2\gamma^2(\gamma - 2)}{3(\gamma + 1)}\right]\tilde{\kappa}_{e-}^{33}$$
$$+ \frac{2\gamma^2(2 + \gamma + (3\beta_3^2 - 1)\gamma^2)}{3(\gamma + 1)^2}\left[\beta_1\beta_2\tilde{\kappa}_{e-}^{12} + \beta_1\beta_3\tilde{\kappa}_{e-}^{13} + \beta_2\beta_3\tilde{\kappa}_{e-}^{23}\right] \qquad \text{(A.58)}$$
$$- \frac{2\beta_1\beta_2\gamma^2}{\gamma + 1}\tilde{\kappa}_{e-}^{12}$$
$$+ \frac{2}{3}\gamma^2\left(1 - \frac{3\beta_3^2\gamma}{\gamma + 1}\right)\left(\beta_3\tilde{\kappa}_{o+}^{12} - \beta_2\tilde{\kappa}_{o+}^{13} + \beta_3\tilde{\kappa}_{o+}^{23}\right) - 2\beta_3\gamma\tilde{\kappa}_{o+}^{12}.$$

The remaining terms can be read off directly from the coefficients of E_jB_k and E_jE_k:

$$\tilde{\kappa}_{e-}'^{12} = -2\beta_1\beta_2\gamma^2\tilde{\kappa}_{tr} + \frac{\beta_1\beta_2(\beta_2^2 - \beta_1^2)\gamma^4}{(\gamma + 1)^2}\tilde{\kappa}_{e-}^{22}$$
$$- \frac{\beta_1\beta_2\gamma^2(1 + \gamma + (\beta_1^2 - \beta_3^2)\gamma^2)}{(\gamma + 1)^2}\tilde{\kappa}_{e-}^{33}$$
$$+ \left(1 + \frac{\gamma^2(\beta_1^2 + \beta_2^2)}{\gamma + 1} + \frac{2\beta_1^2\beta_2^2\gamma^4}{(\gamma + 1)^2}\right)\tilde{\kappa}_{e-}^{12} + \frac{\beta_2\beta_3\gamma^2}{\gamma + 1}\left(1 + \frac{2\beta_1^2\gamma^2}{\gamma + 1}\right)\tilde{\kappa}_{e-}^{13} \qquad \text{(A.59)}$$
$$+ \frac{\beta_1\beta_3\gamma^2}{\gamma + 1}\left(1 + \frac{2\beta_2^2\gamma^2}{\gamma + 1}\right)\tilde{\kappa}_{e-}^{23} - \frac{2\beta_1\beta_2\beta_3\gamma^3}{\gamma + 1}\tilde{\kappa}_{o+}^{12}$$
$$+ \beta_1\gamma\left(1 + \frac{2\beta_2^2\gamma^2}{\gamma + 1}\right)\tilde{\kappa}_{o+}^{13} - \beta_2\gamma\left(1 + \frac{2\beta_1^2\gamma^2}{\gamma + 1}\right)\tilde{\kappa}_{o+}^{23},$$

$$\tilde{\kappa}_{e-}'^{13} = -2\beta_1\beta_3\gamma^2\tilde{\kappa}_{tr} + \frac{\beta_1\beta_3(\beta_3^2 - \beta_1^2)\gamma^4}{(\gamma+1)^2}\tilde{\kappa}_{e-}^{33}$$

$$- \frac{\beta_1\beta_3\gamma^2(1 + \gamma + (\beta_1^2 - \beta_2^2)\gamma^2)}{(\gamma+1)^2}\tilde{\kappa}_{e-}^{22}$$

$$+ \frac{\beta_2\beta_3\gamma^2}{\gamma+1}\left(1 + \frac{2\beta_1^2\gamma^2}{\gamma+1}\right)\tilde{\kappa}_{e-}^{12} + \left(1 + \frac{\gamma^2(\beta_1^2 + \beta_3^2)}{\gamma+1} + \frac{2\beta_1^2\beta_3^2\gamma^4}{(\gamma+1)^2}\right)\tilde{\kappa}_{e-}^{13} \quad \text{(A.60)}$$

$$+ \frac{\beta_1\beta_2\gamma^2}{\gamma+1}\left(1 + \frac{2\beta_3^2\gamma^2}{\gamma+1}\right)\tilde{\kappa}_{e-}^{23} - \beta_1\gamma\left(1 + \frac{2\beta_3^2\gamma^2}{\gamma+1}\right)\tilde{\kappa}_{o+}^{12}$$

$$+ \frac{2\beta_1\beta_2\beta_3\gamma^3}{\gamma+1}\tilde{\kappa}_{o+}^{13} - \beta_3\gamma\left(1 + \frac{2\beta_1^2\gamma^2}{\gamma+1}\right)\tilde{\kappa}_{o+}^{23},$$

$$\tilde{\kappa}_{e-}'^{23} = -2\beta_2\beta_3\gamma^2\tilde{\kappa}_{tr} + \frac{\beta_2\beta_3\gamma^2}{\gamma+1}\left(1 + \frac{(\beta_2^2 - \beta_1^2)\gamma^2}{(\gamma+1)^2}\right)\tilde{\kappa}_{e-}^{22}$$

$$+ \frac{\beta_2\beta_3\gamma^2}{\gamma+1}\left(1 + \frac{(\beta_3^2 - \beta_1^2)\gamma^2}{(\gamma+1)^2}\right)\tilde{\kappa}_{e-}^{33}$$

$$+ \frac{\beta_1\beta_3\gamma^2}{\gamma+1}\left(1 + \frac{2\beta_2^2\gamma^2}{\gamma+1}\right)\tilde{\kappa}_{e-}^{12} + \frac{\beta_1\beta_2\gamma^2}{\gamma+1}\left(1 + \frac{2\beta_3^2\gamma^2}{\gamma+1}\right)\tilde{\kappa}_{e-}^{13} \quad \text{(A.61)}$$

$$+ \left(1 + \frac{\gamma^2(\beta_2^2 + \beta_3^2)}{\gamma+1} + \frac{2\beta_2^2\beta_3^2\gamma^4}{(\gamma+1)^2}\right)\tilde{\kappa}_{e-}^{23} - \beta_2\gamma\left(1 + \frac{2\beta_3^2\gamma^2}{\gamma+1}\right)\tilde{\kappa}_{o+}^{12}$$

$$+ \beta_3\gamma\left(1 + \frac{2\beta_2^2\gamma^2}{\gamma+1}\right)\tilde{\kappa}_{o+}^{13} - \frac{2\beta_1\beta_2\beta_3\gamma^3}{\gamma+1}\tilde{\kappa}_{o+}^{23},$$

$$\tilde{\kappa}_{o+}'^{12} = 2\beta_3\gamma^2\tilde{\kappa}_{tr} - \frac{(\beta_2^2 - \beta_1^2)\beta_3\gamma^3}{\gamma+1}\tilde{\kappa}_{e-}^{22} - \left(\beta_3\gamma + \frac{(\beta_3^2 - \beta_1^2)\beta_3\gamma^3}{\gamma+1}\right)\tilde{\kappa}_{e-}^{33}$$

$$- \frac{2\beta_1\beta_2\beta_3\gamma^3}{\gamma+1}\tilde{\kappa}_{e-}^{12} - \gamma\left(1 + \frac{2\beta_3^2\gamma^2}{\gamma+1}\right)\left[\beta_1\tilde{\kappa}_{e-}^{13} + \beta_2\tilde{\kappa}_{e-}^{23}\right] \quad \text{(A.62)}$$

$$+ \gamma\tilde{\kappa}_{o+}^{12} + \frac{\beta_3\gamma^2(1 + 2\gamma)}{\gamma+1}\left[\beta_3\tilde{\kappa}_{o+}^{12} - \beta_2\tilde{\kappa}_{o+}^{13} + \beta_1\tilde{\kappa}_{o+}^{23}\right],$$

$$\tilde{\kappa}_{o+}'^{13} = -2\beta_2\gamma^2\tilde{\kappa}_{tr} - \left(\beta_2\gamma + \frac{(\beta_2^2 - \beta_1^2)\beta_2\gamma^3}{\gamma+1}\right)\tilde{\kappa}_{e-}^{22} - \frac{(\beta_3^2 - \beta_1^2)\beta_2\gamma^3}{\gamma+1}\tilde{\kappa}_{e-}^{33}$$

$$+ \frac{2\beta_1\beta_2\beta_3\gamma^3}{\gamma+1}\tilde{\kappa}_{e-}^{13} + \gamma\left(1 + \frac{2\beta_2^2\gamma^2}{\gamma+1}\right)\left[\beta_1\tilde{\kappa}_{e-}^{12} + \beta_3\tilde{\kappa}_{e-}^{23}\right] \quad \text{(A.63)}$$

$$+ \gamma\tilde{\kappa}_{o+}^{13} + \frac{\beta_2\gamma^2(1 + 2\gamma)}{\gamma+1}\left[\beta_3\tilde{\kappa}_{o+}^{12} - \beta_2\tilde{\kappa}_{o+}^{13} + \beta_1\tilde{\kappa}_{o+}^{23}\right],$$

$$\tilde{\kappa}_{o+}^{\prime 23} = 2\beta_1\gamma^2\tilde{\kappa}_{tr} + \beta_1\gamma\left[1 - \frac{(\beta_2^2 - \beta_1^2)\gamma^2}{\gamma + 1}\right]\tilde{\kappa}_{e-}^{22} + \beta_1\gamma\left[1 - \frac{(\beta_3^2 - \beta_1^2)\gamma^2}{\gamma + 1}\right]\tilde{\kappa}_{e-}^{33}$$
$$- \gamma\left(1 + \frac{2\beta_1^2\gamma^2}{\gamma + 1}\right)\left[\beta_2\tilde{\kappa}_{e-}^{12} + \beta_3\tilde{\kappa}_{e-}^{13}\right] - \frac{2\beta_1\beta_2\beta_3\gamma^3}{\gamma + 1}\tilde{\kappa}_{e-}^{23} \qquad \text{(A.64)}$$
$$+ \gamma\tilde{\kappa}_{o+}^{23} - \frac{\beta_1\gamma^2(1 + 2\gamma)}{\gamma + 1}\left[\beta_3\tilde{\kappa}_{o+}^{12} - \beta_2\tilde{\kappa}_{o+}^{13} + \beta_1\tilde{\kappa}_{o+}^{23}\right].$$

A.3 Second Order Sidereal Signals for Optical Resonator Experiments

To maximize the utility of this result, we now translate it to the $A_{0,1,2,3,4}$, $B_{0,1,2,3,4}$ and $C_{0,1,2,3,4}$ coefficients of [28] which describe the time-dependence of potential LV signals in optical cavity experiments. Such time dependence would arise from the variation of the mixing between photon sector SME parameters as defined in the Sun-centered frame due to the changing boost of the Earthbound laboratory frame. To move from the Sun-centered frame to a frame at rest with respect to some point on the Earth requires both a boost and a rotation. To simplify our calculations, we perform the rotation in the Sun-centered frame prior to applying the boost. As a result, all time-modulation of LV signals takes place at frequencies defined in the rest frame of the Sun, and not on Earth. The effects of time-dilation upon these signal frequencies are small, and as they are well-separated from one another, should not lead to significant errors in experimental analyses. The boost from the Sun-centered frame to the laboratory frame is, as in [28],

$$\vec{\beta} = \beta_\oplus\begin{pmatrix} \sin\Omega_\oplus T \\ -\cos\eta\cos\Omega_\oplus T \\ -\sin\eta\cos\Omega_\oplus T \end{pmatrix} + \beta_L\begin{pmatrix} -\sin\omega_\oplus T \\ \cos\omega_\oplus T \\ 0 \end{pmatrix}, \qquad \text{(A.65)}$$

and the rotation is

$$R = \begin{pmatrix} \cos\chi\cos\omega_\oplus T_\oplus & \cos\chi\sin\omega_\oplus T_\oplus & -\sin\chi \\ -\sin\omega_\oplus T_\oplus & \cos\omega_\oplus T_\oplus & 0 \\ \sin\chi\cos\omega_\oplus T_\oplus & \sin\chi\sin\omega_\oplus T_\oplus & \cos\chi \end{pmatrix}. \qquad \text{(A.66)}$$

Taken from [28], the observable for optical resonator experiments is a fractional frequency shift:

$$
\begin{aligned}
\frac{\delta\nu}{\nu} = &-\frac{1}{4}\left[2(\kappa_{DE})_{\text{lab}}^{33}/\epsilon - (\kappa_{HB})_{\text{lab}}^{11} - (\kappa_{HB})_{\text{lab}}^{22}\right] \\
&-\frac{1}{2}(\kappa_{HB})_{\text{lab}}^{12}\sin 2\theta - \frac{1}{4}\left[(\kappa_{HB})_{\text{lab}}^{11} - (\kappa_{HB})_{\text{lab}}^{22}\right]\cos 2\theta.
\end{aligned}
\tag{A.67}
$$

Where θ is the angle between the x-axis and the cavity orientation for horizontally positioned resonators, and ϵ is the transverse relative permittivity of any medium within the cavity. In what follows, unprimed $\tilde{\kappa}$'s are laboratory-frame parameters, primed $\tilde{\kappa}'$s are in the rest frame of the Sun, and the standard Sun-centered frame $\tilde{\kappa}$s are distinguished by the use of capital X, Y, and Z indices. In terms of the lab-frame $\tilde{\kappa}_{e-}^{jk}$, and $\tilde{\kappa}_{tr}$, the observable is

$$
\begin{aligned}
\frac{\delta\nu}{\nu} &= -\left[\frac{1+\epsilon}{2\epsilon}\tilde{\kappa}_{tr} + \frac{2-\epsilon}{4\epsilon}\tilde{\kappa}_{e-}^{33}\right] + \frac{1}{2}(\tilde{\kappa}_{e-}^{12})\sin 2\theta - \frac{1}{4}\left[2\tilde{\kappa}_{e-}^{22} + \tilde{\kappa}_{e-}^{33}\right]\cos 2\theta \\
&= A + B\sin 2\theta + C\cos 2\theta.
\end{aligned}
\tag{A.68}
$$

Defining

$$
\epsilon_+ = \frac{2+\epsilon}{3\epsilon} \quad \text{and} \quad \epsilon_- = \frac{2-\epsilon}{\epsilon},
\tag{A.69}
$$

the A coefficient is given by

$$
\begin{aligned}
A = &-\frac{1}{8}\left[(9+3|\beta|^2)\gamma^2\epsilon_+ - (1+4\beta_3^2\gamma^2)\epsilon_-\right]\tilde{\kappa}_{tr}' \\
&+ \frac{(\beta_2^2 - \beta_1^2)\gamma^2}{4}\left(\epsilon_+ - \frac{\beta_3^2\gamma^2}{(\gamma+1)^2}\epsilon_-\right)\tilde{\kappa}_{e-}'^{22} \\
&- \frac{\epsilon_-}{4}\left[1 + \frac{2\beta_3^2\gamma^2}{\gamma+1} - \frac{\beta_3^2(\beta_1^2 - \beta_3^2)\gamma^4}{(\gamma+1)^2}\right]\tilde{\kappa}_{e-}'^{33} + \frac{3(\beta_3^2 - \beta_1^2)\gamma^2\epsilon_+}{4}\tilde{\kappa}_{e-}'^{33} \\
&+ \frac{\beta_1\beta_2\gamma^2}{2(\gamma+1)}\epsilon_-\tilde{\kappa}_{e-}'^{12} \\
&+ \frac{\gamma^2}{2}\left(3\epsilon_+ - \left(\frac{1}{1+\gamma} + \frac{\beta_3^2\gamma^2}{(\gamma+1)^2}\right)\epsilon_-\right)\left[\beta_1\beta_2\tilde{\kappa}_{e-}'^{12} + \beta_1\beta_3\tilde{\kappa}_{e-}'^{13} + \beta_2\beta_3\tilde{\kappa}_{e-}'^{23}\right] \\
&- \frac{\gamma}{2}\left(3\gamma^2\epsilon_+ - \frac{\beta_3^2\gamma^2}{\gamma+1}\epsilon_-\right)\left[\beta_3\tilde{\kappa}_{o+}'^{12} - \beta_2\tilde{\kappa}_{o+}'^{13} + \beta_1\tilde{\kappa}_{o+}'^{23}\right] + \frac{\beta_3\gamma}{2}\epsilon_-\tilde{\kappa}_{o+}'^{12}
\end{aligned}
\tag{A.70}
$$

and the B coefficient by

$$
\begin{aligned}
B = &-\beta_1\beta_2\gamma^2\tilde{\kappa}'_{tr} + \frac{1}{2}\tilde{\kappa}'^{12}_{e-} + \frac{\gamma}{2}\left(\beta_1\tilde{\kappa}'^{13}_{o+} - \beta_2\tilde{\kappa}'^{23}_{o+}\right) \\
&+ \frac{\gamma^2}{2(\gamma+1)}\left[\beta_2\beta_3\tilde{\kappa}'^{13}_{e-} + \beta_1\beta_3\tilde{\kappa}'^{23}_{e-} - \beta_1\beta_2\tilde{\kappa}'^{33}_{e-} + (\beta_1^2 + \beta_2^2)\tilde{\kappa}'^{12}_{e-}\right. \\
&\hspace{4cm}\left. - 2\beta_1\beta_2\gamma\left(\beta_3\tilde{\kappa}'^{12}_{o+} - \beta_2\tilde{\kappa}'^{13}_{o+} + \beta_1\tilde{\kappa}'^{23}_{o+}\right)\right] \\
&+ \frac{\beta_1\beta_2\gamma^4}{(\gamma+1)^2}\left[\frac{1}{2}\left((\beta_2^2 - \beta_1^2)\tilde{\kappa}'^{22}_{e-} + (\beta_3^2 - \beta_1^2)\tilde{\kappa}'^{33}_{e-}\right)\right. \\
&\hspace{4cm}\left. + \beta_1\beta_2\tilde{\kappa}'^{12}_{e-} + \beta_1\beta_3\tilde{\kappa}'^{13}_{e-} + \beta_2\beta_3\tilde{\kappa}'^{23}_{e-}\right],
\end{aligned}
\tag{A.71}
$$

and the C coefficient by

$$
\begin{aligned}
C = &\frac{1}{2}(\beta_2^2 - \beta_1^2)\gamma^2\tilde{\kappa}'_{tr} - \frac{1}{2}\tilde{\kappa}'^{22}_{e-} - \frac{1}{4}\left[2\gamma - 1\right]\tilde{\kappa}'^{33}_{e-} - \frac{\gamma}{2}\left(\beta_2\tilde{\kappa}'^{13}_{o+} + \beta_1\tilde{\kappa}'^{23}_{o+}\right) \\
&+ \frac{\gamma^2}{2(\gamma+1)}\left[\beta_1\beta_3\tilde{\kappa}'^{13}_{e-} - \beta_2\beta_3\tilde{\kappa}'^{23}_{e-} - (\beta_1^2 + \beta_2^2)\tilde{\kappa}'^{22}_{e-} - (\beta_2^2 + \beta_3^2)\tilde{\kappa}'^{33}_{e-}\right. \\
&\hspace{4cm}\left. - \gamma(\beta_1^2 - \beta_2^2)\left(\beta_3\tilde{\kappa}'^{12}_{o+} - \beta_2\tilde{\kappa}'^{13}_{o+} + \beta_1\tilde{\kappa}'^{23}_{o+}\right)\right] \\
&+ \frac{(\beta_1^2 - \beta_2^2)\gamma^4}{2(\gamma+1)^2}\left[\frac{1}{2}\left((\beta_2^2 - \beta_1^2)\tilde{\kappa}'^{22}_{e-} + (\beta_3^2 - \beta_1^2)\tilde{\kappa}'^{33}_{e-}\right)\right. \\
&\hspace{4cm}\left. + \beta_1\beta_2\tilde{\kappa}'^{12}_{e-} + \beta_1\beta_3\tilde{\kappa}'^{13}_{e-} + \beta_2\beta_3\tilde{\kappa}'^{23}_{e-}\right].
\end{aligned}
\tag{A.72}
$$

If we include only contributions to second order in components of β, and thus set $\gamma = 1$, since there are no terms proportional to γ and not a component of β (except in the C coefficient, where we find $2\gamma - 1 \sim 1 + |\beta|^2...$), we find

$$
\begin{aligned}
A = & -\frac{1}{8}(9\epsilon_+ - \epsilon_-)\tilde{\kappa}'_{tr} + \frac{3}{16}(\epsilon_+ - \epsilon_-)\left(\tilde{\kappa}'^{33}_{e-} - 2\beta_3\tilde{\kappa}'^{12}_{o+}\right) \\
& + \frac{1}{24}(33\epsilon_+ - \epsilon_-)\left[-|\vec{\beta}|^2\tilde{\kappa}'_{tr} - \frac{(\beta_2^2 - \beta_1^2)}{2}\tilde{\kappa}'^{22}_{e-} - \frac{(\beta_1^2 + \beta_3^2)}{2}\tilde{\kappa}'^{33}_{e-} \right. \\
& \left. \quad + \frac{1}{2}\left[\left(\beta_3^2\tilde{\kappa}'^{33}_{e-} + \beta_1\beta_2\tilde{\kappa}'^{12}_{e-} + \beta_1\beta_3\tilde{\kappa}'^{13}_{e-} + \beta_2\beta_3\tilde{\kappa}'^{23}_{e-}\right) \right.\right. \\
& \left.\left. \quad\quad - \left(\beta_3\tilde{\kappa}'^{12}_{o+} - \beta_2\tilde{\kappa}'^{13}_{o+} + \beta_1\tilde{\kappa}'^{23}_{o+}\right)\right]\right] \\
& - \frac{3\beta_3^2}{8}(\epsilon_+ - \epsilon_-)\tilde{\kappa}'_{tr} - \frac{3\beta_1\beta_2}{16}\tilde{\kappa}'^{12}_{e-} \\
& + \frac{1}{48}(42\epsilon_+ - 10\epsilon_-)\left(\beta_3^2\tilde{\kappa}'^{33}_{e-} + \beta_1\beta_2\tilde{\kappa}'^{12}_{e-} + \beta_1\beta_3\tilde{\kappa}'^{13}_{e-} + \beta_2\beta_3\tilde{\kappa}'^{23}_{e-}\right),
\end{aligned}
\tag{A.73}
$$

$$
\begin{aligned}
B = & -\beta_1\beta_2\tilde{\kappa}'_{tr} + \frac{1}{2}\tilde{\kappa}'^{12}_{e-} + \frac{1}{2}\left(\beta_1\tilde{\kappa}'^{13}_{o+} - \beta_2\tilde{\kappa}'^{23}_{o+}\right) \\
& + \frac{1}{4}\left[\beta_2\beta_3\tilde{\kappa}'^{13}_{e-} + \beta_1\beta_3\tilde{\kappa}'^{23}_{e-} - \beta_1\beta_2\tilde{\kappa}'^{33}_{e-} + (\beta_1^2 + \beta_2^2)\tilde{\kappa}'^{12}_{e-}\right],
\end{aligned}
\tag{A.74}
$$

$$
\begin{aligned}
C = & \frac{1}{2}(\beta_2^2 - \beta_1^2)\tilde{\kappa}'_{tr} - \frac{1}{2}\tilde{\kappa}'^{22}_{e-} - \frac{1}{4}\left[1 + |\beta|^2\right]\tilde{\kappa}'^{33}_{e-} - \frac{1}{2}\left(\beta_2\tilde{\kappa}'^{13}_{o+} + \beta_1\tilde{\kappa}'^{23}_{o+}\right) \\
& + \frac{1}{4}\left[\beta_1\beta_3\tilde{\kappa}'^{13}_{e-} - \beta_2\beta_3\tilde{\kappa}'^{23}_{e-} - (\beta_1^2 + \beta_2^2)\tilde{\kappa}'^{22}_{e-} - (\beta_2^2 + \beta_3^2)\tilde{\kappa}'^{33}_{e-}\right].
\end{aligned}
\tag{A.75}
$$

Breaking this result up into different sidereal components, and ignoring terms proportional to $\beta_\oplus\beta_L$ and β_L^2, as such are significantly smaller than $\beta_\oplus^2$, we finally obtain

$$
A = A_0 + A_1 \sin\omega_\oplus T_\oplus + A_2 \cos\omega_\oplus T_\oplus + A_3 \sin 2\omega_\oplus T_\oplus + A_4 \cos 2\omega_\oplus T_\oplus \tag{A.76}
$$

$$
B = B_0 + B_1 \sin\omega_\oplus T_\oplus + B_2 \cos\omega_\oplus T_\oplus + B_3 \sin 2\omega_\oplus T_\oplus + B_4 \cos 2\omega_\oplus T_\oplus \tag{A.77}
$$

$$
C = C_0 + C_1 \sin\omega_\oplus T_\oplus + C_2 \cos\omega_\oplus T_\oplus + C_3 \sin 2\omega_\oplus T_\oplus + C_4 \cos 2\omega_\oplus T_\oplus \tag{A.78}
$$

where[1]

$$
\begin{aligned}
A_0 = & -\tfrac{1}{8}(9\epsilon_+ - \epsilon_-)(\tilde{\kappa}_{tr}) + \tfrac{1}{8}\epsilon_-(1 - 3\cos^2\chi)(\tilde{\kappa}_{e-})^{ZZ} \\
& + \tfrac{1}{4}\beta_\oplus\{2(3\epsilon_+ - \epsilon_-\cos^2\chi)\sin\eta\cos\Omega_\oplus T_\oplus(\tilde{\kappa}_{o+})^{XY} \\
& - \tfrac{1}{2}(6\epsilon_+ - \epsilon_-\sin^2\chi)(\cos\eta\cos\Omega_\oplus T_\oplus(\tilde{\kappa}_{o+})^{XZ} + \sin\Omega_\oplus T_\oplus(\tilde{\kappa}_{o+})^{YZ})\} \\
& - \tfrac{1}{4}\beta_\oplus^2\Big\{\sin\Omega_\oplus T_\oplus\cos\Omega_\oplus T_\oplus\cos\eta(6\epsilon_+ - \epsilon_-\sin^2\chi)(\tilde{\kappa}_{e-})^{XY} \\
& + \tfrac{1}{2}\left[6\epsilon_+ - \epsilon_-\sin^2\chi\right] \times \left[\sin^2\Omega_\oplus T_\oplus - \cos^2\eta\cos^2\Omega_\oplus T_\oplus\right](\tilde{\kappa}_{e-})^{YY} \\
& + \tfrac{1}{2}\Big[\sin^2\Omega_\oplus T_\oplus(6\epsilon_+ - \epsilon_-\sin^2\chi) \\
& \qquad\qquad -2\sin^2\eta\cos^2\Omega_\oplus T_\oplus(3\epsilon_+ - \epsilon_-\cos^2\chi)\Big](\tilde{\kappa}_{e-})^{ZZ} \\
& + \left[6\epsilon_+ - \epsilon_-\left(\sin^2\chi - (1 - 3\cos^2\chi)\sin^2\eta\cos^2\Omega_\oplus T_\oplus\right)\right](\tilde{\kappa}_{tr}) \\
& + \tfrac{1}{2}\sin\eta\cos\Omega_\oplus T_\oplus(12\epsilon_+ - \epsilon_- + \epsilon_-\cos^2\chi) \\
& \qquad \times \left[\sin\Omega_\oplus T_\oplus(\tilde{\kappa}_{e-})^{XZ} - \cos\eta\cos\Omega_\oplus T_\oplus(\tilde{\kappa}_{e-})^{YZ}\right]\Big\}
\end{aligned}
\tag{A.79}
$$

$$
\begin{aligned}
A_1 = & -\tfrac{1}{2}\epsilon_-\sin\chi\cos\chi(\tilde{\kappa}_{e-})^{YZ} \\
& + \tfrac{1}{2}\beta_\oplus\epsilon_-\sin\chi\cos\chi\Big\{\sin\eta\cos\Omega_\oplus T_\oplus(\tilde{\kappa}_{o+})^{XZ} \\
& - \cos\eta\cos\Omega_\oplus T_\oplus(\tilde{\kappa}_{o+})^{XY}\Big\} \\
& + \tfrac{3}{2}\beta_L\epsilon_+(\tilde{\kappa}_{o+})^{YZ} \\
& - \tfrac{1}{4}\beta_\oplus^2\epsilon_-\sin\chi\cos\chi\cos\Omega_\oplus T_\oplus\Big\{\cos\Omega_\oplus T_\oplus(\tilde{\kappa}_{e-})^{YZ} \\
& - \sin\Omega_\oplus T_\oplus\left[\sin\eta(\tilde{\kappa}_{e-})^{XY} + \cos\eta(\tilde{\kappa}_{e-})^{XZ}\right] \\
& - \sin\eta\cos\eta\cos\Omega_\oplus T_\oplus\left[4(\tilde{\kappa}_{tr}) + (\tilde{\kappa}_{e-})^{XX}\right]\Big\}
\end{aligned}
\tag{A.80}
$$

---

[1]Note that the following table of A_j coefficients does not agree with those presented in [28]. This is the result of a minor calculation error on the part of [28], where the transformation in their equation (30) is not correctly applied. Their error effectively mapped ϵ_- to $3\epsilon_+$ and ϵ_+ to $\epsilon_-/3$. This is of no great consequence to any experimental limits derived from either expression, since none yet reported have relied upon the value of the A_j coefficients.

$$A_2 = -\tfrac{1}{2}\epsilon_- \sin\chi\cos\chi(\tilde{\kappa}_{e-})^{YZ}$$
$$+ \tfrac{1}{2}\epsilon_-\beta_\oplus \sin\chi\cos\chi\Big\{ \sin\Omega_\oplus T_\oplus(\tilde{\kappa}_{o+})^{XY}$$
$$- \sin\eta\cos\Omega_\oplus T_\oplus(\tilde{\kappa}_{o+})^{YZ}\Big\}$$
$$+ \tfrac{3}{2}\epsilon_+\beta_L(\tilde{\kappa}_{o+})^{XZ}$$
$$- \tfrac{1}{4}\beta_\oplus^2\epsilon_- \sin\chi\cos\chi\Big\{ \left(1 - \cos^2\eta\cos^2\Omega_\oplus T_\oplus\right)(\tilde{\kappa}_{e-})^{XZ}$$
$$+ \sin\eta\sin\Omega_\oplus T_\oplus\cos\Omega_\oplus T_\oplus\left(4(\tilde{\kappa}_{tr}) + (\tilde{\kappa}_{e-})^{YY}\right)$$
$$- \cos\eta\cos\Omega_\oplus T_\oplus\sin\eta\cos\Omega_\oplus T_\oplus(\tilde{\kappa}_{e-})^{XY}$$
$$- \cos\eta\cos\Omega_\oplus T_\oplus\sin\Omega_\oplus T_\oplus(\tilde{\kappa}_{e-})^{YZ}\Big\}$$

$$\text{(A.81)}$$

$$A_3 = -\tfrac{1}{4}\epsilon_- \sin^2\chi(\tilde{\kappa}_{e-})^{XY}$$
$$- \tfrac{1}{4}\epsilon_-\beta_\oplus \sin^2\chi\Big\{ \sin\Omega_\oplus T_\oplus(\tilde{\kappa}_{o+})^{XZ}$$
$$+ \cos\eta\cos\Omega_\oplus T_\oplus(\tilde{\kappa}_{o+})^{YZ}\Big\}$$
$$- \tfrac{1}{8}\epsilon_-\beta_\oplus^2 \sin^2\chi\Big\{ (1 - \sin^2\eta\cos^2\Omega_\oplus T_\oplus)(\tilde{\kappa}_{e-})^{XY}$$
$$+ \sin\eta\cos\eta\cos^2\Omega_\oplus T_\oplus(\tilde{\kappa}_{e-})^{XZ}$$
$$+ \sin\eta\sin\Omega_\oplus T_\oplus\cos\Omega_\oplus T_\oplus(\tilde{\kappa}_{e-})^{YZ}$$
$$+ \cos\eta\sin\Omega_\oplus T_\oplus\cos\Omega_\oplus T_\oplus\left(4(\tilde{\kappa}_{tr}) + (\tilde{\kappa}_{e-})^{ZZ}\right)\Big\}$$

$$\text{(A.82)}$$

$$A_4 = +\tfrac{1}{8}\epsilon_- \sin^2\chi\left[(\tilde{\kappa}_{e-})^{YY} - (\tilde{\kappa}_{e-})^{XX}\right]$$
$$+ \tfrac{1}{4}\epsilon_-\beta_\oplus \sin^2\chi\Big\{ \sin\Omega_\oplus T_\oplus(\tilde{\kappa}_{o+})^{YZ}$$
$$- \cos\eta\cos\Omega_\oplus T_\oplus(\tilde{\kappa}_{o+})^{XZ})\Big\}$$
$$- \tfrac{1}{8}\epsilon_-\beta_\oplus^2 \sin^2\chi\Big\{ (\tilde{\kappa}_{e-})^{XX}$$
$$+ \sin^2\eta\cos^2\Omega_\oplus T_\oplus(\tilde{\kappa}_{e-})^{YY} - \sin^2\Omega_\oplus T_\oplus(\tilde{\kappa}_{e-})^{ZZ}$$
$$+ 2(\cos^2\eta\cos^2\Omega_\oplus T_\oplus - \sin^2\Omega_\oplus T_\oplus)(\tilde{\kappa}_{tr})$$
$$- \sin\eta\sin\Omega_\oplus T_\oplus\cos\Omega_\oplus T_\oplus(\tilde{\kappa}_{e-})^{XZ}$$
$$- \sin\eta\cos\eta\cos^2\Omega_\oplus T_\oplus(\tilde{\kappa}_{e-})^{YZ}\Big\}$$

$$\text{(A.83)}$$

$$B_0 = \tfrac{1}{2}\beta_L \sin\chi(\tilde{\kappa}_{o+})^{XY} \tag{A.84}$$

$$
\begin{aligned}
B_1 = &+\tfrac{1}{2}\sin\chi(\tilde{\kappa}_{e-})^{XZ} \\
&-\tfrac{1}{2}\beta_\oplus \sin\chi\Big\{ \sin\Omega_\oplus T_\oplus(\tilde{\kappa}_{o+})^{XY} \\
&-\sin\eta\cos\Omega_\oplus T_\oplus(\tilde{\kappa}_{o+})^{YZ}\Big\} \\
&+\tfrac{1}{2}\beta_L \cos\chi(\tilde{\kappa}_{o+})^{XZ} \\
&+\tfrac{1}{4}\beta_\oplus^2 \sin\chi\Big\{ \sin\eta\cos\eta\cos^2\Omega_\oplus T_\oplus(\tilde{\kappa}_{e-})^{XY} \\
&+\sin\eta\sin\Omega_\oplus T_\oplus\cos\Omega_\oplus T_\oplus\left[4(\tilde{\kappa}_{tr})+(\tilde{\kappa}_{e-})^{YY}\right] \\
&+\left(\sin^2\eta+\cos^2\eta\sin^2\Omega_\oplus T_\oplus\right)(\tilde{\kappa}_{e-})^{XZ} \\
&-\cos\eta\sin\Omega_\oplus T_\oplus\cos\Omega_\oplus T_\oplus(\tilde{\kappa}_{e-})^{YZ}\Big\}
\end{aligned}
\tag{A.85}
$$

$$
\begin{aligned}
B_2 = &-\tfrac{1}{2}\sin\chi(\tilde{\kappa}_{e-})^{YZ} \\
&+\tfrac{1}{2}\beta_\oplus \sin\chi\Big\{ \sin\eta\cos\Omega_\oplus T_\oplus(\tilde{\kappa}_{o+})^{XZ} \\
&-\cos\eta\cos\Omega_\oplus T_\oplus(\tilde{\kappa}_{o+})^{XY}\Big\} \\
&-\tfrac{1}{2}\beta_L \cos\chi(\tilde{\kappa}_{o+})^{YZ} \\
&-\tfrac{1}{4}\beta_\oplus^2 \sin\chi\Big\{ \cos^2\Omega_\oplus T_\oplus(\tilde{\kappa}_{e-})^{YZ} \\
&-\sin\Omega_\oplus T_\oplus\cos\Omega_\oplus T_\oplus\left[\sin\eta(\tilde{\kappa}_{e-})^{XY}+\cos\eta(\tilde{\kappa}_{e-})^{XZ}\right] \\
&-\sin\eta\cos\eta\cos^2\Omega_\oplus T_\oplus\left[4(\tilde{\kappa}_{tr})+(\tilde{\kappa}_{e-})^{XX}\right]\Big\}
\end{aligned}
\tag{A.86}
$$

$$
\begin{aligned}
B_3 = &+\tfrac{1}{4}\cos\chi\left((\tilde{\kappa}_{e-})^{YY}-(\tilde{\kappa}_{e-})^{XX}\right) \\
&+\tfrac{1}{2}\beta_\oplus \cos\chi\Big\{ \sin\Omega_\oplus T_\oplus(\tilde{\kappa}_{o+})^{YZ} \\
&-\cos\eta\cos\Omega_\oplus T_\oplus(\tilde{\kappa}_{o+})^{XZ}\Big\} \\
&+\tfrac{1}{4}\beta_\oplus^2 \cos\chi\Big\{ \sin\eta\sin\Omega_\oplus T_\oplus\cos\Omega_\oplus T_\oplus(\tilde{\kappa}_{e-})^{XZ} \\
&+\sin^2\Omega_\oplus T_\oplus\left[2(\tilde{\kappa}_{tr})-(\tilde{\kappa}_{e-})^{XX}\right] \\
&-\cos^2\eta\cos^2\Omega_\oplus T_\oplus\left[2(\tilde{\kappa}_{tr})-(\tilde{\kappa}_{e-})^{YY}\right] \\
&+\cos\eta\sin\eta\cos^2\Omega_\oplus T_\oplus(\tilde{\kappa}_{e-})^{YZ}\Big\}
\end{aligned}
\tag{A.87}
$$

$$
\begin{aligned}
B_4 = {} & +\tfrac{1}{2}\cos\chi(\tilde{\kappa}_{e-})^{XY} \\
& + \tfrac{1}{2}\beta_\oplus\cos\chi\Big\{\sin\Omega_\oplus T_\oplus(\tilde{\kappa}_{o+})^{XZ} \\
& + \cos\eta\cos\Omega_\oplus T_\oplus(\tilde{\kappa}_{o+})^{YZ}\Big\} \\
& + \tfrac{1}{4}\beta_\oplus^2\cos\chi\Big\{\sin\eta\cos\eta\cos^2\Omega_\oplus T_\oplus(\tilde{\kappa}_{e-})^{XZ} \\
& - \sin\eta\sin\Omega_\oplus T_\oplus\cos\Omega_\oplus T_\oplus(\tilde{\kappa}_{e-})^{YZ} \\
& + (1 - \sin^2\eta\cos^2\Omega_\oplus T_\oplus)(\tilde{\kappa}_{e-})^{XY} \\
& + \cos\eta\sin\Omega_\oplus T_\oplus\cos\Omega_\oplus T_\oplus\left[(\tilde{\kappa}_{tr}) + (\tilde{\kappa}_{e-})^{ZZ}\right]\Big\}
\end{aligned}
\tag{A.88}
$$

$$
\begin{aligned}
C_0 = {} & +\tfrac{3}{8}\sin^2\chi(\tilde{\kappa}_{e-})^{ZZ} \\
& + \tfrac{1}{4}\sin^2\chi\beta_\oplus\Big\{\sin\Omega_\oplus T_\oplus(\tilde{\kappa}_{o+})^{YZ} \\
& + \cos\Omega_\oplus T_\oplus\left[2\sin\eta(\tilde{\kappa}_{o+})^{XY} + \cos\eta(\tilde{\kappa}_{o+})^{XZ}\right]\Big\} \\
& + \tfrac{1}{8}\beta_\oplus^2\sin^2\chi\Big\{\left[2(\tilde{\kappa}_{tr}) - (\tilde{\kappa}_{e-})^{YY}\right] \\
& + \sin^2\eta\cos^2\Omega_\oplus T_\oplus\left[(\tilde{\kappa}_{e-})^{ZZ} - (\tilde{\kappa}_{e-})^{XX} - 6(\tilde{\kappa}_{tr})\right] \\
& + \sin^2\Omega_\oplus T_\oplus\left[(\tilde{\kappa}_{e-})^{YY} - (\tilde{\kappa}_{e-})^{XX}\right] \\
& + 2\cos\eta\sin\Omega_\oplus T_\oplus\cos\Omega_\oplus T_\oplus(\tilde{\kappa}_{e-})^{XY} \\
& - \sin\eta\sin\Omega_\oplus T_\oplus\cos\Omega_\oplus T_\oplus(\tilde{\kappa}_{e-})^{XZ} \\
& + \sin\eta\cos\eta\cos^2\Omega_\oplus T_\oplus(\tilde{\kappa}_{e-})^{YZ}\Big\}
\end{aligned}
\tag{A.89}
$$

$$
\begin{aligned}
C_1 = &-\tfrac{1}{2}\sin\chi\cos\chi(\tilde{\kappa}_{e-})^{YZ} \\
&+\tfrac{1}{2}\beta_\oplus\sin\chi\cos\chi\Big\{\sin\eta\cos\Omega_\oplus T_\oplus(\tilde{\kappa}_{o+})^{XZ} \\
&-\cos\eta\cos\Omega_\oplus T_\oplus(\tilde{\kappa}_{o+})^{XY}\Big\} \\
&-\tfrac{1}{2}\beta_L(\tilde{\kappa}_{o+})^{YZ} \\
&+\tfrac{1}{4}\beta_\oplus^2\sin\chi\cos\chi\Big\{\sin\Omega_\oplus T_\oplus\cos\Omega_\oplus T_\oplus\sin\eta(\tilde{\kappa}_{e-})^{XY} \\
&+\sin\Omega_\oplus T_\oplus\cos\Omega_\oplus T_\oplus\cos\eta(\tilde{\kappa}_{e-})^{XZ} \\
&+\sin\eta\cos\eta\cos^2\Omega_\oplus T_\oplus\left[4(\tilde{\kappa}_{tr})+(\tilde{\kappa}_{e-})^{XX}\right] \\
&-\cos^2\Omega_\oplus T_\oplus(\tilde{\kappa}_{e-})^{YZ}\Big\}
\end{aligned}
\tag{A.90}
$$

$$
\begin{aligned}
C_2 = &-\tfrac{1}{2}\cos\chi\sin\chi(\tilde{\kappa}_{e-})^{XZ} \\
&+\tfrac{1}{2}\beta_\oplus\cos\chi\sin\chi\Big\{\sin\Omega_\oplus T_\oplus(\tilde{\kappa}_{o+})^{XY} \\
&-\sin\eta\cos\Omega_\oplus T_\oplus(\tilde{\kappa}_{o+})^{YZ}\Big\} \\
&-\tfrac{1}{2}\beta_L(\tilde{\kappa}_{o+})^{XZ} \\
&-\tfrac{1}{4}\beta_\oplus^2\cos\chi\sin\chi\Big\{\cos\eta\sin\eta\cos^2\Omega_\oplus T_\oplus(\tilde{\kappa}_{e-})^{XY} \\
&+(1-\cos^2\eta\cos^2\Omega_\oplus T_\oplus)(\tilde{\kappa}_{e-})^{XZ} \\
&-\cos\eta\sin\Omega_\oplus T_\oplus\cos\Omega_\oplus T_\oplus(\tilde{\kappa}_{e-})^{YZ} \\
&+\sin\eta\sin\Omega_\oplus T_\oplus\cos\Omega_\oplus T_\oplus\left(4(\tilde{\kappa}_{tr})+(\tilde{\kappa}_{e-})^{YY}\right)\Big\}
\end{aligned}
\tag{A.91}
$$

$$
\begin{aligned}
C_3 = &+\tfrac{1}{4}\left(1+\cos^2\chi\right)(\tilde{\kappa}_{e-})^{XY} \\
&+\tfrac{1}{4}\left(1+\cos^2\chi\right)\beta_\oplus\Big\{\sin\Omega_\oplus T_\oplus(\tilde{\kappa}_{o+})^{XZ} \\
&+\cos\eta\cos\Omega_\oplus T_\oplus(\tilde{\kappa}_{o+})^{YZ}\Big\} \\
&+\tfrac{1}{8}\left(1+\cos^2\chi\right)\beta_\oplus^2\Big\{(1-\sin^2\eta\cos^2\Omega_\oplus T_\oplus)(\tilde{\kappa}_{e-})^{XY} \\
&+\sin\eta\cos\eta\cos^2\Omega_\oplus T_\oplus(\tilde{\kappa}_{e-})^{XZ} \\
&-\sin\eta\sin\Omega_\oplus T_\oplus\cos\Omega_\oplus T_\oplus(\tilde{\kappa}_{e-})^{YZ} \\
&+\cos\eta\sin\Omega_\oplus T_\oplus\cos\Omega_\oplus T_\oplus\left[4(\tilde{\kappa}_{tr})+(\tilde{\kappa}_{e-})^{ZZ}\right]\Big\}
\end{aligned}
\tag{A.92}
$$

$$
\begin{aligned}
C_4 = {} & +\tfrac{1}{8}\left(1+\cos^2\chi\right)\left((\tilde{\kappa}_{e-})^{XX}-(\tilde{\kappa}_{e-})^{YY}\right) \\
& -\tfrac{1}{4}\left(1+\cos^2\chi\right)\beta_\oplus\Big\{\sin\Omega_\oplus T_\oplus(\tilde{\kappa}_{o+})^{YZ} \\
& -\cos\eta\cos\Omega_\oplus T_\oplus(\tilde{\kappa}_{o+})^{XZ}\Big\} \\
& -\tfrac{1}{8}\left(1+\cos^2\chi\right)\beta_\oplus^2\Big\{\sin\eta\sin\Omega_\oplus T_\oplus\cos\Omega_\oplus T_\oplus(\tilde{\kappa}_{e-})^{XZ} \\
& +\sin\eta\cos\eta\cos^2\Omega_\oplus T_\oplus(\tilde{\kappa}_{e-})^{YZ} \\
& -\left(1-\sin^2\eta\cos^2\Omega_\oplus T_\oplus\right)\left[(\tilde{\kappa}_{tr})-(\tilde{\kappa}_{e-})^{YY}\right] \\
& +\sin^2\Omega_\oplus T_\oplus\left[3(\tilde{\kappa}_{tr})+(\tilde{\kappa}_{e-})^{ZZ}\right] \\
& -\cos^2\eta\cos^2\Omega_\oplus T_\oplus(\tilde{\kappa}_{tr})\Big\}
\end{aligned}
\tag{A.93}
$$

A.4 Coordinate Rescalings

Here we present the details of our calculation of the scale $\mathcal{S}$ at which Lorentz violation has been constrained for photons relative to electrons, based entirely upon constraints obtained from terrestrial experiments. To accomplish this, we must make direct comparisons between the results of several experiments which variously report constraints upon Lorentz violation for photons, electrons, and protons. Making use of these constraints is somewhat complicated by the assumptions made regarding the possibility of Lorentz violation in other sectors of the SME.

The result of any physical measurement is necessarily a dimensionless quantity, as any statement of a system's length, mass, or velocity can only be expressed in units defined by the characteristics of a selected reference. Similarly, measurements of shifts and anisotropies in the vacuum speed of light must be defined in terms of the velocity of a chosen reference particle. In the SME, the limiting velocity of any such reference particle is also subject to Lorentz-symmetry violating shifts and anisotropies. As a result, constraints upon the deviation of the speed of light based upon interactions of light with electrons must be narrowly interpreted as limits on the difference between the degree to which Lorentz symmetry is violated in each sector. This is a general feature of all tests of Lorentz symmetry, which generally must be described as setting limits on combinations of coefficients associated with not one, but all involved particle

species. As we outline below, the specific combination depends upon our choice of coordinate system.

Of particular interest in estimating $\mathcal{S}$ are the constraints on the electron $c_e^{\mu\nu}$ coefficients. As has been noted elsewhere [27, 28, 39], in the context of one-flavor QED where for simplicity we have set all other SME coefficients to zero, a symmetric and traceless $c_e^{\mu\nu}$ exhibits the same phenomenology as a theory in which $c_e^{\mu\nu} = 0$ but

$$(k_F)^{\mu\nu\rho\sigma} = \frac{1}{2}(\eta^{\mu\rho}\tilde{k}^{\nu\sigma} - \eta^{\mu\sigma}\tilde{k}^{\nu\rho} + \eta^{\nu\sigma}\tilde{k}^{\mu\rho} - \eta^{\nu\rho}\tilde{k}^{\mu\sigma}) \tag{A.94}$$

in the photon sector, where

$$\tilde{k}^{\mu\nu} = -2c^{\mu\nu} + \mathcal{O}\left((c^{\mu\nu})^2\right) . \tag{A.95}$$

Note that $\tilde{k}^{\mu\nu} = (k_F)_\alpha{}^{\mu\alpha\nu}$ is composed of $\tilde{\kappa}_{e-}$, $\tilde{\kappa}_{o+}$, and $\tilde{\kappa}_{tr}$. Thus, $\tilde{k}^{\mu\nu}$ parameterizes the ways that c_{ph} can deviate from the canonical c, which in this theory is the limiting velocity for electrons. It follows that a $\tilde{k}^{\mu\nu}$ model must be physically equivalent to a $c^{\mu\nu}$ model if equation (A.95) holds. This equivalence can be formally established via coordinate rescalings that transform one model into the other [27,28,39]. This implies that for experiments in which the relevant physics is confined to the interaction of photons with electrons, constraints on $\tilde{k}^{\mu\nu}$ can be interpreted as limits on the electron $c_e^{\mu\nu}$ coefficients. More generally, the results of such tests can only depend upon (and thus provide bounds for) the value of $2c_e^{\mu\nu} - \tilde{k}^{\mu\nu}$.

Experimental tests of Lorentz and CPT symmetry are not usually confined to one-flavor QED; other particle species are often involved. In such situations, the above analysis is readily generalized. Because we may only measure differences between $\tilde{k}^\mu$ and the species specific $c^{\mu\nu}$ coefficients, we may choose one particle species to serve as the reference "ruler", and thus work in a coordinate system in which that species' $c^{\mu\nu}$ coefficient (or $\tilde{k}^{\mu\nu}$, if the reference is light) is zero.

In this context, we may now estimate the value $\mathcal{S}$ provided by terrestrial experiments for the interaction of light with electrons. Specifically, we will use the results of a Cs-fountain clock experiment [72], and those of a series of tests involving optical resonators [7]. These tests are sensitive to Lorentz violation in conventional matter, which is made up of protons, neutrons, and electrons, interacting electromagnetically.

In this four-species system, there can exist only three independent combinations of $c_p^{\mu\nu}$, $c_n^{\mu\nu}$, $c_e^{\mu\nu}$ and $\tilde{k}^{\mu\nu}$, where the subscripts p, n, and e respectively denote the coefficients belonging to protons, neutrons, and electrons. We define our coordinates such that the protons' $c_p^{\mu\nu}$ vanish.

Although the Cs-fountain test [72] involves protons, neutrons, electrons, and electromagnetism, the particular transitions under consideration are insensitive at leading order to the neutron SME coefficients [68]. To eliminate the strong magnetic-field dependence present in each of the observed transition frequencies, the analysis of [72] uses a specific observable constructed from three frequencies so as to be insensitive to the electron's SME coefficients. As a result, the Cs-fountain of [72] is only sensitive to the value of $2c_p^{\mu\nu} - \tilde{k}^{\mu\nu}$. The result is a constraint upon the eight spatially anisotropic components of this term at the level of

$$|2c_p^{\mu\nu} - \tilde{k}^{\mu\nu}| < 10^{-21} \ldots 10^{-25} \ . \tag{A.96}$$

We note that Ref. [72] chooses to state these limits in coordinates such that $\tilde{k}^{\mu\nu} = 0$, which corresponds to using light as a reference. In our coordinates, the Cs-fountain experiment provides the constraint $|\tilde{k}^{\mu\nu}| < 10^{-21} \ldots 10^{-25}$ for the anisotropic components of $\tilde{k}^{\mu\nu}$.

Next, we consider optical resonator experiments [7], which as mentioned in Sec.3.2, measure the resonance frequencies f of light propagating in vacuum inside two differently oriented Fabry-Pérot cavities. As previously shown [21,27,28], these experiments are sensitive to spatial anisotropies in the speed of light ($\tilde{k}^{\mu\nu}$) and to variations in the dimensions of the resonators themselves. As before, all four of the above particle species are involved in this experiment. The cavity size, however, is primarily determined by the electromagnetic interactions in the chemical bonds. It therefore follows that the neutron's contribution to the cavity size must be suppressed because it is uncharged, having only a magnetic moment. Moreover, the cavities are made of fused silica SiO_2, and the common isotopes of Oxygen and Silicon have even numbers of neutrons and spin zero. Pairing effects would therefore tend to further suppress the influence of the neutron spin, and so we conclude that the cavity frequencies should be largely unaffected by $c_n^{\mu\nu}$. This leaves two independent combinations of parame-

ters capable of influencing the observable F constructed from the cavity frequencies f. This observable is given by, to leading order

$$F = \text{const.} + A_{\mu\nu}(2c_e^{\mu\nu} - \tilde{k}^{\mu\nu}) + B_{\mu\nu}(2c_p^{\mu\nu} - \tilde{k}^{\mu\nu}) , \qquad (A.97)$$

where $A_{\mu\nu}$ and $B_{\mu\nu}$ are constants, and $c_p^{\mu\nu} = 0$ in our chosen coordinates. This decomposition has been explicitly derived for resonators made of different materials, including fused silica [21, 33, 61], permitting independent constraints upon the anisotropic components of $c_e^{\mu\nu}$ and $\tilde{k}^{\mu\nu}$ to be obtained by combining the results of two different optical resonator experiments [33]. Based on this comparison, the parity-even anisotropic components of $\tilde{k}^{\mu\nu}$ and $c_e^{\mu\nu}$ are independently constrained at the level of 10^{-16} [33]. More recent improvements upon the fused silica resonator experiment, combined with the result [61] that $A_{\mu\nu}$ and $B_{\mu\nu}$ are of similar size, provides limits on the parity-odd components of $2c_e^{\mu\nu} - 2\tilde{k}^{\mu\nu}$ at the level of 10^{-13} [7].

Taken together, the data in Refs. [11, 57–62] establishes that $\mathcal{S} \sim 10^{-13}$, dominated by the contribution of the parity-odd $\tilde{\kappa}_{o+}$ and c_e^{0J} coefficients. Because the limit we will derive on $\tilde{\kappa}_{tr}$ lies above this scale, we may drop all other Lorentz-violating corrections from our analysis, as claimed in the text.

Because our analysis deals only with the interaction of photons with electrons, we are free to express our analysis in coordinates in which $c_e^{\mu\nu} = 0$, and do so in the main text. This leaves only the $\tilde{\kappa}_{tr}$ component of $(k_F)^{\mu\nu\rho\sigma}$, and so equation (A.95) implies that a model with

$$c_e^{\mu\nu} = -\frac{1}{4}\tilde{\kappa}_{tr} \, \text{diag}(3, 1, 1, 1) \qquad (A.98)$$

will exhibit the same phenomenology. This is done with the understanding that our constraint on $\tilde{\kappa}_{tr}$ based on the (3.43) and (3.44) effects is really a constraint upon $\tilde{\kappa}_{tr} - \frac{4}{3}c_e^{00}$. An exception to this convention can be found in the calculation presented in Appendix A.5, which is more easily performed using the $c_e^{\mu\nu}$ model.

A.5 Photon-decay rate

Photon decay rates in the presence of Lorentz violation have already been determined [219]. However, this result is not directly applicable in the present context

because it refers to the dimension-three Chern–Simons type SME coefficient $(k_{AF})^\mu$. Moreover, it considers photon triple splitting instead of pair creation. In this appendix, we derive the tree-level photon decay rate into a fermion–antifermion pair in the presence of the dimension-four $\tilde{\kappa}_{tr}$ coefficient appropriate for our purposes.

Our starting point is a model with Lorentz-violating photons and conventional charged leptons. However, in the present situation it is more convenient to consider a physically equivalent model constructed with the coordinate redefinition discussed in part 2.5. In particular, we remove all Lorentz violation from the photon sector at the cost of introducing a Lorentz-breaking $c^{\mu\nu}$ coefficient in the lepton sector:

$$\mathcal{L}' = \frac{1}{2} i \overline{\psi} \left(\gamma^\mu + c^{\mu\nu} \gamma_\nu \right) \overset{\leftrightarrow}{D^\mu} \psi - m \overline{\psi}\psi - \frac{1}{4} F^2 \, , \tag{A.99}$$

where $D_\mu = \partial_\mu + ieA_\mu$ is the usual covariant derivative. The Lorentz-violating SME coefficient $c^{\mu\nu}$ is given explicitly by equation (A.98). We have chosen to calculate the effects of $\tilde{\kappa}_{tr}$ using this alternative representation for two reasons. First, perturbative calculations in quantum field theory rely on the quantization of the free-field sectors of the model. Such quantization has not yet been fully addressed, whereas the quantization of SME fermions is comparatively well understood [4, 5, 26]. Second, this choice of coordinates permits us to employ the methodology and notation of previous tree-level calculations involving $c^{\mu\nu}$ fermions [52].

Due to the presence of $\tilde{\kappa}_{tr}$, the lepton sector of the model (A.99) contains unconventional time derivatives. It follows that the time evolution of ψ can be non-unitary, so its asymptotic states cannot directly be identified with physical free-particle states. A standard approach to avoid this potential interpretational difficulty is a redefinition of the spinor field chosen to eliminate the additional time derivatives [52, 220]. In the present situation, the field redefinition just amounts to a rescaling

$$\psi \equiv \frac{1}{\sqrt{1 - \frac{3}{4}\tilde{\kappa}_{tr}}} \chi \, , \tag{A.100}$$

so it is not strictly mandatory. We nevertheless implement the redefinition (A.100) both for generality and compatibility to previous [52] and future studies.

With these considerations, the Lagrangian (A.99) becomes

$$\mathcal{L} = \frac{1}{2} i \, \bar{\chi} \, \tilde{\eta}^{\mu\nu} \gamma_\nu \, \overleftrightarrow{D^\mu} \, \chi - \tilde{m} \, \bar{\chi}\chi - \frac{1}{4} F^2 \, , \qquad\qquad \text{(A.101)}$$

where we have defined

$$\tilde{m} \equiv \frac{m}{1 - \frac{3}{4}\tilde{\kappa}_{tr}},$$

$$\tilde{\eta}^{\mu\nu} \equiv \text{diag}(1, -\lambda, -\lambda, -\lambda), \qquad\qquad \text{(A.102)}$$

$$\lambda \equiv \frac{1 + \frac{1}{4}\tilde{\kappa}_{tr}}{1 - \frac{3}{4}\tilde{\kappa}_{tr}}.$$

We emphasize that the field redefinition (A.100) is a canonical transformation, and as such it leaves unchanged the physics. In particular, the free fermions in model (A.99) possess the same dispersion relation as those in (A.101).

We remark that equation (A.100) fails to be manifestly Lorentz coordinate covariant, so the specific form of Lagrangian (A.101) holds only in the frame in which the field redefinition has been performed. Here, we specify this to be the Sun-centered celestial equatorial frame (SCCEF). Since $\tilde{\kappa}_{tr}$ is isotropic, and the fractional contribution from all other SCCEF $\tilde{\kappa}$'s in the Earth's inertial frame is suppressed by at least four orders of magnitude, (A.101) is also the leading order Lagrangian in the frame of any Earth-based laboratory. Note also that $\tilde{\eta}^{\mu\nu}$, and thus the Lagrangians (A.99) and (A.101), are singular for $\tilde{\kappa}_{tr} = -4$ and $\tilde{\kappa}_{tr} = \frac{4}{3}$ as λ becomes zero or infinite in these limits. On the other hand, the dispersion relation (3.46) establishes that at $\tilde{\kappa}_{tr} = 1$ the model becomes singular. This apparent paradox arises because the coordinate rescaling required to generate Lagrangian (A.99) from the original $\tilde{\kappa}_{tr}$ model has been implemented only at leading order in $\tilde{\kappa}_{tr}$.

The Feynman rules can now be inferred from Lagrangian (A.99). The appropriate tree-level Feynman diagram for photon decay is depicted in Figure A.1. For the corresponding matrix element, we obtain

$$i\mathcal{M}_{rs} = -ie \, \epsilon_\mu(p) \, \tilde{\eta}^{\mu\nu} \, \bar{u}^{(r)}(q) \, \gamma_\nu \, v^{(s)}(k) \, , \qquad\qquad \text{(A.103)}$$

where the various polarization and momentum assignments are defined in Figure A.1. The next step is the calculation of $|\mathcal{M}_{rs}|^2$ followed by the usual summation over final
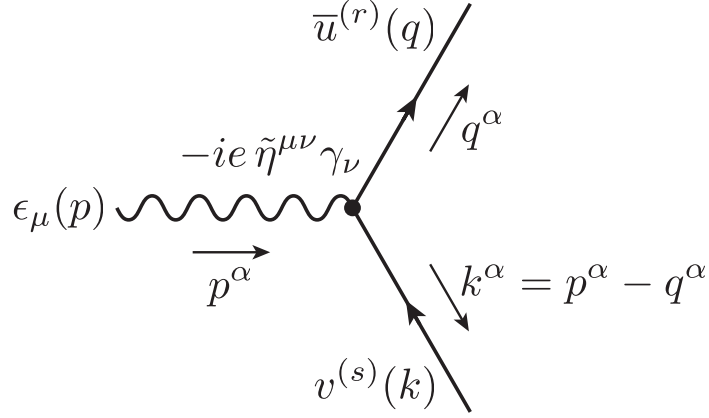
Figure A.1: Tree-level Feynman diagram for photon decay. Lorentz-violating effects are contained in the modified dispersion relation for q^α and k^α as well as in the electromagnetic vertex containing $\tilde{\eta}_{\mu\nu}$.

spin states and averaging over the initial photon polarizations. We obtain

$$\overline{|\mathcal{M}|^2} \equiv \frac{1}{2} \sum_{\epsilon} \sum_{r,s} |\mathcal{M}_{rs}|^2 = e^2 \left[4\tilde{m}^2 + 2\lambda^2(1-\lambda^2)(\vec{q}^{\,2} + \vec{k}^{\,2}) + (1-\lambda^2)^2 E_\gamma^2 \right],$$

(A.104)

where $E_\gamma = |\vec{p}|$ is the photon energy and $\vec{q}$ and $\vec{k}$ are the lepton and anti-lepton 3-momenta, respectively. To arrive at this result, energy–momentum conservation, the usual relation for photon-polarization sums, and trace identities for Dirac matrices have been used. Moreover, we have employed the results for SME spinor projectors in [52] with the normalization chosen such that $N(\vec{q}) = 2E_q = 2\sqrt{\tilde{m}^2 + \lambda^2 \vec{q}^{\,2}}$, etc.

The final step is the phase-space integration. In the conventional Lorentz-symmetric case, the decay rate for massive particles is defined in the particle's rest frame with a kinematic factor inversely proportional to its mass. This fact seems to interfere with a trivial extension to the present massless case. We therefore adopt the convention of [128] and define the decay rate in terms of the photon energy E_γ in the Sun-centered celestial equatorial frame:

$$\Gamma_{\text{pair}} = \frac{1}{4\pi^2} \frac{1}{2E_\gamma} \int \frac{d^3q}{2E_q} \frac{d^3k}{2E_k} \overline{|\mathcal{M}|^2}\, \delta^{(4)}(p - q - k)\,.$$

(A.105)

This yields

$$\Gamma_{\text{pair}} = \alpha \frac{[\tilde{\kappa}_{tr}(\tilde{\kappa}_{tr} - 4)E_\gamma^2 + 4m^2]\sqrt{\tilde{\kappa}_{tr}(\tilde{\kappa}_{tr} - 4)E_\gamma^2 - 8m^2}}{\frac{3}{8}E_\gamma^2(4 + \tilde{\kappa}_{tr})(4 - 3\tilde{\kappa}_{tr})\sqrt{\tilde{\kappa}_{tr}(\tilde{\kappa}_{tr} - 4)}} \tag{A.106}$$

for the exact tree-level decay rate within the context of Lagrangian (A.101). It should be understood that equation (A.106) applies only for $-4 < \tilde{\kappa}_{tr} < 0$ and for photons above threshold. We note that undoing our initial coordinate redefinition would generate sub-leading corrections to (A.106).

Appendix B

Appendices to Chapter 4

B.1 (k_F) Identities

Since k_F has the symmetries of the Riemann tensor, we know that

$$(k_F)_{\kappa\lambda\mu\nu} = (k_F)_{\mu\nu\kappa\lambda} = -(k_F)_{\lambda\kappa\mu\nu} = -(k_F)_{\kappa\lambda\nu\mu} \tag{B.1}$$

and

$$(k_F)_{\kappa\lambda\mu\nu} + (k_F)_{\kappa\nu\lambda\mu} + (k_F)_{\kappa\mu\nu\lambda} = 0. \tag{B.2}$$

This means that given a set of four 4-vectors

$$v = (v^0, \vec{v}) \tag{B.3}$$

$$x = (x^0, \vec{x}) \tag{B.4}$$

$$y = (y^0, \vec{y}) \tag{B.5}$$

$$z = (z^0, \vec{z}), \tag{B.6}$$

then the product (summed over repeated indexes) $(k_F)_{\kappa\lambda\mu\nu}w^\kappa x^\lambda y^\mu z^\nu$ can be written as

$$
\begin{aligned}
(k_F)_{\kappa\lambda\mu\nu}w^\kappa x^\lambda y^\mu z^\nu \;=\;& (k_F)_{0\lambda\mu\nu}w^0 x^\lambda y^\mu z^\nu + (k_F)_{j\lambda\mu\nu}w^j x^\lambda y^\mu z^\nu \\
=\;& (k_F)_{0\lambda0\nu}w^0 x^\lambda y^0 z^\nu + (k_F)_{0\lambda j\nu}w^0 x^\lambda y^j z^\nu \\
& + (k_F)_{j\lambda0\nu}w^j x^\lambda y^0 z^\nu + (k_F)_{j\lambda k\nu}w^j x^\lambda y^k z^\nu \\
=\;& (k_F)_{0j0k}w^0 x^j y^0 z^k + (k_F)_{0kj\nu}w^0 x^k y^j z^\nu \\
& + (k_F)_{j\lambda0k}w^j x^\lambda y^0 z^k + (k_F)_{j\lambda k\nu}w^j x^\lambda y^k z^\nu \\
=\;& (k_F)_{0j0k}w^0 x^j y^0 z^k + (k_F)_{j\lambda k\nu}w^j x^\lambda y^k z^\nu \\
& + (k_F)_{0kj0}w^0 x^k y^j z^0 + (k_F)_{0kjl}w^0 x^k y^j z^l \\
& + (k_F)_{j00k}w^j x^0 y^0 z^k + (k_F)_{jl0k}w^j x^l y^0 z^k \\
=\;& (k_F)_{0j0k}w^0 x^j y^0 z^k + (k_F)_{j0k0}w^j x^0 y^k z^0 + (k_F)_{jlk0}w^j x^l y^k z^0 \\
& + (k_F)_{j0kl}w^j x^0 y^k z^l + (k_F)_{jlkm}w^j x^l y^k z^m + (k_F)_{0kj0}w^0 x^k y^j z^0 \\
& + (k_F)_{0kjl}w^0 x^k y^j z^l + (k_F)_{j00k}w^j x^0 y^0 z^k + (k_F)_{jl0k}w^j x^l y^0 z^k \\
=\;& (k_F)_{0j0k}w^0 x^j y^0 z^k + (k_F)_{0j0k}w^j x^0 y^k z^0 - (k_F)_{jl0k}w^j x^l y^k z^0 \\
& + (k_F)_{j0kl}w^j x^0 y^k z^l + (k_F)_{jlkm}w^j x^l y^k z^m - (k_F)_{0j0k}w^0 x^k y^j z^0 \\
& + (k_F)_{jl0k}w^0 x^k y^j z^l - (k_F)_{0j0k}w^j x^0 y^0 z^k + (k_F)_{jl0k}w^j x^l y^0 z^k \\
=\;& (k_F)_{0j0k}\left(w^0 x^j y^0 z^k + w^j x^0 y^k z^0 - w^0 x^k y^j z^0 - w^j x^0 y^0 z^k\right) \\
& + (k_F)_{jl0k}\left(w^0 x^k y^j z^l - w^j x^l y^k z^0 + w^j x^l y^0 z^k\right) \\
& + (k_F)_{j0kl}w^j x^0 y^k z^l + (k_F)_{jlkm}w^j x^l y^k z^m \\
=\;& (k_F)_{0j0k}\left(w^0 x^j y^0 z^k + w^j x^0 y^k z^0 - w^0 x^k y^j z^0 - w^j x^0 y^0 z^k\right) \\
& + (k_F)_{jl0k}\left(w^0 x^k y^j z^l - w^j x^l y^k z^0 + w^j x^l y^0 z^k - w^k x^0 y^j z^l\right) \\
& + (k_F)_{jlkm}w^j x^l y^k z^m
\end{aligned}
$$

In terms of $\tilde{\kappa}_{e-}$, $\tilde{\kappa}_{o+}$, and $\tilde{\kappa}_{tr}$, this becomes

$$
\begin{aligned}
(k_F)_{\kappa\lambda\mu\nu} w^\kappa x^\lambda y^\mu z^\nu = & -\frac{1}{2} \left(\left[w^0 \vec{x} - \vec{w} x^0 \right] \cdot (\tilde{\kappa}_{e-} + I\tilde{\kappa}_{tr}) \cdot \left[y^0 \vec{z} - \vec{y} z^0 \right] \right) \\
& -\frac{1}{2} \left(\left[w^0 \vec{x} - \vec{w} x^0 \right] \cdot \tilde{\kappa}_{o+} \cdot \left[\vec{y} \times \vec{z} \right] + \left[y^0 \vec{z} - \vec{y} z^0 \right] \cdot \tilde{\kappa}_{o+} \cdot \left[\vec{w} \times \vec{x} \right] \right) \\
& -\frac{1}{2} \left(\left[\vec{w} \times \vec{x} \right] \cdot (\tilde{\kappa}_{e-} + I\tilde{\kappa}_{tr}) \cdot \left[\vec{y} \times \vec{z} \right] \right).
\end{aligned}
$$

$$\text{(B.7)}$$

Appendix C

Appendices to Chapter 5

C.1 Exact Time Distribution

C.1.1 Probability of Beam Passage

The angular distribution relative to the surface normal of thermally emitted particles emitted from a locally smooth surface is commonly known to follow a cosine distribution [221]. According to [222], the first to show the cosine law was [223], using the 2nd law of thermodynamics as a foundation. The result follows from the assumption that the gas and surface are in thermodynamic equilibrium with one another, and so the angular distribution of particles emitted from the surface must precisely complement the angular distribution of particle impinging upon it, lest there be any net transfer of energy between the surface and the gas. Since one can show that the angular distribution with which particles in gaseous thermal equilibrium impinge upon a given point on a fixed surface is proportional to $\cos \theta$, the emitted particles must also follow the cosine distribution. Microscopic theories which yield the cosine law have also appealed to reciprocity and detailed balance considerations, although [224] provided a derivation of the cosine law which depends merely upon such reciprocity without relying on detailed balance. Note that this ignores such processes as atomic/molecular diffraction from the coated surface of the cell. It is commonly accepted that in equilibrium, the overall distribution of scattered atoms/molecules

must go as $\cos\theta$, although atoms belonging to a particular class of scattering process may not. Cases in which the atomic/molecular vapor is not in thermal equilibrium with the cell walls also yield different results. For example, it has been demonstrated by [225] that the parallel and normal velocity components of nonthermalized atoms impinging on a surface will thermalize at different rates.

For our purposes, we shall assume that the system is in equilibrium, no diffraction takes place, and that at the cell walls, all atoms are adsorbed and subsequently re-emitted according to a $\cos\theta$ distribution. This guarantees that the atomic velocities are Maxwell distributed at all points inside the cell, and precludes any net flow of the gas due to the cell walls. We may effectively treat the cell wall as if it were a completely permeable interface between the cell interior and a larger gas reservoir. If we count only those atoms which cross *into* the cell-region from this imaginary reservoir, we would find a total flux Φ_R, proportional only to the surface area of the cell, equal to the flux desorbed from the actual cell walls. Similarly, for the beam interaction region, we can define a flux Φ_r, of atoms entering the region $\rho < r$, proportional to its surface area. Because there is no correlation between an atom's position and its velocity, and since an atom which contributes to the flux Φ_r must necessarily have contributed to the flux Φ_R, the conditional probability that an atom contributes to Φ_r given its contribution to Φ_R is simply the ratio of the fluxes, and thus the ratio of the surface area of the interaction region to that of the enclosing vessel. Thus, for the case of an infinite cylindrical cell, the probability that an atom which is desorbed from the coating will pass through the interaction region is r/R. To properly determine the properties of the ultra-narrow EIT resonance in an anti-relaxation coated cell, however, we need not only the probability of interacting with the beam, but also the mean time of and between such interactions.

C.1.2   General Form of the Crossing Time Distribution

In general, there will exist a function which expresses the time necessary for a particle to move from one boundary to another as a function of the initial particle velocity v and some geometric parameters θ which define the particle's trajectory in

relation to the boundaries. This function will be given as

$$t(v, \theta), \tag{C.1}$$

whose solution for v is given by $T(t, \theta)$, and whose partial derivative with respect to v is $t'(v, \theta)$. We now wish to find the probability density function (p.d.f.) for the time spent crossing from one boundary to another. Given a thermal gas in equilibrium at temperature T, the p.d.f. for each of the particle velocity components is a simple Maxwellian. The distribution of the two-dimensional projection of those velocities is given by

$$f(v) = 2\pi v \left(\frac{M}{2\pi kT} \right) e^{-v^2 M/2kT}, \tag{C.2}$$

from which we may infer that the p.d.f. for the time t for a randomly selected crossing is then

$$g(t, \theta) = -2\pi T(t, \theta) \left(\frac{M}{2\pi kT} \right) e^{-T(t,\theta)^2 M/2kT} \frac{1}{t'(T(t, \theta), \theta)} \Theta(\theta), \tag{C.3}$$

with $\Theta(\theta)$ accounting for the distribution of trajectories, and the minus sign results from swapping the limits of integration (time goes to zero as velocity goes to infinity).

For free particles, the function $t(v, \theta) = (1/v)d(\theta)$, and so $t'(v, \theta) = -(1/v^2)d(\theta)$, and $T(t, \theta) = (1/t)d(\theta)$. This decoupling of the free trajectory from the initial particle velocity neglects the effects of external forces such as gravity, and should be valid for small vapor cells. This has the result that

$$g(t, \theta) = 2\pi \left(\frac{M}{2\pi kT} \right) \frac{d(\theta)^2}{t^3} e^{-d(\theta)^2 M/2kTt^2} \Theta(\theta) \tag{C.4}$$

It may easily be verified that integrating this p.d.f. over t from 0 to ∞, one obtains $\Theta(\theta)$. Integrating $tg(t, \theta)$ over the same region yields

$$\int_0^\infty dt\, tg(t, \theta) = \sqrt{\frac{\pi}{2} \frac{M}{kT}} d(\theta) \Theta(\theta) \tag{C.5}$$

Which means that the mean time crossing the geometrical region is simply $\sqrt{\frac{\pi}{2} \frac{M}{kT}}$ times the mean distance the particle must travel.

C.1.3 Cylindrical Cell with Infinite Length

We need to know the p.d.f. for the time atoms spend crossing the beam and sitting in the dark. We shall begin by seeking the p.d.f. for the time an atom spends traveling between two points on a circle (which may represent the circular cross section of a cylindrical or spherical cell). The distance an atom must cover depends as the cosine of the angle (θ) the atom's trajectory makes with the normal to the surface, thus for a cell with a circular cross section of diameter D,

$$t_{cross} = \frac{D}{v} \cos \theta, \tag{C.6}$$

Thanks to equation (C.6), we may infer the probability distribution of the time the atoms spend crossing the cell to be

$$g(t,\theta) = \frac{M}{kT} \frac{(D \cos \theta)^2}{t^3} e^{-\frac{M(D\cos\theta)^2}{t^2 2kT}} \cos \theta \tag{C.7}$$

Where we have also set $\Theta(\theta) \equiv \cos \theta$, as must be the case for the angular distribution of atoms desorbed from a smooth surface (see part C.1.1). We may express the above p.d.f. in the more general form:

$$g(t,\theta) = \frac{32\tau^2 \cos^3 \theta}{\pi^3 t^3} e^{-\frac{16\tau^2 \cos^2 \theta}{\pi^3 t^2}} \tag{C.8}$$

Where $\tau = D\sqrt{\frac{\pi^3 M}{32kT}}$, so that τ is the mean of t, assuming θ may vary between 0 and $\pi/2$. Note that because $g(t,\theta) \propto 1/t^3$, the variance of this distribution in t is undefined. This is a common characteristic of systems dominated by particles in free ballistic motion, exhibiting effusive rather than diffusive transport [226]. Despite this complication, the mean of $e^{-(\alpha-i\Delta)t}$ does exist, and has a formal definition (for complex x):

$$\begin{aligned}
\langle e^{-xt} \rangle &= \int_{-\pi/2}^{\pi/2} d\theta \, \frac{\tau^2 x^2 \cos^3 \theta}{4\sqrt{\pi}} G_{0,3}^{3,0} \left(\frac{\tau^2 x^2 \cos^2 \theta}{2} \bigg|_{-1,-\frac{1}{2},0} \right) \\
&= \frac{\tau^2 x^2}{4} G_{1,4}^{3,1} \left(\frac{\tau^2 x^2}{2} \bigg|_{-1,-\frac{1}{2},0,-\frac{3}{2}}^{-1} \right).
\end{aligned} \tag{C.9}$$

where $G_{p,q}^{m,n}$ is the Meijer-G function. $G_{1,4}^{3,1}$ can only be evaluated numerically, and becomes progressively more difficult to compute for large absolute values of the argument $\tau^2(\alpha - i\Delta)^2/2$. Examination of the function (C.9) in figure C.1 reveals a

(a)   (b)
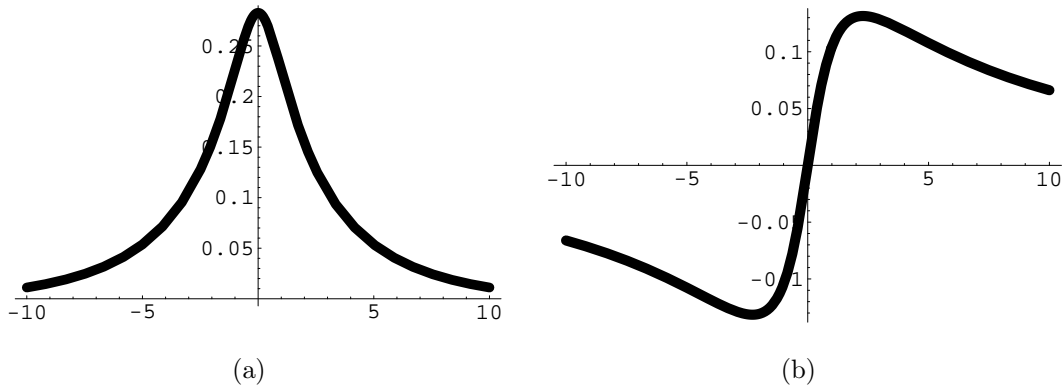
Figure C.1: Real (a) and imaginary (b) parts of the mean of $\langle e^{-(\alpha-i\Delta)t}\rangle$ over the exact p.d.f. with mean $\tau = 1$, as a function of Δ, in units of Δ/α.

Lorentzian structure, which suggests that we might approximate the marginal probability density function $g(t)$ with an exponential. Figure C.2 depicts the mean of $\langle e^{-(\alpha-i\Delta)t}\rangle$ over the exponential p.d.f.

$$g(t) = \frac{\sqrt{\pi}e^{-\sqrt{\frac{\pi}{2}}\frac{t}{\tau}}}{\sqrt{2}\tau}. \tag{C.10}$$

The rescaling of τ for the exponential p.d.f. is carried out to ensure that the mean of $\langle e^{-(\alpha-i\Delta)t}\rangle$ over the exponential has a width similar to that of the average over the exact p.d.f. A similar rescaling is commonly used when approximating gaussians with lorentzians in convolutions [227, 228].

C.1.4   Endcap Corrections

Now we will consider how to account for the ends of the cylinder. For a cylinder of radius R and length L, the probability that an atom will hit the end of the cylinder rather than the side is simply the ratio of the surface areas of the end and the sides, or

$$\frac{2\pi R^2}{2\pi RL} = \frac{R}{L} \tag{C.11}$$

which is simply half of the the inverse aspect ratio. Having already calculated the average time of flight for atoms which hit the cylinder walls, we may easily infer the

(a)   (b)
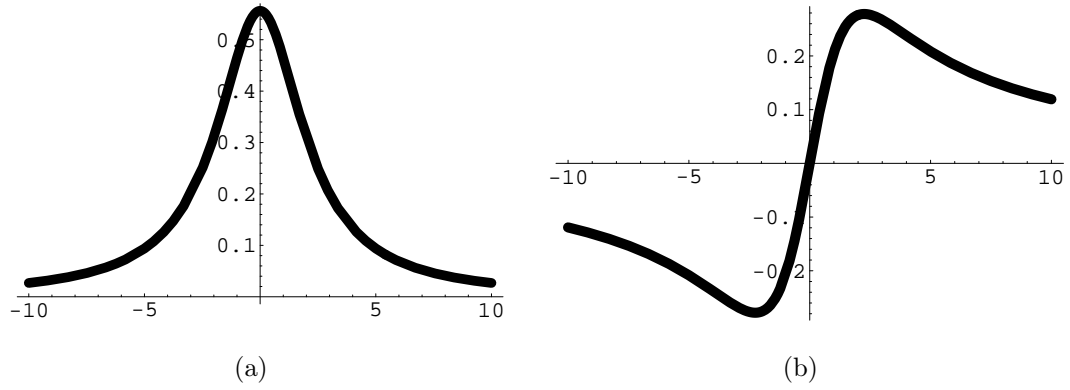
Figure C.2: Real (a) and imaginary (b) parts of the mean of $\langle e^{-(\alpha - i\Delta)t}\rangle$ over an exponential function with mean $\sqrt{\pi/2}\tau$, $\tau = 1$, as a function of Δ, in units of Δ/α.

average time of flight for atoms which hit the endcaps. If the atom hits the endcap, it must necessarily land at some distance R' from the center of the endcap. The average time of flight, for atoms starting from the side and landing on the endcap, is given by

$$\frac{1}{2}(\tau_w + \tau_{end,R'}) = \frac{1}{2}\frac{R^2\cos^{-1}(r/R) - r\sqrt{R^2 - r^2}}{\langle v_{xy}\rangle(R - r)} + \frac{1}{2}\frac{R'^2\cos^{-1}(r/R') - r\sqrt{R'^2 - r^2}}{\langle v_{xy}\rangle(R' - r)} \tag{C.12}$$

Of course, atoms can hit the endcap at any radius $R' \in [0, R]$, so we must integrate over the various possibilities, to obtain

$$\tau_{end} = \int_r^R \frac{R'dR'}{\pi(R^2 - r^2)} \frac{R'^2\cos^{-1}(r/R') - r\sqrt{R'^2 - r^2}}{\langle v_{xy}\rangle(R' - r)} \tag{C.13}$$

which can be evaluated numerically. By symmetry, this also equals the average time of crossing for an atom which leaves the endcap and hits the side of the cylinder. So the overall average time atoms which miss the beam take to cross the cell is given by

$$\left(1 - \frac{R}{L}\right)^2\tau_w + \left(1 - \frac{R}{L}\right)\frac{R}{L}(\tau_w + \tau_{end}) + \left(\frac{R}{L}\right)^2\tau_{end} = \left(1 - \frac{R}{L}\right)\tau_w + \frac{R}{L}\tau_{end} \tag{C.14}$$

The ends of the cylinder may also affect the average amount of time atoms spend interacting with the beam. Assuming that atoms do not interact with the beam while adsorbed on the cell coating, and since the average time atoms spend in the beam is

a linear function of the beam radius r, we have

$$\tau_{end} = \frac{\langle t_b \rangle}{r} \int_0^r \frac{r' dr'}{\pi r^2} \, r' = \frac{\langle t_b \rangle}{3\pi} \tag{C.15}$$

and so the average time the atoms interact with the field is given by

$$\langle t_b \rangle \left(1 - \frac{(3\pi - 1)r}{3\pi L} \right) \tag{C.16}$$

Thus the net effect of the ends of the cylinder is to decrease the average amount of time the atoms spend in the dark, and interact with the beam. Because the beam diameter is generally smaller than the diameter of the cell (*i.e.*, the beam has a high aspect ratio), this reduction is most significant for estimating the amount of time atoms spend in the dark.

C.1.5 Limitations

This approximation is best for systems with beam diameter much smaller than that of the cell ($d/D \ll 1$). The exponential p.d.f. is sharply peaked at $t = 0$, and so it tends to overestimate the fraction of atoms which cross the beam in a very short time. A result of this is that the approximate model predicts that atoms can survive more beam interactions before being appreciably optically pumped than they do in the exact model, and so tends to predict smaller ultra-narrow EIT bandwidths. For very small beams, when the mean crossing time τ is sufficiently small compared to the optical pumping rate, this overestimate has a relatively small effect, and so our model's predictions achieve better agreement with experiment, as illustrated by Figure 5.9.

Bibliography

[1] Peter J. Mohr, Barry N. Taylor, and David B. Newell, Rev. Mod. Phys **80**, 633 (2008).

[2] Sean M. Carroll, Jeffrey A. Harvey, V. Alan Kostelecký, Charles D. Lane, and Takemi Okamoto, Phys. Rev. Lett. **87**, 141601 (2001).

[3] V. Alan Kostelecký, Phys. Rev. D **69**, 105009 (2004).

[4] Don Colladay and V. Alan Kostelecký, Phys. Rev. D **55**, 6760 (1997).

[5] Don Colladay and V. Alan Kostelecký, Phys. Rev. D **58**, 116002 (1998).

[6] Paul L. Stanwix, Michael Edmund Tobar, Peter Wolf, Clayton R. Locke, and Eugene N. Ivanov, Phys. Rev. D **74**, 081101 (2006).

[7] Sven Herrmann, Alexander Senger, Katharina Moehle, Evgeny V. Kovalchuk, and Achim Peters, in *Proc. of Fourth Meeting on CPT and Lorentz Symmetry*, edited by V. Alan Kostelecký (World Scientific Publishing, Hackensack, NJ, 2007), Vol. IV, pp. 9–15.

[8] Michael Edmund Tobar, Peter Wolf, Alison Fowler, and John Gideon Hartnett, Phys. Rev. D **71**, 025004 (2005).

[9] Michael Hohensee, Alex Glenday, Chih-Hao Li, Michael Edmund Tobar, and Peter Wolf, Phys. Rev. D **75**, 049902(E) (2007).

[10] Michael A. Hohensee, Ralf Lehnert, David F. Phillips, and Ronald L. Walsworth, Phys. Rev. Lett. **102**, 170402 (2009).

[11] V. Alan Kostelecký and Neil Russell, `http://arxiv.org/abs/0801.0287` (2008.)

[12] Albert Einstein, Annalen der Physik **17**, 891 (1905).

[13] Hendrik Antoon Lorentz, KNAW, Proceedings **6**, 809 (1904).

[14] Albert A. Michelson, American Journal of Science **22**, 120 (1881).

[15] Albert A. Michelson and Abraham Morley, American Journal of Science **34**, 333 (1887).

[16] Roy J. Kennedy and Edward M. Thorndike, Phys. Rev. **42**, 400 (1932).

[17] Herbert E. Ives, JOSA **27**, 177 (1937).

[18] Herbert E. Ives, JOSA **27**, 389 (1937).

[19] Herbert E. Ives and George R. Stilwell, JOSA **28**, 215 (1938).

[20] Howard P. Robertson, Rev. Mod. Physics **21**, 378 (1949).

[21] Holger Müller, Sven Herrmann, Alejandro Saenz, and Achim Peters, Phys. Rev. D **68**, 116006 (2003).

[22] Peter Wolf, Sebastien Bize, Andre Clairon, Andre N. Luiten, Giorgio Santarelli, and Michael Edmund Tobar, Phys. Rev. Lett. **90**, 060402 (2003).

[23] G. Saathoff, S. Karpuk, U. Eisenbarth, G. Huber, S. Krohn, R. Munoz Horta, S. Reinhardt, D. Schwalm, A. Wolf, and G. Gwinner, Phys. Rev. Lett. **91**, 190403 (2003).

[24] V. Alan Kostelecký and Stuart Samuel, Phys. Rev. D **39**, 683 (1989).

[25] Robert Bluhm, Lect. Notes. Phys. **702**, 191 (2006).

[26] V. Alan Kostelecký, `http://lanl.arxiv.org/abs/hep-ph/0412406` (2004).

[27] V. Alan Kostelecký and Matthew Mewes, Phys. Rev. Lett. **87**, 251304 (2001).

[28] V. Alan Kostelecký and Matthew Mewes, Phys. Rev. D **66**, 056005 (2002).

[29] J. A. Lipa, J. A. Nissen, S. Wang, D. A. Stricker, and D. Avaloff, Phys. Rev. Lett. **90**, 060403 (2003).

[30] Peter Wolf, Sebastien Bize, Andre Clairon, Giorgio Santarelli, Michael Edmund Tobar, and Andre N. Luiten, Phys. Rev. D **70**, 051902 (2004).

[31] Sven Herrmann, Alexander Senger, Evgeny V. Kovalchuk, Holger Müller, and Achim Peters, Phys. Rev. Lett. **95**, 150401 (2005).

[32] Peter Wolf, Michael Edmund Tobar, Sebastien Bize, Andre Clairon, Andre N. Luiten, and Giorgio Santarelli, Gen. Relativ. and Grav. **36**, 2351 (2004).

[33] Holger Müller, Paul L. Stanwix, Michael Edmund Tobar, Eugene Ivanov, Peter Wolf, Sven Herrmann, Alexander Senger, Evgeny Kovalchuk, and Achim Peters, Phys. Rev. Lett. **99**, 050401 (2007).

[34] Sascha Reinhardt, Guido Saathoff, Henrik Buhr, Lars A. Carlson, Andreas Wolf, Dirk Schwalm, Sergei Karpuk, Christian Novotny, Gerhard Huber, Marcus Zimmermann, Ronald Holzwarth, Thomas Udem, Theodor W. Hansch, and Gerald Gwinner, Nature Physics **3**, 861 (2007).

[35] Sean M. Carroll, George B. Field, and Roman Jackiw, Phys. Rev. D **41**, 1231 (1990).

[36] Roman Jackiw and V. Alan Kostelecký, Phys. Rev. Lett. **82**, 2372 (1999).

[37] V. Alan Kostelecký and Matthew Mewes, Phys. Rev. Lett. **97**, 140401 (2006).

[38] V. Alan Kostelecký and Matthew Mewes, Phys. Rev. Lett. **99**, 011601 (2007).

[39] Quentin G. Bailey and V. Alan Kostelecký, Phys. Rev. D **70**, 076006 (2004).

[40] Christopher D. Carone, Marc Sher, and Marc Vanderhaeghen, Phys. Rev. D **74**, 077901 (2006).

[41] Brett Altschul, Phys. Rev. Lett. **96**, 201101 (2006).

[42] Brett Altschul, Phys. Rev. Lett. **98**, 041603 (2007).

[43] Brett Altschul, Phys. Rev. D **75**, 105003 (2007).

[44] F. R. Klinkhamer and M. Risse, Phys. Rev. D **77**, 016002 (2008).

[45] F. R. Klinkhamer and M. Schreck, Phys. Rev. D **78**, 085026 (2008).

[46] H. Dehmelt, R. Mittleman, R. S. Van Dyck, and P. Schwinberg, Phys. Rev. Lett. **83**, 4694 (1999).

[47] R. K. Mittleman, I. I. Ioannou, H. G. Dehmelt, and Neil Russell, Phys. Rev. Lett. **83**, 2116 (1999).

[48] G. Gabrielse, A. Khabbaz, D. S. Hall, C. Heimann, H. Kalinowsky, and W. Jhe, Phys. Rev. Lett. **82**, 3198 (1999).

[49] Robert Bluhm, V. Alan Kostelecký, and Neil Russell, Phys. Rev. Lett. **82**, 2254 (1999).

[50] Robert Bluhm, V. Alan Kostelecký, and Neil Russell, Phys. Rev. Lett. **79**, 1432 (1997).

[51] Robert Bluhm, V. Alan Kostelecký, and Neil Russell, Phys. Rev. D **57**, 3932 (1998).

[52] Don Colladay and V. Alan Kostelecký, Phys. Lett. B **511**, 209 (2001).

[53] Graham M. Shore, Nuclear Physics B **717**, 86 (2005).

[54] F. W. Stecker and S. L. Glashow, Astropart. Phys. **16**, 97 (2001).

[55] Brett Altschul, Phys. Rev. D **74**, 083003 (2006).

[56] Brett Altschul, Astropart. Phys. **28**, 380 (2007).

[57] B. R. Heckel, C. E. Cramer, T. S. Cook, E. G. Adelberger, S. Schlamminger, and U. Schmidt, Phys. Rev. Lett. **97**, 021603 (2006).

[58] Li-Shing Hou, Wei-Tou Ni, and Yu-Chu M. Li, Phys. Rev. Lett. **90**, 201101 (2003).

[59] Robert Bluhm and V. Alan Kostelecký, Phys. Rev. Lett. **84**, 1381 (2000).

[60] Holger Müller, Sven Herrmann, Alejandro Saenz, Achim Peters, and Claus Läemmerzahl, Phys. Rev. D **70**, 076004 (2004).

[61] Holger Müller, Phys. Rev. D **71**, 045004 (2005).

[62] B. R. Heckel, E. G. Adelberger, C. E. Cramer, T. S. Cook, S. Schlamminger, and U. Schmidt, Phys. Rev. D **78**, 092006 (2008).

[63] D. Bear, R. E. Stoner, R. L. Walsworth, V. Alan Kostelecký, and Charles D. Lane, Phys. Rev. Lett. **85**, 5038 (2000).

[64] David F. Phillips, Marc A. Humphrey, Edward M. Mattison, Richard E. Stoner, Robert F. C. Vessot, and Ronald L. Walsworth, Phys. Rev. D **63**, 111101 (2001).

[65] Marc A. Humphrey, David F. Phillips, Edward M. Mattison, Robert F. C. Vessot, Richard E. Stoner, and Ronald L. Walsworth, Phys. Rev. A **68**, 063807 (2003).

[66] F. Canè, David Bear, David F. Phillips, Matthew S. Rosen, Chris L. Smallwood, Richard E. Stoner, Ronald L. Walsworth, and V. Alan Kostelecký, Phys. Rev. Lett. **93**, 230801 (2004).

[67] S. J. Smullin, T. W. Kornack, G. Vasilakis, and M. V. Romalis, in *Proc. of Fourth Meeting on CPT and Lorentz Symmetry*, edited by V. Alan Kostelecký (World Scientific Publishing, Hackensack, NJ, 2007), Vol. IV, pp. 129–135.

[68] V. Alan Kostelecký and Charles D. Lane, Phys. Rev. D **60**, 116010 (1999).

[69] V. Alan Kostelecký and Charles D. Lane, J. Math. Phys. **40**, 6245 (1999).

[70] Charles D. Lane, Phys. Rev. D **72**, 016005 (2005).

[71] Don Colladay and Patrick McDonald, Phys. Rev. D **73**, 105006 (2006).

[72] Peter Wolf, Frederic Chapelet, Sebastien Bize, and Andre Clairon, Phys. Rev. Lett. **96**, 060801 (2006).

[73] Robert Bluhm, V. Alan Kostelecký, Charles D. Lane, and Neil Russell, Phys. Rev. Lett. **88**, 090801 (2002).

[74] Robert Bluhm, V. Alan Kostelecký, Charles Lane, and Neil Russell, Phys. Rev. D **68**, 125008 (2003).

[75] Orfeu Bertolami, Don Colladay, V. Alan Kostelecký, and Robertus Potting, Physics Letters B **395**, 178 (1997).

[76] G. Lambiase, Phys. Rev. D **72**, 087702 (2005).

[77] Jose Manuel Carmona, Jose Luis Cortes, Ashok Das, Jorge Gamboa, and Fernando Mendez, Mod. Phys. Lett. **21A**, 883 (2006).

[78] David Mattingly, Living Reviews in Relativity **8**, (2005).

[79] Brett Altschul, Phys. Rev. D **79**, 016004 (2009).

[80] LEP Energy Working Group, R. Assmann *et al.*, Eur. Phys. J. C **39**, 253 (2005).

[81] Holger Müller, Sheng wey Chiow, Sven Herrmann, Steven Chu, and Keng-Yeow Chung, Phys. Rev. Lett. **100**, 031101 (2008).

[82] Paul L. Stanwix, Michael Edmund Tobar, Peter Wolf, Mohamad Susli, Clayton R. Locke, Eugene N. Ivanov, John Winterflood, and Frank van Kann, Phys. Rev. Lett. **95**, 040404 (2005).

[83] V. Alan Kostelecký and Matthew Mewes, The Astrophysical Journal **689** L1 (2008).

[84] Matthew Mewes, Phys. Rev. D **78**, 096008 (2008).

[85] M. E. Tobar, Paul L. Stanwix, Mohamad Susli, Peter Wolf, Clayton R. Locke, and Eugene N. Ivanov, in *Rotating Resonator-Oscillator Experiments to Test Lorentz Invariance in Electrodynamics*, Vol. 702 of *Lecture Notes in Physics* (Springer, New York, NY, 2006), pp. 416–450.

[86] Michael A. Hohensee, Paul L. Stanwix, Michael Edmund Tobar, David F. Phillips, and Ronald L. Walsworth, to be published (2009).

[87] V. Alan Kostelecký and Ralf Lehnert, Phys. Rev. D **63**, 065008 (2001).

[88] D. P. Musumbu, H. B. Geyer, and W. D. Heiss, J. Phys. A: Math. Theor. **40**, F75 (2007).

[89] Suraj N. Gupta, *Quantum electrodynamics* (Gordon and Breach, New York, NY, 1977).

[90] Claude Cohen-Tannoudji, Jacques Dupont-Roc, and Gilbert Grynberg, *Photons and Atoms* (Wiley, New York, NY, 1997).

[91] Leslie L. Foldy and Siegfried A. Wouthuysen, Phys. Rev. **78**, 29 (1950).

[92] Michael A. Hohensee, Ralf Lehnert, David F. Phillips, and Ronald L. Walsworth, http://arxiv.org/abs/0809.3442 (2008).

[93] Erling Riis, Lars-Ulrik Aaen Andersen, Nis Bjerre, Ove Poulsen, Siu Au Lee, and John L. Hall, Phys. Rev. Lett. **60**, 81 (1988).

[94] Roger W. McGowan, David M. Giltner, Scott J. Sternberg, and Siu Au Lee, Phys. Rev. Lett. **70**, 251 (1993).

[95] R. Grieser, R. Klein, G. Huber, S. Dickopf, I. Klaft, P. Knobloch, P. Merz, F. Albrecht, M. Grieser, D. Habs, D. Schwalm, and T. Kuell, Appl. Phys. B **59**, 127 (1994).

[96] Willis E. Lamb, Phys. Rev. **134**, A1429 (1964).

[97] C. Novotny, B. Bernhardt, G. Ewald, C. Geppert, G. Gwinner, T. W. Haensch, R. Holzwarth, G. Huber, S. Karpuk, H.-J. Kluge, T. Kuel, W. Noertershaeuser, S. Reinhardt, G. Saathoff, D. Schwalm, T. Udem, and A. Wolf, Hyperfine Interactions **171**, 57 (2006).

[98] R. Grieser, P. Merz, G. Huber, M. Schmidt, V. Sebastian, V. Then, M. Grieser, D. Habs, D. Schwalm, and T. Kuell, Hyperfine Interactions **99**, 135 (1996).

[99] Dieter Hils and J. L. Hall, Phys. Rev. Lett. **64**, 1697 (1990).

[100] Eugeniy E. Mikhailov, Yuri V. Rostovtsev, and George R. Welch, J. Mod. Opt. **49**, 2535 (2002).

[101] Maneesh Jain, Hui Xia, G. Y. Yin, A. J. Merriam, and S. E. Harris, Phys. Rev. Lett. **77**, 4326 (1996).

[102] John L. Hall, Rev. Mod. Physics **78**, 1279 (2006).

[103] Savas Dimopoulos, Peter W. Graham, Jason M. Hogan, and Mark A. Kasevich, Phys. Rev. Lett. **98**, 111102 (2007).

[104] Savas Dimopoulos, Peter W. Graham, Jason M. Hogan, and Mark A. Kasevich, Phys. Rev. D **78**, 122002 (2008).

[105] M. Lewenstein, Ph. Balcou, M. Yu. Ivanov, Anne L'Huillier, and P. B. Corkum, Phys. Rev. A **49**, 2117 (1994).

[106] R. Jason Jones, Kevin D. Moll, Michael J. Thorpe, and Jun Ye, Phys. Rev. Lett. **94**, 193201 (2005).

[107] C. R. Locke, E. N. Ivanov, J. G. Hartnett, P. L. Stanwix, and M. E. Tobar, Rev. Sci. Instrum. **79**, 051301 (2008).

[108] Brett Altschul, Nucl. Phys. B **796**, 262 (2008).

[109] Sidney Coleman and Sheldon L. Glashow, Phys. Rev. D **59**, 116008 (1999).

[110] F. R. Klinkhamer and M. Risse, Phys. Rev. D **77**, 117901 (2008).

[111] E. F. Beall, Phys. Rev. D **1**, 961 (1970).

[112] T. Jacobson, S. Liberati, and D. Mattingly, Phys. Rev. D **67**, 124011 (2003).

[113] Ralf Lehnert, Phys. Rev. D **68**, 085003 (2003).

[114] Ralf Lehnert and Robertus Potting, Phys. Rev. Lett. **93**, 110402 (2004).

[115] Ralf Lehnert and Robertus Potting, Phys. Rev. D **70**, 125010 (2004).

[116] Ralf Lehnert and Robertus Potting, Phys. Rev. D **70**, 129906 (2004).

[117] S. K. Lamoreaux, J. P. Jacobs, B. R. Heckel, F. J. Raab, and E. N. Fortson, Phys. Rev. Lett. **57**, 3125 (1986).

[118] S. K. Lamoreaux, J. P. Jacobs, B. R. Heckel, F. J. Raab, and E. N. Fortson, Phys. Rev. A **39**, 1082 (1989).

[119] T. E. Chupp, R. J. Hoare, R. A. Loveman, E. R. Oteiza, J. M. Richardson, M. E. Wagshul, and A. K. Thompson, Phys. Rev. Lett. **63**, 1541 (1989).

[120] C. Adam and F. R. Klinkhamer, Nuclear Physics B **607**, 247 (2001).

[121] The HEGRA Collaboration, F. Aharonian *et al.*, Astrophys. J. **614**, 897 (2004).

[122] The OPAL Collaboration, K.Ackerstaff *et al.*, Eur. Phys. J. C **2**, 39 (1998).

[123] L3 Collaboration, P. Achard *et al.*, Phys. Lett. B **531**, 28 (2002).

[124] OPAL Collaboration, G. Abbiendi *et al.*, Eur. Phys. J. C **26**, 331 (2003).

[125] D0 Collaboration, V.M. Abazov *et al.*, Phys. Lett. B **639**, 151 (2006) [Erratum-ibid. B **658**, 285 (2008)].

[126] D0 Collaboration, V.M. Abazov *et al.*, Phys. Lett. B **666**, 435 (2008).

[127] D0 Collaboration, S. Abachi *et al.*, Nucl. Instrum. Meth. A **338**, 185 (1994).

[128] V. Alan Kostelecký and Austin G. M. Pickering, Phys. Rev. Lett. **91**, 031801 (2003).

[129] Stephen A. Fulling, Phys. Rev. D **7**, 2850 (1973).

[130] I. Fuentes-Schuller and R. B. Mann, Physical Review Letters **95**, 120404 (2005).

[131] F. Mandl and G. Shaw, *Quantum Field Theory* (Wiley, New York, NY, 1993).

[132] N. Cyr, M. Tetu, and M. Breton, Instrumentation and Measurement, IEEE Transactions on **42**, 640 (1993).

[133] Jacques Vanier, Aldo Godone, and Filippo Levi, Phys. Rev. A **58**, 2345 (1998).

[134] N. Vukicevic, A.S. Zibrov, L. Hollberg, F.L. Walls, J. Kitching, and H.G. Robinson, Ultrasonics, Ferroelectrics and Frequency Control, IEEE Transactions on **47**, 1122 (2000).

[135] J. Kitching, S. Knappe, N. Vukicevic, L. Hollberg, R. Wynands, and W. Weidmann, IEEE Transations on Instrumentation and Measurement **49**, 1313 (2000).

[136] Svenja Knappe, Vishal Shah, Peter D. D. Schwindt, Leo Hollberg, John Kitching, Li-Anne Liew, and John Moreland, Applied Physics Letters **85**, 1460 (2004).

[137] V. V. Yashchuk, D. Budker, and Max Zolotorev, preprint LBNL-43338 (unpublished).

[138] M. Stahler, S. Knappe, C. Affolderbach, W. Kemp, and R. Wynands, EPL (Europhysics Letters) **54**, 323 (2001).

[139] D. Budker, D. F. Kimball, S. M. Rochester, and V. V. Yashchuk, Phys. Rev. A **65**, 033401 (2002).

[140] Peter D. D. Schwindt, Svenja Knappe, Vishal Shah, Leo Hollberg, John Kitching, Li-Anne Liew, and John Moreland, Applied Physics Letters **85**, 6409 (2004).

[141] J. P. Cotter and B. Varcoe, `http://xxx.lanl.gov/abs/physics/0603111` (2006).

[142] D. Grischkowsky, Phys. Rev. A **7**, 2096 (1973).

[143] S. E. Harris, J. E. Field, and A. Kasapi, Phys. Rev. A **46**, R29 (1992).

[144] Michael M. Kash, Vladimir A. Sautenkov, Alexander S. Zibrov, Leo Hollberg, George R. Welch, Mikhail D. Lukin, Yuri Rostovtsev, Edward S. Fry, and Marlan O. Scully, Phys. Rev. Lett. **82**, 5229 (1999).

[145] David F. Phillips, A. Fleischhauer, A. Mair, and Ronald L. Walsworth, Phys. Rev. Lett. **86**, 783 (2001).

[146] H.-J. Briegel, W. Duer, J. Ignacio Cirac, and P. Zoller, Phys. Rev. Lett. **81**, 5932 (1998).

[147] W. Duer, H.-J. Briegel, J. Ignacio Cirac, and P. Zoller, Phys. Rev. A **59**, 169 (1999).

[148] L.-M. Duan, J. I. Cirac, P. Zoller, and E. S. Polzik, Phys. Rev. Lett. **85**, 5643 (2000).

[149] Mikhail D. Lukin, Axel Andre, Matthew Dixon Eisaman, Michael A. Hohensee, David F. Phillips, and Caspar H. van der Wal, in *Proceedings of the International Conference on Atomic Physics*, edited by H. R. Sadeghpour, D. E. Pritchard, and Eric J. Heller (World Scientific, Singapore, 2002), Vol. XVIII.

[150] Michael Fleischhauer and Mikhail D. Lukin, Phys. Rev. A **65**, 022314 (2002).

[151] L.-M. Duan and R. Raussendorf, Phys. Rev. Lett. **95**, 080503 (2005).

[152] L. Jiang, J. M. Taylor, and M. D. Lukin, Phys. Rev. A **76**, 012301 (2007).

[153] Mason Klein, Ph.d. thesis, Harvard University, 2009.

[154] Mason Klein, Yanhong Xiao, Alexey V. Gorshkov, Michael Hohensee, Cleo D. Leung, Mark R. Browning, David F. Phillips, Irina Novikova, and Ronald L. Walsworth, in *Optimizing slow and stored light for multidisciplinary applications*, edited by Selim M. Shahriar, Philip R. Hemmer, and John R. Lowell (SPIE, San Jose, 2008), No. 1, p. 69040C.

[155] L. V. Hau, S. E. Harris, Zachary Dutton, and C. H. Behroozi, Nature **397**, 594 (1999).

[156] Danielle A. Braje, Vlatko Balic, Sunil Goda, G. Y. Yin, and S. E. Harris, Phys. Rev. Lett. **93**, 183601 (2004).

[157] Chien Liu, Zachary Dutton, Cyrus H. Behroozi, and L. V. Hau, Nature **409**, 490 (2001).

[158] Zachary Dutton and L. V. Hau, Phys. Rev. A **70**, 053831 (2004).

[159] Christopher Slowe, Naomi S. Ginsberg, Trygve Ristroph, Anne Goodsell, and L. V. Hau, Optics and Photonics News **16**, 30 (2005).

[160] Naomi S. Ginsberg, Sean R. Garner, and L. V. Hau, Nature **445**, 623 (2007).

[161] L. V. Hau, Nature Photonics **2**, 451 (2008).

[162] Jevon Joseph Longdell, Phd thesis, Australian National University, 2003.

[163] E. Fraval, M. J. Sellars, and J. J. Longdell, http://arxiv.org/abs/quant-ph/0412061v2 (2004).

[164] E. Fraval, M. J. Sellars, and J. J. Longdell, Phys. Rev. Lett. **92**, 077601 (2004).

[165] J. J. Longdell and M. J. Sellars, Phys. Rev. A **69**, 032307 (2004).

[166] E. Fraval, M. J. Sellars, and J. J. Longdell, Phys. Rev. Lett. **95**, 030506 (2005).

[167] J. J. Longdell, E. Fraval, M. J. Sellars, and N. B. Manson, Phys. Rev. Lett. **95**, 063601 (2005).

[168] Matthew D. Eisaman, Sergey Polyakov, Michael A. Hohensee, Jingyun Fan, Philip Hemmer, and Alan Migdall, Proc. SPIE **6780**, 67800K (2007).

[169] Mason Klein, Irina Novikova, David F. Phillips, and Ronald L. Walsworth, http://xxx.lanl.gov/abs/quant-ph/0602131 (2006).

[170] Yanhong Xiao, Mason Klein, Michael Hohensee, Liang Jiang, David F. Phillips, Mikhail D. Lukin, and Ronald L. Walsworth, Phys. Rev. Lett. **101**, 043601 (2008).

[171] H. Mark Goldenberg, Daniel Kleppner, and Norman F. Ramsey, Phys. Rev. **123**, 530 (1961).

[172] H. G. Robinson, E. S. Ensberg, and H. G. Dehmelt, Bull. Am. Phys. Soc. **3**, 9 (1958).

[173] M. A. Bouchiat and J. Brossel, Phys. Rev. **147**, 41 (1966).

[174] Gurbax Singh, Philip Dilavore, and Carroll O. Alley, Review of Scientific Instruments **43**, 1388 (1972).

[175] H. G. Robinson and C. E. Johnson, Appl. Phys. Lett. **40**, 771 (1982).

[176] D. Budker, V. V. Yashchuk, and M. Zolotorev, Phys. Rev. Lett. **81**, 5788 (1998).

[177] Evgeny B. Alexandrov and Victor A. Bonch-Bruevich, Optical Engineering **31**, 711 (1992).

[178] S. I. Kanorsky, A. Weis, and J. Skalla, Appl. Phys. B **60**, S165 (1995).

[179] D. Budker, W. Gawlik, D. F. Kimball, S. M. Rochester, V. V. Yashchuk, and A. Weis, Rev. Mod. Physics **74**, 1153 (2002).

[180] E. B. Alexandrov, Marcis Auzinsh, D. Budker, D. F. Kimball, S. M. Rochester, and V. V. Yashchuk, J. Opt. Soc. Am. B **22**, 7 (2005).

[181] D. Budker, D. F. Kimball, S. M. Rochester, and V. V. Yashchuk, Phys. Rev. Lett. **83**, 1767 (1999).

[182] Yanhong Xiao, Irina Novikova, David F. Phillips, and Ronald L. Walsworth, Phys. Rev. Lett. **96**, 043601 (2006).

[183] Yanhong Xiao, Irina Novikova, David F. Phillips, and Ronald L. Walsworth, Optics Express **16**, 14128 (2008).

[184] A. I. Okunevich, Optics and Spectroscopy **97**, 834 (2004).

[185] A. I. Okunevich, Optics and Spectroscopy **97**, 842 (2004).

[186] A. I. Okunevich, J. Opt. Soc. Am. B **22**, 29 (2005).

[187] J. E. Field, K. H. Hahn, and S. E. Harris, Phys. Rev. Lett. **67**, 3062 (1991).

[188] J. E. Field, K. H. Hahn, and S. E. Harris, Phys. Rev. Lett. **67**, 3733 (1991).

[189] Hui Xia, S. J. Sharpe, A. J. Merriam, and S. E. Harris, Phys. Rev. A **56**, R3362 (1997).

[190] A. Mair, J. Hager, David F. Phillips, Ronald L. Walsworth, and Mikhail D. Lukin, Phys. Rev. A **65**, 031802(R) (2002).

[191] Michael Fleischhauer and Aaron S. Manka, Phys. Rev. A **54**, 794 (1996).

[192] Michael Fleischhauer and Mikhail D. Lukin, Phys. Rev. Lett. **84**, 4 (2000).

[193] Marlan O. Scully and M. Suhail Zubairy, *Quantum Optics*, 1st ed. (Cambridge University Press, New York, NY, 2001).

[194] Axel Andre, Ph.d. thesis, Harvard University, Cambridge, MA 02138, 2005.

[195] M. S. Shahriar, P. R. Hemmer, D. P. Katz, A. Lee, and M. G. Prentiss, Phys. Rev. A **55**, 2272 (1997).

[196] W. R. Bennett, Phys. Rev. **126**, 580 (1962).

[197] G. J. Pryde and A. G. White, Phys. Rev. A **68**, 052315 (2003).

[198] Yoav Sagi, Phys. Rev. A **68**, 042320 (2003).

[199] E. Knill, R. Laflamme, and G. J. Milburn, Nature **409**, 46 (2001).

[200] E. Knill, `http://arxiv.org/abs/quant-ph/0110144v2` (2001).

[201] E. Knill, Phys. Rev. A **66**, 052306 (2002).

[202] Federico M. Spedalieri, Hwang Lee, and Jonathan P. Dowling, Phys. Rev. Lett. **73**, 012334 (2006).

[203] Pieter Kok, W. J. Munro, Kae Nemoto, T. C. Ralph, Jonathan P. Dowling, and G. J. Milburn, Rev. Mod. Physics **79**, 135 (2007).

[204] John David Jackson, *Classical Electrodynamics*, 3rd ed. (Wiley, New York, NY, 1999).

[205] Eugen Merzbacher, *Quantum Mechanics*, 3rd ed. (Wiley, New York, NY, 1998).

[206] Axel Andre and Mikhail D. Lukin, Phys. Rev. Lett. **89**, 143602 (2002).

[207] J. Vanier, M. W. Levine, S. Kendig, D. Janssen, C. Everson, and M. J. Delaney, IEEE Transations on Instrumentation and Measurement **54**, 2531 (2005).

[208] S. Knappe, P. D. D. Schwindt, V. Shah, L. Hollberg, and J. Kitching, Optics Express **13**, 1249 (2005).

[209] Jacques Vanier, A. Godone, and F. Levi, Frequency and Time Forum, 1999 and the IEEE International Frequency Control Symposium **1**, 96 (1999).

[210] Sergei Zibrov, Irina Novikova, David F. Phillips, Aleksei V. Taichenachev, Valeriy I. Yudin, Ronald L. Walsworth, and Alexander S. Zibrov, Phys. Rev. A **72**, 011801(R) (2005).

[211] J. Vanier, M. W. Levine, D. Janssen, and M. J. Delaney, IEEE Trans. Instrum. Meas. **52**, 258 (2003).

[212] J. Vanier, M. W. Levine, D. Janssen, and M. J. Delaney, Phys. Rev. A **67**, 065801 (2003).

[213] J. Vanier, Appl. Phys. B **81**, 421 (2005).

[214] Irina Novikova, David F. Phillips, Alexander S. Zibrov, and Ronald L. Walsworth, Optics Letters **31**, 622 (2006).

[215] Irina Novikova, David F. Phillips, Alexander S. Zibrov, Ronald L. Walsworth, Aleksei V. Taichenachev, and Valeriy I. Yudin, Optics Letters **31**, 2353 (2006).

[216] Michael Crescimanno and Michael A. Hohensee, J. Opt. Soc. Am. B **25**, 2130 (2008).

[217] Kristan L. Corwin, Zheng-Tian Lu, Carter F. Hand, Ryan J. Epstein, and Carl E. Wieman, Applied Optics **37**, 3295 (1998).

[218] A. V. Taichenachev, A. M. Tumaikin, V. I. Yudin, M. Staehler, R. Wynands, J. Kitching, and L. Hollberg, Phys. Rev. A **69**, 024501 (2004).

[219] C. Adam and F. R. Klinkhamer, Nuclear Physics B **657**, 214 (2003).

[220] Ralf Lehnert, J. Math. Phys. **45**, 3399 (2004).

[221] D. Budker, L. Hollberg, D. F. Kimball, J. Kitching, S. Pustelny, and V. V. Yashchuk, Phys. Rev. A **71**, 012903 (2005).

[222] W. Steckelmacher, Rep. Prog. Phys. **49**, 1083 (1986).

[223] M. Knudsen, Ann. Phys., Lpz. **48**, 1113 (1916).

[224] E. P. Wenaas, J. Chem. Phys. **54**, 376 (1971).

[225] K. D. Gibson, N. Isa, and S. J. Sibener, J. Chem. Phys. **119**, 13083 (2003).

[226] G. M. Zaslavsky, Phys. Rep. **371**, 461 (2002).

[227] Yuri V. Rostovtsev, Igor Protsenko, Hwang Lee, and Ali Javan, J. Mod. Opt. **49**, 2501 (2002).

[228] Ali Javan, Olga Kocharovskaya, Hwang Lee, and Marlan O. Scully, Phys. Rev. A **66**, 013805 (2002).